12-9-2011

Nuclear Phenomena in Covariant Density Functional Theory

Hazem Abusara

Nuclear Phenomena in Covariant Density Functional Theory

Comments

Density functionals.||Nuclear structure.||Quantum theory.

NUCLEAR PHENOMENA IN COVARIANT DENSITY FUNCTIONAL THEORY

By

Hazem Abusara

A Dissertation
Submitted to the Faculty of
Mississippi State University
in Partial Fulfillment of the Requirements
for the Degree of Doctor of Philosophy
in Applied Physics
in the Department of Physics & Astronomy

Mississippi State, Mississippi

December 2011

NUCLEAR PHENOMENA IN COVARIANT DENSITY FUNCTIONAL THEORY

By

Hazem Abusara

Approved:

Anatoli V. Afanasjev
Professor of Physics
(Major Professor)

David L. Monts
Professor of Physics
(Graduate Coordinator)

Wenchao Ma
Professor of Physics
(Committee Member)

Jeff A. Winger
Professor of Physics
(Committee Member)

Gautam Rupak
Assistant Professor of Physics
(Committee Member)

Yaroslav Koshka
Associate Professor of Electrical & Computer Engineering
(Committee Member)

Sarah A. Rajala
Dean of the Bagley College of Engineering

Name: Hazem Abusara

Date of Degree: December 9, 2011

Institution: Mississippi State University

Major Field: Applied Physics

Major Professor: Dr. Anatoli Afanasjev

Title of Study: NUCLEAR PHENOMENA IN COVARIANT DENSITY FUNCTIONAL THEORY

Pages in Study: 246

Candidate for Degree of Doctor of Philosophy

In this dissertation, covariant density functional theory has been applied to a variety of nuclear phenomena in the ground and excited states of rotating and non-rotating nuclei. It has been applied for the interpretation of excited superdeformed bands in ^{154}Dy using the effective alignment methods. The properties of the predicted hyperdeformed nuclei at high spin in the $Z = 40 - 58$ region were investigated and the spins at which such configuration become yrast were defined. The moments of inertia, the role of single-particle energies and necking degree of freedom have also been studied. It also predicted that ^{107}Cd is the best nucleus for its observation.

The impact of time-odd mean fields (nuclear magnetism NM) in both non-rotating and rotating frame works, on physical observables has been studied. It is shown that nuclear magnetism always provide additional binding to the binding energies of odd-mass nuclei. Time-odd mean fields affect odd-even mass differences. However, the modifications of the strength of pairing correlations required to compensate for their effects are modest.

In contrast, time-odd mean fields have a profound effect on the properties of odd-proton nuclei in the vicinity of the proton drip line. Their presence can modify the half-lives of proton emitters and considerably affect the possibilities of their experimental observation. They also have a profound effect on the dynamic and kinematic moments of inertia, particle number, configuration, and rotational frequency dependencies of their impact on the moments of inertia. The effect of NM on the binding energy and moments of inertia weakly depend on the choice of the RMF parametrization.

Fission barriers are studied systematically with the allowence for triaxial deformations, in the actinide and superheavy regions. It is shown that covariant density functional theory is able to describe fission barriers, in actinides, on a level of accuracy comparable with nonrelativistic calculations. Triaxiality in the region of the first saddle plays a crucial role in achieving that. However, in the $Z = 112$ - 120 superheavy nuclei, the inner fission barriers are not affected by triaxiality. General trends of the evolution of inner fission heights are discussed.

DEDICATION

To my parents for the love and support during the past five years, and to my sister and brother for their encourgment. To my wife for her patience during the writing of the dissertation, and for my baby girl, I will always be there for you.

ACKNOWLEDGMENTS

I would like to thank Dr. Anatoli Afanasjev for his guidance and encouragement for the past five years, he taught me the concepts and tools of nuclear physics. It was a complete honor and privilege to do my dissertation under his supervision. I would like to thank the staff of the department of Physics & Astronomy for the help and kindness they showed through these years and many thanks to the amazing faculty who taught me the physics classes. I can't find enough words to express my gratitude to my colleagues who I've spent the past five years with, many thanks to: Saurabh Dayal, Nimisha Srivastava, Quarat-Ul-Ann Ijaz, Amrenda Narayan, Luwani Ndukum and Omadillo Abdurazakov.

TABLE OF CONTENTS

LIST OF TABLES

LIST OF FIGURES

CHAPTER 1

INTRODUCTION

1.1 Density functional theory

The development of self-consistent many-body theories aiming at the description of low-energy nuclear phenomena provides the necessary theoretical tools for an exploration of the nuclear chart into known and unknown regions. Theoretical methods (both relativistic and non-relativistic) formulated within the framework of density functional theory (DFT) and effective field theory (EFT) are the most promising tools for the global investigation of the properties of atomic nuclei. The DFT and EFT concepts in nuclear structure models have been extensively discussed in a number of recent articles [1, 2, 3, 4]. The power of the models based on these concepts is essentially unchallenged in medium and heavy mass nuclei where 'ab-initio' type few-body calculations are computationally impossible and the applicability of the spherical shell model is restricted to a few regions in the vicinity of doubly shell closures.

The self-consistent mean-field approach to nuclear structure represents an approximate implementation of Kohn-Sham density functional theory (DFT) [5, 6, 7, 8], which is successfully employed in the treatment of the quantum many-body problem in atomic, molecular and condensed matter physics. The DFT enables a description of the nuclear many-body problem in terms of energy density functionals (EDF), and self-consistent mean-field

models approximate these functionals, which include all higher-order correlations, with powers and gradients of ground-state nucleon densities (see Refs. [9, 10, 11, 3, 12] and references therein). EDF functionals are universal in the sense that they can be applied to nuclei all over the periodic table. Although they model the effective interaction between nucleons, EDF are not necessarily related to any nucleon-nucleon (NN) potential. By employing these energy functionals, adjusted to reproduce the empirical properties of symmetric and asymmetric nuclear matter, and bulk properties of some spherical nuclei, the current generation of self-consistent mean-field methods has achieved a high level of accuracy in the description of the ground states and the properties of excited states in arbitrarily heavy nuclei, exotic nuclei far from β-stability, and in nuclear systems at the nucleon driplines (see Refs. [10, 11, 13] and references therein). The self-consistent methods (such as Hartree-Fock (HF) or Hartree-Fock-Bogoliubov (HFB)) based on zero range Skyrme forces or finite range Gogny forces are frequently used in nuclear structure calculations [14, 10]. These approaches represent non-relativistic energy density functionals based on the Schrodinger equation for many-body nuclear problem [10].

On the other hand, one can formulate the class of relativistic models based on the Dirac formalism, which can generally be defined as *covariant density functionals* (CDF) [11]. These models, such as quantum hadrodynamics (QHD) [15, 9], are based on concepts of non-renormalizable effective relativistic field theories and DFT, and they provide a very interesting relativistic framework for the studies of nuclear structure phenomena at and far from the valley of $\beta-$stability [11]. Relativistic mean field (RMF) models [15] are analogs of the Kohn-Sham formalism of DFT [7], with local scalar and vector fields ap-

pearing in the role of local relativistic Kohn-Sham potentials [9, 1]. The energy density functional is approximated with the powers and gradients of auxiliary meson fields or nucleon densities. The EFT building of the energy density functional allows error estimates to be made, provides a power counting scheme which separates long- and short-distance dynamics and, therefore, removes model dependences from the self-consistent mean field approach [16]. In the description of nuclear ground states and the properties of excited states the self-consistent mean-field implementations of quantum hadrodynamics, the relativistic Hartree-Bogoliubov model (RHB) and the relativistic (quasiparticle) random phase approximation (RQRPA) and their subversions, are employed [11].

1.2 Nuclear phenomena

The aim of this dissertation is to discuss the application of covariant density functional theory (CDFT) to describe and explain several physical phenomena that are of interest to the nuclear physics community. The first one is the behavior of nuclei at extremes of high spin and deformation (Super- and hyoer-deformation). Since the discovery of superdeformation (SD) in ^{152}Dy two decades ago [17], nuclear SD has been in the focus of attention of the nuclear structure community; it has been discovered in different mass regions and extensively studied experimentally [18] and theoretically (see, for example, Refs. [19, 20, 21] and references therein). New phenomena such as identical bands [19] were discovered, and rich variety of experimental data allowed to test modern theoretical tools under extreme conditions of large deformation and fast rotation. Hyperdeformation (HD) is one of critical phenomena in nuclear structure, the study of which will consider-

ably advance our knowledge of nuclei at extreme conditions of very large deformation and fast rotation [21]. The studies of HD will also contribute into understanding of the crust of neutron stars, where extremely deformed nuclear structures are expected (see Ref. [22] and references therein). Although some experimental evidences of the existence of HD at low [23, 24] and high spin [25, 26, 27, 28] exist, the current experimental knowledge of HD is very limited. New generation of detectors such as GRETA [29] and AGATA [30] will definitely allow to study this phenomenon in more details. However, these detectors will become functional only around 2016. Thus, it is very important to understand whether new experimental information on HD can be obtained with existing detectors such as GAMMASPHERE [31].

The second topic is the importance of time-odd mean fields in the development of density functional theory and their impact on physical observables in both nonrotating and rotating nuclear systems. There was a dedicated effort to better understand time-odd mean fields in the framework of the Skyrme energy density functional (EDF) theory (see Refs. [32, 33, 34, 35] and references therein). On the contrary, much less attention has been paid to these fields in covariant density functional theory (CDFT) [36, 37, 38, 39]. This is due to the fact that time-odd mean fields are defined through the Lorentz invariance in the CDFT [11], and thus they do not require additional coupling constants. On the other hand, time-odd mean fields are not well defined in non-relativistic density functional theories [33, 35] and, as a consequence, there are a number of open questions related to these fields.

Finally, the description of fission barriers in actinides and superheavy regions of the nuclear chart. A study of the (static) inner fission barrier heights B_f^{st} of even-even nuclei is

motivated by the importance of this quantity for several physical phenomena. Many heavy nuclei decay by spontaneous fission, and the size of the fission barrier is a measure for the stability of a nucleus reflected in the spontaneous fission lifetimes of these nuclei [13]. The probability for the formation of a superheavy nucleus in a heavy-ion-fusion reaction is also directly connected to the height of its fission barrier [40]. The height B_f^{st} is a decisive quantity in the competition between neutron evaporation and fission of a compound nucleus in the process of its cooling. The large sensitivity of the cross section σ for the synthesis of the fissioning nuclei on the barrier height B_f^{st} stresses a need for accurate calculations of this value. For example, a change of B_f^{st} by 1 MeV changes the calculated survival probability of a synthesized nucleus by about one order of magnitude or even more [40]. The population and survival of hyperdeformed states at high spin also depends on the fission barriers [21]. In addition, the $r-$process of stellar nucleosynthesis depends (among other quantities such as masses and β-decay rates) on the fission barriers of very neutron-rich nuclei [41, 42].

During the last decade the role of triaxiality in the region of the saddle point of fission barriers has been recognized and tested in many theoretical frameworks. It was found that the height of the barrier is reduced when triaxial shapes are allowed [43, 44]. However, this lowering strongly depends on the proton and neutron numbers and on the model employed. The investigations of inner fission barriers with triaxiality included are available within the frameworks of the microscopic+macroscopic method [46, 47, 48, 49, 50], the extended Thomas-Fermi plus Strutinsky integral [51], and non-relativistic energy density functionals based on Skyrme [52, 53, 54, 43] and Gogny [44, 55, 56] forces.

This dissertation is organized in the following way: Ch.2 contains the formalism of different models of the covariant density functional theory in rotating and non-rotating frames, and the pairing correlation which is described through the BCS theory. Ch.3 is devoted for the study of the properties of hyperdeformed structures and the prediction of experimental observation of discrete hyperdeformed bands in the Cd isotopes. In Ch.4 systematic investigation of the properties and effects of time-odd mean field on different observables in non-rotating and rotating nuclear systems is performed. The systematic study of the effects of triaxiality on the height on the inner fission barrier in the actinide and superheavy regions of the nuclear chart are discussed in Ch.5. The summary of the major results is presented in Ch.6.

CHAPTER 2

FORMALISIM

2.1 General concepts of covariant density functional theory

In covariant density functional different models are intdoruced to describe the atomic nuclei. In this dissertation three of these models will be used in discribing at least one of the topics mentioned earlier in the introduction: the nonlinear meson nucleon coupling model, the density-dependent meson nucleon coupling model and a density-dependent point coupling model. The main difference between them is the treatment of the range of the interaction, the mesons, and density dependence. The interaction in the first two classes has a finite range, while the third class uses zero-range interaction. The mesons are absent in the density-dependent point coupling model. The density dependence is explicit in the last two models, while it shows up in the nonlinear meson nucleon coupling model through the non-linearity in the σ-meson. Each of these classes is represented by a set of parameters that is considered to be the state of the art. These parameterizations were adjusted to reproduce the properties of symmetric and asymmetric nuclear matter, binding energies, charge radii and differences between neutron and proton radii in spherical nuclei.

2.1.1 Lagrangian density for the meson-exchange models

In the meson-exchange models [57, 58, 59], the nucleus is described as a system of point like nucleon, Dirac spinors, interacting via the exchange of mesons with finite masses leading to the interactions of finite range. The starting point is a standard Lagrangian density [60]

$$\mathcal{L} = \mathcal{L}_N + \mathcal{L}_m + \mathcal{L}_{int} \tag{2.1}$$

The free nucleon Lagrangian density is given by:

$$\mathcal{L}_N = \bar{\psi}\gamma\left(i\partial - m\right)\psi \tag{2.2}$$

ψ is the Dirac spinor and m is the bare nucleon mass. The Lagrangian density of the meson and electromagnetic field is

$$\begin{aligned}\mathcal{L}_m = \frac{1}{2}\partial_\mu\sigma\partial_\mu\sigma - \frac{1}{2}m_\sigma^2\sigma^2 - \frac{1}{4}\Omega_{\mu\nu}\Omega^{\mu\nu} + \frac{1}{2}m_\omega^2\omega^2 \\ -\frac{1}{4}\vec{R}_{\mu\nu}\vec{R}^{\mu\nu} + \frac{1}{2}m_\rho^2\vec{\rho}^2 - \frac{1}{4}F_{\mu\nu}F^{\mu\nu}\end{aligned} \tag{2.3}$$

where

$$\begin{aligned}\Omega_{\mu\nu} &= \partial_\mu\omega_\nu - \partial_\nu\omega_\mu \\ \vec{R}_{\mu\nu} &= \partial_\mu\vec{\rho}_\nu - \partial_\nu\vec{\rho}_\mu \\ F_{\mu\nu} &= \partial_\mu A_\nu - \partial_\nu A_\mu\end{aligned} \tag{2.4}$$

and the interaction Lagrangian density is given by:

$$\mathcal{L}_{int} = -\bar{\psi}\left(g_\sigma\sigma + g_\omega\gamma^\mu\omega^\mu + g_\rho\vec{\tau}\gamma^\mu\rho_\mu + e\frac{1-\tau_3}{2}\gamma^\mu A_\mu\right)\psi \tag{2.5}$$

It contains the Dirac spinors with several effective mesons characterized by the quantum numbers of spin J, parity P, and isospin T. These mesons are: the σ meson ($J = 0,\ T = 0,\ P = +1$), the ρ meson ($J = 1,\ T = 1,\ P = -1$), the ω meson ($J = 1,\ T = 0,\ P = -1$). They create effective fields in a Dirac equation, which corresponds to the Kohn-Sham equation [61] in the non-relativistic case.

The Lagrangian (2.1.1) contains as parameters the meson masses m_σ, m_ω, and m_ρ and the coupling constants g_σ, g_ω, and g_ρ. e is the charge of the protons and it vanishes for neutrons. This linear model has first been introduced by Walecka model [62, 15].

To treat the density dependence in this model Boguta and Bodmer [63] introduced a density dependence via a non-linear meson coupling replacing the term $\frac{1}{2}m_\sigma^2\sigma^2$ in Eq. (2.1.1) by

$$U(\sigma) \ = \ \frac{1}{2}m_\sigma^2\sigma^2 + \frac{1}{3}g_2\sigma^3 + \frac{1}{4}g_3\sigma^4. \tag{2.6}$$

The nonlinear meson nucleon coupling is represented by the parameter set NL3* [57] (see Table 2.1), which is a modern version of the widely used parameter set NL3 [64]. Apart from the fixed values for the masses m, m_ω and m_ρ, there are six phenomenological parameters m_σ, g_σ, g_ω, g_ρ, g_2, and g_3.

The density-dependent meson-nucleon coupling model has an explicit density dependence for the meson-nucleon vertices. There are no nonlinear terms in the σ meson, i.e. $g_2 = g_3 = 0$. The meson-nucleon vertices are defined as:

$$g_i(\rho) = g_i(\rho_{sat})f_i(x) \quad \text{for} \quad i = \sigma, \omega, \rho \tag{2.7}$$

where the density dependence is given by

$$f_i(x) = a_i \frac{1 + b_i(x + d_i)^2}{1 + c_i(x + d_i)^2}. \tag{2.8}$$

for σ and ω and by

$$f_\rho(x) = \exp(-a_\rho(x - 1). \tag{2.9}$$

for the ρ meson. x is defined as the ratio between the baryonic density ρ at a specific location and the baryonic density at saturation ρ_{sat} in symmetric nuclear matter. The eight parameters in Eq. (2.8) are not independent, but constrained as follows: $f_i(1) = 1$, $f_\sigma^{''}(1) = f_\omega^{''}(1)$, and $f_i^{''}(0) = 0$. These constrains reduce the number of independent parameters for density dependence to three. This model is represented in the present investigations by the parameter set DD-ME2 [59] given in Table 2.1.

2.1.2 Lagrangian density for the point coupling models

The Lagrangian for the density-dependent point coupling model is given by :

$$\begin{aligned}
\mathcal{L} &= \bar{\psi}\left(i\gamma \cdot \partial - m\right)\psi \\
&- \frac{1}{2}\alpha_S(\hat{\rho})\left(\bar{\psi}\psi\right)\left(\bar{\psi}\psi\right) - \frac{1}{2}\alpha_V(\hat{\rho})\left(\bar{\psi}\gamma^\mu\psi\right)\left(\bar{\psi}\gamma_\mu\psi\right) \\
&- \frac{1}{2}\alpha_T V(\hat{\rho})\left(\bar{\psi}\vec{\tau}\gamma^\mu\psi\right)\left(\bar{\psi}\vec{\tau}\gamma_\mu\psi\right) \\
&- \frac{1}{2}\delta_S\left(\partial_v\bar{\psi}\right)\left(\partial^v\bar{\psi}\right) - e\bar{\psi}\gamma \cdot A\frac{(1 - \tau_3)}{2}\psi
\end{aligned} \tag{2.10}$$

It contains the free-nucleon Lagrangian, the point coupling interactions terms, coupling of the proton to the electromagnetic field. The derivative term accounts for the finite-range interactions.

Table 2.1

NL3* and DD-ME2 parameterizations of the RMF Lagrangian

Parameter	NL3*	DD-ME2
m	939	939
m_σ	502.5742	550.1238
m_ω	782.600	783.000
m_ρ	763.000	763.000
g_σ	10.0944	10.5396
g_ω	12.8065	13.0189
g_ρ	4.5748	3.6836
g_2	-10.8093	0.00000
g_3	-30.1486	0.00000
a_σ	0.00000	1.3881
b_σ	0.00000	1.0943
c_σ	0.00000	1.7057
d_σ	0.00000	0.4421
a_ω	0.00000	1.3892
b_ω	0.00000	0.9240
c_ω	0.00000	1.4620
d_ω	0.00000	0.4775
a_ρ	0.00000	0.5647

In analog to the conventional meson-exchange covariant density functional models, this model contains isoscalar-scalar, isoscalar-vector and isovector-vector interactions. It is represented by the DD-PC1 [65](see Table.2.2).

Table 2.2

DD-PC1 parameterization in the RMF Lagrangian

Parameter	DD-PC1
m	939
a_σ	-10.04616
b_σ	-9.15042
c_σ	-6.42729
d_σ	1.37235
a_ω	5.91946
b_ω	8.86370
d_ω	0.65835
b_ρ	1.83595
d_ρ	0.64025

2.2 The Hamiltonian and the equation of motions

CDFT is easily extended to the rotating frame [66, 67, 68, 20]. It has been successfully tested in a systematic way on the properties of different types of rotational bands in the regime of weak pairing such as normal-deformed [69], superdeformed [70, 20] and smooth terminating bands [11]. It is also able to describe the nuclear systems with broken time-reversal symmetry in intrinsic frame at no rotation as well as the properties of fission barriers in actinides and superheavy regions of the nuclear chart.

In the Hartree approximation, the stationary Dirac equation for the nucleons in the rotating frame (in one-dimensional cranking approximation, with rotation around the x-axis) is given by

$$(\hat{h}_D - \Omega_x \hat{J}_x)\psi_i = \varepsilon_i \psi_i \tag{2.11}$$

where $\hat{h}_D$ is the Dirac Hamiltonian for the nucleon with mass m

$$\hat{h}_D = \boldsymbol{\alpha}(-i\boldsymbol{\nabla} - \boldsymbol{V}(\boldsymbol{r})) \; + \; V_0(\boldsymbol{r}) \; + \; \beta(m + S(\boldsymbol{r})) \tag{2.12}$$

and the term

$$-\Omega_x \hat{J}_x = -\Omega_x \left(\hat{L}_x + \frac{1}{2}\hat{\Sigma}_x \right) \tag{2.13}$$

is just the Coriolis term. Note that the rotational frequency Ω_x along the x-axis is defined from the condition that the expectation value of the total angular momentum at spin I has a definite value [71]

$$J(\Omega_x) = \langle \Phi_\Omega \mid \hat{J}_x \mid \Phi_\Omega \rangle = \sqrt{I(I+1)}. \tag{2.14}$$

the Dirac Hamiltonian contains the average fields determined by the mesons[1], i.e. the attractive scalar field $S(\mathbf{r})$

$$S(\boldsymbol{r}) = g_\sigma \sigma(\boldsymbol{r}), \tag{2.15}$$

and the repulsive time-like component of the vector field $V_0(\boldsymbol{r})$

$$V_0(\boldsymbol{r}) = g_\omega \omega_0(\boldsymbol{r}) + g_\rho \tau_3 \rho_0(\boldsymbol{r}) + e\frac{1-\tau_3}{2} A_0(\boldsymbol{r}). \tag{2.16}$$

[1] discussion here will be restricted to the meson exchange models

A magnetic potential $\boldsymbol{V}(\boldsymbol{r})$

$$\boldsymbol{V}(\boldsymbol{r}) = g_\omega \boldsymbol{\omega}(\boldsymbol{r}) + g_\rho \tau_3 \boldsymbol{\rho}(\boldsymbol{r}) + e\frac{1-\tau_3}{2}\boldsymbol{A}(\mathbf{r}) \tag{2.17}$$

originates from the space-like components of the vector mesons. Note that in these equations, the four-vector components of the vector fields ω^μ, ρ^μ, and A^μ are separated into the time-like (ω_0, ρ_0 and A_0) and space-like [$\boldsymbol{\omega} = (\omega^x, \omega^y, \omega^z)$, $\boldsymbol{\rho} = (\rho^x, \rho^y, \rho^z)$, and $\boldsymbol{A} = (A^x, A^y, A^z)$] components. In the Dirac equation the magnetic potential has the structure of a magnetic field.

The corresponding meson fields and the electromagnetic potential are determined by the Klein-Gordon equations[2]

$$\begin{aligned}
\left\{-\Delta - (\Omega_x L_x)^2 + m_\sigma^2\right\}\ \sigma(\boldsymbol{r}) &= -g_\sigma[\rho_s^n(\boldsymbol{r}) + \rho_s^p(\boldsymbol{r})] \\
&\quad -g_2\sigma^2(\boldsymbol{r}) - g_3\sigma^3(\boldsymbol{r}), && (2.18)\\
\left\{-\Delta - (\Omega_x L_x)^2 + m_\omega^2\right\}\omega_0(\boldsymbol{r}) &= g_\omega[\rho_v^n(\boldsymbol{r}) + \rho_v^p(\boldsymbol{r})], && (2.19)\\
\left\{-\Delta - (\Omega_x J_x)^2 + m_\omega^2\right\}\ \boldsymbol{\omega}(\boldsymbol{r}) &= g_\omega[\boldsymbol{j}^n(\boldsymbol{r}) + \boldsymbol{j}^p(\boldsymbol{r})] && (2.20)\\
\left\{-\Delta - (\Omega_x L_x)^2 + m_\rho^2\right\}\rho_0(\boldsymbol{r}) &= g_\rho[\rho_v^n(\boldsymbol{r}) - \rho_v^p(\boldsymbol{r})], && (2.21)\\
\left\{-\Delta - (\Omega_x L_x)^2 + m_\rho^2\right\}\ \boldsymbol{\rho}(\boldsymbol{r}) &= g_\rho[\boldsymbol{j}^n(\boldsymbol{r}) - \boldsymbol{j}^p(\boldsymbol{r})], && (2.22)\\
-\Delta A_0(\boldsymbol{r}) = e\rho_v^p(\boldsymbol{r}), &\qquad -\Delta\boldsymbol{A}(\boldsymbol{r}) = e\boldsymbol{j}^p(\boldsymbol{r}), && (2.23)
\end{aligned}$$

[2]These equations are only valid for the case of the meson-exchange models, Eq. (2.1.1). The mesons are absent In the case of the point coupling model.

with source terms involving the various nucleonic densities and currents

$$\rho_s^{n,p}(\boldsymbol{r}) = \sum_{i=1}^{N,Z}(\psi_i(\boldsymbol{r}))^\dagger\hat{\beta}\psi_i(\boldsymbol{r}), \tag{2.24}$$

$$\rho_v^{n,p}(\boldsymbol{r}) = \sum_{i=1}^{N,Z}(\psi_i(\boldsymbol{r}))^\dagger\psi_i(\boldsymbol{r}), \tag{2.25}$$

$$\boldsymbol{j}^{n,p}(\boldsymbol{r}) = \sum_{i=1}^{N,Z}(\psi_i(\boldsymbol{r}))^\dagger\hat{\boldsymbol{\alpha}}\psi_i(\boldsymbol{r}) \tag{2.26}$$

where the labels n and p are used for neutrons and protons, respectively. In the equations above, the sums run over the occupied positive-energy shell model states only (*no-sea approximation*) [15, 72]. Note that the spatial components of the vector potential $\boldsymbol{A}(\boldsymbol{r})$ are neglected in the calculations since the coupling constant of the electromagnetic interaction is small compared with the coupling constants of the meson fields. For the case of no rotation one simply substitute $\Omega_x = 0$.

The magnetic potential $\boldsymbol{V}(\boldsymbol{r})$ in the Dirac equation as well as the currents $\boldsymbol{j}^{n,p}(\boldsymbol{r})$ in the Klein-Gordon equations do not appear in the CDFT equations for time-reversal systems [15]. Similar to the nonrelativistic case, their presence leads to the appearance of time-odd mean fields. Thus, we will use the terms *nuclear magnetism* and *time-odd mean fields* interchangeably throughout this dissertation. The magnetic potential is the contribution to the mean field that breaks time-reversal symmetry in the intrinsic frame and induces non-vanishing currents $\boldsymbol{j}^{n,p}$ (Eq. (2.26)) in the Klein-Gordon equations (Eqs. (2.20), (2.22)), which are related to the space-like components of the vector mesons. Note that the current $\boldsymbol{j}^{n,p}(\boldsymbol{r})$ change the sign upon the action of time-reversal operator [73]. Together with densities it forms covariant four-vector $j^\mu = \{\rho, \boldsymbol{j}\}$. As a consequence, these two quantities (ρ and $\boldsymbol{j}$) do not transform independently under Lorentz transformation. This explains

why the structure of the Klein-Gordon equations for time-like and space-like components of vector mesons is the same (compare, for example, Eqs. (2.19) and (2.20) for ω-meson) and why the same coupling constant stands in front of the densities and currents on the right hand side of these equations.

In rotating system one should distinguish time-odd mean fields originating from Coriolis operator and magnetic potential. The Coriolis operator is always present in the description of rotating nuclei in the framework of the cranking model. However, the CDFT calculations in the rotating frame, with only these time-odd fields accounted for, underestimate the experimental moments of inertia [68, 20]. A similar situation also holds in non-relativistic theories [33, 74]. The inclusion of the currents $\boldsymbol{j}^{n,p}(\boldsymbol{r})$ into the Klein-Gordon equations considerably improves the description of experimental moments of inertia.

The spatial components of the vector ω and ρ mesons lead to the interactions between possible currents. For the ω-meson this interaction is attractive for all combinations (pp, nn and pn-currents), and for the ρ-meson it is attractive for pp and nn-currents but repulsive for pn-currents. Within mean field theory such currents occur only in the situations of broken time-reversal symmetry.

The currents are isoscalar and isovector in nature for the ω and ρ mesons (Eqs. (2.20, 2.22)), respectively. As a consequence, the contribution of the ρ-meson to magnetic potential and total energy is marginal in the majority of the cases even at the neutron-drip line. Thus, time-odd mean fields in the CDFT framework depend predominantly on the spatial components of the ω meson. Neglecting the contribution of the ρ meson, one can see that

only two parameters, namely, the mass m_ω and coupling constant g_ω of the ω meson define the properties of time-odd mean fields (Eqs. (2.17), (2.20), and (2.22)).

The stationary solution of the CDFT equations corresponds to the ground state of the nucleus (i.e. corresponds to a local minimum in the potential energy surface). However, in order to obtain a solution for any point in deformation space one has to impose constraints on the mass moments. In this dissertation, calculations are restricted to the quadrupole mass moment unless otherwise stated. The method of quadratic constraints uses a variation of the function

$$\langle H \rangle + \sum_{\mu=0,2} C_{2\mu}(\langle \hat{Q}_{2\mu} \rangle - q_{2\mu})^2 \tag{2.27}$$

where $\langle H \rangle$ is the total energy, and $\langle \hat{Q}_{2\mu} \rangle$ denotes the expectation values of the mass quadrupole operators

$$\hat{Q}_{20} = 2z^2 - x^2 - y^2 \tag{2.28}$$

$$\hat{Q}_{22} = x^2 - y^2 \tag{2.29}$$

In these equations, $q_{2\mu}$ is the constrained value of the multipole moment, and $C_{2\mu}$ the corresponding stiffness constants [14]. The details of the constrained calculations will be discussed in Appendix A

2.3 Energy-density functional

In CDFT the energy can be written as a functional of the density matrix $\hat{\rho}$ and mesons field ${\phi_m}$[3]:

[3] ${\phi_m}$ represents ϕ_σ, ϕ_ρ,ϕ_ω and $\boldsymbol{A}$

$$E[\hat{\rho},\phi_m] = Tr[(\boldsymbol{\alpha p}+\beta m)\hat{\rho}] \pm \int \left[\frac{1}{2}(\nabla\phi_m)^2 + U(\phi_m)\right] d^3r + Tr[(g_m\phi_m)\hat{\rho}] \quad (2.30)$$

The total energy of the system is given in Refs. [66, 20]. We split it into different terms as [4]

$$\begin{aligned} E_{tot} &= E_{part} + E_{cm} - E_\sigma - E_{\sigma NL} - E_\omega^{TL} - E_\rho^{TL} \\ &\quad -E_\omega^{SL} - E_\rho^{SL} - E_{Coul}, \end{aligned} \quad (2.31)$$

where E_{part} and E_{cm} represent the contributions from fermionic degrees of freedom, while the other terms are related to mesonic (bosonic) degrees of freedom. In Eq. (2.31)

$$E_{part} = \sum_i^A \varepsilon_i, \quad (2.32)$$

is the energy of the particles moving in the field created by the mesons (ε_i is the energy of i-th particle and the sum runs over all occupied proton and neutron states)

$$E_\sigma = \frac{1}{2}\, g_\sigma \int d^3r\ \sigma(\boldsymbol{r})\left[\rho_s^p(\boldsymbol{r}) + \rho_s^n(\boldsymbol{r})\right], \quad (2.33)$$

is the linear contribution to the energy of isoscalar-scalar σ-field

$$E_{\sigma NL} = \frac{1}{2}\int d^3r \left[\frac{1}{3}\, g_2\, \sigma^3(\boldsymbol{r}) + \frac{1}{2}\, g_3\, \sigma^4(\boldsymbol{r})\right], \quad (2.34)$$

is the non-linear contribution to the energy of isoscalar-scalar σ-field

$$E_\omega^{TL} = \frac{1}{2}\, g_\omega \int d^3r\, \omega_0(\boldsymbol{r})\left[\rho_v^p(\boldsymbol{r}) + \rho_v^n(\boldsymbol{r})\right], \quad (2.35)$$

[4] We follow Refs. [75, 76] in the selection of the signs of the energy terms.

is the energy of the time-like component of isoscalar-vector ω-field

$$E_{\rho}^{TL} = \frac{1}{2}\, g_{\rho} \int d^3r \rho_0(\boldsymbol{r}) \left[\rho_v^n(\boldsymbol{r}) - \rho_v^p(\boldsymbol{r})\right], \tag{2.36}$$

is the energy of the time-like component of isovector-vector ρ-field

$$E_{\omega}^{SL} = -\frac{1}{2}\, g_{\omega} \int d^3r\, \boldsymbol{\omega}(\boldsymbol{r}) \left[\boldsymbol{j}^p(\boldsymbol{r}) + \boldsymbol{j}^n(\boldsymbol{r})\right], \tag{2.37}$$

is the energy of the space-like component of isoscalar-vector ω-field

$$E_{\rho}^{SL} = -\frac{1}{2}\, g_{\rho} \int d^3r\, \boldsymbol{\rho}(\boldsymbol{r}) \left[\boldsymbol{j}^n(\boldsymbol{r}) - \boldsymbol{j}^p(\boldsymbol{r})\right], \tag{2.38}$$

is the energy of the space-like component of isovector-vector ρ-field

$$E_{Coul} = \frac{1}{2}\, e \int d^3r A_0(\boldsymbol{r}) \rho_v^p(\boldsymbol{r}), \tag{2.39}$$

is the Coulomb energy

$$E_{cm} = -\frac{3}{4}\hbar\omega_0 = -\frac{3}{4}\, 41 A^{-1/3}\ \mathrm{MeV}, \tag{2.40}$$

is the correction for the spurious center-of-mass motion approximated by its value in a non-relativistic harmonic oscillator potential.

However, in the case of the density-dependent models the center of mass correction is given by:

$$E_{c.m.} = -\frac{\left\langle P_{c.m.}^2 \right\rangle}{2Am} \tag{2.41}$$

where $P_{c.m.}$ is the total momentum of a nucleus with A nucleons.

The total energy of the system can alternatively be written as (similar to Refs. [75, 76])

$$E_{tot} = E_{kin} + E_{int} + E_{cm} \tag{2.42}$$

where the kinetic energy E_{kin} is given by

$$E_{kin} = E_{part} - 2\left(E_{\sigma} + E_{\omega}^{TL} + E_{\rho}^{TL} + E_{Coul}\right) \tag{2.43}$$

and the interaction energy between the nucleons E_{int} by

$$\begin{aligned} E_{int} &= E_{\sigma} + E_{\omega}^{TL} + E_{\rho}^{TL} + E_{Coul} \\ &\quad -E_{\sigma NL} - E_{\omega}^{SL} - E_{\rho}^{SL}. \end{aligned} \tag{2.44}$$

2.4 Pairing correlations

Pairing correlations are taken into account through the BCS approximation. The CDFT-equations are solved and at each step of the iteration the BCS occupation probabilities v_k^2 are determined. These quantities are used in the calculation of densities, energies and new fields for the next step of the iteration. We use monopole pairing force with the strength parameters G_τ for neutrons ($\tau = n$) and protons ($\tau = p$); this method is based on the residual interaction of the seniority model [14].

We start with a pairing strength parameters G and solve in each step of the iteration the gap equation [14]

$$\frac{1}{G} = \sum_{k>0} \frac{1}{2E_k} \tag{2.45}$$

with $E_k = \sqrt{(\varepsilon_k - \lambda)^2 + \Delta^2}$, where ε_k are the eigenvalues of the Dirac equation and the chemical potential λ is determined by the average particle number. Then the occupation probabilities

$$v_k^2 = \frac{1}{2}\left(1 - \frac{\varepsilon_k - \lambda}{E_k}\right), \tag{2.46}$$

and the gap parameters

$$\Delta = G \sum_{k>0} u_k v_k \tag{2.47}$$

are determined in a self-consistent way. The pairing energy is defined as

$$E_{\text{pair}} = -\Delta \sum_{k>0} u_k v_k, \tag{2.48}$$

The sum over k in Eqs. (2.45), (2.47) and (2.48) run over all states in the pairing window $E_k < E_{\text{cutoff}}$. The inclusion or the exclusion of pairing correlations from the calculations will depend on the specific nuclear phenomena under study and it will be mentioned in the relevant chapter.

2.5 The wave function

The CDFT equations are solved in the basis of an anisotropic three-dimensional harmonic oscillator in Cartesian coordinates characterized by the deformation parameters β_0 and γ and oscillator frequency $\hbar\omega_0 = 41A^{-1/3}$ MeV, for details see Refs. [66, 20]. They are solved in the parity, signature basis. Single-particle orbitals are labeled by $[Nn_z\Lambda]\Omega^{sign}$. $[Nn_z\Lambda]\Omega$ are the asymptotic quantum numbers (Nilsson quantum numbers) of the dominant component of the wave function at $\Omega_x = 0.0$ MeV. The superscripts *sign* to the orbital labels are used sometimes to indicate the sign of the signature r for that orbital $(r = \pm i)$.

The self-consistent field σ, $\boldsymbol{\omega}$ and $\boldsymbol{\rho}$, are expanded into a complete set of eigenfunctions of the three-dimensional harmonic oscillator in cartesian coordinates. The fields are written as:

$$\sigma(r) = \sum_N \sigma_N \Phi_N(r) \tag{2.49}$$

$$\boldsymbol{\omega}(r) = \sum_N \omega_N \Phi_N(r) \tag{2.50}$$

$$\boldsymbol{\rho}(r) = \sum_N \rho_N \Phi_N(r) \tag{2.51}$$

where

$$\Phi_N(r) = \phi_{n_x}(x)\phi_{n_y}(y)\phi_{n_z}(z) \tag{2.52}$$

$$N = n_x + n_y + n_z$$

$\hat{P}$ is the parity operator and $\hat{R}$ is the signature operator, the parity and signature are good quantum numbers in the case of reflection symmetry, which is the case in all the phenomena discussed in this dissertation. The signature operator is sefined as:

$$\hat{R_x} = e^{-i\pi\hat{j_x}}, \quad \hat{R_x}\psi_i = r_i\psi_i \tag{2.53}$$

with the eigenvalues are $r_i = \pm i$. The simplex operator is defined as:

$$\hat{S_i} = \hat{R_i}\hat{P} \quad i = x, y, z \tag{2.54}$$

$$P = S_x S_y S_z \tag{2.55}$$

The positive simplex state is written as:

$$\Phi_K(\boldsymbol{r}) = \phi_{n_x}(x)\phi_{n_y}(y)\phi_{n_z}(z)\frac{i^{n_y}}{\sqrt{2}}\begin{pmatrix} 1 \\ (-)^{n_x+1} \end{pmatrix} \tag{2.56}$$

The negative simplex state is written as:

$$\Phi_{\bar{K}}(\boldsymbol{r}) = \phi_{n_x}(x)\phi_{n_y}(y)\phi_{n_z}(z)\frac{i^{n_y}}{\sqrt{2}}(-)^{n_x+n_y+1}\begin{pmatrix} 1 \\ (-)^{n_x} \end{pmatrix} \tag{2.57}$$

$$\phi_{n_i}(x_i) = (\sqrt{\pi}2^{n_i}n_i!b_i)^{-\frac{1}{2}}exp(-\frac{1}{2}(\frac{x_i}{b_i})^2)H_{n_i}(\frac{x_i}{b_i}) \quad i = x, y, z \tag{2.58}$$

where H_{n_i} are the Hermite polynomials.

The truncation of basis is performed in such a way that all states belonging to the shells up to fermonic N_F and bosonic N_B are taken into account. Since this dissertation is describing different nuclear phenomena in different parts of the nuclear chart, the truncation scheme of the basis will be discussed for each phenomena separately in the relevant chapter.

CHAPTER 3

SUPER- AND HYPERDEFORMATION AT HIGH SPIN

It was known for a long time from harmonic oscillator studies [77] that very elongated shapes, called as hyperdeformed (HD) and characterized by the semi-axis ratio of around 3:1, are possible. The existence of such stable shapes was later confirmed in the macroscopic+microscopic (MM) method [78, 79, 80, 81, 82, 83, 84, 85, 86]. Theoretical results on the states located in third (HD) minima are also available in self-consistent Hartree-Fock+Bogoliubov (HFB) approaches based on the Skyrme and Gogny forces (see Refs. [87, 88, 89] and references quoted therein), and relativistic mean field approach [90]. However, these results are restricted to spin zero states, which are difficult to measure in experiment. To our knowledge, the description of the HD states at high spin within the self-consistent approach has been attempted only in ^{108}Cd [91] [within the cranked relativistic mean field (CRMF) method] and in four $A \sim 40$ mass nuclei [92] [within the cranked Skyrme-Hartree-Fock approach]. The general feature of all these calculations is the fact that the semi-axis ratio of the HD shapes is less than 3:1 [21]. Let us mention two examples of such studies: one at spin zero, another at high spin. In actinide nuclei, the HD states are so-called third minima states around ^{232}Th [93, 94, 82]. In these nuclei, the second saddle point is split, leading to the excited reflection-symmetric and reflection asymmetric configurations with large quadrupole and octupole deformations, $\beta_2 \sim 0.9$ and

$\beta_3 \sim 0.35$. The density distribution at the HD minimum resembles a di-nucleus consisting of a nearly-spherical nucleus around the doubly-magic nucleus ^{132}Sn and a well-deformed fragment from the neutron-rich $A \sim 100$ region [82]. Unfortunately, it is very difficult to study the HD states at low spin in experiment. In order to overcome this problem, one should use the fact that the larger moment of inertia connected with the larger deformation drives the nucleus towards larger deformations with increasing angular momentum; the HD minimum is thus favored by rotation and becomes ultimately yrast at high spin. For example, cranked Nilsson-Strutinsky calculations suggested the existence of very elongated high-spin minima in nuclei around ^{168}Yb [80]. These HD bands are expected to become yrast at spin around 80$\hbar$.

On the experimental side, very little was known about hyperdeformation apart from some indications of this phenomenon at low spin in the uranium nuclei [23] and light nuclei like ^{12}C [24] and the observation of the HD ridge structures at high spin in the $A \sim 150$ mass region [25, 26]. Recent observation of the very extended shapes in ^{108}Cd [95, 96], strongly motivated by earlier calculations of Ref. [83] and more recent studies of Ref. [86], has renewed interest in the study of hyperdeformation at high spin. Although the hyperdeformed nature of the bands in this nucleus has not been confirmed in the subsequent cranked relativistic mean field analysis of Ref. [91] (see also Sect. VB in Ref. [97]), this experiment provided a strong motivation for subsequent experimental searches in the $A \sim 125$ mass region (see Refs. [98, 99, 27]) and theoretical studies of Refs. [21, 97] within the framework of the MM method. These experiments revealed rotational patterns in the form of ridge-structures in three-dimensional (3D) rotational mapped spectra with

dynamic moments of inertia $J^{(2)}$ ranging from 63 to 111 MeV^{-1} in 12 different nuclei [27]; the values around 110 MeV^{-1} observed in ^{118}Te, ^{124}Xe and ^{124,125}Cs suggest that the HD structures were populated in these experiments. However, no discrete rotational HD bands have been identified. It is also necessary to mention that several previous attempts to search for high spin HD structures in ^{147}Gd [100, 101], ^{152}Dy [25, 26], and ^{168}Yb [102] did not lead to convincing evidences for discrete HD bands.

So far, theoretical investigations of HD at high spin were carried out mainly in the framework of the MM method. One of the main goals of this dissertation is to perform for the first time a systematic study of HD within the framework of fully self-consistent theory, the CRMF theory. Fig.3.1 shows the part of the nuclear chart where our studies are performed. We restrict our investigation to even-even nuclei; the only exceptions are odd-mass nuclei ^{111}I [in which extremely SD doubly magic band has been found] and ^{123,124}Xe, ^{123}I and ^{125}Cs [which are used in the study of the relative properties of the HD bands]. In each isotope chain we consider nuclei ranging from the most proton-rich ones up to the ones located at the neutron-rich side of the β-stability valley. Neutron-rich nuclei beyond the valley of the β-stability are excluded from consideration because of the experimental difficulties of studying them at high spins relevant for HD. With the goal to guide future experimental explorations and to find the nuclei in which the HD may be studied with current and future experimental facilities, we define the spins at which the HD bands become yrast in these nuclei. In addition, available experimental data on the HD ridge-structures in the Te, Xe, and Cs nuclei are analyzed. The general features of the HD bands are outlined.

The role of the single-particle degrees of freedom at hyperdeformation has not been studied in detail till now. The study of their role is motivated by the desire to understand to what extent theoretical methods developed in the study of the SD bands are also applicable to the HD bands. It is very unlikely that the spins, parities and excitations energies of the HD bands will be known in the initial stage of their experimental study. The direct test of the structure of the wave functions of the single-nucleonic orbitals (e.g. via magnetic moments) will also not be possible at that stage. Thus, similar to the case of superdeformation [103, 104, 19, 105], the relative properties of different HD bands may play an important role in the interpretation of their structure. In this context, it is important to understand which changes of the single-particle orbitals are involved in going from one HD band to another, and how they affect physical observables like dynamic moments of inertia $J^{(2)}$, transition quadrupole moments Q_t, total spin I, etc. In particular, we will study whether the theoretical methods which were systematically used in the configuration assignment of the SD bands are also applicable to the HD bands. These include the methods based on the relative properties of the dynamic moments of inertia $J^{(2)}$ [103, 19], on the effective alignments i_{eff} [104, 19, 105] and on the relative transition quadrupole moments ΔQ_t [106, 107].

This chapter is organized as follow: the definition of physical observables and the details of numerical calculations are discussed in Sect. 3.1. Configuration assignment of the excited superdeformed bands in ^{154}Dy was performed in Sec. 3.2. The spins at which the HD bands become yrast, the regions of nuclear chart where the experimental search for the HD structures may be successful and the general properties of the HD bands are

outlined in Sect. 3.3. The data obtained in the search of the HD structures in the $A \sim 120$ mass region and the single-particle degrees of freedom are also analyzed in this section. Sec. 3.4 is devoted to the analysis of extremely superdeformed (ESD) structure in ^{111}I. The calculations predict the existence of doubly magic ESD structure in this nucleus with the deformations being close to HD, which may be observed with the current generation of γ-ray detectors.

3.1 Physical observables and details of calculations

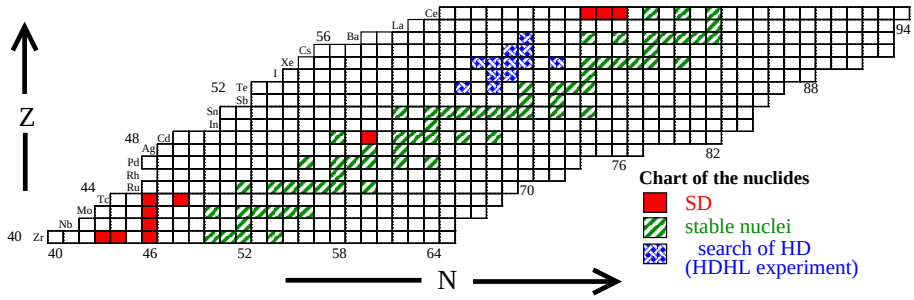

Figure 3.1

The chart of nuclei in the $Z = 40 - 58$ region.

Similar to the case of the SD bands, it is reasonable to expect that the HD bands will not be linked to the low-spin level scheme for a long period of time. Thus, the spins and parities of the HD bands will not be known and it will not be possible to define the kinematic moment of inertia $J^{(1)}$ since it depends on the absolute values of the spin. In such a situation, the dynamic moment of inertia $J^{(2)}$ will play an important role in our understanding of the structure of the HD bands. This is similar to the case of the SD bands

(see Refs. [103, 19]). Other observables, such as transition quadrupole moments Q_t and effective (relative) alignments i_{eff}, will also be important.

In the CRMF calculations, the rotational frequency Ω_x, the kinematic moment of inertia $J^{(1)}$ and the dynamic moment of inertia $J^{(2)}$ are defined by

$$\Omega_x = \frac{dE}{dJ}, \tag{3.1}$$

$$J^{(1)}(\Omega_x) = J\left\{\frac{dE}{dJ}\right\}^{-1}, \tag{3.2}$$

$$J^{(2)}(\Omega_x) = \left\{\frac{d^2E}{dJ^2}\right\}^{-1}. \tag{3.3}$$

The charge quadrupole Q_0 and mass hexadecupole Q_{40} moments are calculated by using the expressions

$$Q_0 = e\sqrt{\frac{16\pi}{5}}\sqrt{\langle r^2Y_{20}\rangle_p^2 + 2\langle r^2Y_{22}\rangle_p^2}, \tag{3.4}$$

$$Q_{40} = \left\langle r^4Y_{40}\right\rangle_p + \left\langle r^4Y_{40}\right\rangle_n, \tag{3.5}$$

where the labels p and n are used for protons and neutrons, respectively, and e is the electrical charge. At axially symmetric shapes, typical for the hyperdeformed states, the transition quadrupole moment Q_t is equal to Q_0.

The quadrupole deformation β_2 for axially-symmetric shapes is frequently defined in self-consistent calculations from calculated and/or experimental quadrupole moments using simple relation [89, 39, 110]

$$\beta_2 = \frac{1}{XR^2}\sqrt{\frac{5\pi}{9}}Q_0^X, \tag{3.6}$$

where $R = 1.2A^{1/3}$ fm is the radius of the nucleus, and Q_0^X is a quadrupole moment of the X-th (sub)system expressed in fm^2. Here X refers either to proton ($X = Z$) or neu-

tron ($X = N$) subsystem or represents total nuclear system ($X = A$). This expression, however, neglects the higher powers of β_2 and higher multipolarity deformations $\beta_4, \beta_6, ...$ [111], which play an important role at hyperdeformation. Considering that the definition of the deformation is model dependent [111], and that this quantity is not experimentally measurable, we prefer to use transition quadrupole moment Q_t for the description of deformation properties of hyperdeformed states. This is experimentally measurable quantity, so in the future our predictions can be directly compared with experiment. The deformation properties of the yrast SD band in ^{152}Dy (which is one of the most deformed SD bands [95]) are used as a reference. This is done by introducing normalized transition quadrupole moment $Q_t^{norm}(Z, A)$ in the (Z, A) system

$$Q_t^{norm}(Z, A) = \frac{ZA^{2/3}}{100.36} \ e\text{b} \tag{3.7}$$

This equation is based on the ratio $Q_t^{norm}(Z, A)/Q_t(^{152}\text{Dy})$ calculated using Eq. (3.6) under the assumption that the β_2-values in the (Z, A) system and in ^{152}Dy are the same. We use the value $Q_t(^{152}\text{Dy}) = 18.73\ e$b obtained in the CRMF calculations with the NL1 parametrization of the RMF Lagrangian for the yrast SD band in ^{152}Dy at $I = 60\hbar$ in Ref. [20]. Thus, in first approximation (neglecting the higher powers of β_2 and higher multipolarity deformations $\beta_4, \beta_6, ...$)) the equilibrium deformation of the band in the (Z, A) system having the $Q_t^{norm}(Z, A)$ value is the same as in the yrast SD band of ^{152}Dy. We describe the band as hyperdeformed if its Q_t value exceeds $Q_t^{norm}(Z, A)$ by at least 40%. This criteria is somewhat relaxed in the $Z = 40,\ 42,\ 44$ nuclei for which the band is defined as HD if its Q_t value exceeds $Q_t^{norm}(Z, A)$ by at least 30%.

The effective (relative) alignment i_{eff} between two bands is defined as the difference between the spins of two levels in bands A and B at the same rotational frequency Ω_x [104]:

$$i_{eff}^{B,A}(\Omega_x) = I_B(\Omega_x) - I_A(\Omega_x) \tag{3.8}$$

This quantity has been used frequently in the analysis of the single-particle structure of the SD bands and the configuration assignment (see Refs. [104, 105] and references quoted therein). It depends on both the alignment properties of the single-particle orbitals(s) by which the two bands differ and the polarization effects induced by the particles in these orbitals [38]. The latter are in part related to nuclear magnetism.

Because the pairing correlations are relatively weak in the HD bands of interest (see Sect. 3.3.3), their intrinsic structure can be described by means of the dominant single-particle components of the hyperintruder states occupied. The calculated configurations will be labeled by $[p, n_1 n_2]$, where p, n_1 and n_2 are the number of proton $N = 7$ and neutron $N = 7$ and $N = 8$ hyperintruder orbitals occupied, respectively. For most of the HD configurations, neutron $N = 8$ orbitals are not occupied, so the label n_2 will be omitted in the labeling of such configurations.

The spins at which the SD and HD configurations become yrast in the calculations are defined as crossing spins I_{cr}^{SD} and I_{cr}^{HD}, respectively.

3.1.1 Numerical scheme of the CRMF calculations

The impact of the truncation of basis on the numerical accuracy of the calculations has first been studied in the axially symmetric RMF code, see Fig. 3.2. In the mass region

of interest, the calculations with $N_F = 12$ provide a reasonable approximation to the fully convergent $N_F = 26$ solution up to a deformation typical for the SD shapes, the value of $N_B = 26$ is fixed for all N_F values. However, this truncation scheme becomes a poor approximation when the quadrupole moment appreciably exceeds the one corresponding to the lower limit of HD; the difference between the $N_F = 12$ and $N_F = 26$ solutions increases rapidly with the increase of quadrupole moment (see Fig. 3.2). On the other hand, in this quadrupole moment range the results of the calculations with $N_F = 14$ are closer to exact solution, although still exceeding it by $\sim 1 - 2$ MeV at the upper end of the calculated quadrupole moment range. It was tested that with the decrease of the mass, the difference between the $N_F = 14$ and $N_F = 26$ solutions will also decrease as well, so that the difference falls within the range of 1 MeV for the majority of the nuclei under study. The normalized value of transition quadrupole moment Q_t^{norm} corresponding to the deformation of the yrast SD band in ^{152}Dy is indicated by arrow. The range of hyperdeformation is also indicated. The gaps in the PES lines are due to the jumps of the solution from one single-particle configuration to another. These conclusions have also been tested in triaxial CRMF calculations. It was concluded that physical observables of interest are described with sufficient numerical accuracy when $N_F = 12$ is used for the SD and ND states and $N_F = 14$ for the HD states. Thus, we employ a hybrid calculational scheme in which the CRMF solutions in the ND- and SD minima are sought using $N_F = 12$, while the ones in the HD minima using $N_F = 14$. In all CRMF calculations, we use $N_B = 20$. In order to eliminate the numerical inaccuracies in the definition of the crossing spin I_{cr}^{HD}, the yrast ND/SD configurations, which are crossed by the yrast HD

configuration, were recalculated in the crossing region using $N_F = 14$, and only then the crossing spin was defined. One should keep in mind that even with $N_F = 14$ the spins at which the HD configurations become yrast in the calculations may be overestimated by $1 - 2\hbar$ when the deformation of the HD configurations exceeds appreciably the one corresponding to the lower limit of HD.

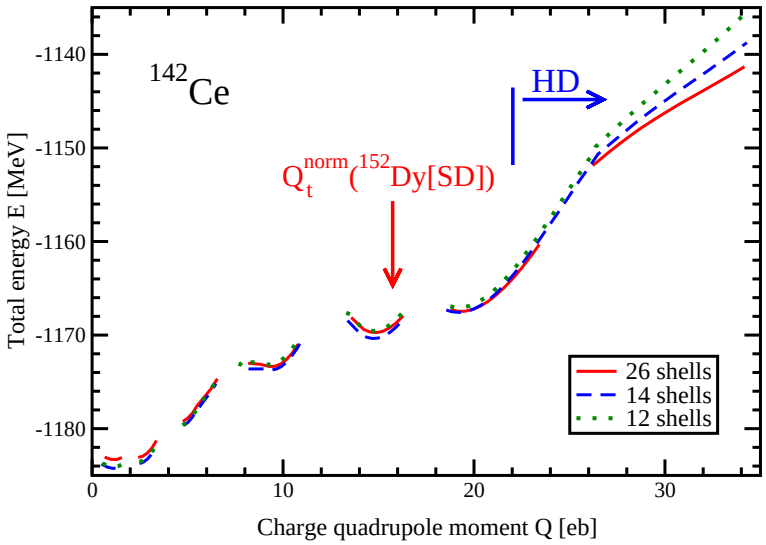

Figure 3.2

Axial symmetric potential energy surfaces RMF calculations without pairing.

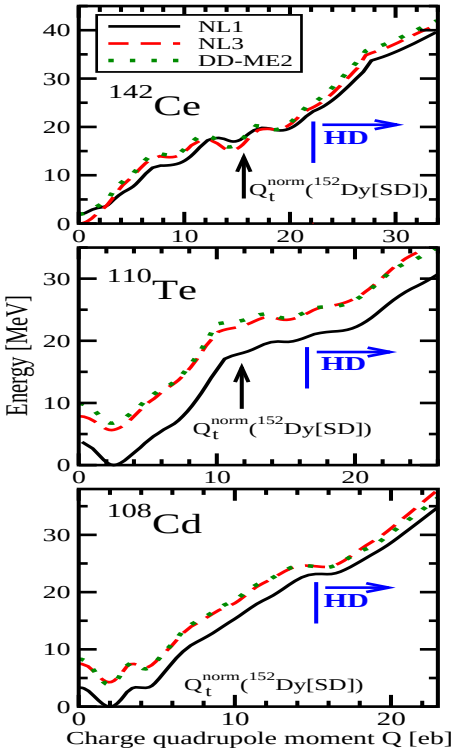

Figure 3.3

The same as in Fig. 3.2, but for the results obtained with pairing.

When searching for different types of rotational structures it is important to find the solutions in all local minima which are close to the yrast line in order to properly define the crossing spins between the rotational structures of different nature. This is easily achievable in the macroscopic+microscopic approach by creating potential energy surfaces (PES) in the deformation space covering quadrupole and triaxial deformations [83, 112]. However, the computational cost to create similar PES in the self-consistent models is enormous, thus, it has never been attempted in rotating nuclei. In order to overcome this problem, we use the fact that in self-consistent approaches without pairing the deformation of the basis defines to a large extent the local minima where the solutions will be obtained. Thus, the solutions in the ND minima, including triaxial ones, are searched using three combinations of the deformation of basis: $(\beta_0 = 0.30, \gamma = -30^\circ)$, $(\beta_0 = 0.30, \gamma = 0^\circ)$, and $(\beta_0 = 0.30, \gamma = +30^\circ)$. In a similar way, the solutions in the SD minima are searched using the following combinations of the deformations of basis $(\beta_0 = 0.65, \gamma = -30^\circ)$, $(\beta_0 = 0.65, \gamma = 0^\circ)$, $(\beta_0 = 0.65, \gamma = +30^\circ)$, and $(\beta_0 = 0.8, \gamma = 0^\circ)$. The latter deformation of basis also leads frequently to the HD solutions. The deformation of basis $(\beta_0 = 1.0, \gamma = 0^\circ)$ has been used for the search of the solutions in the HD minima. Non-zero γ-deformations of basis at large β_0 lead either to the same solution as $\gamma = 0^\circ$ or to the highly excited configurations. For each of the above mentioned values of the deformation of basis, the lowest in energy solutions are calculated as a function of spin, and the yrast line is formed from these solutions.

3.1.2 The selection of the RMF parametrization.

The NL1 parametrization of the RMF Lagrangian [72] is used in the majority of the calculations in the current manuscript. As follows from previous studies, this parametrization provides a good description of the moments of inertia of the rotational bands in unpaired regime in the SD and ND minima [20, 105, 70, 11], the single-particle energies for the nuclei around the valley of β stability [105, 39] and the excitation energies of the SD minima [113]. NL3 [64] is an alternative parametrization, the quality of which has been tested in rotating nuclei (but less extensively than in the case of NL1) [105, 114, 70, 69]. Some results with this parametrization will be presented. Few results obtained with the NLSH [115] and NLZ [116] parametrizations will be shown in Sect. 3.3.3 in order to illustrate the possible spread of calculated quantities. It is necessary to keep in mind that the quality of the NLSH parametrization in respect of the description of rotational properties of the nuclei as well as their single-particle energies is not as good as that of the NL1 and NL3 [70, 105, 39], and the force NLZ has not been tested in that respect.

The spins at which the rotational structures belonging to different minima in potential energy surfaces become yrast depend in general on the relative energies of these minima and on the moments of inertia of rotational structures in these minima. Previous experience shows that different parametrizations of the RMF Lagrangian give similar moments of inertia for the same configuration [105, 70, 114, 11] (see also Fig. 3.16 below). Fig. 3.3 also illustrates that the potential energy surfaces at spin zero as a function of charge quadrupole moment obtained with the NL1 and NL3 parametrizations are similar in shape. These two facts suggest that the HD configurations should become yrast at approximately

the same spins in both parametrizations: this conclusion is confirmed in Sect. 3.3.1. It is interesting to note that the NL3 curve in Fig. 3.3 is similar to the one obtained with recently developed density-dependent meson-exchange effective interaction DD-ME2 [59], which represents a new class of the RMF parametrizations as compared with NL1 and NL3. However, so far this interaction has not been used in the studies of rotating nuclei, thus, it is not employed in the current study since its reliability in the description of rotational properties is not known.

3.2 Excited superdeformed bands in ^{154}Dy

Theoretical interpretation of the observed superdeformed bands was performed with the Cranked Relativistic Mean Field (CRMF) approach [20, 105]. This approach has been successfully applied to the interpretation of different properties of SD bands in the $A \sim 150$ mass region [20, 105]. In the past, the interpretation of the single-particle structure of the majority of observed SD bands was performed by means of the effective alignment approach [104, 105]. This approach is also used here as an illustration of how this approach is applied. The effective alignment i_{eff} of two bands A and B, i.e. the difference between their spins at constant rotational frequency $\hbar\omega$, is defined as [104, 105]:

$$i_{eff}(\hbar\omega) = I_B(\hbar\omega) - I_A(\hbar\omega) \tag{3.9}$$

This quantity includes both the alignment of the single-particle orbital by which two compared bands differ and the polarization effects associated with the occupation of this orbital. The spins are not known for the SD bands observed in ^{154}Dy, however, they are known for the yrast SD band in ^{152}Dy [123]. The latter serves as a reference band (band

A) in the effective alignment method. Thus, by comparing calculated and experimental effective alignments in the pairs of the SD bands ^{152}Dy(1)/^{154}Dy(i) one can not only establish the structure of the SD bands in ^{154}Dy, but also suggest spins for these bands.

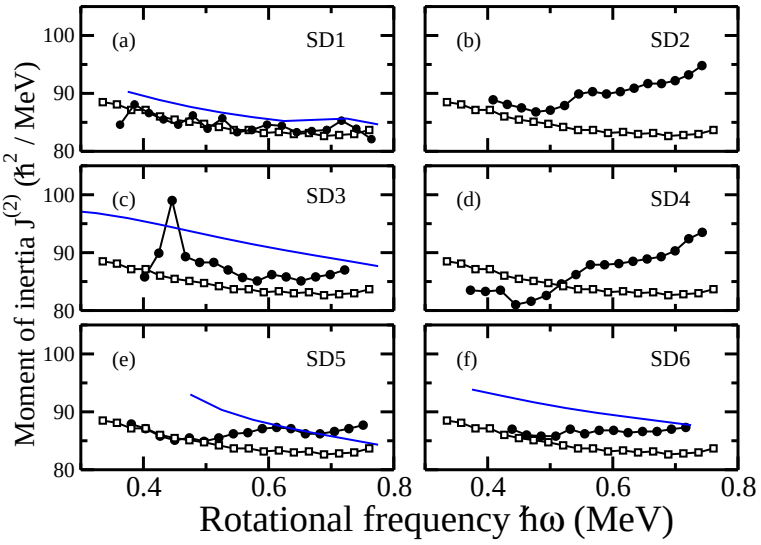

Figure 3.4

The dynamic moments of inertia J$^{(2)}$ of the six SD bands in ^{154}Dy.

The pairing correlations are neglected in the CRMF calculations. As seen from systematic studies in this mass region, this is a fairly good approximation for rotational frequencies above $\hbar\omega \sim 0.5$ MeV [104, 20, 105]. The $J^{(2)}$ values of the SD1, SD3 and SD5 bands decrease with increasing rotational frequency, see Fig. 3.4. This is a feature typical for rotational bands with weak pairing [20], and justifies their interpretation within the CRMF formalism without pairing. The calculations are performed with the NL1 parameterization of the RMF Lagrangian. The CRMF equations are solved in the basis of

an anisotropic three-dimensional harmonic oscillator in Cartesian coordinates characterized by the deformation parameters $\beta_2 = 0.5$ and $\gamma = 0°$, and the oscillator frequency $\hbar\omega_0 = 41A^{-1/3}$ MeV. The truncation of the basis is performed in such a way that all states belonging to the shells up to fermionic number N_F=14 and bosonic number N_B=16 are taken into account. Our numerical analysis indicates that this truncation scheme provides sufficient numerical accuracy for the physical quantities of interest.

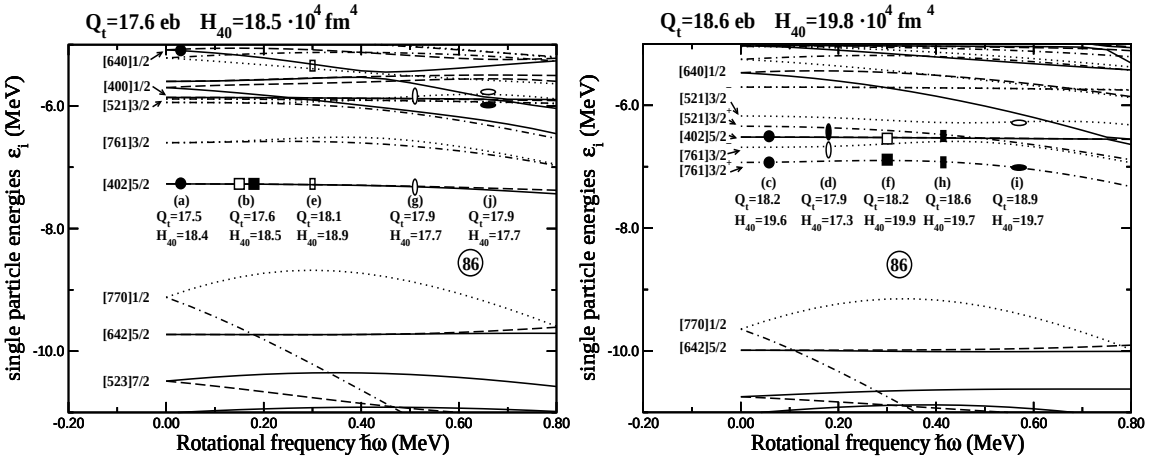

Figure 3.5

Neutron and proton routhians for ^{154}Dy

All configurations in ^{154}Dy are labeled by the occupation of the two neutron orbitals above the $N = 86$ SD shell gap. This means that the ^{152}Dy yrast SD configuration $\pi 6^4 \nu 7^2$, in terms of the occupation of the intruder proton $N = 6$ and neutron $N = 7$ orbitals, serves as a reference for labeling ^{154}Dy configurations. All possible low-lying SD configurations, for which convergence has been achieved in the calculations, are included in the analysis,

and their structures are shown in Fig. 3.5. The single-particle orbitals in this figure are given along the deformation path of the yrast configuration in ^{154}Dy and obtained in the calculations with the NL1 parametrization of the RMF Lagrangian. Long-dashed, solid, dot-dashed and dotted lines indicate $(\pi = +, r = +i)$, $(\pi = +, r = -i)$, $(\pi = -, r = +i)$ and $(\pi = -, r = -i)$ orbitals, respectively. They are labeled by $[Nn_z\Lambda]\Omega^{sign}$ where $[Nn_z\Lambda]\Omega$ are the asymptotic quantum numbers (Nilsson quantum numbers) of the dominant component of the wave function. The superscripts *sign* to the orbital labels are sometimes used to indicate the sign of the signature r for that specific orbital $(r = \pm i)$.

Before performing a detailed theoretical analysis, it is important to understand the experimental features of the observed bands, and to decide whether they agree with predictions based on the analysis of the SD bands in the neighboring nuclei ^{153}Dy and ^{155}Dy. This is because the lowest SD bands in these three nuclei are expected to be built on neutron single-particle orbitals located above the $N = 86$ SD shell gap (Fig. 3.5). The large $Z = 66$ SD shell gap makes proton excitations across this gap energetically unfavored in the frequently used parametrizations of the RMF Lagrangian (see, for example, Figs. 4, 11, and 12 in Ref. [105]). Only one neutron is located above the $N = 86$ SD shell gap in ^{153}Dy, allowing one to test the available single-neutron orbitals by comparing experimental and calculated effective alignments. Such CRMF analysis has been performed in Ref. [105], which suggests that SD1 band in ^{153}Dy is based on the $\nu[761]3/2^+$ orbital (see Fig. 5a in Ref. [105]), and the signature-degenerate bands SD2 and SD3 in ^{153}Dy are based on $\nu[402]5/2^+$ and $\nu[402]5/2^-$ orbitals, respectively (see Fig. 3c in Ref. [105]). This interpretation is in agreement with the one obtained in the framework of the cranked

Nilsson-Strutinsky (CNS) approach [104, 117]. Previous CRMF calculations did not give a consistent interpretation for the signature-degenerate SD4 and SD5 bands in ^{153}Dy within a pure single-particle picture, although the possibility of the occupation of the $\nu[514]9/2^{\pm}$ orbitals was considered in Ref. [105]. According to the cranked Woods-Saxon calculations of Ref. [118] and the CRMF calculations of Ref. [20], the $\nu[521]3/2$ orbital may be the neutron orbital associated with these bands. SD1 bands in ^{154}Dy and ^{155}Dy have been assigned the $(\nu[402]5/2)^2$ and $(\nu[402]5/2)^2 \otimes \nu[761]3/2^+)$ structure in Ref. [105], respectively. Under this configuration assignment, the lowest state in SD1 band of ^{154}Dy has spin $I_0 = 24\hbar$. However, the comparison of the experimental and calculated effective alignments in the ^{152}Dy(1)/^{154}Dy(1) and ^{153}Dy(1,2)/^{155}Dy(1) pairs under these configuration assignments reveals a systematic discrepancy of about $0.5\hbar$ [105], which is somewhat larger than is normally seen.

Under these configuration assignments it is reasonable to expect that some of the excited SD bands in ^{154}Dy would originate from the occupation of the single $\nu[402]5/2$ orbital and of some other neutron orbital located above the $N = 86$ SD shell gap. This would lead to signature-degenerate SD bands due to signature degeneracy for the $\nu[402]5/2^{\pm}$ orbitals. Indeed, the SD5 and SD6 bands in ^{154}Dy are interpreted as signature-degenerate bands based on these orbitals (see below). A similar situation is expected if the excited SD bands are built on neutron orbitals active in either the SD4 or SD5 bands of ^{153}Dy and some other neutron orbital above the $N = 86$ SD shell gap, as the latter two ^{153}Dy SD bands are signature degenerate. However, no expected signature-degenerate partner band to the SD3 band in ^{154}Dy has been observed in the experiment.

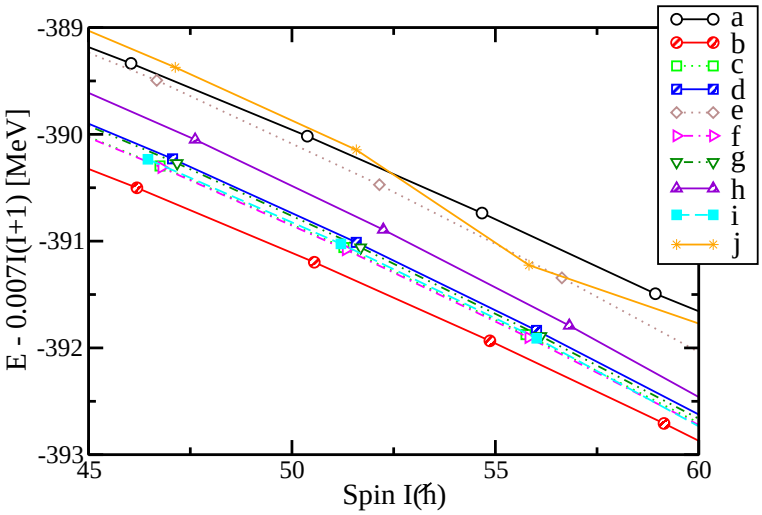

Figure 3.6

The energies of the calculated SD configurations in ^{154}Dy.

The energies of the calculated configurations are presented in Fig. 3.6. The $(\nu[402]5/2)^2$ configuration (conf. b) is the lowest one in the calculations. The effective alignment in the ^{152}Dy(1)/^{154}Dy(1) pair is overestimated by $\sim 0.5\hbar$ in the calculations (Fig. 3.7a). In comparison, the effective alignments in the ^{152}Dy(1)/^{153}Dy(2) and ^{152}Dy(1)/^{153}Dy(3) pairs, where the compared bands differ in the occupations of the $\nu[402]5/2^+$ and $\nu[402]5/2^-$ orbitals, is reproduced well in the calculations (see Fig. 3a in Ref. [105]). If the additivity principle for effective alignments [120, 107] would hold, then i_{eff} in the pair ^{152}Dy(1)/^{154}Dy(1) would be close to zero above $\hbar\omega \sim 0.4$ MeV. This value is achieved in the calculations; however, the experimental value $i_{eff} \sim -0.5\hbar$ for this pair of bands suggests that the additivity of effective alignments is violated in the data. Indeed, the effective alignment due to the $(\nu[402]5/2)^2$ configuration (Fig. 3.7a) is approximately equal to the

sum of effective alignments due to the $\nu[402]5/2^+$ and $\nu[402]5/2^-$ orbitals (as extracted from the comparison of the bands in ^{153}Dy and ^{152}Dy, see Fig. 3a in Ref. [105]).

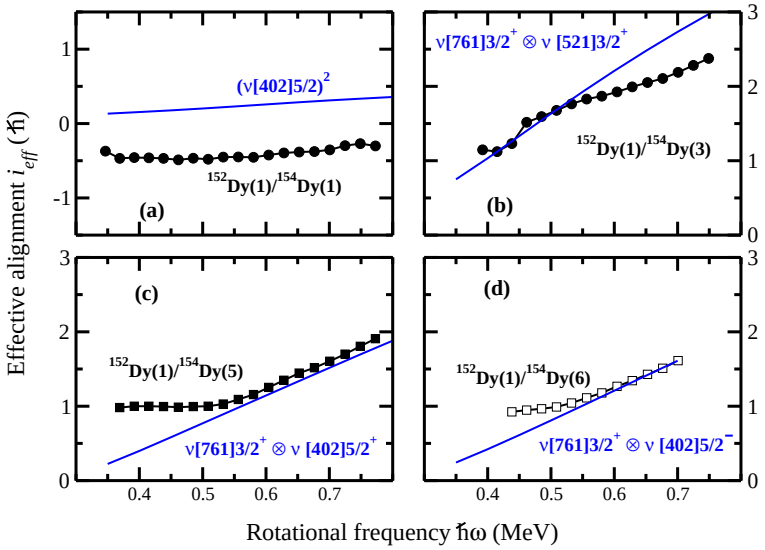

Figure 3.7

i_{eff} for the observed SD bands in ^{154}Dy and for the assigned configurations.

The likely explanation of this experimental feature is related to the increase of pairing in the ^{154}Dy SD1 band as compared to SD1 in ^{152}Dy. The pairing in the yrast SD band in ^{152}Dy is considerably quenched because it is energetically expensive to scatter pairs of particles from the states below the large $N = 86$ and $Z = 66$ SD shell gaps to the levels above these gaps [121]. Although pairing is still present [121, 122], it is weak. As a result, the calculations performed without pairing are successful in describing the properties of many SD bands [104, 20, 105, 123] in this mass region. The addition of one neutron to the ^{152}Dy SD core, resulting in the ^{153}Dy SD bands, does not change the pairing since

a single neutron above the $N = 86$ SD shell gap does not form a pair. This explains why the experimental data in ^{153}Dy are described well in the unpaired CRMF formalism [105]. The situation is changed when two neutrons are placed into two different signatures of the same Nilsson orbital above the $N = 86$ SD shell gap, as is the case in ^{154}Dy. The scattering of this neutron pair to other single-particle orbitals above the $N = 86$ SD shell gap is energetically inexpensive in view of the high density of the available single-particle states (see Fig. 3.5). Note that this density is also higher than the one below the $N = 86$ SD shell gap. This will result in increased neutron pairing for the $(\nu[402]5/2)^2$ configuration. In turn, this leads to a decrease in angular momentum at a given frequency and, thus, to negative values of the effective alignment i_{eff} for the ^{152}Dy(1)/^{154}Dy(1) pair. This mechanism, however, is not effective (due to the broken pair) in configurations where two neutrons are placed in different Nilsson states above the $N = 86$ SD shell gap.

It was pointed out in Ref. [103] that the behavior of $J^{(2)}$ moments with respect to $\hbar\omega$ is primarily influenced by the number of high-*N* intruder orbitals occupied in situations where the pairing is weak. The $J^{(2)}$ values of ^{154}Dy SD1 are essentially the same at all frequencies as those of SD1 in ^{152}Dy, and SD2 and SD3 in ^{153}Dy [118]. This is because these four bands, as discussed above, have the same high-*N* intruder configuration, $\pi 6^4 \nu 7^2$. As is seen in Fig. 3.4(a), the dynamic moment of inertia of the SD1 band is described rather well by the calculations.

The SD3 band undergoes a band crossing at $\hbar\omega \sim 0.45$ MeV (Fig. 3.4b), above which it exhibits a rather smooth behavior, as follows from the effective alignments i_{eff} (Fig. 3.7b) and the dynamic moments of inertia (Fig. 3.4b). The $J^{(2)}$ values of this band are

markedly higher than those seen in ^{152}Dy(1) band, but are very similar to those seen in the ^{153}Dy SD1 band, where an additional $j_{15/2}$ orbital is believed to be occupied [119, 105]. The analysis of the effective alignments (Fig. 3.7b) suggests that the SD3 band has the $\nu[761]3/2^+ \otimes \nu[521]3/2^+$ structure above the band crossing. Under this configuration assignment the lowest state in the band has spin $I_0 = 33\hbar$. The experimental effective alignment is reproduced well around $\hbar\omega \sim 0.5$ MeV, but it is overestimated by $0.5\hbar$ at the highest frequencies observed. This is, however, the typical accuracy for the description of effective alignments of the high-N intruder orbitals (see Ref. [105]). The experimental dynamic moment of inertia is also slightly overestimated in the calculations (Fig. 3.4b). The calculations suggest that band SD3 should have a signature partner band with the $\nu[761]3/2^+ \otimes \nu[521]3/2^-$ structure. As follows from Fig. 3.5 (right panel), these two bands should be almost signature degenerate because of very small signature splitting of the $\nu[521]3/2^{\pm}$ orbitals at rotational frequency $\hbar\omega \geq 0.5$ MeV. However, no such band has been seen in experiment. This could be due to the fact that the band population is at the very limit of experimental sensitivity.

The SD5 band undergoes a band crossing at $\hbar\omega \sim 0.55$ MeV (Fig. 3.4e and Fig. 3.7c). Above this crossing, the effective alignment i_{eff} and dynamic moment of inertia are described very well by the $\nu[761]3/2^+ \otimes \nu[402]5/2^+$ configuration. Under this assignment, the lowest state in this band has spin $I_0 = 31\hbar$. The $J^{(2)}$ values are similar to those of ^{152}Dy(1) band at frequencies lower than $\hbar\omega = 0.53$ MeV, but increase compared to the latter above the crossing. This suggests that a strong interaction of some $\nu N = 5^+$ (here we label the orbital only by its principal quantum number *N* and the sign of the signature)

and $\nu[761]3/2^+$ orbitals may be responsible for this band crossing, and that the SD5 band does not contain a $\nu[761]3/2^+$ neutron below the crossing.

The SD6 band is the signature-partner of SD5. This is supported by a comparison of effective alignments of the two bands, which indicates that the bands are signature-degenerate (Fig. 3.7c,d). The $\nu[761]3/2^+ \otimes \nu[402]5/2^-$ structure is assigned to the SD6 band. Under this configuration assignment, the effective alignment i_{eff} and dynamic moment of inertia are described very well above the band crossing (Fig. 3.4f and Fig. 3.7d). The effective alignment analysis suggests that the lowest state in this band has spin $I_0 = 36\hbar$. The effective alignments due to the $\nu[402]5/2^{\pm}$ and $\nu[761]3/2^+$ orbitals in ^{153}Dy are well described in the CRMF calculations (see Figs. 3c and 5a in Ref. [105]). Furthermore, the effective alignments due to combined $\nu[761]3/2^+ \otimes \nu[402]5/2^{\pm}$ configurations in ^{154}Dy (Fig. 3.7c and d) are very close to the sum of effective alignments due to individual $\nu[402]5/2^{\pm}$ and $\nu[761]3/2^+$ orbitals which were seen in ^{153}Dy. The experimental effective alignments of these bands with respect to the ^{152}Dy(1) band are also described well in the calculations for rotational frequency $\hbar\omega \geq 0.5$ MeV. Thus, the additivity of effective alignments is fulfilled in the case of bands SD5 and SD6. This is contrary to the case of the SD1 band in ^{154}Dy (see discussion above), where the violation of additivity of effective alignments is most likely due to the increase of neutron pairing in the SD1 band of ^{154}Dy as compared to SD1 band in ^{152}Dy. This increase is not present in bands SD5 and SD6 since their configurations do not involve a neutron pair above the $N = 86$ SD shell gap. This is, most likely, the reason why the effective alignments in the ^{152}Dy(1)/^{154}Dy(5,6) pairs are described well in the calculations.

The $J^{(2)}$ values of the SD2 and SD4 bands exhibit a very different trend than those discussed above (see Fig. 3.4). The shape of these $J^{(2)}$ curves allows one to suggest a possible scenario for structure changes. The moments of these two bands decrease gradually with increasing rotational frequency up to $\hbar\omega \sim 0.5$ MeV. This type of behavior is typical for configurations in which the pairing is weak. Considering the relative properties of dynamic moments of inertia of these two bands with respect to that of ^{152}Dy(1) band (see Fig. 3.4), it is reasonable to suggest that SD4 (SD2) band has less (more) intruder orbitals occupied than the SD1 band in ^{152}Dy at these frequencies. The dynamic moments of inertia increase considerably with increasing rotational frequency in the $\hbar\omega = 0.5 - 0.6$ MeV range. Unpaired band crossings due to a strong interaction of two orbitals with the same quantum numbers is a possible source for this feature. The fact that the band crossing in the SD2 and SD4 bands takes place in the same frequency suggests that the same pair of orbitals is involved in both instances. Above this crossing, the rate of increase in $J^{(2)}$ with $\hbar\omega$ is very similar to the one seen in the ^{152}Dy SD4 and SD5 bands [124] and in the ^{151}Dy SD1 band [125]. This increase quite likely indicates the rise of pairing correlations above the band crossing. As shown in Ref. [20], for the example of ^{151}Dy SD1 band, it is unlikely that unpaired CRMF calculations can reproduce this trend in $J^{(2)}$. Calculations based on the CNS approach [104], another type of unpaired formalism, face the same problem [126]. Band crossings are also seen at the highest observed frequencies in the SD2 and SD4 bands of ^{154}Dy (Fig. 3.4). There might also be one additional crossing in the SD2 band at $\hbar\omega \sim 0.65$ MeV. Experience tells that the calculations of such structures are quite complicated and seldom lead to a reliable interpretation in the unpaired

formalism. Therefore, a detailed interpretation of the structure of bands SD2 and SD4 was not attempted. Nevertheless, the properties of the SD2 and SD4 bands above $\hbar\omega \sim 0.6$ MeV suggest that they have more intruder orbitals occupied than the configuration $\pi 6^4 \nu 7^2$ assigned to the SD1 band in ^{152}Dy.

3.3 Hyperdeformation at high spin: where to expect and its general features

3.3.1 The systematics of crossing spins and transition quadrupole moments of the HD bands

Figs. 3.8, 3.9, 3.10 and 3.11 display the spins at which the SD and HD configurations become yrast (crossing spins) in the CRMF calculations. In addition, the calculated transition quadrupole moments of these configurations at spin values close to the crossing spins are shown. The values for the SD configurations are shown only when they become yrastat lower spins than the HD configurations. The calculated HD configurations are near-prolate. One can see that the crossing spins I_{cr}^{HD} are typically lower for proton-rich nuclei. Such a feature is seen in most of the isotope chains; by going from the β-stability valley toward the proton-drip line, one can lower I_{cr}^{HD} by approximately $10\hbar$. The minimum of crossing spins I_{cr}^{HD} is reached at $N \approx Z + 10$ in the Pd, Te and Ru isotope chains (see Figs. 3.9e, 3.9a and 3.11a), and the Mo isotope chain (Fig. 3.11c) shows almost no dependence of I_{cr}^{HD} on mass number. In other isotope chains, the minima in crossing spins I_{cr}^{HD} appear in most proton-rich nuclei. Considering that the sensitivity of modern γ-ray detectors allows to study discrete rotational bands only up to $\approx 65\hbar$ in medium mass nu-

clei [127, 123, 128], and that the observation of higher spin states will most likely require a new generation of γ-ray tracking detectors such as GRETA or AGATA, these features of crossing spins I_{cr}^{HD} represent an important constraint.

As suggested by the studies of the Jacobi shape transition in Ref. [97], the coexistence of the SD and HD minima at the feeding spins may have an impact on the survival of the HD minima because of the decay from the HD to SD configurations. If this mechanism is active, then only the nuclei in which the HD minimum is lower in energy than the SD one at the feeding spin and/or the nuclei characterized by the large barrier between the HD and SD minima will be the reasonable candidates for a search of the HD bands. Figs. 3.8, 3.9, 3.10 and 3.11 show that the HD configurations become yrast at lower spin than the SD ones only in a specific mass range which depends on the isotope chain. This range can be narrow as in the case of Te isotopes (Fig. 3.9a) or wide as in the case of Ce isotopes (Fig. 3.8a). The question of the population of the HD bands within the RMF framework definitely deserves an additional study, but such a study is beyond the scope of the present manuscript. Fig. 3.10 compares the results of the calculations for Cd isotopes obtained with the NL1 and NL3 parametrizations of the RMF Lagrangian. One can see that both parametrizations predict similar crossing spins I_{cr}^{SD} and I_{cr}^{HD} and similar transition quadrupole moments. However, in average, the crossing spins I_{cr}^{HD} calculated with NL3 are somewhat lower (by $1-2\hbar$) than the ones obtained in the calculations with NL1.

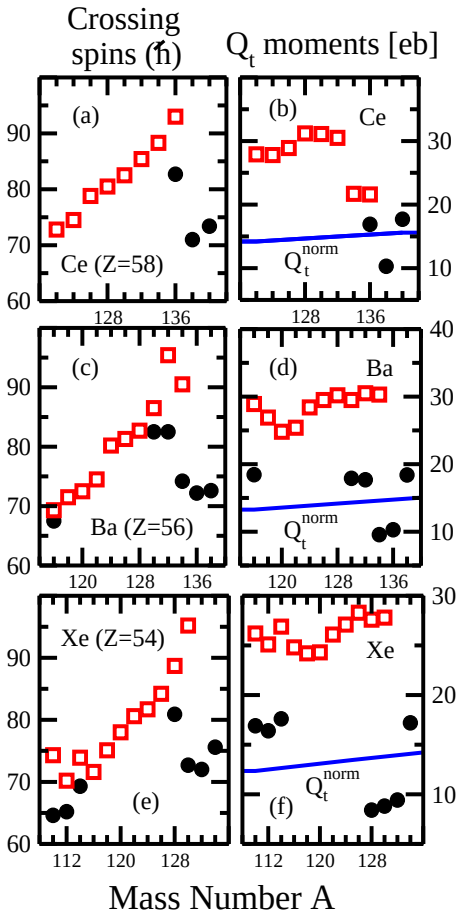

Figure 3.8

The crossing spins and the Q_t for the yrast SD (circles) and HD (squares).

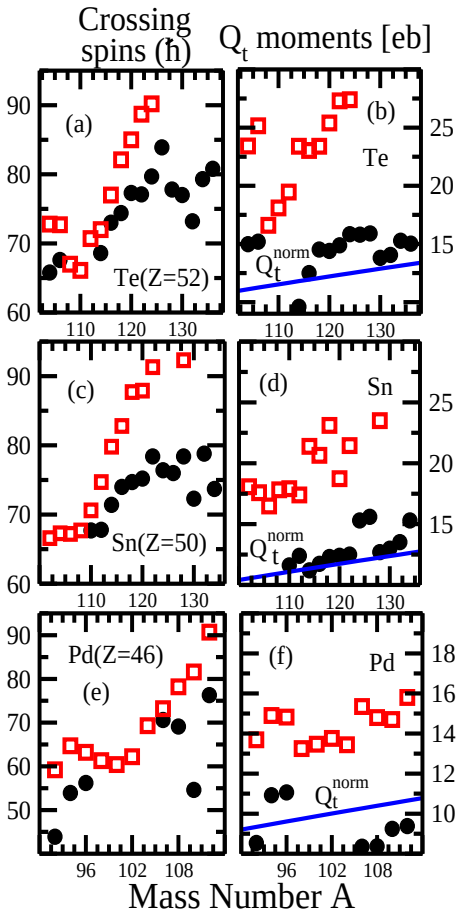

Figure 3.9

The same as in Fig. 3.8, but for Te, Sn and Pd isotopes.

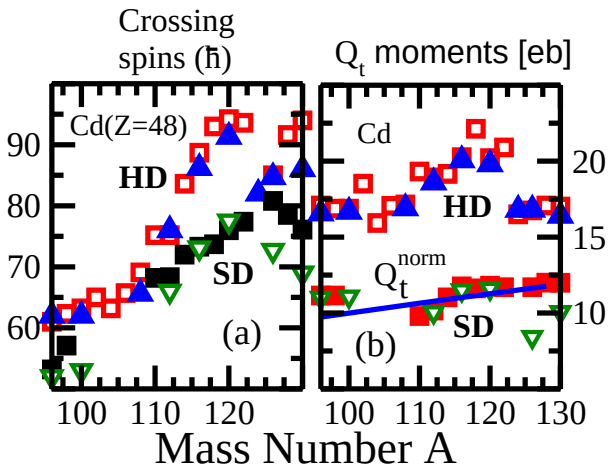

Figure 3.10

Similar to Fig. 3.8, but for NL1 (HD -□, SD - ■) and NL3 (HD - ▲, SD - ▽).

3.3.2 The $A \sim 120$ region: the analysis of experimental data

EUROBALL-IV γ-detector array revealed some features expected for HD nuclei [98, 99, 27]. Although no discrete HD rotational bands have been identified, rotational patterns in the form of ridge-structures in three-dimensional (3D) rotational mapped spectra are identified with dynamic moments of inertia $J^{(2)}$ ranging from 71 to 111 MeV^{-1} in 12 different nuclei selected by charged particle- and/or γ-gating (see Table 3.1). The four nuclei, ^{118}Te, ^{124}Cs, ^{125}Cs and ^{124}Xe, found with moment of inertia $J^{(2)} \sim 110$ MeV^{-1} are most likely hyperdeformed [1] while the remaining nuclei with smaller values of $J^{(2)}$ are expected to be superdeformed. The width in energy of the observed ridges indicates that there are $\approx 6-10$ transitions in the HD cascades, and a fluctuation analysis shows that the number of bands in the ridges exceeds 10. The HD ridges are observed in the

[1] The HD ridges in ^{152}Dy are characterized by $J^{(2)} \sim 130$ MeV^{-1} [26].

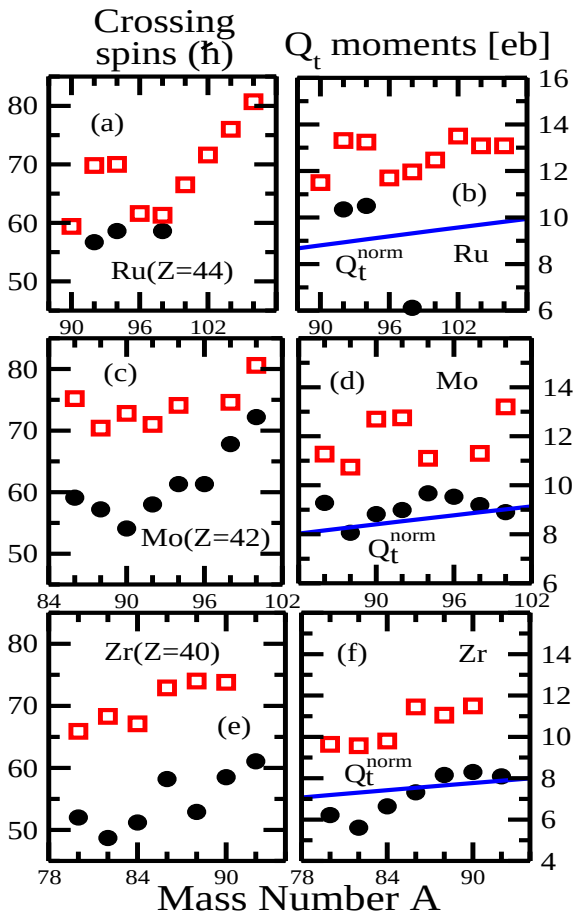

Figure 3.11

The same as in Fig. 3.8, but for Ru, Mo and Zr isotopes.

frequency range of about 650 to 800 keV, and their dynamic moments of inertia have typical uncertainty of 10% (e.g. 111 ± 11 MeV^{-1} in ^{124}Xe) [129].

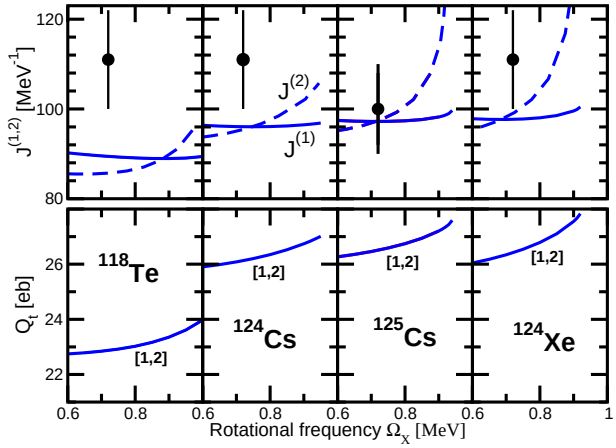

Figure 3.12

Calculated $J^{(1)}$ and $J^{(2)}$ and Q_t.

Table 3.1

The experimental values of $J^{(2)}$ [27]. Theoretical results from Ref.[97].

Nucleus	$J^{(2)}_{exp}$	$J^{(2)}_{MM}$
^{126}Ba	77	118
^{123}Xe	71	
^{122}Xe	77	108
^{121}Xe	63	
^{120}Te	71	
^{118}Te	111	97
^{125}Cs	100	106
^{124}Cs	111	
^{124}Xe	111	111
^{122}I	71	
^{121}I	77	102
^{126}Xe	83	110

The experimental data show unusual features never before seen in the studies of the SD bands. For example, the addition of one neutron on going from ^{124}Cs to ^{125}Cs decreases the experimental $J^{(2)}$ value by $\sim 10\%$ (from 111 MeV^{-1} down to 100 MeV^{-1}, see Table 3.1). A similar situation is also seen in the SD minimum: the addition of one neutron on going from ^{121}Xe to ^{122}Xe increases the experimental $J^{(2)}$ value by $\sim 22\%$ (from 63 MeV^{-1} to 77 MeV^{-1}, see Table 3.1). It is impossible to find an explanation for such a big impact of the single particle on the properties of nuclei: previous studies in the SD minima in different parts of the nuclear chart never showed such features. The case of the pair of ^{123}Xe and ^{124}Xe is even more intriguing: a single particle triggers the transition from the SD to HD minima (see Table 3.1). Considering the fact that the ridges corresponding to the SD and HD minima are observed in neighboring nuclei, it is difficult to understand why the ridges corresponding to both minima have not been seen in the same nucleus.

The calculated kinematic and dynamic moments of inertia as well as transition quadrupole moments of the lowest HD solutions in the candidate HD nuclei are shown in Fig. 3.12. The calculated $J^{(2)}$ moments of inertia somewhat underestimate experimental data. The results of the MM calculations for ^{118}Te, ^{124}Xe and ^{125}Cs (see Table 3.1) are closer to experimental data, but they are obtained at fixed quadrupole deformation β_2 while other deformation parameters β_4, β_6 and β_8 are automatically readjusted so as to minimize the total free Routhian for the vacuum configuration.

In the MM calculations, the kinematic moments of inertia of the configurations in the HD minimum decrease smoothly with the spin, while their dynamic moments of inertia are nearly constant (see Figs. 10 and 11 in Ref. [97]). The behaviour of these observables as a function of rotational frequency (or spin) is completely different in the self-consistent CRMF calculations (see Figs. 3.12, 3.15 and Fig. 3.19 below). The kinematic moment of inertia is either nearly constant or very gradually increases with rotational frequency. The dynamic moment of inertia gradually increases over the calculated frequency range showing the features typical to the SD bands in the $A \sim 190$ mass region which are affected by pairing [130, 19]: this is despite the fact that pairing is neglected in the CRMF calculations. The transition quadrupole moment Q_t is also increasing with rotational frequency; such a feature has not been seen before in the calculations without pairing for the SD bands. The microscopic origin of these unusual features will be discussed in more details in Sect. 3.3.3.

3.3.3 ^{124}Xe nucleus

The results of the CRMF calculations for some HD configurations in ^{124}Xe are displayed in Fig. 3.13. The HD minimum becomes lowest in energy at spin $82\hbar$, and the [1,2] configuration is the yrast HD configuration in the spin range of interest. The occupation of the single-particle orbitals in this configuration is presented in Fig. 3.14. The excited HD configurations displayed in Fig. 3.13 are built from this configuration by exciting either one proton or one neutron or simultaneously one proton and one neutron. The total number of excited HD configurations shown is 35. It interesting to mention that the configuration involving the lowest $N = 8$ neutron orbital (the [1,21] conf. in Fig. 3.13) is calculated at low excitation energy.

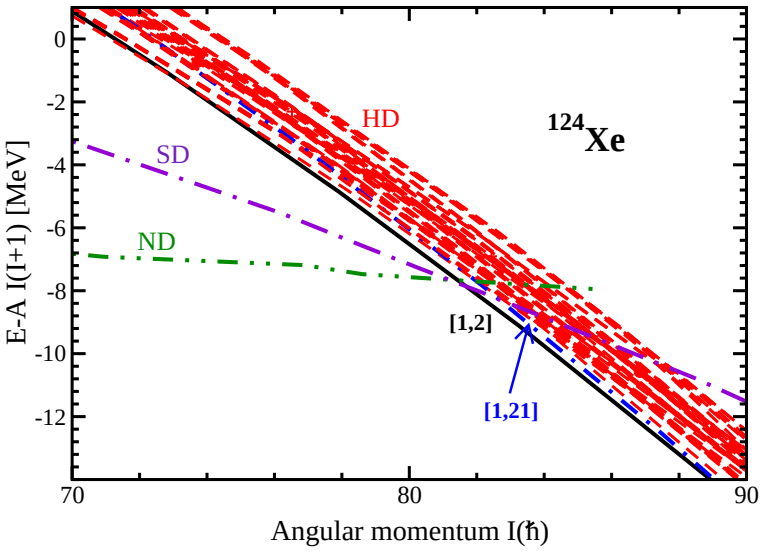

Figure 3.13

Energies of the calculated configurations relative to a liquid drop reference.

The calculations reveal a high density of the HD configurations which will be even higher if the additional calculations for the excited configurations would be performed starting from the low-lying excited HD configurations, such as the [1,21] configuration. This high density is due to two facts: relatively small $Z = 54$ and $N = 70$ HD shell gaps in the frequency range of interest (see Fig. 3.14) and the softness of the potential energy surfaces in the HD minimum. Fig. 3.15b illustrates the latter feature: the particle-hole excitations discussed above, characterised by low excitation energy, lead to appreciable changes in the transition quadrupole moments Q_t. It is interesting to mention that there are large similarities between the single-particle routhians in the vicinity of the $Z = 54$ and $N = 70$ HD shell gaps obtained in the CRMF calculations for yrast HD configuration in ^{124}Xe (Fig. 3.14) and the ones obtained in the Woods-Saxon calculations for the HD minimum in ^{122}Xe employing the so-called universal parametrization of the Woods-Saxon potential (see Figs. 8 and 9 in Ref. [97]). As a consequence, the high density of the excited HD states in ^{124}Xe is also expected in the MM calculations based on the formalism of Ref. [97].

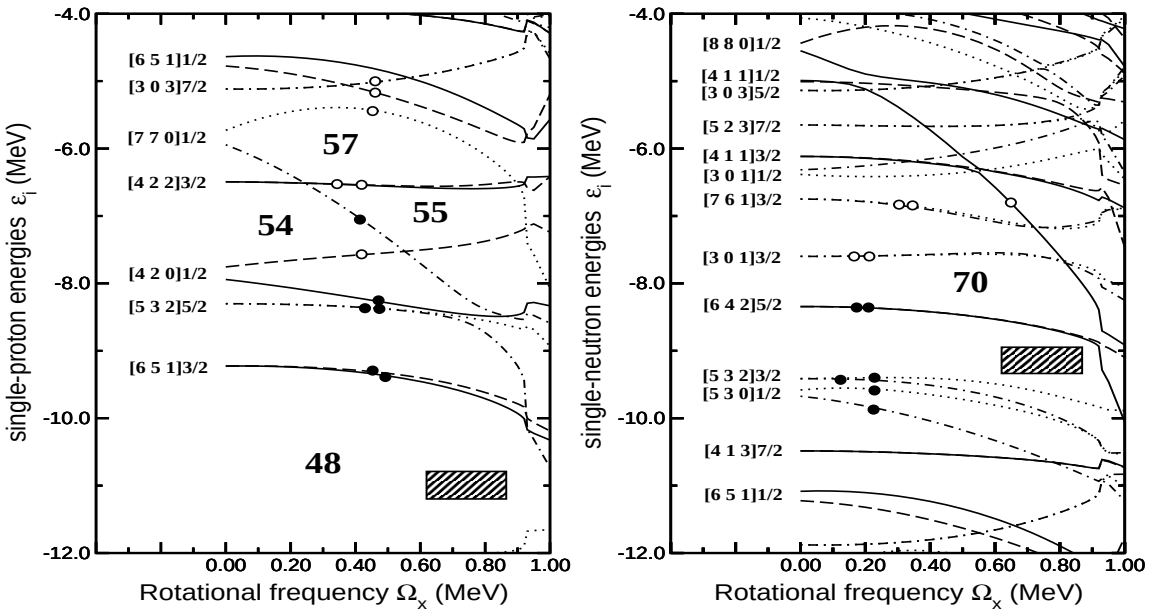

Figure 3.14

Proton (left) and neutron (right) single-particle routhians in ^{124}Xe.

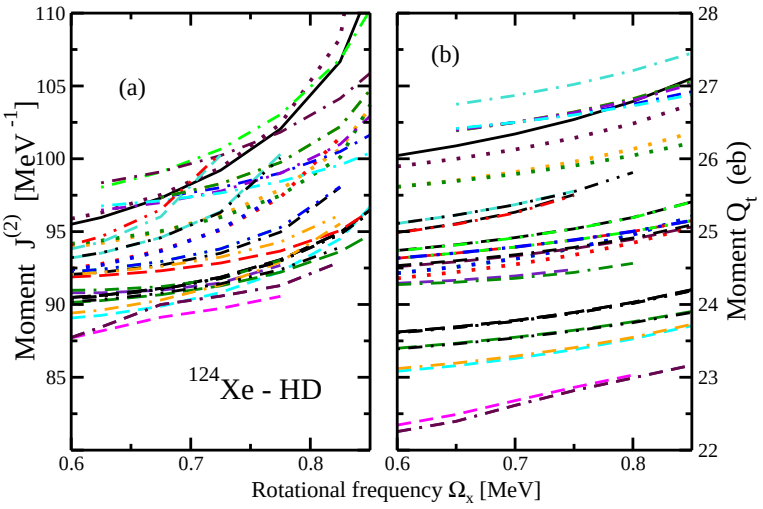

Figure 3.15

$J^{(2)}$ (panel (a)) and Q_t (panel (b))

The high density of the HD configurations may question our neglect of pairing. This is because there are numerous possibilities to scatter proton and neutron pairs and this process is energetically inexpensive due to the high density of the calculated configurations. In order to test the impact of pairing on the moments of inertia and binding energies, the comparative studies of the vacuum HD configuration and its unpaired analog in ^{124}Xe and of the vacuum SD configuration and its unpaired analog in ^{152}Dy have been performed within the cranked relativistic Hartree+Bogoliubov (CRHB) [131] and CRMF approaches. An approximate particle number projection by means of the Lipkin-Nogami method is employed in the CRHB approach. Note that unpaired analog of the vacuum HD configuration in ^{124}Xe (built from the [1,2] configuration by the excitation of the proton from the $\pi[770]1/2(r = +i)$ orbital into the $\pi[420]1/2(r = +i)$ orbital, see Fig. 3.14) is non-yrast in the spin range of interest. As follows from this study, in both nuclei the pairing has a similar impact on the moments of inertia of the configurations under consideration. Taking into account that the SD bands in the $A \sim 150$ mass region are well described in the calculations without pairing [20, 105], it is reasonable to expect that the neglect of pairing is a valid approximation for the moments of inertia of the HD bands in ^{124}Xe. Pairing leads to an additional binding of ~ 500 keV in the case of yrast SD band in ^{152}Dy; this additional binding slightly exceeds 1 MeV in the case of the vacuum HD configuration in ^{124}Xe. The dominant effects in the quenching of pairing correlations are the Coriolis antipairing effect and the quenching due to shell gaps: the latter effect being more pronounced in the SD bands of the $A \sim 150$ mass region because of the larger size of the SD shell gaps (see Fig. 4 in Ref. [20]). The third mechanism of the decrease of

pairing is the blocking effect [14]. Due to this effect the impact of pairing on physical observables will be even lower in the HD bands of ^{124}Xe based on the excitation(s) of one (two) particles considered in Fig. 3.13. Thus, although weak pairing will somewhat modify the relative energies of different configurations, in no way will it create an energy gap between the vacuum and excited configurations.

The calculations suggest that it will be difficult to observe discrete HD bands in ^{124}Xe since their high density will lead to a situation in which the feeding intensity will be redistributed among many low-lying bands, thus drastically reducing the intensity with which each individual band is populated. On the other hand, the high density of the HD bands may favor the observation of the rotational patterns in the form of ridge-structures in three-dimensional rotational mapped spectra as it has been seen in the HLHD experiment [27].

Fig. 3.12 shows that the HD shapes undergo a centrifugal stretching that result in an increase of the transition quadrupole moments Q_t with increasing rotational frequency. This process also reveals itself in the moments of inertia: the kinematic moments of inertia are either nearly constant or slightly increase with increasing rotational frequency, while the dynamic moments of inertia increase continuously and substantially over the frequency region of interest. On the contrary, the dynamic moments of inertia of the HD bands are almost constant as a function of rotational frequency in the MM calculations (see Figs. 10 and 20 in Ref. [97]), which is most likely a consequence of fixed quadrupole deformation. The above mentioned features are general ones for the HD bands in the $A \sim 120$ mass region, see Figs. 3.12, 3.15 and 3.19. They are in complete contract to the features of

the SD bands in unpaired regime, in which the Q_t, $J^{(1)}$ and $J^{(2)}$ values (apart from the unpaired band crossing regions) decrease with increasing rotational frequency (see Refs. [103, 20, 70, 11] and references therein).

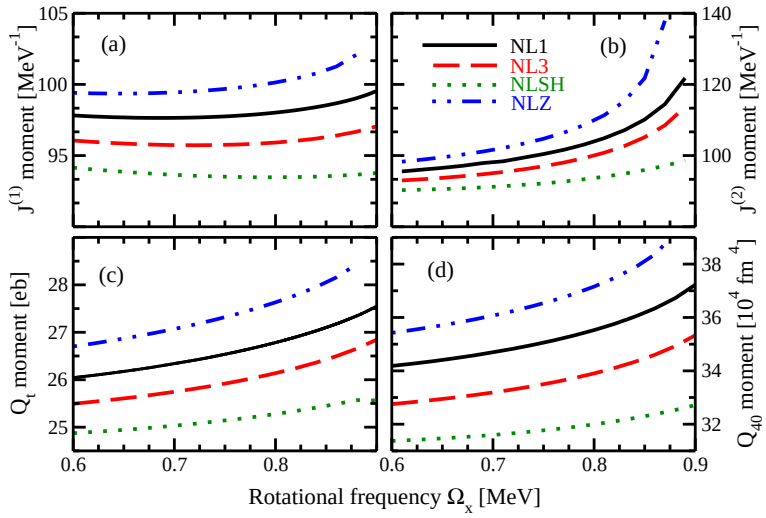

Figure 3.16

$J^{(1)}$, $J^{(2)}$, Q_t and Q_{40} of the [1,2] configuration in ^{124}Xe.

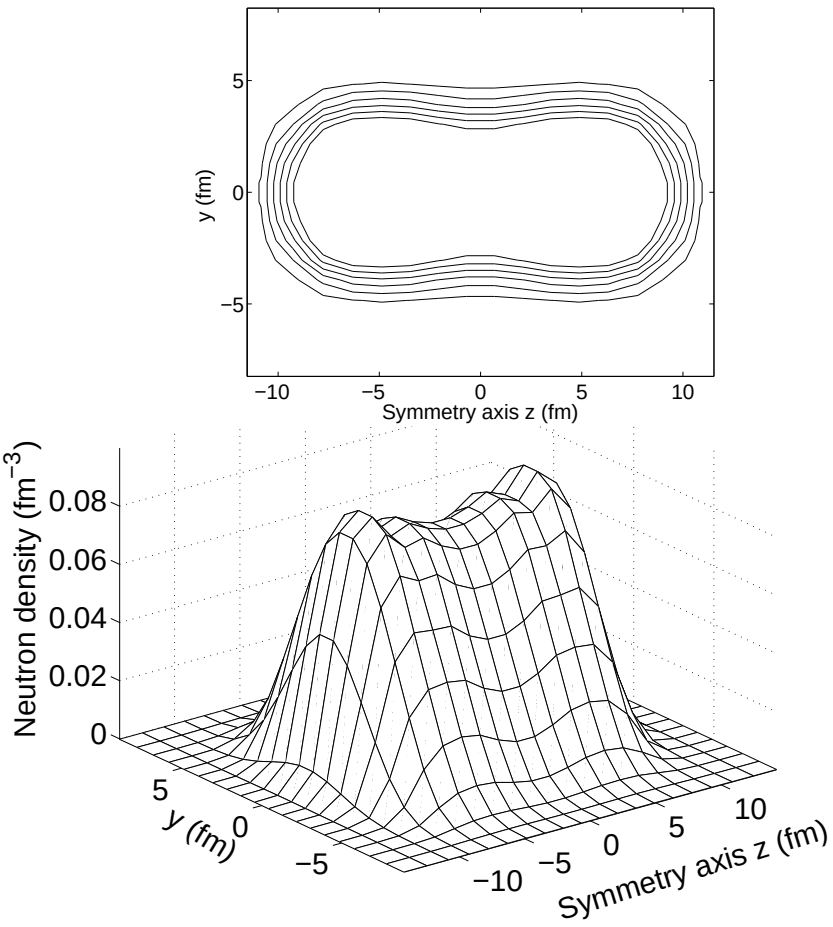

Figure 3.17

Neutron density $\rho_n(y, z)$ for the [1,2] configuration in ^{124}Xe at $\Omega_x = 0.75$ MeV.

Systematic analysis of the yrast/near-yrast HD configurations in the part of the nuclear chart under investigation shows that the centrifugal stretching is a general feature. At the spins, where the HD minimum is lowest in energy, it reveals itself (with very few exceptions) by the increase of transition quadrupole Q_t and mass hexadecapole Q_{40} moments. Only in a few HD bands, characterized by the modest transition quadrupole moment, at low rotational frequencies these quantities decrease with increasing Ω_x. However, even in these bands the Q_t and Q_{40} values start to increase above specific value of rotational frequency. Similar features are also seen in the dynamic moments of inertia; with a few exceptions the $J^{(2)}$ values increase in the spin range of interest. The variations (both the increases and decreases) in the kinematic moments of inertia are rather small ($\sim 2\%$ of absolute value) in the frequency range of interest.

The basis of the CRMF model is sufficiently large to see if there is a tendency for the development of necking. Fig. 3.17 shows some indications of the necking and the clusterization of the density into two fragments in the [1,2] configuration of ^{124}Xe, but this effect is not very pronounced in this nucleus.

The kinematic and dynamic moments of inertia as well as the transition quadrupole and mass hexadecapole moments of the [1,2] configuration in ^{124}Xe are shown for different parametrizations of the RMF Lagrangian in Fig. 3.16. The gradual increase of all physical observables is due to centrifugal stretching. The NLZ (NLSH) parametrizations provide the largest (smallest) values of the above mentioned physical observables, while the results obtained with NL1 and NL3 are in between those results. Similar relations between the results obtained with these parametrizations also exist in other regions of nuclear chart

studied so far in the CRMF or CRHB frameworks, namely, in the $A \sim 60$ [70], $A \sim 150$ [105] and $A \sim 190$ [131] regions of superdeformation and in the $A \sim 250$ [39] region of normal deformation. The NL1 and NL3 parametrizations, which have been extensively used in the previous studies of rotating systems and superdeformation [11], give the values of physical observables of interest which differ only by few %. It is known that the NLSH parametrization somewhat underestimates the experimental moments of inertia [70, 105]. The NLZ parametrization has not been used in the previous studies of rotating systems, so it is unknown how well it describes such systems.

3.3.4 Single-particle properties at hyperdeformation: an example of neighbourhood of ^{124}Xe.

The role of the single-particle degrees of freedom at hyperdeformation was mainly overlooked in the previous studies. It has been studied to some extent only within the MM method in Refs. [81, 97]. However, the studies of Ref. [97] suggest that the ^{124}Xe nucleus is very rigid in the HD minimum: the dynamic moments of inertia of different HD bands differ by no more than 2%, and their changes as a function of spin are very small (see Fig. 10 in Ref. [97]). Similar results were obtained for HD bands in ^{146}Gd and ^{152}Dy in Ref. [81].

On the contrary, the CRMF calculations for the dynamic moment of inertia of the yrast and excited HD configurations in ^{124}Xe show much larger spread and much larger variations as a function of rotational frequency, see Fig. 3.15a. In addition, large variations in the calculated transition quadrupole moments Q_t of these configurations are clearly seen

in Fig. 3.15b. This suggests that the HD minimum is relatively soft and that the individual properties of the single-particle orbitals play an important role in the definition of the properties of the HD bands. One of our goals is to investigate the impact of the particle in a specific single-particle orbital on the properties of the HD bands and to study whether the methods of configuration assignment based on the relative properties of different bands are also applicable at HD.

3.3.4.1 The structure of the wave function

The structure of the wave function at HD is analysed on the example of a few single-particle orbitals of the [1,2] configuration in ^{124}Xe (Fig. 3.18). The evolution of these orbitals in energy with rotational frequency is displayed in Fig. 3.14. The wave function Ψ is expanded into the basis states by

$$\Psi = \sum_{N,\alpha} c_{N,\alpha} |N\alpha > \tag{3.10}$$

where N and α represent the principal quantum number and the set of additional quantum numbers specifying the basis state, respectively. We specify the weight a_N^2 of the basis states belonging to the specific value of N in the structure of the wave function as

$$a_N^2 = \sum_{N-\mathrm{fixed},\alpha} c_{N,\alpha}^2 \tag{3.11}$$

with the condition $\sum_N a_N^2 = 1$ following from the orthonormalization of the wave function of the single-particle orbital.

Hyperdeformation leads to a considerable fragmentation of the wave function over N, which is much larger than in the case of SD. In the regions away from the band crossing the

weight a_N^2 of the dominant N-component of the wave function does not exceed 0.8 while the weight of second largest component is typically around 0.2 (Fig. 3.18). Very strong fragmentation of the wave function is seen in the case of the $\nu[761]3/2^+$ orbital: before the band crossing the weights of the $N = 7$ and $N = 5$ components of the wave function are approximately 0.6 and 0.3, respectively. Even stronger fragmentation is seen in the region of the band crossing of the $\nu[761]3/2^+$ and $\nu[301]3/2^+$ orbitals at $\Omega_x \sim 0.7$ MeV (Fig. 3.14) where they strongly interact and gradually exchange their character (Figs. 3.18a and c). Similar fragmentation is also seen for the $\pi[770]1/2^+$ orbital (Fig. 3.18) which interacts strongly with the $\pi[532]5/2^+$ orbital in the band crossing region at $\Omega_x \sim 0.8$ MeV (Fig. 3.14). For the $\nu[880]1/2^-$ orbital, dotted lines in Fig. 3.18 are used to connect the weights before and after crossing.

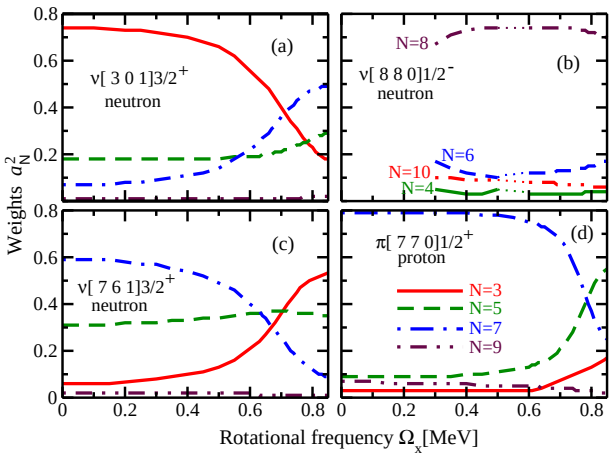

Figure 3.18

The weights of different N-components in the structure of the wave functions.

3.3.4.2 The methods of configuration assignment

The HD bands in nuclei neighboring to ^{124}Xe, which differ by either one proton or one neutron from the [1,2] configuration in ^{124}Xe, and their relative properties with respect of the [1,2] configuration in ^{124}Xe are studied in order to investigate the applicability of different methods of configuration assignment at HD. The dynamic moments of inertia for the four HD bands in each of these nuclei are compared with the one of the [1,2] configuration in ^{124}Xe in Fig. 3.19. The difference between the dynamic moments of inertia of the configurations in nuclei with masses A and $A \pm 1$ is due to the impact of the particle in the specific single-particle orbital by which two compared configurations differ. The results of the calculations question conventional wisdom [103] that the largest impact on the dynamic moment of inertia is coming from the particles in the intruder orbitals. Indeed, the impact of the neutron in the hyperintruder $\nu[880]1/2^-$ orbital on the dynamic moments of inertia (Fig. 3.19d) is comparable to the one of non-intruder $\nu[642]5/2^+$ orbital or even smaller by a factor of ~ 2 than the impact due to the neutron in non-intruder $\nu[532]3/2^+$ orbital (Fig. 3.19b). A similar situation is also seen for protons, where, for example, the impact of the proton in the hyperintruder $\pi[770]1/2^+$ orbital is smaller than its impact in the non-intruder $\pi[420]1/2^-$ orbital. This suggests that not only angular momentum, carried by the particle in specific single-particle orbital, but also polarization effects it induces into time-even and time-odd mean fields [38] are important when considering relative properties of two configurations. Based on this example, one can conclude that the configuration assignment of the HD bands, based only on the relative properties of the dynamic moments of inertia of two compared bands, is unreliable.

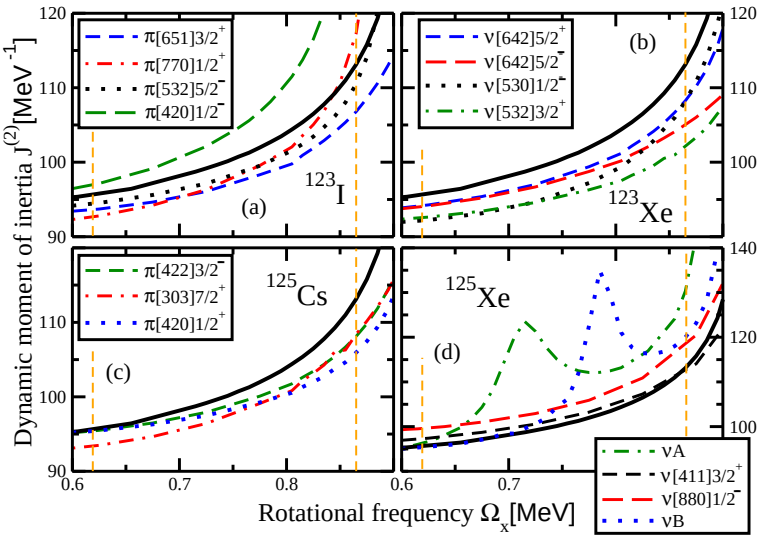

Figure 3.19

$J^{(2)}$ of selected configurations in ^{124}Xe and neighbouring nuclei.

The configuration assignments at SD have been mostly based on the effective alignment approach (see Refs. [104, 105, 70] and references therein). The success of this method is due to the fact that it was possible to separate intruder and non-intruder orbitals since the former show pronounced dependence of the effective alignments i_{eff} on the rotational frequency (see, for example, Figs. 2, 3, 5, 6 and 8 in Ref. [105]). On the contrary, the effective alignments of non-intruder orbitals are typically constant as a function of rotational frequency. It also follows from the studies in the $A \sim 140 - 150$ region of superdeformation that the change of effective alignment by $\approx 1\hbar$ within the observed frequency range allows to identify aligning intruder orbitals with a high level of confidence.

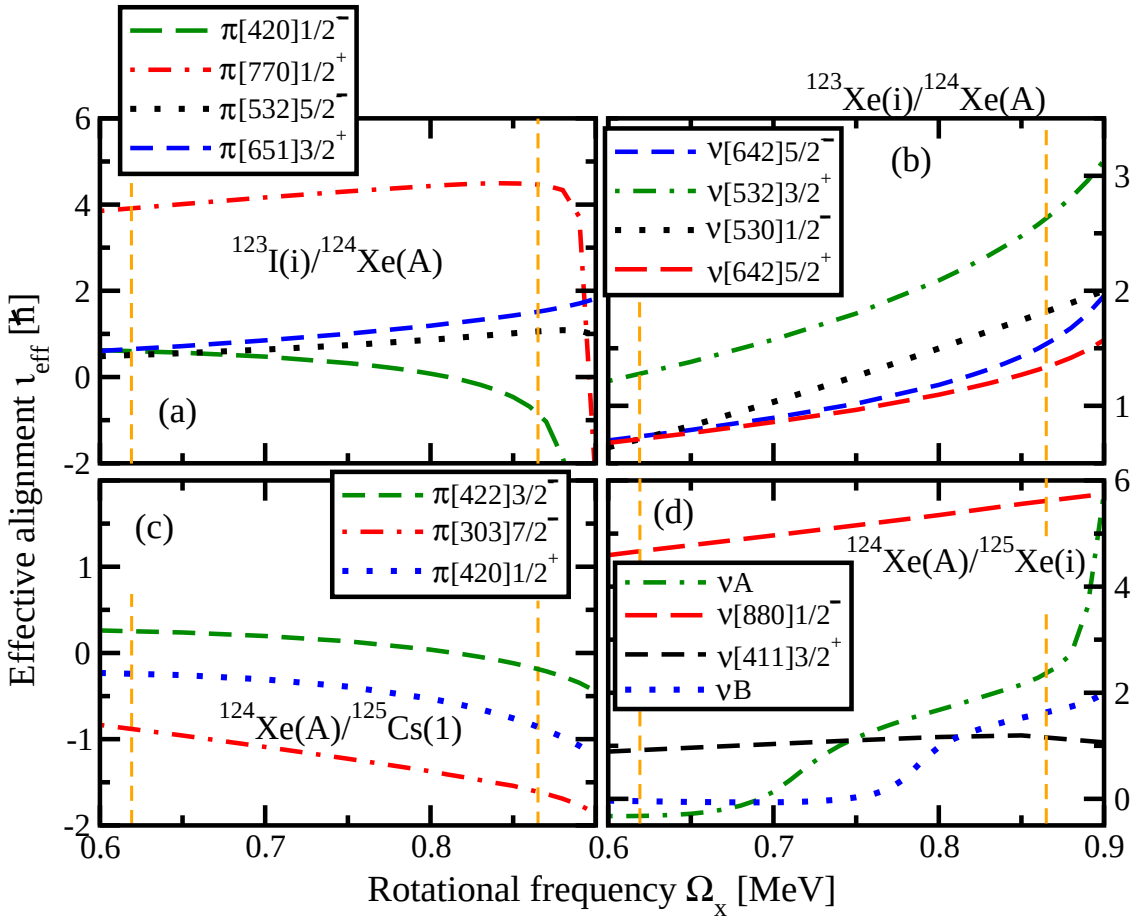

Figure 3.20

i_{eff} of the orbitals near the $Z = 54/55$ and $N = 70$ HD shell gaps.

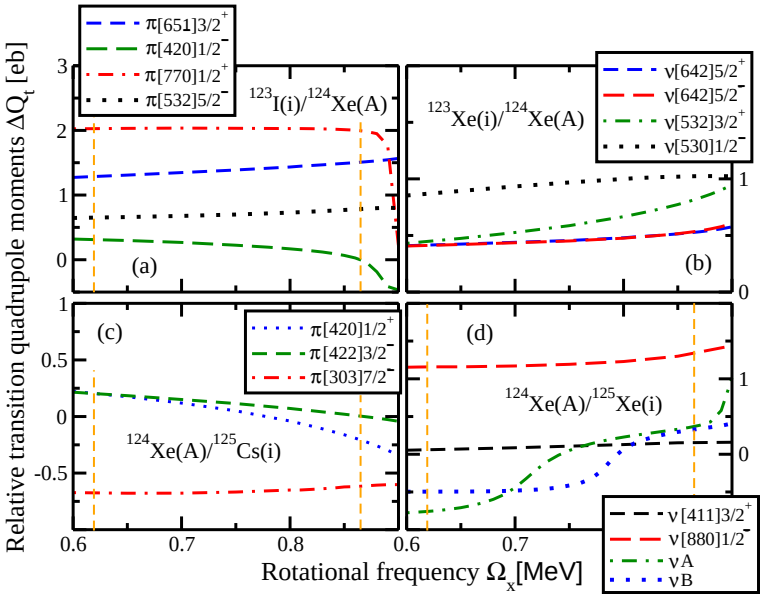

Figure 3.21

Similar to Fig. 3.20 but for $\Delta Q_t = Q_t(A+1) - Q_t(A)$.

A configuration assignment based on the effective alignments depends on how accurately these alignments can be predicted. For example, the application of the effective alignment approach in the $A \sim 140 - 150$ region of superdeformation requires an accuracy in the prediction of i_{eff} on the level of $\sim 0.3\hbar$ and $\sim 0.5\hbar$ for nonintruder and intruder orbitals, respectively [105, 104, 19]. In the highly deformed and SD bands from the $A \sim 60 - 80$ mass region, these requirements for accuracy are somewhat relaxed [70, 69]. We expect that in the $A \sim 125$ mass region of HD, the effective alignments should be predicted with a precision similar to that in the $A \sim 140 - 150$ region for a reliable configuration assignment. The effective alignment between configurations X and Y is indicated as "X/Y". In figure 3.20 the configuration X in the lighter nucleus is taken as a reference, so the effective alignment measures the effect of the additional particle. Our analysis shows that a reliable configuration assignment for the HD bands based solely on the effective alignment approach will be problematic (at least in the $A \sim 125$ mass region) because of several reasons. First, the hyperintruder orbitals do not show appreciable variations of i_{eff} with rotational frequency. Fig. 3.20 shows that the effective alignments of the hyperintruder orbitals such as $\pi[770]1/2^+$ and $\nu[880]1/2^-$ show little variations with rotational frequency (see Fig. 3.20a,d). On the contrary, the effective alignments of the $\nu[532]3/2^+$ and $\nu[530]1/2^-$ orbitals show much larger variations reaching $1.5\hbar$ in the spin range $I = 60 - 85\hbar$ in the case of the latter orbital (see Fig. 3.20b). However, the variations of i_{eff} as a function of rotational frequency are small for the majority of the orbitals in the spin range of interest. Thus, contrary to the case of SD, it will be more difficult to distinguish between hyperintruder, intruder and non-intruder orbitals based on the varia-

tions of i_{eff} with rotational frequency. This situation will become even more complicated if the suggestion of Ref. [97] that the spin range over which the HD bands are expected to be observed ($24\hbar$ at the most; this is shorter than in the case of SD) is true. These two features (small variations of i_{eff} and expected spin (frequency) range of the HD bands) will lead to a situation where the i_{eff} values for many orbitals will look alike within the typical 'error bars' of the description of i_{eff} by theoretical models, so that it will be difficult to distinguish between them within the framework of the effective alignment approach.

Similar to the case of SD [106, 107], additional information on how the single particle affects the properties of the HD bands can be extracted from the relative transition quadrupole moments ΔQ_t. Fig. 3.21 shows that the hyperintruder $\pi[770]1/2^+$ and $\nu[880]1/2^-$ orbitals with $\Delta Q_t \approx 2$ eb and $\Delta Q_t \approx 1.25$ eb have the largest impact on the transition quadrupole moments among the studied proton and neutron orbitals. One has to keep in mind that the addition of a proton changes the proton number by one. This change contributes approximately 0.5 eb in relative transition quadrupole moment ΔQ_t of the proton orbitals. This effect is not present in the ΔQ_t values of the neutron orbitals.

The ΔQ_t values were used only as a complimentary tool of the configuration assignment at SD. This is because of the difficulty to measure them in experiment [108, 109] and the fact that they show little variation as a function of rotational frequency, thus providing less information than i_{eff}. The same features are also valid at HD; see Fig. 3.21 for the variations of the ΔQ_t values. In addition, some single-particle orbitals such as $\pi[422]3/2^-$ and $\pi[303]7/2^-$ (Fig. 3.21c) show very similar ΔQ_t values. This will not allow to make a unique configuration assignment even if the experimental ΔQ_t values for these orbitals

are available. On the other hand, their i_{eff} values differ by $\sim 1\hbar$ (Fig. 3.20c), and this fact can be used in the configuration assignment.

However, the fact that in general the effective alignment approach fails to provide a unique configuration assignment at HD increases the role of the method of configuration assignment based on relative transition quadrupole moments. Our analysis shows that *only simultaneous application of these two methods by comparing experimental and theoretical* $(i_{eff}, \Delta Q_t)$ *values will lead to a reliable configuration assignment at HD.*

Let us illustrate this on the hypothetical example of two "experimental" bands; one in ^{123}I and another in ^{124}Xe. In this example, the [1,2] configuration is assigned to the band in ^{124}Xe. Let us assume that the effective alignments in the ^{123}I/^{124}Xe pair of the bands increase from $4.0\hbar$ to $4.25\hbar$ in the frequency range 0.62-0.87 MeV under selected spins of these bands. Under these conditions, the "experimental" bands differ in the occupation of the $\pi[770]1/2^+$ orbital (Fig. 3.20a). However, it is reasonable to expect that the spins of "experimental" bands will not be fixed, so these changes in effective alignment should be from $(4.0 + n)\hbar$ to $(4.25 + n)\hbar$, where $n = 0, \pm1, \pm2, ...$ Assuming that the accuracy of the description of effective alignments in theoretical calculations is around $0.4\hbar$, one can conclude that for $n = -3$ the "experimental" bands can also differ in the occupation of either the $\pi[532]5/2^-$ or $\pi[651]3/2^+$ orbitals (Fig. 3.20a). In a similar way to the $A \sim 150$ region of SD [104, 105], the systematic studies of the pairs of the bands which differ by one proton may narrow the choice of the orbitals involved. On the other hand, the ΔQ_t values for these orbitals are drastically different; $\Delta Q_t \approx 2.0$ eb for the $\pi[770]1/2^+$ orbital, $\Delta Q_t \approx 1.4$ eb for $\pi[651]3/2^+$, and $\Delta Q_t \approx 0.7$ eb for $\pi[532]5/2^-$ (see Fig. 3.21).

So, if both quantities, i_{eff} and ΔQ_t, are measured simultaneously, a unique configuration assignment for "experimental" band in ^{123}I will be possible.

The band crossing features of the HD bands provide an additional tool of configuration assignment which can be used more frequently than in the case of the SD bands because of strong mixing between the different N-shells at HD. The large peaks in $J^{(2)}$ of the νA and νB configurations in ^{125}Xe (Fig. 3.19d) are due to the band crossings with a strong interaction. These crossings are also visible in the effective alignments i_{eff} (Fig. 3.20d) and relative transition quadrupole moments ΔQ_t (Fig. 3.21d). They originate from the crossing of the same signatures of the $\nu[301]3/2$ and $\nu[761]3/2$ orbitals, where νA and νB have signatures $r = +i$ and $r = -i$, respectively. The former orbital is occupied before band crossing, the latter after band crossing. An unusual feature of these band crossings is the fact that they originate from the interaction of the orbitals, the dominant N-components of which differ by $\Delta N = 4$. At SD, the crossings between the orbitals dominated by different N-shells have been characterized by a weak interaction leading to a sharp jump in $J^{(2)}$ [20, 132, 133]. The observed unpaired SD band crossings with strong interaction are between the orbitals with the same dominant N-shells and they were observed in the nuclei around ^{147}Gd [120, 20].

3.3.5 General observations: the density of the HD bands and the necking degree of freedom

As discussed in Sect. 3.3.3 on the example of ^{124}Xe, the high density of the HD bands is one of the major obstacles for the observation of discrete HD bands. It will lead to a situation where the feeding intensity will be redistributed among many low-lying HD bands, thus, drastically reducing the intensity with which each individual band is populated. As a consequence, the feeding intensity of an individual HD band will drop below the observational limit of experimental facility; this fact has to be taken into account when planning future experiments for a search of discrete HD bands. Two factors contribute to the high density of the HD bands, namely, relatively small proton and neutron HD shell gaps in the frequency range of interest and the softness of the potential energy surfaces in the HD minimum (see Sect. 3.3.3). Systematic mapping of the density of the HD states as a function of the proton and neutron numbers is too costly in the computational sense because it involves the calculation of the lowest in energy particle-hole excitations. Thus, we decided to look at the problem of the density of the HD states in a somewhat simplistic way by considering the proton and neutron energy gaps between the last occupied and the first unoccupied states in the yrast HD configurations; the small size of these gaps will most likely point to the high density of the HD bands.

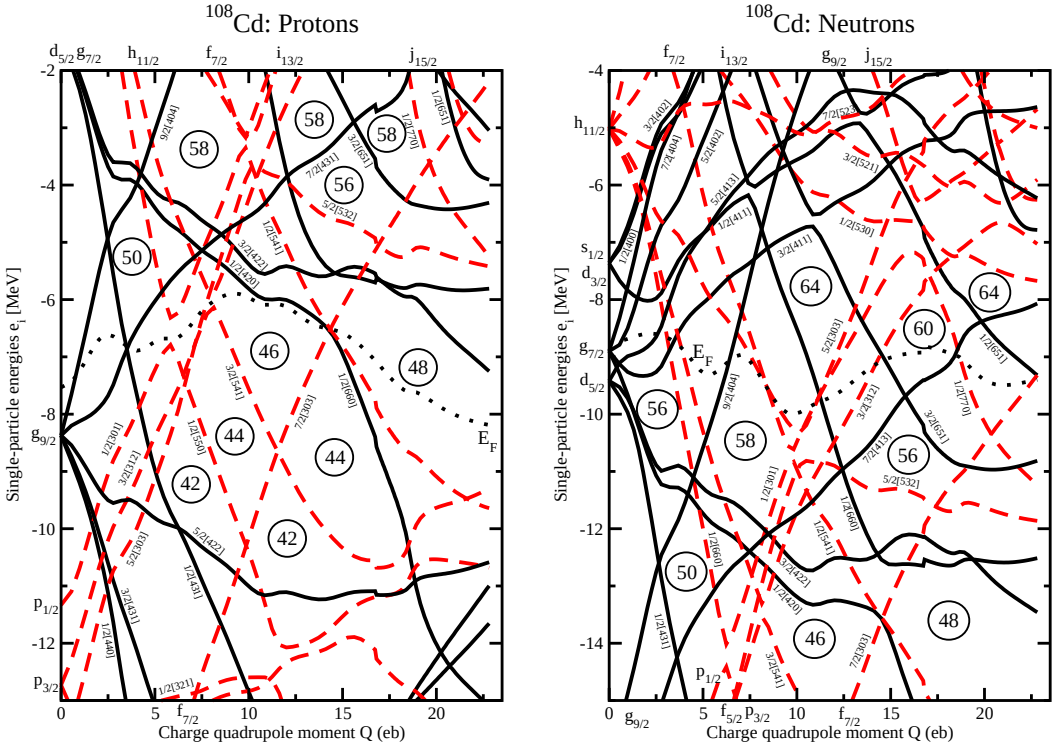

Figure 3.22

Proton and neutron single-particle energies in ^{108}Cd.

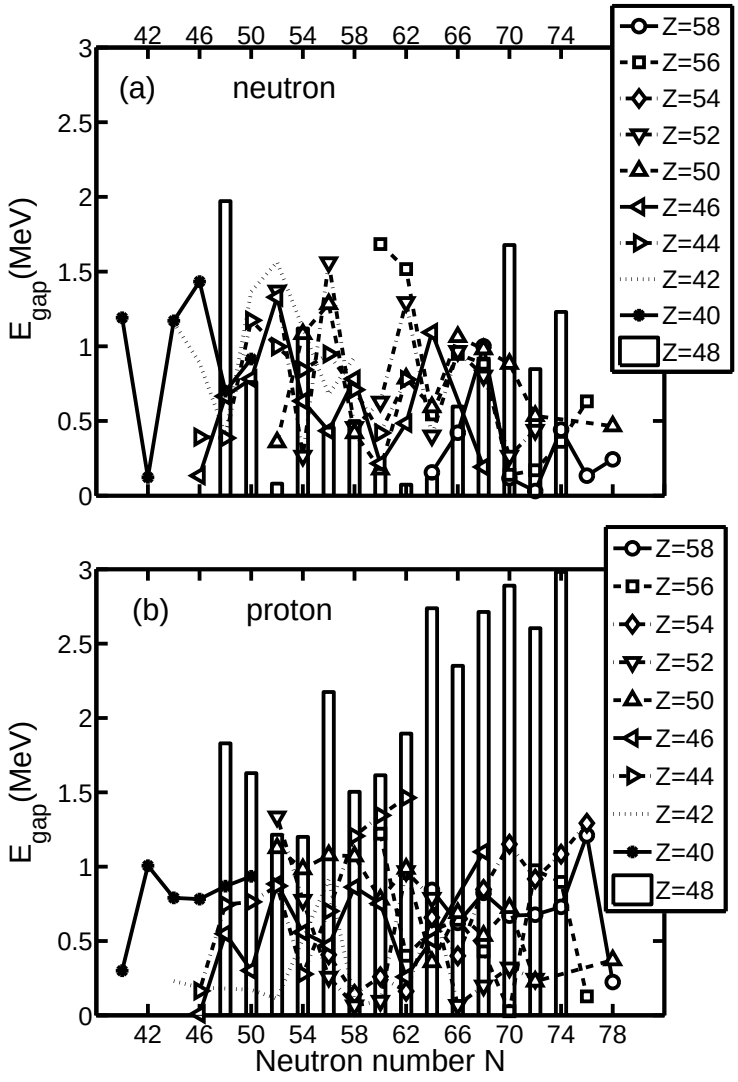

Figure 3.23

The energy gaps between the last occupied and first unoccupied orbitals.

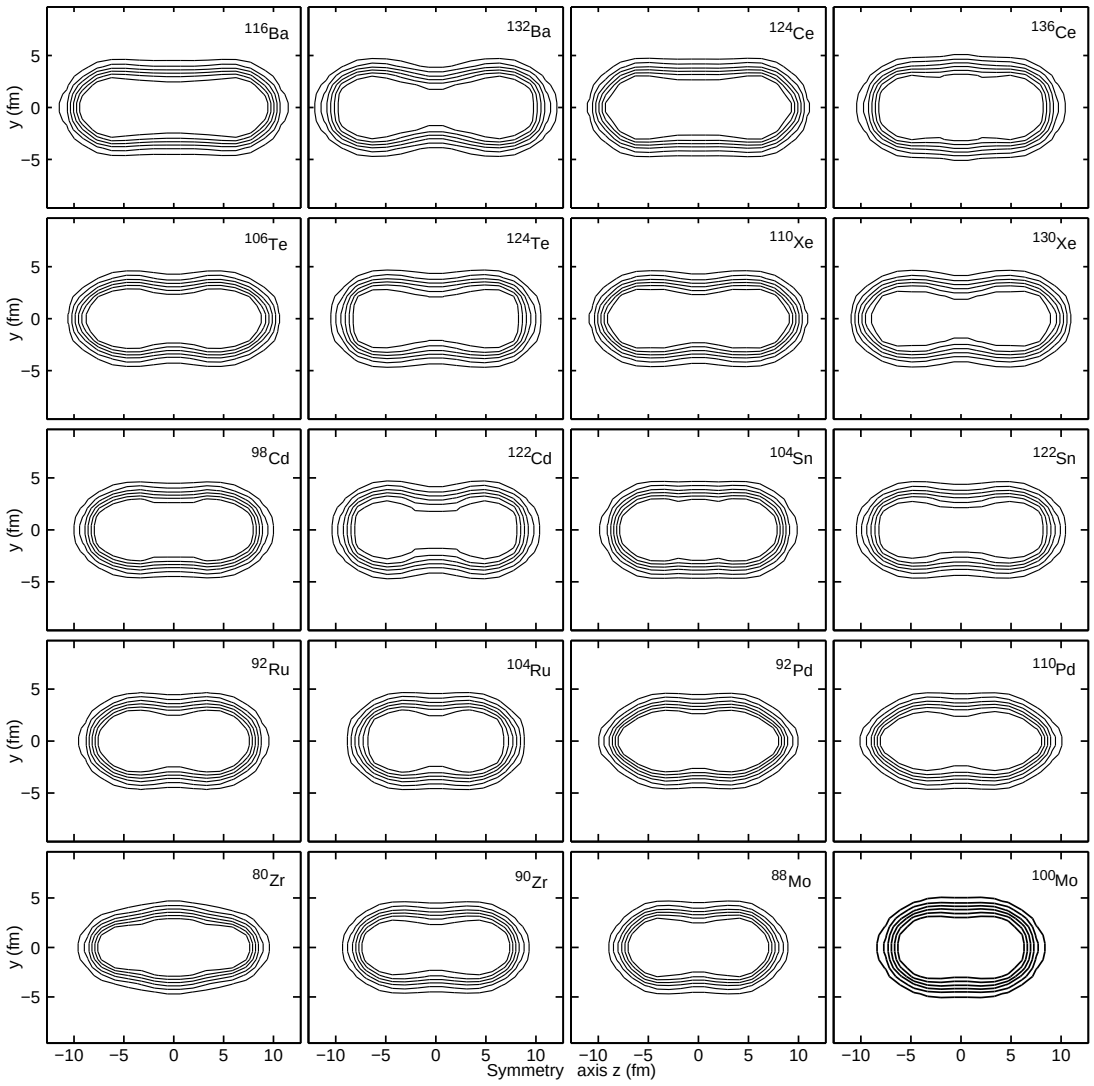

Figure 3.24

Proton densities $\rho_p(y, z)$ at the spins these configurations become yrast.

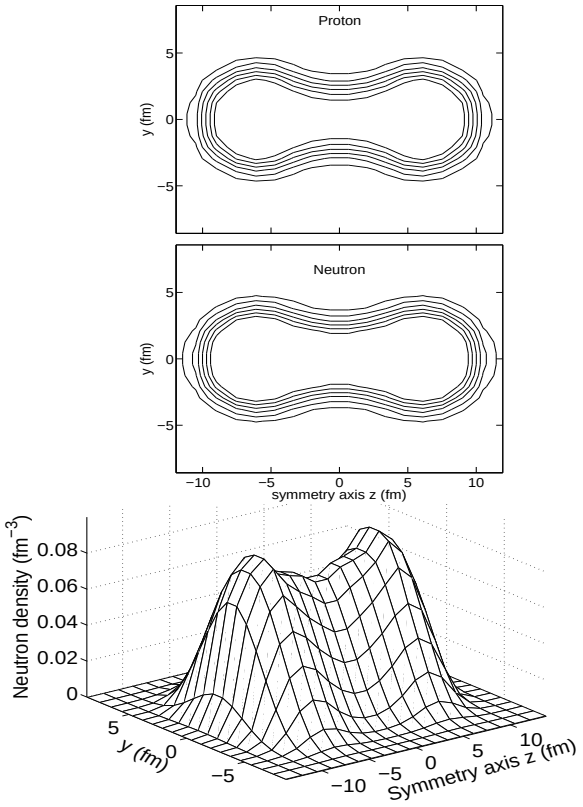

Figure 3.25

The same as in Fig. 3.17, but for ^{102}Pd at rotational frequency $\Omega_x = 0.95$ MeV.

The analysis of the Nilsson diagrams in Fig. 3.22 already reveals some HD gaps in the single-particle spectra. At the values of $Q_0 \sim 17-20\ e$b typical for the HD configurations in Cd isotopes (Fig. 3.10b), there are very large proton $Z = 48$ and neutron $N = 48$ HD shell gaps and smaller neutron gaps at $N = 58$ and 60. In Fig. 3.22 solid and dashed lines denote positive and negative parity orbitals, respectively, and the Fermi energy $\mathrm{E_F}$ is shown by dotted line. In general, this figure suggests that the hyperdeformation will be more favoured in the nuclei with a similar number of protons and neutrons because the proton and neutron shell effects for the HD shapes will act coherently; this trend has already been seen in the crossings spins I_{cr}^{HD} for different isotope chains in Sect. 3.3.1.

The size of these gaps and their presence will be altered (especially, for medium and small size energy gaps) when the rotation and the self-consistent readjustment of the neutron and proton densities with the change of particle number are taken into account. Indeed, this is seen in Fig. 3.23 which shows the energy gaps between the last occupied and first unoccupied single-particle orbitals as a function of the neutron number for different isotope chains. The largest proton gap at $Z = 48$ is seen in Cd isotopes; its size is around 1.5 MeV in proton-rich nuclei and it increases up to 3 MeV with the increase of neutron number. In other isotope chains, the size of the proton energy gap is smaller than in Cd isotopes and it fluctuates around 1 MeV. For the majority of the nuclei, the size of the neutron energy gap fluctuates around 1 MeV. However, its size increases up to 1.5 MeV in some nuclei and in ^{96}Cd it reaches 2 MeV (see Fig. 3.23 for details).

Taking into account that the proton and neutron HD shell gaps in ^{124}Xe are around 1 MeV (Fig. 3.14) and considering the results for the density of the HD states in this nucleus

as a reference (Sect. 3.3.3), one can conclude that the analysis of the energy gaps suggests that in most of the nuclei the density of the HD bands will be high. For these nuclei, the observation of discrete HD bands using existing facilities is most likely not possible. The only exceptions are Cd nuclei and a few nuclei in which the size of at least one gap reaches 1.5 MeV (see Fig. 3.23 for details). For example, in Cd nuclei the large size of the $Z = 48$ HD shell gap (especially, for nuclei in the valley of the β-stability) will make proton particle-hole excitations energetically expensive. As a consequence, the density of the HD bands has to be lower in Cd isotopes as compared with the one in other isotopes.

One has to remember that the high density of the HD bands is not necessarily a negative factor. It favors the observation of the rotational patterns in the form of ridge-structures in three-dimensional rotational mapped spectra as it has been seen in the HLHD experiment for a few nuclei [27]. The observation of ridge-structures as a function of proton and neutron number, which seems to be feasible with existing experimental facilities such as GAMMASPHERE, will provide invaluable information about HD at high spin.

The importance of the necking degree of freedom for the high-spin HD states has been studied in the MM approach in Refs. [79, 86]. However, this degree of freedom has not been investigated in detail at high spin in self-consistent approaches so far. In order to fill this gap in our knowledge, the systematics of the self-consistent proton density distributions in the HD states obtained in the CRMF calculations are shown in Fig. 3.24. One can see that in some nuclei such as ^{124}Te, ^{130}Xe, ^{132}Ba the necking degree of freedom plays an important role, while others (for example, ^{100}Mo and ^{136}Ce) show no necking. The neck is typically less pronounced in the HD states of the lighter nuclei because of

their smaller deformation (see also Fig. 5 in Ref. [91]). It becomes even more important in extremely deformed structures which according to the language of Ref. [21] can be described as megadeformed. Fig. 3.25 shows an example of density distribution for the megadeformed state in ^{102}Pd, which becomes yrast at $I \sim 85\hbar$ in the CRMF calculations. The neck is more pronounced in the proton subsystem than in the neutron one both in the HD and megadeformed structures due to the Coulomb repulsion of the segments. This is illustrated in Fig. 3.25. Our self-consistent calculations indicate that the shell structure is also playing a role in a formation of neck. For example, the neck is visible in ^{132}Ba but is not seen in ^{116}Ba (Fig. 3.24). This is contrary to the fact that the calculated transition quadrupole moments of the HD states in these nuclei (Fig. 3.8d) and their density elongations (Fig. 3.24) are comparable. These results indicate that, in general, the necking degree of freedom is important in the HD states and that it should be treated within the self-consistent approach which, in particular, allows different necking for the proton and neutron subsystems.

3.4 ^{111}I nucleus: a candidate for a doubly magic extremely SD band.

The results of the CRMF calculations for the configurations forming the yrast line or located close to it in energy are shown in Fig. 3.26. According to the calculations, normal- and highly-deformed bands, many of which show the high triaxiality that is indicative of approaching band termination [112], dominate the yrast line up to $I \approx 64\hbar$. At higher spin, more deformed structures become yrast. The configuration A has the structure $\pi 6^1 \nu 6^2$ and is yrast in the spin range $I = 64 - 73\hbar$: no hyperintruder $N = 7$ orbitals are involved in its structure. In this spin range it is characterized by the transition quadrupole moment $Q_t \sim 15.7$ eb and by the γ-deformation of $\sim 1^\circ$. The normalized transition quadrupole moment in this system is $Q_t^{norm} = 11.7$ eb, thus, this band is approximately 35% more deformed than the SD band in ^{152}Dy. As a consequence, in terms of deformation, this band can be characterized as an extremely superdeformed (ESD) band which is only slightly less deformed than the HD bands.

Table 3.2

The size of the Z=53 and N=58 shell gaps for the configuration A in ^{111}I .

	NL1	NL3	NLZ	NLSH
Z=53	1.45	1.25	1.65	0.70
N=58	1.75	1.85	1.60	2.00

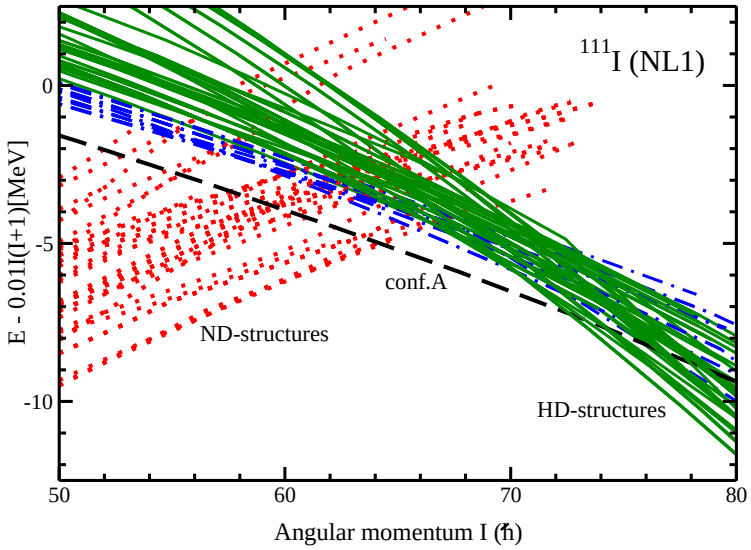

Figure 3.26

Similar to Fig.3.13 but for ^{111}I.

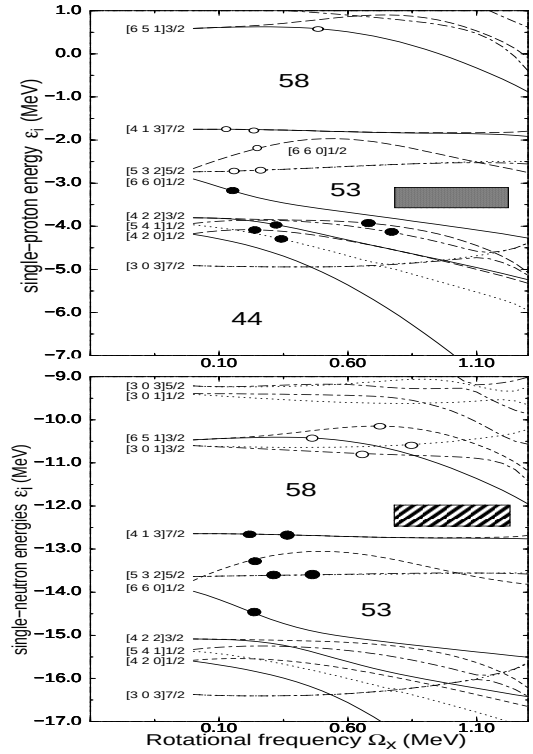

Figure 3.27

The same as in Fig. 3.5, but for the configuration A in ^{111}I.

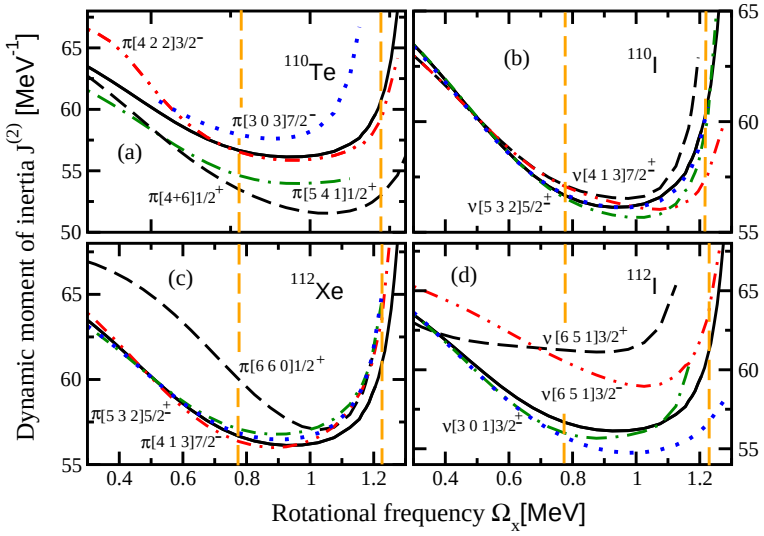

Figure 3.28

The same as in Fig. 3.19, but for $J^{(2)}$.

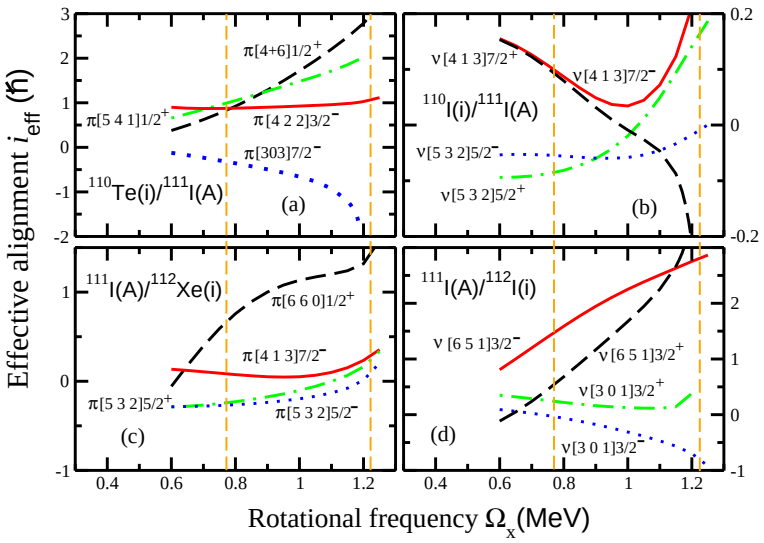

Figure 3.29

The same as in Fig. 3.20, but for i_{eff} of the single-particle orbitals.

In addition, the configuration A is well separated from the excited SD/HD configurations below $I \sim 73\hbar$ (see Fig. 3.26). This is due to the presence of the large $Z = 53$ and $N = 58$ ESD shell gaps in the single-particle spectra (see Fig. 3.27). In this configuration, all single-particle states below the $Z = 53$ and $N = 58$ ESD shell gaps are occupied by protons and neutrons, respectively. Thus, this ESD band is a doubly-magic one. This band appears as doubly-magic also in the calculations with widely used NL3 [64] and NLZ [116] parametrizations of the RMF Lagrangian, see Table 3.2. Extensive calculations with the NL3 parametrization (similar to the ones presented in Fig. 3.26) show that this band become yrast at $I \sim 62\hbar$. The $Z = 53$ ESD shell gap is smaller than 1 MeV only in the NLSH [115] parametrization of the RMF Lagrangian (see Table 3.2). However, it is known that the single-particle energies are not well described in this parametrization [39]. One should note, however, that the size of the ESD gaps in the configuration A of ^{111}I is somewhat smaller than the one for the yrast SD band in ^{152}Dy (compare Fig. 3.26 in the present manuscript with Fig. 3 in Ref. [20]; see also Figs. 4, 11, 12 in Ref. [105] obtained with different parametrizations of the RMF Lagrangian and relevant for ^{151}Tb).

The dynamic moments of inertia of the configuration A in ^{111}I and the configurations in neighboring nuclei are shown in Fig. 3.28. The increase of $J^{(2)}$ at $\Omega_x \sim 1.2$ MeV is in part due to unpaired band crossing caused by the interaction of the occupied $\nu[413]7/2^-$ and unoccupied $\nu[651]3/2^-$ orbitals (Fig. 3.27). A centrifugal stretching may also contribute to this increase of $J^{(2)}$. The effect of the occupation of a single proton (neutron) intruder orbital on the properties of the ESD bands is much more pronounced than that in the HD bands of the nuclei around ^{124}Xe (see Sect. 3.3.4); the changes induced into dynamic

moment of inertia reach at least 10% of its absolute value for the $\pi[660]1/2^+$ (Fig. 3.28c), $\pi[4+6]1/2^+$ (Fig. 3.28a), $\nu[651]3/2^+$ (Fig. 3.28d) and $\nu[651]3/2^-$ (Fig. 3.28d) orbitals. In a similar way, the effective alignments of these orbitals as well as of the $\pi[541]1/2^+$ orbital show appreciable variations as a function of rotational frequency (see Fig. 3.29), reaching at least $1\hbar$ in the spin range of interest. This suggests that the configuration assignment based on the effective alignment method will be more reliable in the case of ESD bands as compared with the HD bands in the nuclei around ^{124}Xe (see Sect. 3.3.4 for a discussion of these methods). Relative properties of the dynamic moments of inertia of two compared bands will also play a complimentary role in the configuration assignment.

3.5 Cd isotopes: Prediction of discrete hyperdeformed bands

Based on the energy gap between the last occupied and first unoccupied routhians in the yrast HD configurations shown in Fig.3.23, it suggests that the density of the HD bands in the spin range where they are yrast is high in the majority of the cases. It also indicates the Cd isotopes as the best candidates for a search of discrete HD bands. However, one has to remember that this type of analysis may be too simplistic because the polarization effects induced by particle-hole excitations are neglected. In particular, it can overestimate the size of the energy gap between the yrast and excited HD configurations. Realistic analysis of the density of the HD bands should include significant number of the HD configurations calculated in a fully self-consistent manner with all polarization effects included. Such analysis is time-consuming in computational sense. Thus, a fully self-consistent analysis of the density of the HD bands will be performed in the Cd isotopes to

find the best nuclei in which experimental study of discrete HD bands can be feasible with existing experimental facilities.

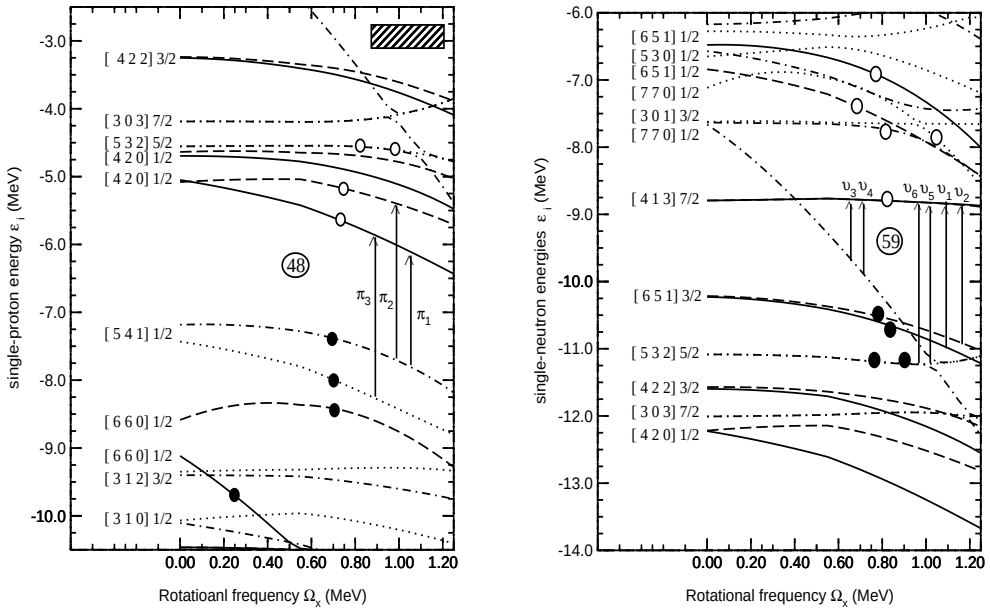

Figure 3.30

The same as in Fig.3.5 but for ^{107}Cd .

The excited HD configurations were built from the yrast HD configurations obtained in the previous section 3.3.1 by exciting either one proton or one neutron or both together. Proton and neutron configurations generated in this way are labeled by π_i and ν_j, where $i = 0, 1, 2, ...$ and $j = 0, 1, 2, ...$ are integers indicating the corresponding configurations. $\pi_0 \otimes \nu_0$ represents the yrast HD configuration. Total excited configurations $\pi_i \otimes \nu_j$ are constructed from all possible combinations of proton π_i and neutron ν_j configurations excluding the one with $i = 0$ and $j = 0$.

Table 3.3

Neutron particle-hole excitations in ^{107}Cd shown in Fig. 3.30.

label	Excitation
ν_1	[770]1/2$^+$ $\rightarrow$ [413]7/2$^+$
ν_2	[770]1/2$^+$ $\rightarrow$ [413]7/2$^-$
ν_3	[532]3/2$^-$ $\rightarrow$ [413]7/2$^+$
ν_4	[532]3/2$^-$ $\rightarrow$ [413]7/2$^-$
ν_5	[651]3/2$^-$ $\rightarrow$ [413]7/2$^+$
ν_6	[651]3/2$^+$ $\rightarrow$ [413]7/2$^-$

The selection of excited configurations is also constrained by the condition that the energy gap between the orbital from which the particle is excited and the orbital into which it is excited do not exceed 2.5 MeV in the routhian diagram for the yrast HD configuration. All configurations are calculated in a fully self-consistent manner so that their total energies are defined as a function of spin.

Fig. 3.30 illustrates the selection of excited configurations. It shows the occupation of the proton and neutron orbitals in the yrast HD configuration in ^{107}Cd. The arrows indicate the particle-hole excitations leading to excited HD configurations. According to our criteria only three proton excitations across the $Z = 48$ HD gap are considered. On the contrary, more neutron ph-excitations are allowed across the $N = 59$ HD shell gap. Table 3.3 shows their detailed structure. For example, the ν_1 configuration is created by exciting one neutron from the [770]1/2$^+$ into [413]7/2$^+$ orbitals. One can notice that we only consider the ph-excitations between the states which do not have the same combination (π,r) of parity π and signature r. The computer code in general can handle the excitations

between the states with the same (π, r), but the configurations based on such excitations are less numerically stable and require more computational time. Because of this reason and the fact that they do not alter significantly the results for the density of the HD states, it was decided to neglect them in the calculations. However, in the cases of large energy gaps between the yrast and excited HD configurations, they are taken into account.

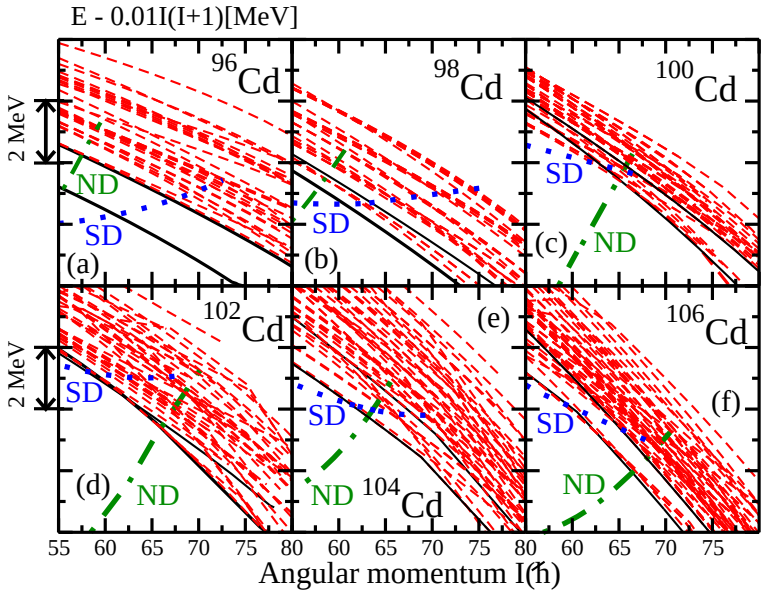

Figure 3.31

The same as in Fig. 3.13 but for the even-even $^{96-106}$Cd nuclei.

Figs. 3.31 and 3.32 show the density of the HD states in even-even $^{96-108}$Cd and odd mass ^{107,109}Cd nuclei studied using above outlined procedure. The energy gap between the yrast HD configuration and lowest excited HD configurations is around 1.5 MeV in ^{96}Cd (Fig. 3.31a). It is comparable with the energy gap between the yrast and excited

SD configurations in doubly magic SD nucleus ^{152}Dy (Fig. 7 in Ref. [20]). This energy gap in ^{96}Cd is due to large energy cost of particle-hole excitations across the $Z = 48$ and $N = 48$ HD shell gaps which have similar size (see Fig. 3.30 and Table 3.4). All that together indicates that the ^{96}*Cd is a doubly magic HD nucleus.* Only proton excitations to the $[420]1/2^-$ orbital above the $Z = 48$ HD shell gap result in bound excited proton configurations, the excitations to other orbitals located above the $Z = 48$ HD shell gap produce the proton-emitting states. The doubly magic nature of ^{96}Cd nucleus is confirmed also in the calculations with other RMF parametrizations (Table 3.4). It is interesting to mention that the RMF parametrizations aimed at the description of the nuclei far from stability such as NL3, NL3*, NLSH show larger $Z = 48$ and $N = 48$ HD shells gaps in $^{96,107-109}$Cd than the parametrizations NL1 and NLZ fitted predominantly to β-stability nuclei (Table 3.4).

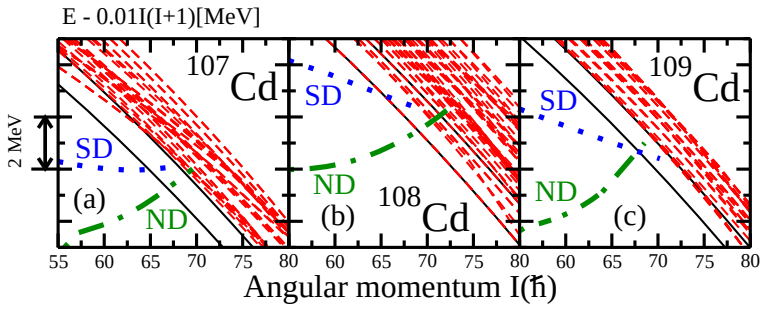

Figure 3.32

The same as in Fig. 3.13 but for ^{107,108,109}Cd.

With increasing neutron number the energy gap between the yrast and excited HD configurations disappears (Fig. 3.31). This is due to relatively high density of the neutron states above the $N = 48$ HD shell gap (Fig. 3.30). Indeed, many excited neutron configurations are located below the lowest excited proton configurations (Fig. 3.31). One can also see that even-even $^{100-104}$Cd nuclei are characterized by appreciable density of the HD states in the vicinity of the yrast HD line (Fig. 3.31). The analysis of the single-particle structure in these nuclei indicates that similar density of the HD bands is expected also in odd mass nuclei $^{99-105}$Cd. In no way these nuclei have to be considered as good candidates for a search of discrete HD bands since the feeding intensity will be redistributed among many low-lying HD bands. As a result, the feeding intensity of an individual HD band will most likely drop below the observational limit of modern experimental facilities. Although there is some energy gap between the lowest four HD configurations and other excited configurations in ^{106}Cd, this nucleus does not appear to be a good candidate for a search of discrete HD bands because the presence of four low-lying HD configurations will lead to a fragmentation of feeding intensity. This is one of possible reasons why the HD bands have not been observed in this nucleus [134].

On the other hand, the high density of the HD bands in above discussed nuclei will most likely favor the observation of the rotational patterns in the form of ridge structures in three-dimensional rotational mapped spectra [27]. The study of these patterns as a function of neutron number can provide a valuable information about HD at high spin.

Further increase of the neutron number brings the neutron Fermi level to the region of low density of the neutron states characterized by the large $N = 59$ and $N = 61$ HD

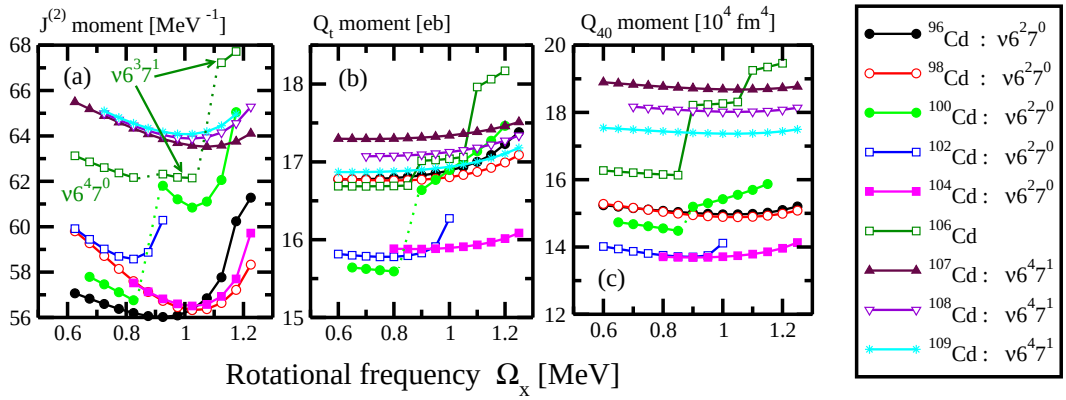

Figure 3.33

$J^{(2)}$, Q_t and Q_{40} of the yrast HD bands in the nuclei under study.

shell gaps (Fig. 3.30) with the combined size of these two gaps being around 2.5 MeV (Table 3.4). As a result, the $^{107-109}$Cd nuclei show appreciable energy gap between the yrast and lowest excited HD configurations (Fig. 3.32). This gap is especially pronounced in the case of ^{107}Cd for which it is around 1.3 MeV. Note that the size of this gap is defined by the size of the $Z = 48$ HD shell gap, since the lowest excited configuration is based on proton excitation (Fig. 3.32a). Similar or even larger energy gap between the yrast and excited HD configurations is expected in the NLZ, NL3, NL3* and NLSH parametrizations for which the size of the $Z = 48$ and $N = 59$ HD shell gaps is at least 1.7 MeV in ^{107}Cd (Table 3.4). The energy gaps between the yrast and excited HD configurations at the spins where the HD configurations become yrast are somewhat lower in ^{108,109}Cd being around 0.9 and 1.1 MeV. This energy gap in ^{108}Cd is dictated by the size of the $N = 61$ HD shell gap since lowest excited HD configurations are based on

neutron excitations. Thus, in ^{108}Cd it will be smaller (similar) in the case of the NLZ (NL3, NL3*) parametrizations and larger in the NLSH parametrization as compared with the one obtained in the NL1 parametrization (Table 3.4). In the case of ^{109}Cd, the energy gap between the yrast and excited configurations will be larger (smaller) in the NL3, NL3* and NLSH (NLZ) parametrizations (Table 3.4).

Table 3.4

The size of the Z=48, N=59, and N=61 HD shell gapsat $\Omega_x = 1.00$ MeV.

		RMF Parametrizations				
Nucleus	Gap	NL1	NLZ	NL3	NL3*	NLSH
^{96}Cd	Z=48	**1.75**	1.93	2.43	2.27	2.71
	N=48	**2.00**	2.07	2.59	2.44	3.03
^{108}Cd	Z=48	**1.62**	1.66	2.23	1.99	2.06
	N=59	1.30	1.70	1.50	1.46	**1.20**
	N=61	1.20	**0.74**	1.20	1.19	1.50
	59+61	2.50	**2.44**	2.70	2.65	2.70
^{107}Cd	Z=48	**1.70**	1.73	2.22	2.18	2.27
	N=59	1.89	2.16	2.08	2.04	**1.74**
^{109}Cd	Z=48	**1.52**	1.61	1.89	1.84	1.54
	N=61	1.37	**1.16**	1.83	1.74	2.16

Two factors make the observation of discrete HD bands in ^{108}Cd [2] with existing facilities less probable than in odd-mass ^{107,109}Cd nuclei. First, the yrast HD line in this nucleus is built from two signature degenerate configurations (Fig. 3.32b) in which the last neutron is placed into one of the signatures of the $[413]7/2$ orbital (see Fig. 3.30 and

[2]Two bands with very extended shapes observed in ^{108}Cd in Refs. [95, 96] were assigned as superdeformed in Ref. [91].

Ref. [91]). This reduces the feeding intensity of each of these bands by factor of 2 as compared with the case when the yrast HD line is built from single configuration. Second, the energy gap between the yrast and excited HD configurations decreases with increasing spin (Fig. 3.31b). As a result, further reduction of feeding intensity of the yrast HD bands is expected if the bands are populated at spins higher than the spin at which they become yrast. On the contrary, the energy gap between the yrast and excited HD configurations is more constant as a function of spin in ^{109}Cd and especially in ^{107}Cd. *All these results strongly suggest that the ^{107}Cd nucleus is the best candidate for the experimental search of the discrete HD bands.* This conclusion is also supported by detailed analysis of the single-particle routhians in the yrast HD configurations of even-even nuclei studied in Sec. 3.3; this analysis does not suggest any alternative case which would provide similar or larger gap between the yrast and excited HD configurations in even-even, odd and odd-odd nuclei of the $Z = 40 - 58$ part of the nuclear chart.

The calculated properties of the yrast HD bands in studied nuclei are shown in Fig. 3.33. The HD shapes undergo a centrifugal stretching that result in an increase of the transition quadrupole moments Q_t with increasing rotational frequency. This process also reveals itself in the dynamic moments of inertia: they increase with increasing rotational frequency in the frequency range of interest. On the other hand, the mass hexadecapole moments Q_{40} do not show a clear trend as a function of rotational frequency and stay nearly constant in the majority of the HD bands. Unpaired band crossings due to interaction of different single-particle orbitals are seen in the configurations of the yrast HD bands in ^{100,102,106}Cd nuclei. For example, the interaction between the $(r = +i)$ signatures of the

$\nu[770]1/2$ and $\nu[532]5/2$ orbitals is responsible for the crossing seen at $\Omega_x \sim 1.05$ MeV in the yrast HD band in ^{106}Cd. This crossing may be an extra factor (in addition to the density of the near-yrast HD bands) which complicates the observation of the HD bands in ^{106}Cd: such bands have not been observed in experiment of Ref. [134].

The current study clearly shows that the polarization effects in time-even and time-odd mean fields have an important impact on the density of the HD states and especially on the energy gap between the yrast and excited HD states. The latter quantity is appreciably smaller (by up to ~ 0.5 MeV; compare Figs. 3.31 and 3.32 with Table 3.4) than the respective HD shell gap in the routhian diagram.

The role of time-odd mean fields in the definition of the energy gap between the yrast and excited HD configurations is quite complicated. This is illustrated by the fact that the energy gap between the yrast HD and the lowest excited proton and neutron HD configurations is larger by ≈ 0.2 MeV in the calculations without NM than in the ones with NM at spins where the HD configurations become yrast ($I \approx 67\hbar$). This fact reflects two different mechanisms by which the time-odd mean fields affect the relative energies of different rotational bands. In the first mechanism, the angular momentum content of the single-particle orbitals is modified in the presence of time-odd mean fields, see Ref. [38] for details. There are two important consequences of this mechanism. First, the same total angular momentum of the system is built at rotational frequency which is by $\sim 25\%$ lower in the calculations with NM than in the calculations without NM. Second, the changes of the single-particle angular momenta of the single-particle orbitals surrounding the HD gaps of interest (the $\pi[420]1/2$ and $\pi[541]1/2$ orbitals for proton subsystem and $\nu[413]7/2$ and

$\nu[651]3/2$ for neutron subsystem (Fig. 3.30)) induced by NM modify the single-particle energies of these orbitals. As a result, these gaps are smaller by ~ 0.12 MeV in the calculations with NM at $I = 67\hbar$. The second mechanism is related to additional binding due to time-odd mean fields. The time-odd mean fields are stronger in the excited HD configuration than in the yrast HD configuration. Thus, additional binding due to NM is stronger in excited HD configuration than in the yrast HD configuration. This also leads to the decrease of the energy gap between the yrast and excited HD configurations in the calculations with NM as compared with the ones without NM.

The presence of time-odd mean fields reveals itself also in the energy splitting of the opposite signatures of the $\nu[770]1/2$ orbital visible at $\Omega_x = 0.0$ MeV (Fig. 3.30); the occupied orbital is more bound than unoccupied one in the RMF theory (Ref. [20]). Detailed investigation on the properties of time-odd mean fields will be presented in Ch.4.

When considering theoretical predictions one has to keep in mind that they are subject of the errors in the description of the energies of the single-particle states, which exist in the RMF theory at spherical shape [135], normal deformation [39] and quite likely at superdeformation [91]. The extrapolation from spherical and normal deformation towards HD is itself a potential source of errors since it is not know how well the response of the mean field (or the single-particle potential and liquid drop in the MM method) to the extreme elongation of the nucleus is reproduced in model calculations. Such errors are not restricted to the self-consistent models; they are also expected in the phenomenogical potentials (used in the MM method) which describe single-particle energies at normal deformation better than self-consistent models. However, several facts support the results

and interpretations given above. First, all RMF parametrizations used in this study lead to the same HD configurations in $^{96,107-109}$Cd nuclei which become yrast at similar spins (see Fig. 3.10 for comparison of the results obtained with NL1 and NL3) and to similar sizes of the proton and neutron HD shell gaps (Table 3.4). Second, the large size of the $Z = 48$ and $N = 59$ (and especially of combined neutron $59 + 61$ gap) HD shell gaps reduces the importance of the errors in the description of the energies of specific single-particle states. Third, the MM results of Ref. [86] suggest similar conclusions for the nuclei around ^{108}Cd. Indeed, large $Z = 48$ shell gap and low density of the single-particle states in the vicinity of the $N = 59$ and $N = 61$ HD shell gaps is clearly visible in Figs. 4 and 5 of Ref. [86]. The $N = 59$ and $N = 61$ shell gaps are separated by the signature-degenerated $7/2^+$ state (Fig. 5 in Ref. [86]). Thus, similar to our case, the yrast HD line in ^{108}Cd will be formed from two signature degenerated configurations in the MM calculations.

CHAPTER 4

THE PHYSICS OF TIME-ODD MEAN FIELDS

The *mean field* is a basic concept of every DFT. One can specify *time-even* and *time-odd* mean fields [33, 38] dependent on the response of these fields to the action of time-reversal operator. The properties of time-even mean fields in nuclear density functionals are reasonably well understood and defined [10, 11]. This is due to the facts that (i) many physical observables such as binding energies, radii etc. are sensitive only to these fields, and (ii) the model parameters are fitted to such physical observables.

On the other hand, the properties of time-odd mean fields, which appear only in nuclear systems with broken time-reversal symmetry, are still poorly understood. However, it is already known that these fields are important for proper description of rotating nuclei [32, 67, 68, 33, 38], band terminations [34, 136], magnetic moments [36], isoscalar monopole vibrations [137], electric giant resonances [138], large amplitude collective dynamics [139], fussion process [140], the strengths and energies of Gamow-Teller resonances [35], the binding energies of odd-mass nuclei [141, 142, 39] and the additivity of angular momentum alignments [107]. They also may play a role in the $N = Z$ nuclei [45, 141] and affect the definition of the strength of pairing correlations [37, 39]. Note that the effects, produced by the magnetic potential in the Dirac equation and called as *nuclear magnetism* (NM) [66] in the framework of the CDFT, are due to time-odd mean fields.

Rotating nuclei represent a system which is strongly affected by time-odd mean fields. The representative studies of few examples [32, 68, 33, 20, 38] clearly show that the kinematic and dynamic moments of inertia of the nuclei rotating in collective manner are considerably affected by time-odd mean fields. It was shown in the CDFT framework [38] that microscopic mechanism of this modification is traced back to the modifications of the expectation values of the single-particle angular momentum $\langle\hat{j}_x\rangle_i$ in the presence of NM. The contribution to $\langle\hat{j}_x\rangle_i$ due to NM is defined as

$$\Delta\langle j_x\rangle_i = \langle\hat{j}_x\rangle_i^{NM} - \langle\hat{j}_x\rangle_i^{WNM} \tag{4.1}$$

where the subscripts NM and WNM indicate the values obtained in the calculations with and without NM, respectively. The $\Delta\langle j_x\rangle_i$ is positive at the bottom and negative at the top of the N-shell [38]. The absolute value of $\Delta\langle j_x\rangle_i$ correlates with the absolute value of $\langle\hat{j}_x\rangle_i$. Note that the contributions to $\langle\hat{j}_x\rangle_i$ due to NM are small in the middle of the shell. The $\Delta\langle j_x\rangle_i$ contributions can be decomposed into the contributions due to spin ($\Delta\langle s_x\rangle_i$) and orbital ($\Delta\langle l_x\rangle_i$) angular momenta, which have complicated dependences both on the frequency and the structure of the single-particle orbital under study [38]. Similar features are expected also in non-relativistic DFT [38].

The changes in the alignment properties of the single-particle orbitals induced by NM (Eq. (4.1)) reflect themselves also in physical observables such as effective alignments and the energy splittings between signature partner orbitals (signature splitting), measured experimentally [38]. Moments of inertia and effective alignments in normal- and superdeformed nuclei in different parts of nuclear chart [68, 20, 105, 70, 69, 131, 11, 136] are well described by the parametrizations which include non-linear self-couplings only for

the σ-meson. This fact strongly suggests that NM is well accounted in this type of the relativistic mean field (RMF) parametrizations. In addition, NM can have an impact on the terminating states [136] and on the additivity of angular momentum alignments [107].

Many-particle configurations (further nuclear configurations or configurations) are specified by the occupation of available single-particle orbitals. In the calculations without pairing, the occupation numbers n are integer ($n = 0$ or 1). In odd nuclei, all single-particle states with exception of one are pairwise occupied. We will call this occupied single-particle state of fixed signature for which its time-reversal (signature) counterpart state is empty as *blocked state* in order to simplify the discussion. The total signature and the parity of the configuration are the same as the ones of the blocked state. In the CRMF code, it is possible to specify the occupation of either $r = +i$ or $r = -i$ signature of the single-particle state. The specification of nuclear configuration by means of listing all occupied single-particle states is unpractical. Thus, we label the nuclear configuration in odd mass nuclei by the Nilsson label and the signature of the blocked state. Note that many physical observables, such as additional binding due to NM, do not depend on the signature of the blocked state in odd-mass nuclei. In these cases, we will omit the signature from the configuration label. In odd-odd nuclei, the Nilsson labels of the blocked proton and neutron states and their signatures are used for configuration labelling. Note that the labelling by means of Nilsson labels is performed only when the calculated shape of nuclear configuration is prolate or near-prolate.

In order to investigate the impact of NM (time-odd mean fields) on physical observables, the CRMF calculations are performed in three calculational schemes for the fixed configurations:

- fully self-consistent calculations with NM included (further denoted as NM calculations which take into account space-like components of the vector mesons (Eqs. (2.20), (2.22) and (2.17)), currents (Eqs. (2.20), (2.22), and (2.26)), and magnetic potential $\boldsymbol{V}(\boldsymbol{r})$ (Eq. (2.17));
- fully self-consistent calculations without NM (further denoted as WNM calculations which omit space-like components of the vector mesons (Eqs. (2.20), (2.22) and (2.17)), currents (Eqs. (2.20), (2.22), and (2.26)), and magnetic potential $\boldsymbol{V}(\boldsymbol{r})$ (Eq. (2.17)). Note that the results of the NM and WNM calculations are always compared for the same nuclear configuration;
- perturbative calculations (the physical quantities of interest are indicated by superscript *pert*). Fully self-consistent calculations with NM provide a starting point. Using their fields as input fields, only one iteration is performed in the calculations without NM: this provides perturbative results. Time-even mean fields are the same in both (fully self-consistent and perturbative) calculations. Then, the impact of time-odd mean fields on calculated quantities (for example, different terms in the total energy (see Eq. 2.31)) is defined as the difference between the values of this quantity obtained in these two calculations. In this way, the pure effects of time-odd mean fields in fermionic and mesonic channels of the model are isolated because no polarization effects are introduced into time-even mean fields.

These are the ways in which the effects of time-odd mean fields can be studied, and as such they are frequently used in the DFT studies for non-rotating and rotating systems, both in relativistic and non-relativistic frameworks [33, 141, 74, 142, 36, 68, 38, 136]. One should, however, keep in mind that if time-odd fields are neglected, the local Lorentz invariance (Galilean invariance in non-relativistic framework [33, 12]) is violated. The inclusion of time-odd mean fields restores the Lorentz invariance.

It is interesting to compare the basic features such as Lorentz invariance and the definition of the coupling constants of the time-odd channel of the CDF theory discussed above

with the ones of non-relativistic Skyrme energy density functional (EDF) theory. It was recognized in earlier Skyrme DFT studies, that the connection between the coupling constants of time-odd and time-even channels depends on what entity, namely, Skyrme force or energy density functional is considered to be more fundamental [33, 12, 143]. If the Skyrme force is considered more fundamental then the time-odd constants are determined as a function of time-even constants [33, 143]. However, since the time-even coupling constants are usually adjusted solely to the time-even observables, the resulting values of the time-odd coupling constants simply "fictitious" or "illusory", as noted already in Ref. [144] (see also Ref. [143]). On the contrary, in the framework of the Skyrme energy density functional theory, time-odd properties of the functional are independent of time-even properties which is a consequence of broken link between the Skyrme force and the density functional.

The question of whether Galliean invariance must be imposed in Skyrme EDF is not yet resolved [12], despite the fact that it is imposed in many studies. Note that in many phenomenological approaches, such as the noninteracting or interacting shell models, Galilean symmetry is not considered, because the translational motion is not within the scope of such models [12]. It is also important to mention that the cranking models based on phenomelogical Woods-Saxon or Nilsson potentials do not incorporate time-odd mean fields. However, they succesfully describe rotating nuclei [145, 147].

4.1 Binding energies in odd mass nuclei

The time-reversal invariance is conserved in the ground states of even-even nuclei. The nucleon states are then pairwise degenerated, and the contribution of the state to the currents cancels with the contribution of its time-reversed partner. Time-odd mean fields reveal themselves in odd- and odd-odd mass nuclei and in two-(multi-)quasiparticle states of even-even nuclei. This is because an unpaired (odd) nucleon breaks the time-reversal invariance in intrinsic frame and produces the contribution to the currents and spin. In this case, the Kramer's degeneracy of time-reversal partner orbitals is also broken.

While there was a considerable interest in the study of time-odd mean fields in odd- and odd-odd mass nuclei at no rotation within the Skyrme EDF [141, 142], relatively little is known about their role in the framework of the CDFT. So far, the impact of time-odd mean fields on binding energies has been studied in the CDFT framework only in odd-mass nuclei around doubly magic spherical nuclei in Ref. [135], and in few deformed nuclei around ^{32}S [148] and ^{254}No [39].

4.1.1 Binding energies in light nuclei

The impact of NM on the binding energies of light odd-mass nuclei is shown in Fig. 4.1. The calculations have been performed with the NL3 parametrization of the RMF Lagrangian. They cover the nuclei from the proton-drip line up to the neutron-drip line. One can see that in all cases the presence of NM leads to additional binding the magnitude of which is nucleus and state dependent. The absolute value of this additional binding is typically below 200 keV and only reaches 300 keV in some lower mass nuclei. On the

average, the magnitude of additional binding due to NM is inversely correlated with the mass of the nucleus; it is the largest in the lightest nuclei and the smallest in the heaviest nuclei. For each isotope chain, it is the largest in the vicinity of the proton-drip line and the smallest in the vicinity of the neutron-drip line. The polarization effects induced by NM and the energy splitting between blocked state and its unoccupied signature partner induced by NM decrease with the increase of mass (compare Tables 4.1 and 4.2 below). This explains the observed trends in additional binding due to NM.

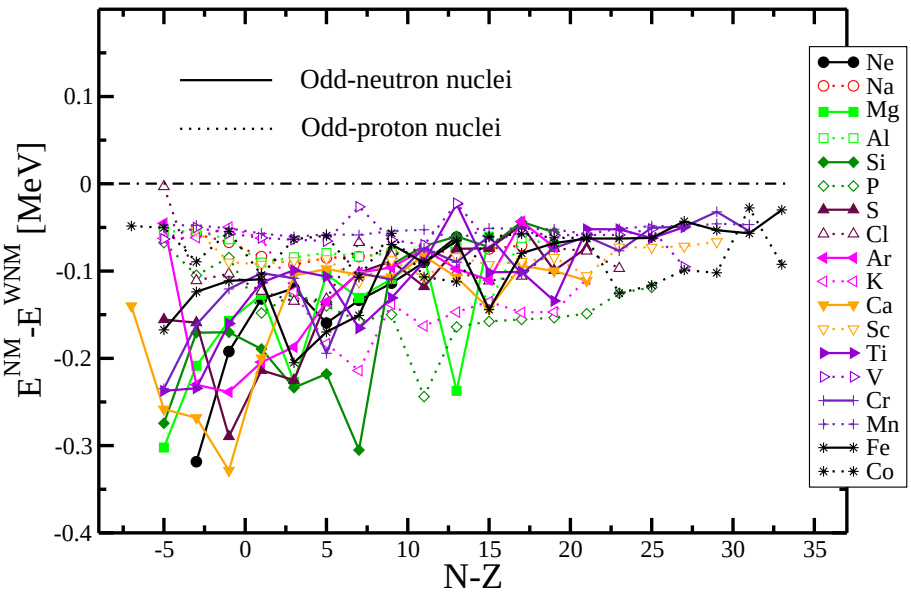

Figure 4.1

The impact of NM on binding energies of light odd-mass nuclei.

The modifications of the binding energies and quasiparticle spectra are the most important issues when considering time-odd mean fields in non-rotating systems. The binding

energies are important in nuclear astrophysics applications [149], and their modifications due to time-odd mean fields may have considerable consequences for the r- and rp-process abundances. Thus, it is important to understand the influence of time-odd mean fields on binding energies of odd- and odd-odd mass nuclei, especially in the context of mass table fits [150]. With the current focus on the spectroscopic quality DFT [151], the knowledge on how time-odd mean fields influence the relative energies of different (quasi)particle states in model calculations is also needed.

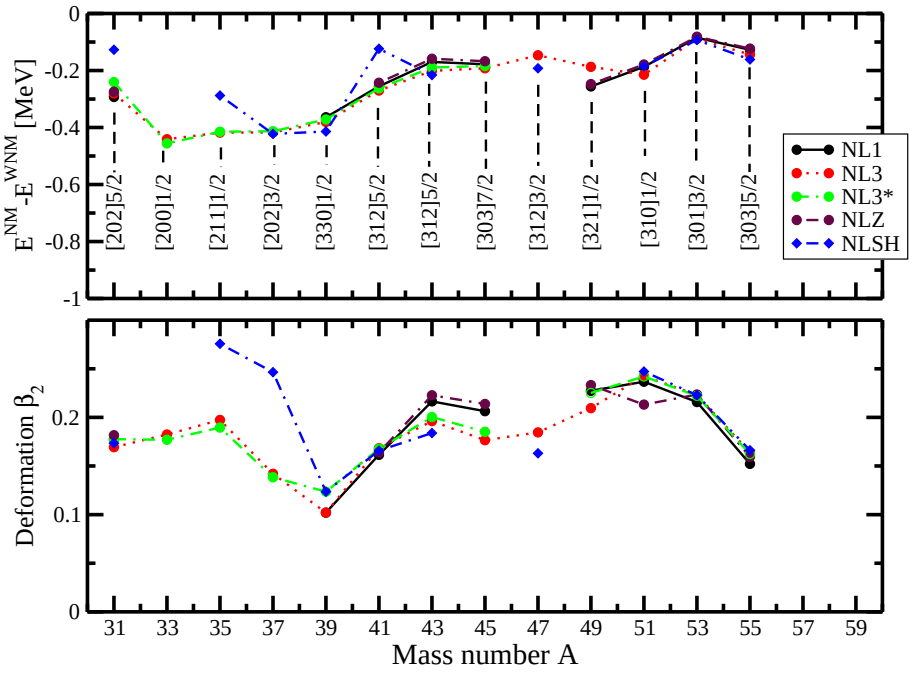

Figure 4.2

The same as in Fig. 4.1 but for Ar isotopes with different parametrizations .

Fig. 4.2 shows that additional binding due to NM only weakly depends on the RMF parametrization; this is also seen in the analysis of terminating states in Ref. [136]. In both cases, the largest deviation from the NL3 results is observed in the case of the NLSH parametrization.

It is interesting to compare these results with the ones obtained in the Skyrme EDF (see Fig. 4 in Ref. [141]). The modifications of total binding energy due to time-odd mean fields are given by the E^{to} quantity in Ref. [141], which is an analog of the $E^{NM} - E^{WNM}$ quantity. The general dependence of both quantities on $N-Z$ is similar in odd-mass nuclei apart from a few cases such as ^{43}Ti and ^{43}Sc in SLy4 Skyrme EDF (Fig. 4 in Ref. [141]). Neither RMF nor Skyrme EDF calculations in odd-mass nuclei indicate the enhancement of time-odd mean fields in the vicinity of the $N = Z$ line. This is contrary to Ref. [141] which suggested that the effects of time-odd mean fields are enhanced at the $N = Z$ line. The absolute values of E^{to} and $E^{NM} - E^{WNM}$ quantities are similar being below 300 keV in the majority of the cases. The principal difference between the RMF and the Skyrme EDF lies in the fact that time-odd mean fields are always attractive and show very small dependence on the parametrization in the RMF calculations (this is also supported by the analysis of terminating states, see Ref. [136]), while they can be both attractive (SLy4 force) or repulsive (SIII force) and show considerable dependence on the parametrization in Skyrme EDF (Ref. [141]).

4.1.2 Binding energies in the Ce $(Z = 58)$ isotopes

The role of time-odd mean fields is studied here in medium mass Ce isotopes in order to facilitate the comparison with the results obtained within the Skyrme EDF with the SLy4 force in Ref. [142]. This reference represents the most detailed study of time-odd mean fields in odd-mass nuclei within the Skyrme EDF. We consider the lowest configurations of positive and negative parities, while Ref. [142] studies only the lowest configurations in each nucleus.

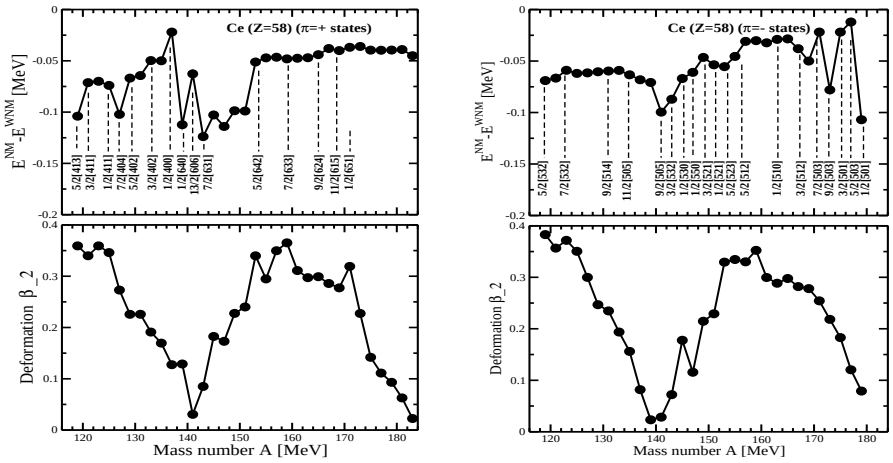

Figure 4.3

E^{NM} - E^{WNM} and deformation in odd mass Ce ($Z = 58$) nuclei.

The configurations in Figs. 4.3 and **??** are labelled by the Nilsson labels of the blocked states; the configurations at and to the right of the Nilsson label up to the next Nilsson label have the same blocked state. Figs. 4.3 and **??** show the additional binding due to NM. The comparison with the Skyrme EDF results of Ref. [142] reveals a number of important

differences. First, similar to the results in light nuclei (Sect. 4.1.1) and in actinide region (Sect. VI H in Ref. [39]), time-odd mean fields are attractive in the RMF calculations for the Ce isotopes. On the contrary, they are repulsive in the SLy4 parametrization of the Skyrme EDF [142]. Note that the SLy4 force produces attractive time-odd mean fields in light nuclei (Ref. [141]). This mass dependence of the effects of time-odd mean fields in the Skyrme EDF may be due to the competition between isovector and isoscalar effects [142]. The average absolute magnitude of the change of binding due to time-odd mean fields in the RMF calculations is only half of the one seen in the Skyrme calculations with the SLy4 parametrization. It was also checked on some examples that additional binding due to NM only weakly depends on the parametrization of the RMF Lagrangian.

Second, the results of the calculations do not reveal a strong dependence of additional binding due to NM on deformation. For example, the deformation of the $\nu[615]11/2$ configuration in the $^{173-181}$Ce chain changes drastically from $\beta_2 \sim 0.23$ down to $\beta_2 \sim 0.06$ (Fig. 4.3, bottom panel), but the additional binding due to NM remains almost the same (Fig. 4.3, top panel). The $\nu[523]7/2$ and $\nu[505]11/2$ configurations are another examples of this feature (Fig. **??**).

Third, the binding energy modifications due time-odd mean fields are completely different in the RMF and Skyrme EDF calculations. In the Skyrme EDF calculations, the magnitude of these binding energy modifications is related with three properties of the blocked orbital. In decreasing order of importance they are [142]: a small Ω quantum number, a down-sloping behavior of the energy of the single-particle state with mass number A, and a large total angular momentum j for the spherical shell from which the single-

particle state originates. For example, the binding energy modifications due to time-odd mean fields will be larger for the configuration based on blocked single-particle state with small Ω than for the configuration with large Ω of the blocked state if both blocked states belong to the same j-shell. On the contrary, the RMF calculations do not reveal this type of correlations between additional binding due to NM and the structure of the blocked state. Indeed, the configurations which have the largest changes in binding energies due to NM ($|E^{NM} - E^{WNM}| \geq 0.1$ MeV) are [413]5/2, [404]7/2, [640]1/2, [631]3/2, [505]9/2 and [501]1/2.

4.1.3 Current distributions

When discussing current distributions, it is important to remember that the calculations are performed in one-dimensional cranking approximation. Although the rotational frequency is equal to zero in the calculations, the results for the currents still obey the symmetries imposed by the cranking approximation. This is clearly seen when considering the signature quantum number in the limit of vanishing rotational frequency Ω_x (see Ref. [152]). In this case definite relations exist between the states $|\nu, r_\nu >$ of good signature r_ν (ν denotes the set of additional quantum numbers) and the single-particle states employed usually in the low spin limit. For the latter states in axially symmetric nuclei, we obtain doubly degenerate single-particle states $|\nu, \Omega_\nu >$ and $|\nu, \bar{\Omega}_\nu >$, where Ω_ν denotes the projection of angular momentum on the symmetry axis. Here, $|\nu, \Omega_\nu >$ is an eigenstate with definite angular momentum projection Ω_ν, while $|\nu, \bar{\Omega}_\nu >$ denotes the time-reversed state (with angular momentum projection $-\Omega_\nu$). In the limit of vanishing rotational fre-

quency $\Omega_x = 0$, the states $|\nu, r_\nu >$ with definite signature r_ν become linear combinations of the states $|\nu, \Omega_\nu >$ and $|\nu, \bar{\Omega}_\nu >$

$$
\begin{aligned}
|\nu, r_\nu = -i > &= \frac{1}{\sqrt{2}}\{-|\nu, \Omega_\nu > +(-1)^{\Omega_\nu - 1/2}|\nu, \bar{\Omega}_\nu >\}, \\
|\nu, r_\nu = +i > &= \frac{1}{\sqrt{2}}\{(-1)^{\Omega_\nu - 1/2}|\nu, \Omega_\nu > +|\nu, \bar{\Omega}_\nu >\}
\end{aligned}
\tag{4.2}
$$

These relations may be considered as a transformation between two representations of the single-particle states: the one with good projection Ω_ν (the $|\nu, \Omega_\nu >$ representation) and the other with good signature r (cranking representation). In the $|\nu, \Omega_\nu >$-representation the alignment of angular momentum vector of a particle is specified along the axis of symmetry. As a result, the axial symmetry is conserved and only azimuthal currents with respect of the symmetry axis are present. In the cranking formalism (which allows also triaxial shapes), the alignment of angular momentum vector of a particle is specified along the $x-$axis perpendicular to the axis of symmetry. As a result, the currents follow the symmetries of cranking approximation and have the distributions discussed below.

Total neutron current distributions in the configurations of selected nuclei having similar quadrupole deformations are shown in Figs. 4.4 and 4.5. The currents in panels (d) and (e) of Fig. 4.4 are plotted at arbitrary units for better visualization. The currents in other panels are normalized to the currents in panels (d) and (e) by using factor F. They are predominantly defined by the currents generated by the blocked orbitals. This is clearly visible from the comparison of Figs. 4.4 and 4.6: the latter figure shows the currents produced by single neutron in different Nilsson states of the $\nu[660]1/2$ configuration in ^{171}Ce.

Neutron currents are characterized by the complicated patterns in different cross-sections of the nucleus. Fig. 4.6 clearly shows that these patterns are defined by the density distributions of the blocked states. Moreover, there are clear correlations between the patterns of the currents in the $y-z$ plane (z is the symmetry axis and x is the rotation axis in the CRMF theory) and the Ω value of the Nillson label of the blocked orbital (Figs. 4.4 and 4.6). At $\Omega = 1/2$, the single-particle densities are concentrated in the vicinity of the axis of symmetry, and, as a consequence, the currents show circulations (vortices) which are concentrated in the central region of the nucleus. However, with increasing Ω, the densities (and, as a consequence, the currents) are pushed away from the axis of symmetry of the nucleus towards the surface area. In addition, the strength of the currents correlates with Ω. As follows from the values of factor F the strongest currents appear for the $\Omega = 1/2$ states. These orbitals are aligned with the axis of rotation (x-axis) already at no rotation. As a result, the single-particle angular momentum vector of the $\Omega = 1/2$ orbitals performs the precession around the x-axis, thus orienting the currents predominantly in the $y-z$ plane. This extra mechanism is not active in other configurations. The strength of the currents decreases with the increase of Ω. For example, the currents generated by the blocked $\Omega = 11/2$ orbitals are weaker by a factor of almost 200 than the currents generated by the blocked $\Omega = 1/2$ orbitals (compare scaling factors F in Fig. 4.4 for the blocked states with different Ω values). In Fig. 4.6 the shape and size of the nucleus are indicated by density line which is plotted at $\rho = 0.01$ fm^{-3} ($\rho = 0.0005$ fm^{-3} in panel (b)). The single-neutron density distribution due to the occupation of the indicated Nilsson state is plotted starting with $\rho = 0.0005$ fm^{-3} in step of 0.0005 fm^{-3} (0.0003 fm^{-3} in panels (d-f)). The currents

in panel (d) are plotted at arbitrary units for better visualization. The currents in other panels are normalized to the currents in panel (d) by using factor F. The currents and densities are shown in intrinsic frame in the $y-z$ plane at $x = 0.48$ fm. In the $x-y$ plane, the majority of the configurations show the current pattern (although with different strength of the currents and their localization in space) visible on Fig. 4.5b, while the typical pattern of the currents in the $x-z$ plane is shown in Fig. 4.5a. Figs. 4.4d,e show that the change of the signature of the blocked orbital leads only to a change in the direction of the currents.

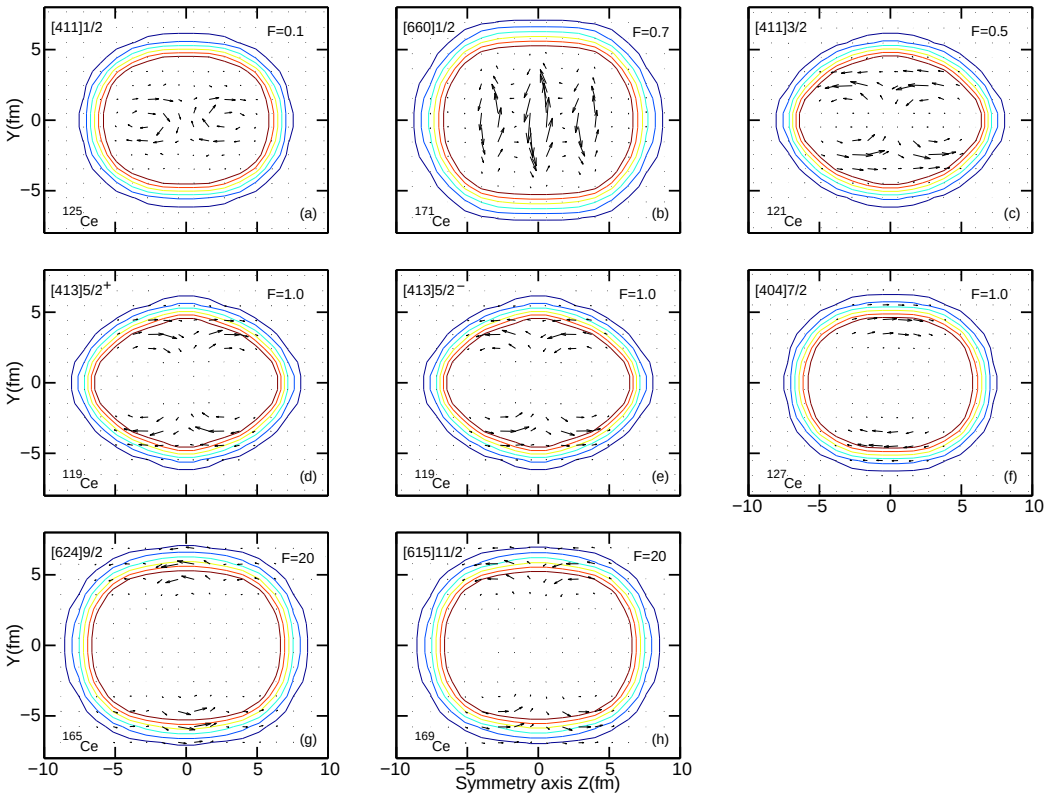

Figure 4.4

Total $\boldsymbol{j}^n(\boldsymbol{r})$ in intrinsic frame in the $y-z$ plane.

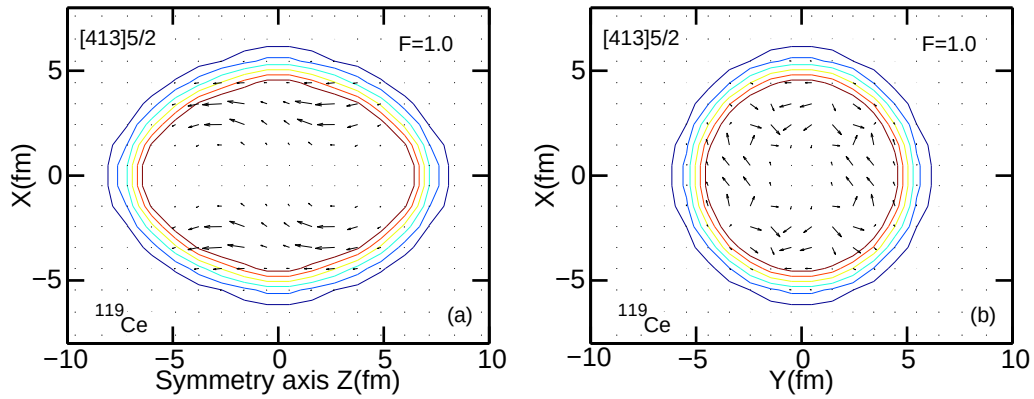

Figure 4.5

The same as in Fig. 4.4 but in the $z-x$ plane and in the $y-x$ plane.

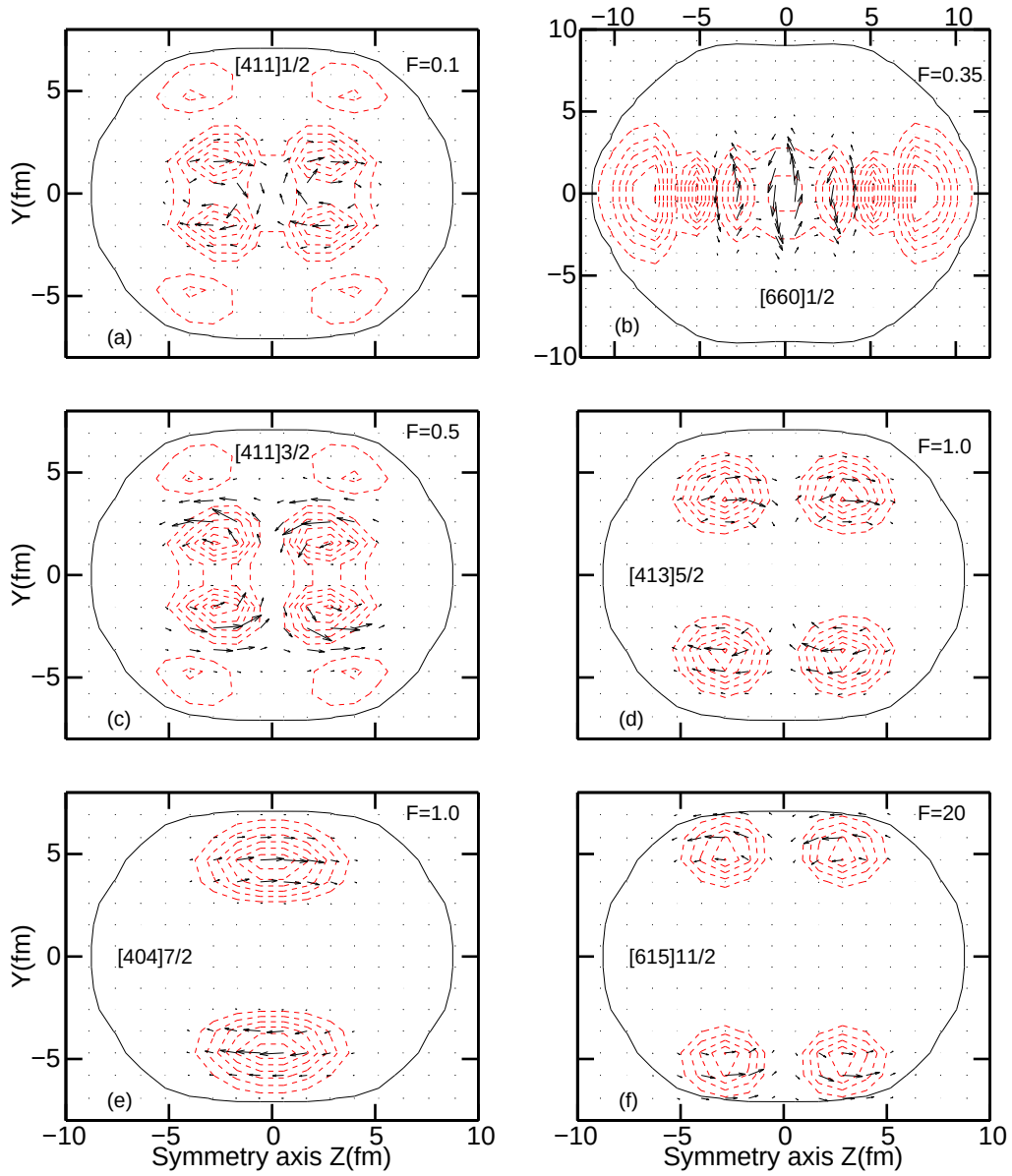

Figure 4.6

$\boldsymbol{j}^n(\boldsymbol{r})$ produced by single-particle states in the $\nu[660]1/2$ configuration ^{171}Ce.

4.1.4 Particle number dependences of additional binding due to NM

Neutron and proton number dependences of additional binding due to NM (the $|E^{NM} - E^{WNM}|$ quantity) are presented in Fig. 4.7. These figures are based on the results obtained in Sects. 4.1.1 and 4.1.2 and on some extra calculations. These extra calculations include odd-Z nuclei with $N = 94$, odd-N nuclei with $Z = 98$, and odd-Z nuclei with $N = 154$ and cover these isotope and isotone chains from proton- to neutron-drip lines.

The calculations of nuclei around ^{249}Cf were also performed in order to check the impact of pairing on the $(E^{NM} - E^{WNM})$ quantity. For the same blocked states, the $(E^{NM} - E^{WNM})$ values obtained in the calculations without pairing in the present manuscript were compared with the ones obtained in the Relativistic Hartree-Bogoliubov calculations of Ref. [39] (see Table IV of Ref. [39]). Although the pairing decreases additional binding due to NM in the most of the cases, there are still one-(quasi)particle configurations in which the $|E^{NM} - E^{WNM}|$ quantity is smaller in the calculations without pairing. This is a consequence of the complicated nature of the $E^{NM} - E^{WNM}$ quantity defined by (i) the interplay of time-odd mean fields and the polarization effects (Sect. 4.2) and by (ii) the differences in the impact of pairing on different terms of total energy.

The calculated $|E^{NM} - E^{WNM}|$ quantities were fitted by simple parametrization

$$\Delta E = \frac{c}{Q^{\alpha}} \tag{4.3}$$

where Q is equal either to proton Z or neutron N numbers. Note that the $|E^{NM} - E^{WNM}|$ values from odd-proton (odd-neutron) nuclei were used in the fit of $Z-(N-)$dependence of ΔE. The results of the fits are shown by solid lines in Fig. 4.7. One can see that

the powers α are similar for different fits (proton or neutron). On the other hand, the magnitudes c differ considerably between proton and neutron quantities, indicating weaker additional binding due to NM for odd-proton nuclei. This result is consistent with the analysis obtained in Sect. 4.3.

The three-point indicator [153]

$$\Delta^{(3)}(N) = \frac{\pi_N}{2}\left[B(N-1) + B(N+1) - 2B(N)\right] \tag{4.4}$$

is frequently used to quantify the odd-even staggering (OES) of binding energies. Here $\pi_N = (-1)^N$ is the number parity and $B(N)$ is the (negative) binding energy of a system with N particles. In Eq. (4.4), the number of protons Z is fixed, and N denotes the number of neutrons, i.e. this indicator gives the neutron OES. The factor depending on the number parity π_N is chosen so that the OES centered on even and odd neutron number N will both be positive. An analogous proton OES indicator $\Delta^{(3)}(Z)$ is obtained by fixing the neutron number N and replacing N by Z in Eq. (4.4).

The $\Delta^{(3)}(N)$ (and similarly $\Delta^{(3)}(Z)$) quantity will be modified in the presence of time-odd mean fields as

$$\Delta^{(3)}_{TO}(N) = \Delta^{(3)}_{WTO}(N) + \delta E_{TO} \tag{4.5}$$

where the subscripts 'TO' and 'WTO' indicate the values obtained in the calculations with and without time-odd mean fields, and δE_{TO} is the contribution coming from time-odd mean fields. If the $\Delta^{(3)}(N)$ quantity is centered at odd-N nucleus, the δE_{TO} quantity represents the change of binging energy of this odd-mass nucleus induced by time-odd mean fields. This is because the time-odd mean fields have no effect on the binding energies of

the ground states of even-even nuclei. Note that with such selection δE_{TO} is negative if the time-odd mean fields provide additional binding in odd-mass nucleus.

In the CDF theory, the δE_{TO} quantity is equal to $E^{NM} - E^{WNM}$ and thus it is always negative: this result does not depend on the RMF parametrization (see Sect. 4.1.1 for the dependence of the $E^{NM} - E^{WNM}$ quantity on the RMF parametrization). In addition, the magnitude of the δE_{TO} quantity depends only weakly on the RMF parametrization. On the contrary, the sign and the magnitude of δE_{TO} depends strongly on the parametrization in the Skyrme EDF calculations. For example, in the calculations with the SLy4 force the δE_{TO} quantity is positive for medium mass nuclei (Refs. [154, 142, 155]) but negative in light nuclei (Ref. [141]). On the other hand, the δE_{TO} quantity will be positive in light nuclei in the calculations with the SIII parametrizations [141].

It is interesting to compare the averaged effects of time-odd mean fields as given by the ΔE quantity with the experimental global trends for OES as shown by dashed lines in Fig. 2 in Ref. [154]. The latter trends were obtained using phenomenological parametrization with the same functional dependence as in Eq. (4.3) with $c = 4.66$ MeV (4.31 MeV) and $\alpha = 0.31$ for neutron (proton) data sets. The comparison of theory and experiment suggests that time-odd mean field contributions into OES can be as large as 10% in light systems and around 5-6% in heavy systems. These are non-negligible contributions which have to be taken into account when the strength of pairing interaction is defined from the fits to experimental OES. The analysis of the Sn isotopes in Ref. [37] showed that time-even and time-odd polarization effects induced by odd nucleon produce OES reduced by about 30% as compared to the ones obtained in standard spherical calculations. As a con-

sequence, an enhancement of pairing strength by about 20% is required to compensate for that effect. Our calculations show much smaller reduction of OES in part because the polarization effects in time-even channel are already taken into account in the calculations without NM. Thus, the current calculations suggest that a much smaller increase of the strength of pairing (by approximately 5%) would be required to compensate for the reduction of OES due to time-odd mean fields.

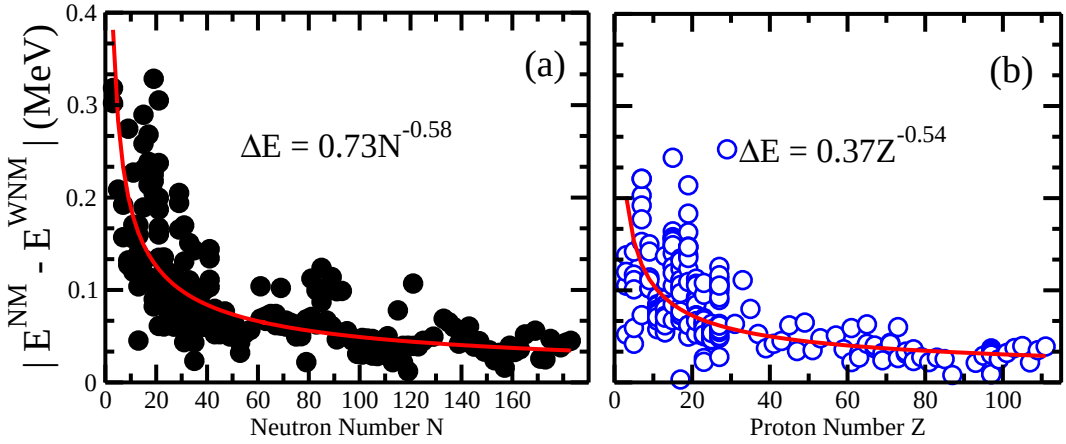

Figure 4.7

Particle dependences of additional binding due to NM.

4.2 The mechanism of additional binding due to NM in odd-mass nuclei

In the current section, a detailed analysis of the impact of NM on the energies of the single-particle states and on different terms in the total energy expression (Eq. (2.31)) is

performed in order to better understand the microscopic mechanism of additional binding due to NM. We use the $\nu[413]5/2$ configuration of ^{119}Ce as an example in this analysis.

4.2.1 Energy splittings of time-reversal counterpart single-particle states in the presence of NM

Fig. 4.8 shows that the presence of time-odd mean fields leads to the energy splitting $\Delta E_{split}(i)$ of the single-particle states which are time-reversal counterparts. This corresponds to the removal of the Kramer's degeneracy of these states. One of these states moves up by $\approx \Delta E_{split}/2$ as compared with its position in the absence of NM, while another moves down by $\approx \Delta E_{split}/2$. The results of the calculations in Fig. 4.8 are shown for the configurations of ^{119}Ce in which either the $\nu[413]5/2^-$ (column (1)) or $\nu[413]5/2^+$ (column (3)) states are blocked. These signatures are degenerated in energy in the calculations without NM (column (2)). Note that the single-particle states of interest are shown at arbitrary absolute energy in the column (2). Solid (open) circles indicate occupied (unoccupied) states. Solid (dotted) lines are used for the $r = +i$ ($r = -i$) states. Detailed analysis of the single-particle spectra in ^{119}Ce and ^{123}Xe reveals general features which are also found in other nuclei. The ^{119}Ce nucleus is axially symmetric ($\gamma = 0^\circ$) while ^{123}Xe is triaxial with $\gamma = -26^\circ$. This difference in the symmetry of nucleus results in important consequences: the energy splittings appear in all single-particle states in triaxial nuclei, while only the states with $\Omega = \Omega_{bl}$ (the subscript *'bl'* indicates the blocked state) experience such splittings in axially symmetric nuclei. The former feature is due to the

fact that Ω is not a good quantum number in triaxial nuclei and each single-particle state represents a mixture of the basic states with different values of Ω.

It is important to mention that the occupied and unoccupied states as well as the proton and neutron states show energy splittings (Fig. 4.8). The splittings of the proton and neutron states of the same structure are similar. This is because the largest contribution to magnetic potential (Eq. (2.17)) is due to space-like components of the ω-meson fields which do not depend on the isospin. In addition, the occupied state is always more bound than its unoccupied time-reversal counterpart.

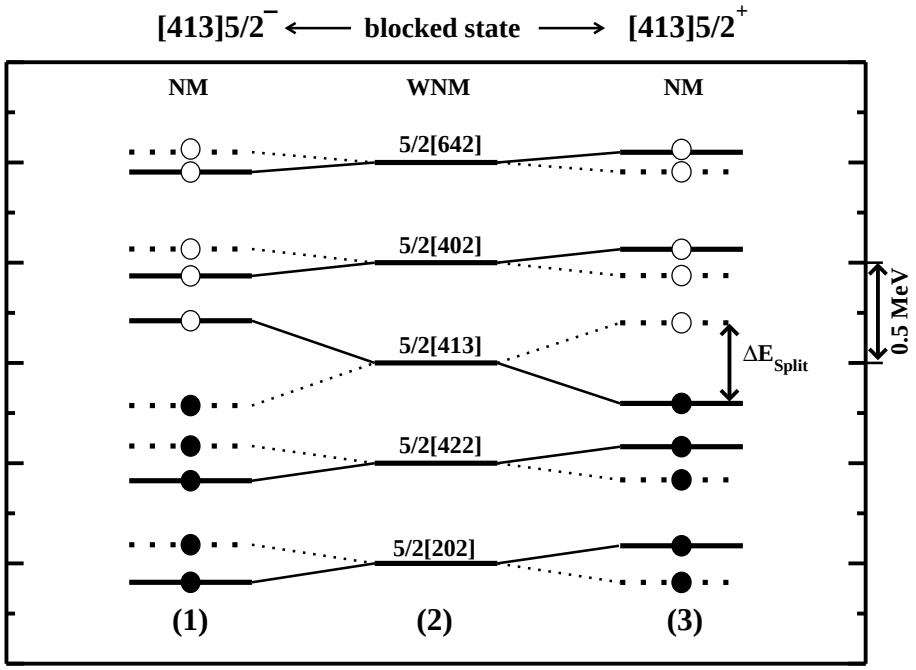

Figure 4.8

ΔE_{split} between different signatures of single-particle states due to NM in ^{119}Ce.

The change of the signature of the blocked state leads to the inversion of the signatures in all pairs of time-reversal orbitals (compare columns (1) and (3) in Fig. 4.8). The explanation for this process is the following. The change of the signature of the blocked state results in the change of the direction of the currents to the opposite one (compare Fig. 4.4d with Fig. 4.4e). This leads to the change of the direction of the vector potential $\boldsymbol{V}(\boldsymbol{r})$ in the Dirac equation to the opposite one, which in turn causes the inversion of the signatures in all pairs of time-reversal orbitals. However, the additional binding due to NM (the $E^{NM} - E^{WNM}$ quantity) does not depend on the signature of the blocked state in odd-mass nuclei.

4.2.2 Polarization effects induced by NM

The polarization effects induced by NM are investigated by considering its impact on different terms of the total energy (Eq. (2.31)). The results of this study are shown in Table 4.1. One can see that the total energy terms can be split into two groups dependent on how they are affected by NM. The first group includes the $E_{\sigma NL}$, E_{ρ}^{TL}, E_{ρ}^{SL} and E_{Coul} terms which are only weekly influenced by NM, and thus, they will not be discussed in detail.

Table 4.1

The impact of NM on the energy in the $[413]5/2^+$ configuration of ^{119}Ce.

Quantity	E_i^{WNM}	ΔE_i	ΔE_i^{pert}
1	2	3	4
E_{part}	-2849.889	-0.410	-0.237
E_σ	-17079.532	-2.231	
$E_{\sigma NL}$	343.341	-0.017	
E_ω^{TL}	14356.156	2.054	
E_ω^{SL}	0.0	-0.124	-0.124
E_ρ^{TL}	2.044	0.003	
E_ρ^{SL}	0.0	-0.010	-0.010
E_{Coul}	481.196	0.017	
E_{cm}	-6.252	0.0	
E_{tot}	-959.349	-0.104	-0.103
E_{kin}	1630.386	-0.099	-0.237

Table 4.2

The same as in Table 4.1 but for the $[606]13/2^+$ configuration in ^{183}Ce.

Quantity	E_i^{WNM}	ΔE_i	ΔE_i^{pert}
1	2	3	4
E_{part}	-4139.512	-0.157	-0.095
E_σ	-23720.872	-0.608	
$E_{\sigma NL}$	541.423	-0.004	
E_ω^{TL}	19696.151	0.538	
E_ω^{SL}	0.0	-0.043	-0.043
E_ρ^{TL}	236.863	0.009	
E_ρ^{SL}	0.0	-0.005	-0.005
E_{Coul}	437.326	0.002	
E_{cm}	-5.416	0.0	
E_{tot}	-1335.818	-0.045	-0.047
E_{kin}	2561.558	-0.045	-0.095

The second group is represented by the E_{part}, E_{σ}, E_{ω}^{TL} and E_{ω}^{SL} terms which are strongly affected by NM. The E_{ω}^{SL} term is directly connected with the nucleonic currents (see Eq. (2.37)). The E_{σ} and E_{ω}^{TL} terms depend only indirectly on time-odd mean fields: the minimization of the total energy in the presence of time-odd terms leads to a very small change of equilibrium deformation induced by NM. The quadrupole and hexadecapole moments change by 10^{-4} of their absolute value when the NM is switched on; a similar magnitude of changes is seen also in E_{σ} and E_{ω}^{TL}. One should keep in mind that only the $E_{\sigma} + E_{\omega}^{TL}$ quantity has a deep physical meaning since it defines a nucleonic potential; this sum is modified by NM only on -177 keV.

The largest modification (by -410 keV) is seen in the E_{part} energy, with the half of it coming from the change of the single-particle energy (by ≈ -200 keV) of the blocked orbital (the $\nu[413]5/2$ orbital) in the presence of NM. Note that since both signatures of other pairs of time-reversal orbitals below the Fermi level are occupied, the large energy splittings E_{split} seen for some of them do not have a considerable impact on E_{part} (see Eq. (2.32)) since this splitting is nearly symmetric with respect to the position of these orbitals in the absence of NM. Thus, the rest of the modification of E_{part} is related to small changes in the single-particle energies of occupied states caused by the changes in the equilibrium deformation induced by NM.

This detailed analysis clearly indicates that the $E^{NM} - E^{WNM}$ quantity is defined by both time-odd mean fields and the polarization effects in time-even mean fields induced by time-odd mean fields. $E^{NM} - E^{WNM} = -104$ keV is a result of near cancellation of the contributions due to fermionic (-410 keV) and mesonic (-306 keV) degrees of freedom.

Note that the latter appears with a negative sign in Eq. (2.31). The fermionic degrees of freedom are represented by the E_{part} and E_{cm} terms, while the other terms of the total energy are related to the mesonic degrees of freedom. The fermionic contribution into $E^{NM} - E^{WNM}$ is defined by more or less equal contributions from time-odd mean fields and the polarization effects in time-even fields. On the contrary, time-odd mean fields define only $\approx 1/3$ ($E^{SL}_{\omega} = -0.124$ keV) of the mesonic contribution into $E^{NM} - E^{WNM}$, while the rest is due to polarization effects in time-even mean fields.

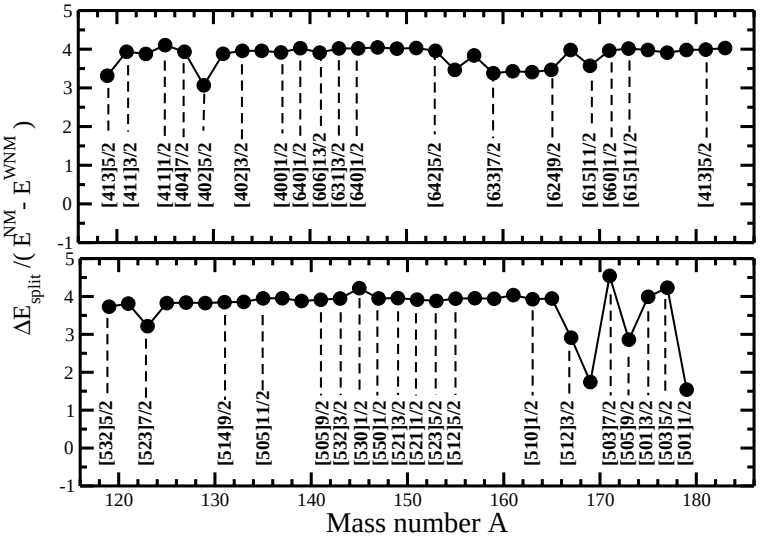

Figure 4.9

The ratio $\Delta E_{split}/(E^{NM} - E^{WNM})$ in the Ce isotopes.

It turns out that these contributions are highly correlated as can be seen from the ratio $\Delta E_{split}/(E^{NM} - E^{WNM})$ in the Ce isotope chain (Fig. 4.9). ΔE_{split} depends only on time-odd mean fields in fermionic channel, while $(E^{NM} - E^{WNM})$ depends both on time-odd mean fields and the polarizations effects in time-even mean fields in fermionic and mesonic channels. One can see that $\Delta E_{split}/(E^{NM} - E^{WNM}) \approx 4$ for the majority of nuclei. Similar relation exists also in the Skyrme EDF calculations for the Ce isotopes (see Eq. (7) in Ref. [142]).

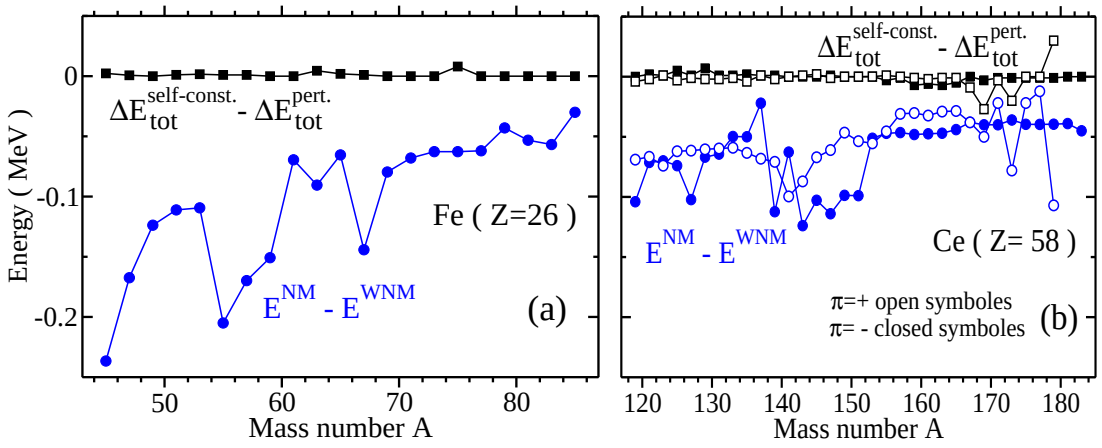

Figure 4.10

The $\Delta E_{tot}^{self-const} - \Delta E_{tot}^{pert}$ and $E^{NM} - E^{WNM}$ for odd-neutron nuclei.

The impact of NM on different terms of the total energy in the $\nu[606]13/2^+$ configuration of the ^{183}Ce nucleus, which is located at the neutron drip line, is shown in Table 4.2. The comparison of Tables 4.1 and 4.2 allows to understand the microscopic origin of gen-

eral trend which shows the decrease of the impact of NM (reflected in the $(E^{NM} - E^{WNM})$ quantity) with increasing particle (proton, neutron or mass) number (see Figs. 4.1 and 4.7).

In the ^{183}Ce nucleus, the impact of NM on the E_{ω}^{SL} and E_{ρ}^{SL} terms, which directly depend on time-odd mean fields, decreases by the factors close to 3 and 2 relative to the ^{119}Ce case (see Table 4.1), respectively. The impact of NM on the E_{σ}, $E_{\sigma NL}$, E_{ω}^{TL}, E_{ρ}^{TL}, E_{Coul} terms, which depend on time-odd mean fields only through polarization effects, decreases even more dramatically (by a factor close to 4). Note that the contribution of the ρ-meson to the $(E^{NM} - E^{WNM})$ quantity is marginal even at the neutron-drip line. Other investigated cases also indicate the decrease of the impact of NM with increasing particle number.

The general trend of the decrease of the impact of NM on binding energies with increasing particle number can be understood in the following way. The effects attributable to NM are produced by odd particle which breaks time-reversal symmetry. With increasing particle (proton, neutron of mass) number the nucleus becomes larger and thus more robust towards time-odd and polarization effects induced by odd particle (or in other words, the effective impact of single particle on total nuclear properties becomes smaller).

It is interesting to compare the results of self-consistent and perturbative calculations. The $\Delta E_i = E_i^{NM} - E_i^{WNM}$ quantities will be used for simplicity in further discussion. These quantities are shown in columns 3 and 4 of Tables 4.1 and 4.2. The ΔE_{σ}, $\Delta E_{\sigma NL}$, ΔE_{ω}^{TL} and ΔE_{ρ}^{TL} quantities are zero in perturbative calculations. $\Delta E_{Coul} = 0$ for odd-neutron system in perturbative calculations (Tables 4.1 and 4.2), but it can differ from 0 in the systems containing odd number of protons (Tables 4.3 and 4.4). The results of self-

consistent and perburbative calculations for the ΔE_{ω}^{SL} and ΔE_{ρ}^{SL} quantities are the same with the exception of conf. B in ^{34}Cl where only small difference exists (Tables 4.1, 4.2 and 4.4).

It is seen from Tables 4.1 and 4.2 that

$$\Delta E_{tot}^{self-const} \approx \Delta E_{tot}^{pert} \tag{4.6}$$

for odd-neutron nuclei. Note that the superscript *'self-const'* refers to fully self-consistent results. Fig. 4.10 shows that this equality is fulfilled in the majority of nuclei of the Fe and Ce isotope chains with high degree of accuracy (as compared with the $E^{NM} - E^{WNM}$ quantities). *These results clearly indicate that the additional binding due NM (the $E^{NM} - E^{WNM}$ quantity) is defined mainly by time-odd fields and that the polarization effects in fermionic and mesonic sectors of the model cancel each other to a large degree.*

As a consequence it is important to understand the relations between different polarization effects. Particle energy $E_{part}^{self-const}$ obtained in self-consistent calculations can be split into two parts: the part E_{part}^{TO} which directly depends on time-odd mean fields and the part E_{part}^{pol} which is defined by the polarization effects in the fermionic sector of model. Thus, $E_{part}^{self-const} = E_{part}^{TO} + E_{part}^{pol}$ and $E_{part}^{pert} \approx E_{part}^{TO}$. Taking into account Eq. (2.31) and above mentioned features of the ΔE_{i}^{pert} terms one can conclude that

$$\begin{aligned} \Delta E_{part}^{pol} = \Delta E_{\sigma}^{self-const} + \Delta E_{\sigma NL}^{self-const} \\ + \Delta E_{\omega}^{TL[self-const]} + \Delta E_{\rho}^{TL[self-const]} \\ + \Delta E_{Coul}^{self-const}. \end{aligned} \tag{4.7}$$

This relation clearly indicates that the polarizations effects in the fermionic (E^{pol}_{part} term) and mesonic ($\Delta E^{self-const}_{\sigma}$, $\Delta E^{self-const}_{\sigma NL}$, $\Delta E^{TL[self-const]}_{\omega}$, and $\Delta E^{TL[self-const]}_{\rho}$ terms) sectors of the model are strongly correlated. Eq. (4.7) also allows to understand clearly the physical origin of ΔE^{pol}_{part}. The terms on right hand side are related to the change of the nucleonic potential induced by NM. This change leads to the modifications of the single-particle energies of all occupied states (as compared with the case when NM is absent) which are reflected in ΔE^{pol}_{part}. On the contrary, the ΔE^{TO}_{part} is due to the breaking of the Kramers degeneracy between the blocked state and its unoccupied time-reversal counterpart. Note that $\Delta E^{TO}_{part} \approx -1/2 \Delta E_{split}$ (minus sign reflects the fact that the blocked state is always more bound in the presence of NM) and the ΔE_{split} values obtained in self-consistent and perturbative calculations are the same for the pairs of time-reversal counterpart states involving blocked state.

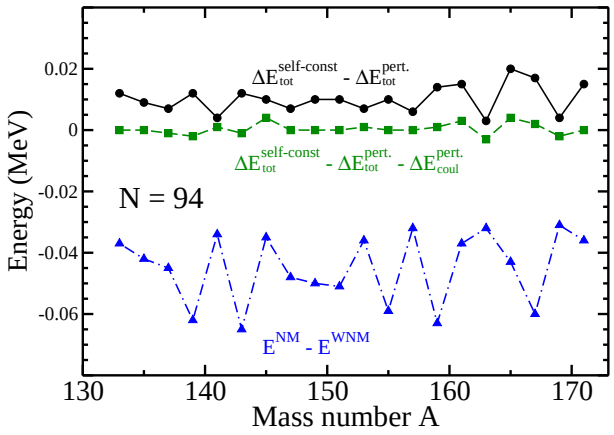

Figure 4.11

The same as in Fig. 4.10, but for odd-proton $N = 94$ nuclei.

The relation similar to Eq. (4.6) exists also in odd-proton nuclei but in this case it has to be corrected for the ΔE^{pert}_{Coul} energy change:

$$\Delta E^{self-const}_{tot} \approx \Delta E^{pert}_{tot} + E^{pert}_{Coul}. \tag{4.8}$$

Fig. 4.11 shows that this relation is fulfilled in odd-proton $N = 94$ nuclei with high degree of accuracy (as compared with the $E^{NM} - E^{WNM}$ quantities). Eq. (4.8) also leads to the condition of Eq. (4.7) and to the interpretation of E^{pol}_{part} discussed above.

4.2.3 The impact of time-odd mean fields on the properties of proton-unstable nuclei

The blocked state always has lower energy than its unoccupied time-reversal counterpart in the calculations with NM; this fact does not depend on the signature of the blocked state (Sect. 4.2.1). The energy of the blocked state in the presence of NM is lower by $\approx \Delta E_{split}/2$ than the energy of the same state in the absence of NM. This additional binding will affect the properties of the nuclei in the vicinity of the proton-drip line via two mechanisms discussed below. They are schematically illustrated in Fig. 4.12.

In the first mechanism, the nucleus, which is proton unbound (state A in Fig. 4.12) in the calculations without NM, becomes proton bound in the calculations with NM (state A' in Fig. 4.12). The necessary condition for this mechanism to be active is the requirement that the energy of the single-particle state in the absence of NM is less than $\Delta E_{split}/2$. This mechanism can be active both in the ground and excited states of the nuclei in the vicinity of the proton-drip line.

In the second mechanism, the energy of the single-particle state (state B' in Fig. 4.12) is lower in the presence of NM, but the state still remains unbound. This will affect the decay properties of proton emitters and the possibilities of their observation. Indeed, the lowering of the energy of the single-proton state will decrease the probability of emission of the proton through combined Coulomb and centrifugal barrier. Many results of the physics of proton emitters are conventionally expressed in terms of the Q_p energies which depend on the difference of the binding energies of parent (odd-proton) and daughter (even-proton) nuclei. Note that for simplicity we consider here only even-N nuclei. NM leads to an additional binding in odd-proton nucleus but it does not affect the binding of even-proton nucleus. Thus, the Q_p values are lower by the value of this additional binding when the NM is taken into account.

Two consequences follow from lower Q_p values. First, experimental observation of proton emission from the nucleus will become impossible if the Q_p value moves outside the Q_p window favorable for the observation of proton emission or becomes possible if the Q_p value moves into the Q_p window favorable for the observation of proton emission. The size of the Q_p window for rare-earth proton emitters is about $0.8 - 1.7$ MeV, while it is much smaller in lighter nuclei [158, 156]. Large Q_p values outside this window result in extremely short proton-emission half-lives, which are difficult to observe experimentally. On the other hand, the decay width is dominated by β^+ decay for low Q_p values below the Q_p window. This consequence of the lowering of Q_p due to NM is especially important in light nuclei where the impact of NM on binding energies is especially pronounced and the Q_p window is narrow.

Second, the lowering of the Q_p values due to NM will increase the half-lives of proton emitters. For example, the lowering of Q_p due to NM will be around 50 keV in rare-earth region since this is typical value of additional binding due to NM in odd-mass nuclei of this region (Sect. 4.1.2). This can increase the half-lives of proton emitters by a factor of ≈ 2 at the upper end of the Q_p window and by a factor of ≈ 4 at the bottom end of the Q_p window (see Fig. 5 in Ref. [156]). The effects of NM have been neglected in the existing RHB studies of proton emitters with $Z \geq 50$ (see, for example, Ref. [157]) but this should not introduce significant error in this mass region.

On the other hand, the impact of NM can be dramatic on the half-lives of proton emitters in lighter nuclei. This is due to two factors, namely, (i) the general increase of additional binding due to NM and the magnitude of ΔE_{split} with decreasing mass and (ii) the narrowing of the Q_p window with the decrease of mass due to the lowering of the Coulomb barrier. This can be illustrated by several examples. The change in proton energy of around 300 keV in ^{69}Br causes a change in the proton decay lifetime of 11 orders of magnitude [158]. This effect is even more pronounced in lighter systems. The half-life window of 10 to 10^{-4} s corresponds to proton energies of $100 - 150$ keV in nuclei around $Z = 20$ [159], while the variation of the Q_p value between 3 to 50 keV in ^{7}B changes the half-lives by 30 orders of magnitude [156]. The energy changes quoted in these examples are either of similar magnitude or even smaller as compared with the changes of the energies of single-proton states and the Q_p values induced by NM. As a result, one can conclude that the effects of time-odd mean fields have to be taken into account when attempting to describe the properties of proton emitters in light nuclei.

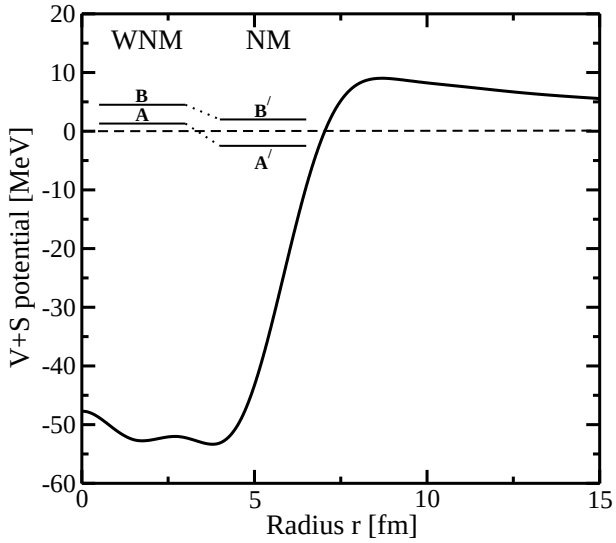

Figure 4.12

Impact of time-odd mean fields on odd-proton nuclei near the proton drip line.

4.3 Odd-odd mass nuclei: a model study of the impact of nuclear magnetism on binding energies.

The nuclei around ^{32}S in superdeformed minimum are considered in the present Section. Their selection is guided in part by the desire to compare the CRMF results with the ones obtained in the Skyrme EDF in Ref. [160], where the signature separation induced by time-odd mean fields has been found in the excited SD bands of ^{32}S. The CRMF calculations have been performed for some SD configurations in ^{32}S and in neighboring nuclei. The starting point is the doubly magic SD configuration $\pi 3^2 \nu 3^2$ in ^{32}S (further 'SD core') (see Ref. [148]) in which all single-particle orbitals below the $N = Z = 16$ SD shell gaps are occupied (Fig. 4.13). Here the configurations are labeled by the numbers of occu-

pied proton (p) and neutron (n) high-N intruder orbitals (the $N = 3$ orbitals in our case): this is commonly accepted shorthand notation $\pi N^n \nu N^p$ of the configurations in high-spin physics [20]. Then the configurations in the nuclei under consideration (Fig. 4.14) are created by either adding particles into the $[202]5/2^{\pm}$ orbital(s) or/and creating holes in the $[330]1/2^{\pm}$ orbitals: these are the orbitals active in signature-separated configurations discussed in Ref. [160].

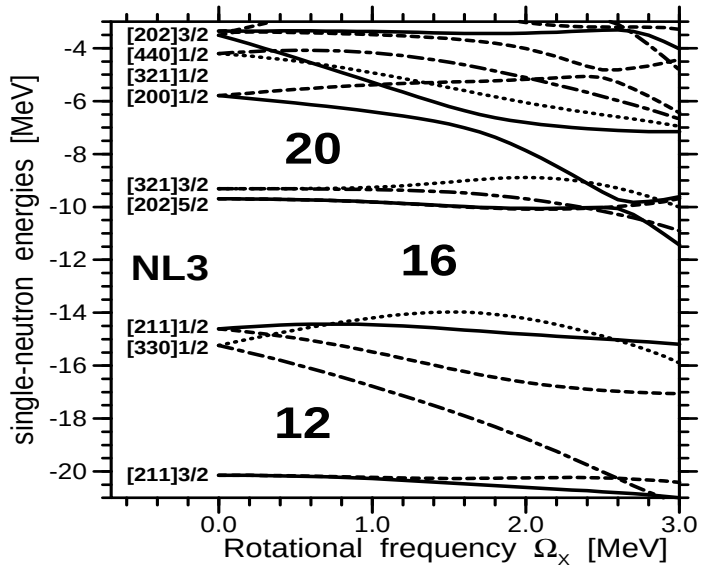

Figure 4.13

Similar to Fig. 3.5 but for the doubly-magic SD configuration $\pi 3^2 \nu 3^2$ in ^{32}S.

Similar to the results shown in Sects. 4.1.1 and 4.1.2, the NM leads to additional binding in the configurations of odd mass nuclei (the configurations in ^{33}S and ^{33}Cl created by

adding a particle to the SD core or the configurations in ^{31}P and ^{31}S created by removing a particle from the SD core, see Fig. 4.14). This additional binding does not depend on the signature of the blocked state.

Fig. 4.14 shows that additional binding due to NM is smaller for the configurations with blocked proton state as compared with the ones with blocked neutron state. For example, the configurations in ^{31}P and ^{31}S are built on the same blocked Nilsson state. However, additional binding due to NM is smaller in odd-proton nucleus (^{31}P) than in odd-neutron one (^{31}S). Similar situation also exists in ^{33}S and ^{33}Cl. These results are consistent with a general systematics (Sect. 4.1.4) which shows that additional binding due to NM is smaller in the proton subsystem than in the neutron one.

The results of perturbative calculations for the configuration with the proton hole in $\pi[330]1/2^-$ in odd-proton ^{31}P nucleus and for the configuration with the neutron hole in $\nu[330]1/2^-$ in odd-neutron ^{31}S nucleus are shown in Table 4.3. These hole configurations are formed by removing either proton (^{31}P) or neutron (^{31}S) from the $N = Z$ ^{32}S SD core. One can see that the decrease of additional binding due to NM on going from neutron to proton configuration of the same structure can be traced to the changes in the particle energy ΔE^{pert}_{part} from -0.349 MeV in odd-neutron ^{31}S nucleus to -0.250 MeV in odd-proton ^{31}P. This explains the major part of the change in the ΔE^{pert}_{tot} quantity on going from odd-neutron ^{31}S ($\Delta E^{pert}_{tot} = -0.165$ MeV) to odd-proton ^{31}P ($\Delta E^{pert}_{tot} = -0.100$ MeV). The contributions of other terms into ΔE^{pert}_{tot} on going from odd-neutron ^{31}S to odd-proton ^{31}P nucleus are smaller: 0.020, 0.001, and 0.013 MeV for the ΔE^{SL}_{ω}, ΔE^{SL}_{ρ} and ΔE_{Coul} terms, respectively.

In perturbative calculations, the changes in particle energy ΔE^{pert}_{part} can be easily related to the energy splitting ΔE_{split} between the blocked state and its unoccupied time-reversal counterpart through $\Delta E^{pert}_{part} \approx -\frac{1}{2}\Delta E_{split}$ since the sum over the energies of other occupied single-particle states is the same in the calculations with and without NM because the polarization effects are absent (Sect. 4.2.2). The energy splittings between different signatures of the blocked $[330]1/2$ state are $\Delta E_{split} = 0.653$ MeV and $\Delta E_{split} = 0.476$ MeV for odd-neutron (^{31}S) and odd-proton (^{31}P) nuclei, respectively. This result clearly indicates that the contributions of the Coulomb force to the proton single-particle energies in the presence of NM are at the origin of the fact that additional binding due to NM is smaller for odd-proton nuclei as compared with odd-neutron ones. The analysis of ^{33}S and ^{33}Cl leads to the same conclusions.

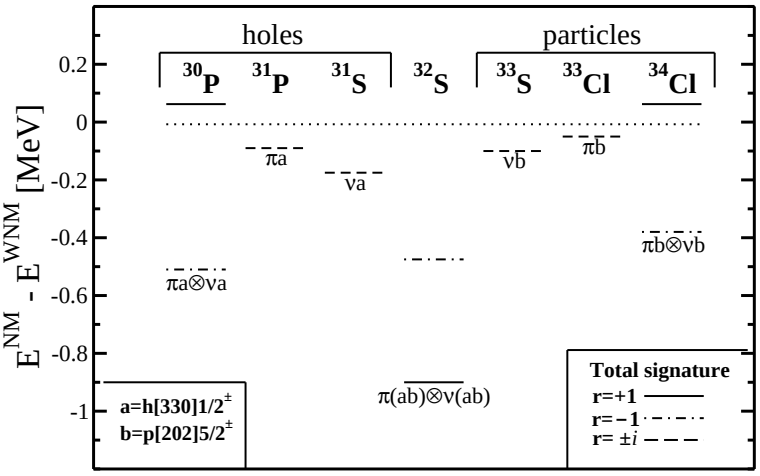

Figure 4.14

The impact of NM on binding energies, in the vicinity of ^{32}S SD core.

Table 4.3

The $\Delta E_i^{pert} = (E_i^{NM} - E_i^{WNM})^{pert}$ for different terms of the total energy.

Quantity	^{31}S	^{31}P	^{33}S	^{33}Cl
1	2	3	4	5
ΔE_{part}^{pert}	-0.349	-0.250	-0.198	-0.136
$\Delta E_{\omega}^{SL[pert]}$	-0.168	-0.148	-0.093	-0.080
$\Delta E_{\rho}^{SL[pert]}$	-0.016	-0.015	-0.010	-0.009
ΔE_{Coul}^{pert}	0.0	0.013	0	0.010
ΔE_{tot}^{pert}	-0.165	-0.100	-0.095	-0.057
ΔE_{kin}^{pert}	-0.348	-0.276	-0.198	-0.155

Table 4.4

$\Delta E_i = E_i^{NM} - E_i^{WNM}$ in the SD configurations of ^{34}Cl.

.

Quantity	$E_i^{WNM}(A,B)$	$\Delta E_i(A)$	$\Delta E_i^{pert}(A)$	$\Delta E_i(B)$	$\Delta E_i^{pert}(B)$
1	2	3	4	5	6
E_{part}	-835.845	-1.471	-0.791	-0.004	-0.003
E_{σ}	-4415.660	-7.862		$+0.004$	
$E_{\sigma NL}$	84.884	-0.036		-0.001	
E_{ω}^{TL}	3698.240	7.126		-0.003	
E_{ω}^{SL}	0.0	-0.414	-0.414	0.0	-0.001
E_{ρ}^{TL}	0.061	0.0		0.0	
E_{ρ}^{SL}	0.0	0.0		-0.043	-0.043
E_{Coul}	59.832	0.052	0.025	-0.002	-0.003
E_{cm}	-9.492	0.0		0.0	
E_{tot}	-272.693	-0.376	-0.402	0.041	0.043
E_{kin}	479.210	-0.103	-0.841	-0.002	0.003

The situation is more complicated in odd-odd nuclei (^{30}P and ^{34}Cl) in which considerable energy splitting between the $r = +1$ and $r = -1$ configurations is obtained in the calculations. The microscopic mechanism of binding modifications is illustrated in Table 4.4 on the example of configurations A and B in ^{34}Cl.

NM provides additional binding of around 0.4 MeV in the configuration A which has signature $r = -1$. In this configuration, proton and neutron currents due to the occupation of proton and neutron 5/2[202]$^-$ states are in the same direction which results in appreciable total baryonic current. This baryonic current leads to sizable modifications in the E_{part}, E_σ, E_ω^{TL}, E_ω^{SL} terms (Table 4.4). These are precisely the same terms which are strongly affected by NM in odd-mass nuclei, see Sect. 4.2.2. The fermionic contribution into $E^{NM} - E^{WNM}$ (the ΔE_{part} term) is defined by more or less equal contributions from time-odd mean fields and the polarization effects in time-even mean fields. On the contrary, time-odd mean fields define only $\approx 1/3$ ($\Delta E_\omega^{SL} = -0.413$ MeV) of the mesonic contribution into $E^{NM} - E^{WNM}$, while the rest is due to the polarization effects in time-even mean fields (the ΔE_σ, ΔE_ω^T terms).

NM leads to the loss of binding in the configuration B which has $r = +1$. In this configuration, the proton and neutron currents due to the $\pi[202]5/2^+$ and $\nu[202]5/2^-$ states are in opposite directions, so the total baryonic current is very close to zero. As a result, the impact of NM is close to zero for the majority of the terms in Eq. (2.31) (see Table 4.4). The only exception is the E_ρ^{SL} term which represents space-like component of the isovector-vector ρ-field. This term depends on the difference of proton and neutron currents (Eq. (2.38)), which for the present case of opposite currents gives a non-zero result.

As follows from Table 4.4, this term is predominantly responsible for the loss of binding due to NM in the configuration B.

It is well known that many physical quantities are additive in the calculations without pairing (see Ref. [107] and references therein). The additivity principle states that the average value of a one-body operator $\hat{O}$ in a given many-body configuration k, $O(k)$, relative to the average value in the core configuration, O^{core}, is equal to the sum of effective contributions o_α^{eff} of particle and hole states by which the k-th configuration differs from that of the core [107]

$$\delta O(k) = O(k) - O^{core} = \sum_\alpha c_\alpha(k) o_\alpha^{eff} \tag{4.9}$$

Coefficients $c_\alpha(k)$ ($c_\alpha(k) = 0,\ \text{or}\ +1\ \text{or}\ -1$) define the s.p. content of the configuration k with respect to the core configuration (see Ref. [107] for details). Let us check whether additional binding due to NM (the $\Delta E_{tot} = E^{NM} - E^{WNM}$ quantity) is additive. The doubly magic SD configuration $\pi 3^2 \nu 3^2$ in even-even ^{32}S nucleus is used as a core for this analysis: the effective contributions δE_i^{eff} of particle state(s) to ΔE_{tot} are given by $\delta E_i^{eff} = [E_i(\text{nucleus A}) - E_i(\text{core})]^{NM} - [E_i(\text{nucleus A}) - E_i(\text{core})]^{WNM} = E_i^{NM}(\text{nucleus A}) - E_i^{WNM}(\text{nucleus A}) = \Delta E_i(\text{nucleus A}))$ because the core configuration is not affected by NM. Thus, the additivity implies that $\Delta E_{tot}(^{34}\text{Cl}(r = +1)) = \Delta E_{tot}(^{33}\text{S}) + \Delta E_{tot}(^{33}\text{Cl})$ ($\Delta E_{tot}(^{34}\text{Cl}(r = -1)) = \Delta E_{tot}(^{33}\text{S}) - \Delta E_{tot}(^{33}\text{Cl})$) for the situation when the proton and neutron currents in ^{34}Cl are in the same (opposite) directions. Fig. 4.14 clearly shows that additivity conditions are not fulfilled and that additional binding due to NM is not additive in self-consistent calculations. The analysis involving odd-odd ^{30}P and odd ^{31}P, ^{31}S nuclei leads to the same conclusion (see Fig. 4.14).

The additivity is also violated in perturbative calculations: the comparison of Tables 4.3 (columns 4 and 5) and 4.4 (columns 4 and 6) reveals that the conditions $\Delta E_i^{pert}(^{34}\mathrm{Cl}(r = \pm 1)) = \Delta E_i^{pert}(^{33}\mathrm{S}) \pm \Delta E_i^{pert}(^{33}\mathrm{Cl})$ are violated both for the total energy ($i = tot$) and individual components of the total energy ($i = part,\ {}^{SL}_{\omega},\ {}^{SL}_{\rho},\ Coul$). The analysis of ΔE_{part}^{pert} (this terms provides the largest contribution to ΔE_{tot}^{pert} (see Tables 4.3 and 4.4)) allows to understand the origin of the violation of additivity for the ΔE_{tot}^{pert} quantity. In odd-proton ^{31}Cl nucleus, $\Delta E_{part}^{p[pert]} \approx -1/2\Delta E_{split}^{p}$ (ΔE_{split}^{p} is the energy splitting between blocked proton state and its signature counterpart) and ΔE_{split}^{p} depends predominantly on the proton current induced by odd proton. The same is true in odd-neutron ^{33}S nucleus where ΔE_{split}^{n} depends predominantly on the neutron current induced by odd neutron. Additivity principle implies $\Delta E_{part}^{odd-odd[pert]} \approx -(1/2\Delta E_{split}^{p} + 1/2\Delta E_{split}^{n})$ for the $^{34}\mathrm{Cl}(r = +1)$ configuration, in which the proton and neutron currents are in the same direction. However, proton $\Delta E_{split}^{p[odd-odd]}$ (neutron $\Delta E_{split}^{n[odd-odd]}$) energy splitting between blocked proton (neutron) state and its time-reversal counterpart in odd-odd nuclei depend on total baryonic (proton+neutron) current in this configuration. On the contrary, the additivity principle implies that these proton and neutron quantities depend on individual proton and neutron currents in odd-odd nucleus, respectively. This total current is approximately two times stronger than individual (proton or neutron) currents in odd mass nuclei. As a consequence, $\Delta E_{split}^{p[odd-odd]}$ and $\Delta E_{split}^{n[odd-odd]}$ values in odd-odd mass nucleus are larger than the same quantities (ΔE_{split}^{p}, ΔE_{split}^{n}) in odd-mass nuclei by a factor close to 2. As a result, $\Delta E_{part}^{pert}(^{34}\mathrm{Cl}(r = +1)) \approx 2(\Delta E_{part}^{pert}(^{33}\mathrm{S}) + \Delta E_{part}^{pert}(^{33}\mathrm{Cl})$ (see Tables 4.3

and 4.4) which clearly indicates the violation of additivity for the ΔE^{pert}_{part} quantity (and for the ΔE^{pert}_{tot} quantity).

Fig. 4.14 also shows the results for the 4-particle excited SD states $\pi(\mathrm{ab}) \otimes \nu(\mathrm{ab})$ in ^{32}S, for which the calculated rotational structures display the signature separation induced by time-odd mean fields [160, 148]. The configurations are formed by exciting proton and neutron from the $[330]1/2^-$ orbitals below the $N = 16$ and $Z = 16$ SD shell gaps into the $[202]5/2^{\pm}$ orbitals located above these gaps. They have the $\pi 3^1 \nu 3^1$ structure in terms of intruder orbitals. When NM is neglected these four configurations are degenerated in energy. This degeneracy is broken and additional binding, which depends on the total signature of the configuration (0.907 MeV for the $r = +1$ configurations and 0.468 MeV for the $r = -1$ configurations in the calculations with the NL3 parametrization), is obtained when NM is taken into account. The NL1 and NLSH parametrizations of the RMF Lagrangian give very similar values of additional binding due to NM. The essential difference between the relativistic and non-relativistic calculations lies in (i) the size of the energy gap between the $r = +1$ and $r = -1$ configurations and (ii) the impact of time-odd mean fields on the energy of the $r = -1$ states. This energy gap is about 2 MeV in the Skyrme EDF calculations with the SLy4 force [160], while it is much smaller being around 0.45 MeV in the CRMF calculations with the NL1, NL3 and NLSH parametrizations. The energies of the $r = -1$ states are not affected by time-odd mean fields in the Skyrme EDF calculations [160], while appreciable additional binding is generated by NM for these states in the CRMF calculations (Fig. 4.14).

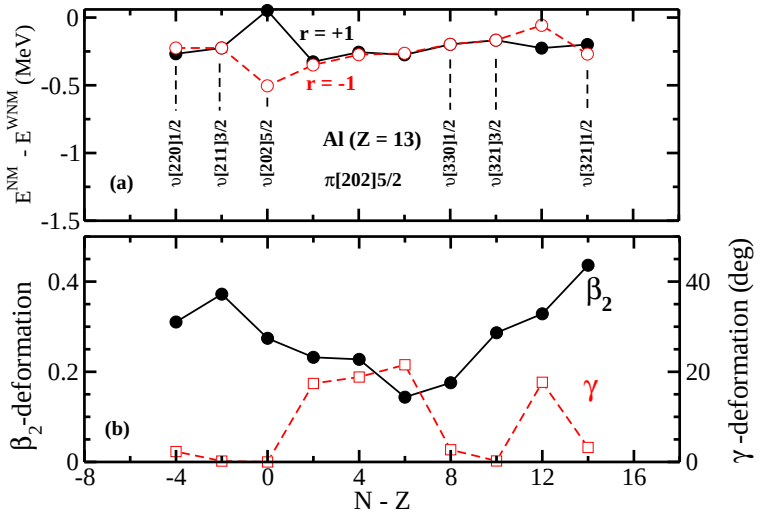

Figure 4.15

The impact of NM on binding energies in odd-odd Al nuclei.

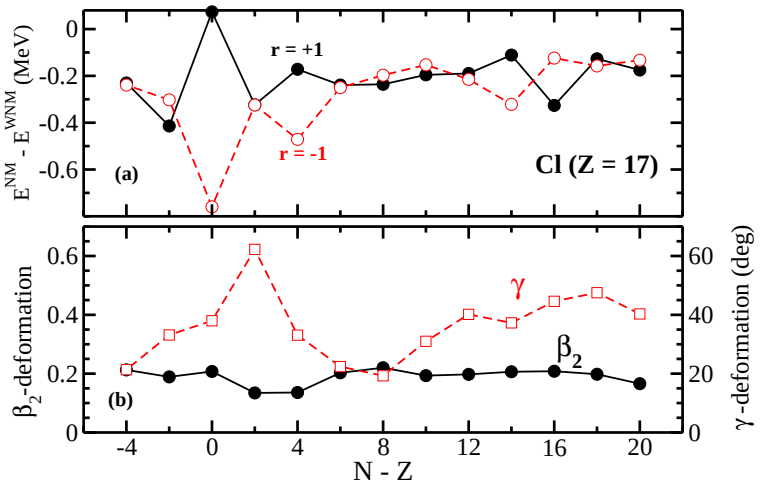

Figure 4.16

The same as in Fig. 4.15 but for odd-odd Cl nuclei.

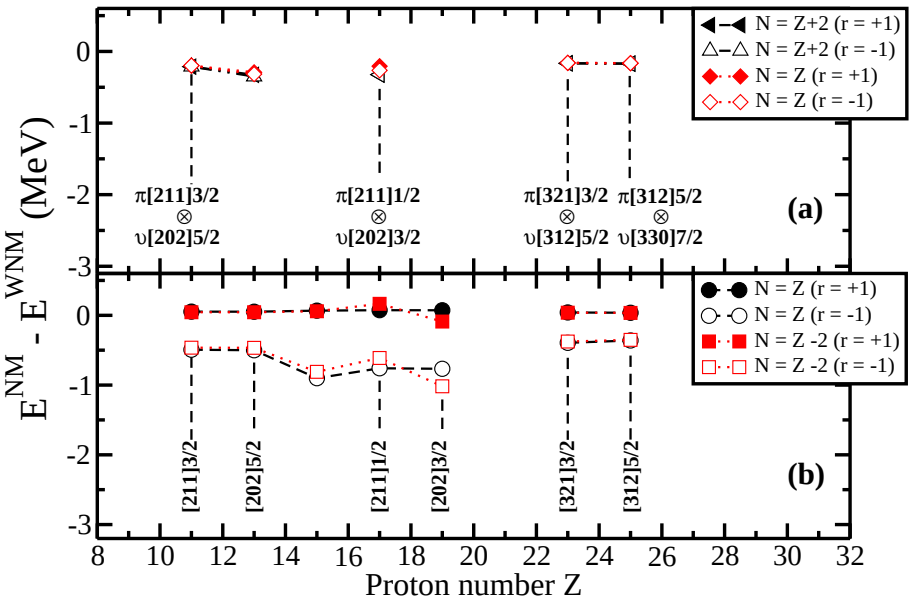

Figure 4.17

Impact of NM on binding energies of odd-odd nuclei near the $N = Z$ line.

Figs. 4.15 and 4.16 show the results of the calculations for ground state configurations in odd-odd Al and Cl nuclei, where the upper panel shows the $E^{NM} - E^{WNM}$ quantity for different signatures. The structure of the blocked states are shown by the Nilsson labels only in the cases when the configurations are near-prolate. The same state is blocked in the proton subsystem of all nuclei. The bottom panel shows the β_2 and γ-deformations of the configurations under study. The calculations suggest that signature separation due to time-odd mean fields is also expected in the configurations of odd-odd nuclei located at zero or low excitation energies. The signature separation is especially pronounced in the $N = Z$ ^{26}Al (the $\pi[202]5/2 \otimes \nu[202]5/2$ configuration) and ^{34}Cl nuclei. This is because proton and neutron currents in these configurations are almost the same both in strength and in spatial distribution. As a result, their contribution to the total energy is large when

these currents are in the same direction (the $r = -1$ configurations) and close to zero when these currents are in opposite directions (the $r = +1$ configurations). Note that ^{26}Al is axially deformed while ^{34}Cl is triaxially deformed with $\gamma \sim 30^{\circ}$. However, both of them show the enhancement of the signature separation at $N = Z$.

The signature separation is rather small for the majority of nuclei away from the $N = Z$ line. This is a consequence of the fact that the strength of the currents in one subsystem (and thus the impact of NM on binding energies) is much stronger than in another subsystem. As a result, there is no big difference (large signature separation) between the cases in which proton and neutron currents are in the same and opposite directions. However, some nuclei away from the $N = Z$ line also show appreciable signature separation. These are ^{38}Al and ^{38,48,50}Cl nuclei (Figs. 4.15, 4.16) for which the strengths of proton and neutron currents (but not necessarily the spatial distribution of the currents) are of the same order of magnitude.

It was suggested in Ref. [141] that the effects of time-odd mean fields are enhanced at the $N = Z$ line. However, Fig. 4.17 clearly shows that the enhancement of signature separation is not restricted to the $N = Z$ line. Indeed, signature separation of the configurations based on the same combination of blocked proton and neutron states are very similar in the $N = Z$ and $N = Z \pm 2$ nuclei despite the fact that the deformations of compared nuclei differ sometimes appreciably. There are considerable signature separation in the configurations based on the same blocked proton and neutron states in the $N = Z$ and $N = Z - 2$ nuclei (Fig. 4.17b). On the other hand, almost no signature splitting is observed in the $N = Z$ and $N = Z + 2$ nuclei when the configurations are based on dif-

ferent blocked proton and neutron states (Fig. 4.17a). This suggests that the enhancement of signature splitting is due to similar proton and neutron current distributions (see discussion in previous paragraph). In Fig. 4.17, the results are shown only in the cases when the convergence has been achieved for both $N = Z$ and $N = Z - 2$ (or $N = Z + 2$) nuclei. When considering odd-odd nuclei one has to keep in mind that the present approach takes into account only the part of correlations between blocked proton and neutron and neglects the pairing. In particular, the residual interaction of unpaired proton and neutron leading to the Gallagher-Moshkowski doublets of two-quasiparticle states with $K_> = \Omega_p + \Omega_n$ and $K_< = |\Omega_p - \Omega_n|$ [161, 162] is not taken into account. Thus, future development of the model is required in order to compare directly the experimental data on odd-odd nuclei with calculations.

4.4 Nuclear magnetism and band crossing features

As mentioned earlier in Ch.2, the Coriolis term is present in NM and WNM calculations in rotraing nuclei. This means that the currents (Eq. (2.26)) are always present in rotating nuclei. However, it is important to distinguish the currents induced by the Coriolis term and the ones which appear due to magnetic potential. The currents, which appear in the WNM calculations, are generated by the Coriolis term. Thus, we will call them as *Coriolis induced currents*. On the contrary, the currents in the NM calculations are generated by both the Coriolis term and magnetic potential. The difference of the currents in the NM and WNM calculations is attributable to magnetic potential. Thus, the currents $[\boldsymbol{j}^{n,p}(\boldsymbol{r})]^{NM} - [\boldsymbol{j}^{n,p}(\boldsymbol{r})]^{WNM}$ will be called *magnetic potential induced currents*.

In the following, the contribution $\Delta O^{NM-contr}$ (in percentage) of NM to the physical observable O is defined as

$$\Delta O^{NM-contr} = \frac{O^{NM} - O^{WNM}}{O^{NM}} \times 100\%. \tag{4.10}$$

The physical observables, most frequently used in the analysis of rotating nuclei, are kinematic ($J^{(1)}$) and dynamic ($J^{(2)}$) moments of inertia which are defined as

$$J^{(1)}(\Omega_x) = \frac{J}{\Omega_x}, \qquad J^{(2)}(\Omega_x) = \frac{dJ}{d\Omega_x} \tag{4.11}$$

where J is the expectation value of the total angular momentum along the x-axis. In the CRMF theory, this quantity is defined as a sum of the expectation values of the single-particle angular momentum operators $\hat{j}_x$ of the occupied states

$$J = \sum_i \langle i|\hat{j}_x|i\rangle. \tag{4.12}$$

Thus, the modifications of the moments of inertia due to NM can be traced back to the changes of the single-particle expectation values $\langle \hat{j}_x \rangle_i = \langle i|\hat{j}_x|i\rangle$ and the corresponding contributions of spin ($\langle \hat{s}_x \rangle_i$) and orbital ($\langle \hat{l}_x \rangle_i$) angular momenta [38].

Since NM substantially modifies the single-particle properties (energies, alignments) [38, 11], it is reasonable to expect that the band crossing features are affected by NM. In order to study this question, the CRMF (without pairing) and the CRHB+LN calculations have been performed for lowest superdeformed (SD) band in ^{194}Pb. In the CRHB+LN calculations, the D1S Gogny force [163] is used in pairing channel and an approximate particle number projection is performed by means of the Lipkin-Nogami method [131].

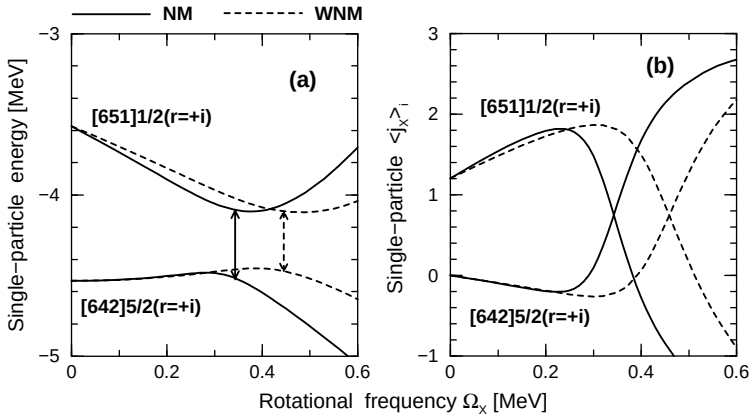

Figure 4.18

(a) Proton Routhians. (b) The expectation values $\langle \hat{j}_x \rangle_i$.

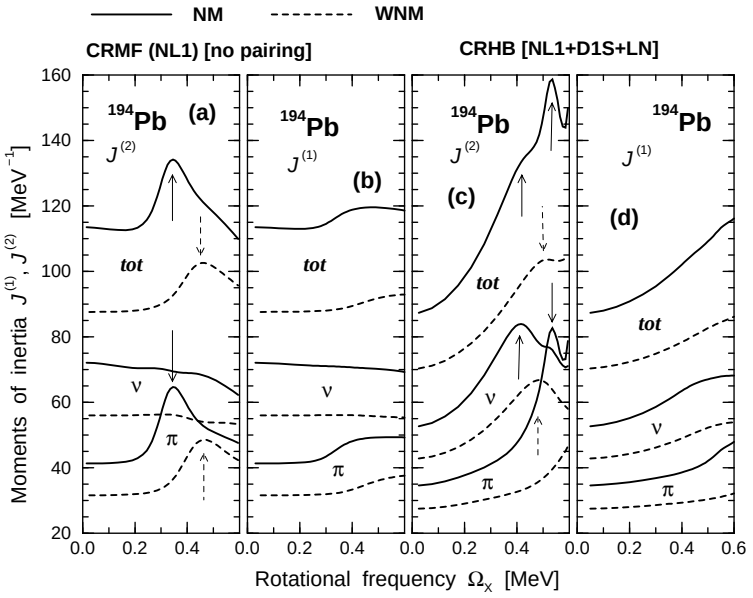

Figure 4.19

$J^{(1)}$ and $J^{(2)}$ for the lowest SD configuration in ^{194}Pb with and without NM.

The unpaired proton band crossing seen in the CRMF calculations originates from the interaction between the $\pi[642]5/2^+$ and $\pi[651]1/2^+$ orbitals (Fig. 4.18a). Since NM increases somewhat the single-particle alignment $\langle \hat{j}_x \rangle_i$ (Fig. 4.18b) and the slope of the routhian for the $\pi[651]1/2^+$ orbital (Fig. 4.18a), the band crossing takes place at lower frequency. The shift of crossing frequency due to NM is considerable (120 keV) from 0.465 MeV (WNM) down to 0.345 MeV (NM), Fig. 4.18a. The calculations also suggest that the strength of the interaction between two interacting orbitals at the band crossing is modified in the presence of NM as seen in the change of the energy distance (gap) between these two orbitals at the crossing frequency (Fig. 4.18a).

An additional mechanism affecting the band crossing frequencies will be active in odd- and odd-odd mass nuclei as well as in excited configurations of even-even nuclei. In such configurations, there is at least one single-particle state the opposite signature of which is not occupied. This results in the currents at $\Omega_x = 0.0$ MeV, which is discussed in Ch 4. The energy splitting between different signatures of the single-particle states at no rotation is a typical consequence of these currents (see Sec. 4.2.1). As a result, the energy gap between interacting orbitals at $\Omega_x = 0.0$ MeV can become larger or smaller dependent on the impact of the currents on the single-particle energies of interacting states. Consequently, this change in the energy gap will translate into higher or lower band crossing frequencies. Note that for simplicity we assume that the $\Omega_x = 0.0$ currents will not modify the alignment properties of interacting orbitals; this translates into the independence of the single-particle routhian slope in the energy versus Ω_x plot (see, for example, Fig. 4.18a) on the $\Omega_x = 0.0$ currents.

Fig. 4.18a can be used to illustrate this mechanism. Let assume that the $\Omega_x = 0.0$ currents will increase the energy gap between the $\pi[642]5/2^+$ and $\pi[651]1/2^+$ orbitals at $\Omega_x = 0.0$ MeV: this will lead to higher band crossing frequencies. However, the band crossing frequencies will decrease in the case when the energy gap between these orbitals at $\Omega_x = 0.0$ MeV becomes smaller in the presence of the $\Omega_x = 0.0$ currents. The assumption that the $\Omega_x = 0.0$ currents do not have an impact on the alignment properties of interacting orbitals is definitely too simplistic but it allows to illustrate the fact that NM can both decrease and increase the band crossing frequencies.

This mechanism is not active in the configuration of even-even ^{194}Pb nucleus discussed above since both signatures of all states below the Fermi level are pairwise occupied. As a result, no current is present at $\Omega_x = 0.0$ MeV.

The impact of NM on band crossing features is also seen in the CRHB+LN calculations where the alignment of the pairs of $j_{15/2}$ neutrons and $i_{13/2}$ protons causes the shoulder and peak in total dynamic moment of inertia $J^{(2)}$ (Fig. 4.19c) (see also Ref. [131]). Note that each of these two alignments creates a peak in the dynamic moment of inertia of corresponding subsystem. NM shifts the paired neutron band crossing to lower frequencies by 70 keV from 0.485 MeV (WNM) to 0.415 MeV (NM). Paired proton band crossing lies in the calculations with NM at $\Omega_x = 0.535$ MeV, while only the beginning of this crossing is seen in the calculations without NM (Fig. 4.19c).

The origin of this effect is twofold. Similar to the unpaired calculations, the part of it can be traced to the fact that NM increases the expectation values $\langle \hat{j}_x \rangle_i$ of the orbitals located at the bottom of the shell (the discussed orbitals are of this kind) [38]. The corre-

sponding larger slope of the quasiparticle routhians causes the shift of the crossing to lower frequencies. However, an additional contribution comes from the modification of the pairing by NM. There is a difference in the pairing energies calculated with and without NM which increases with rotational frequency, see Fig. 4.20c,d. The pairing in the calculations with NM is weaker. This can be explained by the increase of $\langle \hat{j}_x \rangle_i$ of the orbitals located at the bottom of the shell due to NM (see above). The gradual breaking of high-j pairs proceeds faster, which is reflected in a faster decrease of pairing with increasing Ω_x. Thus we can specify this effect as *an anti-pairing effect induced by NM*.

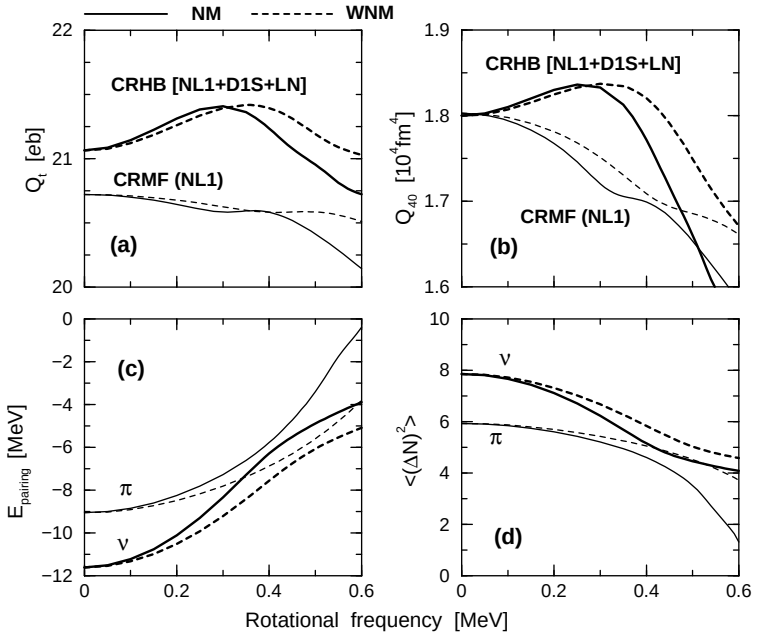

Figure 4.20

The same as Fig. 4.19, but for Q_t , Q_{40}, $E^{n,p}_{pairing}$ and $\langle(\Delta\hat{N})^2\rangle$.

These considerable differences in the crossing frequencies obtained in the calculations with and without NM cannot be attributed to the differences in equilibrium deformations, since calculated transition quadrupole moments Q_t and mass hexadecapole moments Q_{40} obtained in the calculations with and without NM differ only marginally before band crossing, see Figs. 4.20a,b.

The influence of time-odd mean fields on band crossing features has been studied by means of a schematic non-self-consistent model based on the Skyrme forces in Ref. [32]. In this study, time-odd fields emerging from the $\mathbf{S}^2$ and $-\mathbf{S}\Delta\mathbf{S}$ terms of the Skyrme Hamiltonian shift the alignment of the $i_{13/2}$ neutron pair to higher frequencies in ^{158}Dy. On the contrary, this crossing appears at lower frequencies in the CRHB+LN calculations when NM is taken into account. This difference is not surprising considering the fact that time-odd mean fields are not well defined in non-relativistic density functional theories [33, 164]. It was also suggested in the cranked Skyrme Hartree-Fock framework that time-odd mean fields may be responsible for band crossing in yrast superdeformed band of ^{60}Zn [45]. However, this crossing is described as paired band crossing in the CRHB+LN calculations [148].

Above discussed CRMF and CRHB+LN examples clearly show that the modifications of band crossing features (crossing frequencies and the features of the kinematic and dynamic moments of inertia in band crossing region) caused by NM are substantial and depend on the underlying modifications of single-particle properties such as alignments and single-particle (quasi-particle) energies.

4.5 Particle number and deformation dependences of the impact of nuclear magnetism on the moments of inertia

In the current section, the particle number and deformation dependence of the impact of NM on the kinematic moments of inertia are discussed in detail. We consider the contribution of NM to kinematic moment of inertia, namely, the $(J^{(1)}_{NM} - J^{(1)}_{WNM})/J^{(1)}_{NM}$ quantity, and its variations as a function of particle number and deformation. In addition, we investigate how close fully self-consistent value of the kinematic moment of inertia comes to the rigid body moment of inertia J_{rig}. The latter quantity is obtained in one-dimensional cranking approximation with the rotation defined around the x-axis from the calculated density distribution $\rho(\mathbf{r})$ by

$$J_{rig} = \int \rho(\mathbf{r})(y^2 + z^2)d^3r \tag{4.13}$$

The contributions of NM to kinematic moment of inertia (the $(J^{(1)}_{NM} - J^{(1)}_{WNM})/J^{(1)}_{NM}$ quantity) for normal deformed bands in a number of isotope chains with proton number $Z \geq 50$ are shown as a function of neutron number in Fig. 4.21. Only the cases in which the nuclear configurations are the same in the calculations with and without nuclear magnetism are shown in this figure. NM typically increases the calculated kinematic moments of inertia by 10-30%. However, this increase is around 40% in the $N = 108, 110$ W isotopes. Considerable fluctuations of the $(J^{(1)}_{NM} - J^{(1)}_{WNM})/J^{(1)}_{NM}$ quantity as a function of neutron number seen in some isotope chains are due to the changes in underlying single-particle structure. Large changes in the $(J^{(1)}_{NM} - J^{(1)}_{WNM})/J^{(1)}_{NM}$ quantity are seen on going from the isotope with neutron number N to the isotope with $N + 2$ when two neutron

single-particle orbitals, by which the configurations of compared nuclei differ, have the expectation values of the single-particle angular momenta $\langle \hat{j}_x \rangle_i$ strongly affected by NM. The opposite is also true when two neutron single-particle orbitals, by which the configurations of compared nuclei differ, have the expectation values of the single-particle angular momenta $\langle \hat{j}_x \rangle_i$ that are only marginally affected by NM. Note that in some cases proton configurations of two neighboring nuclei with neutron numbers N and $N+2$ are also different due to the deformation changes; this also contributes into the fluctuations of the $(J^{(1)}_{NM} - J^{(1)}_{WNM})/J^{(1)}_{NM}$ quantity as a function of neutron number.

One can also extract from Fig. 4.21 the dependence of the contributions of NM to kinematic moments of inertia on proton number Z by considering the results of the calculations at constant value of neutron number N. Such analysis reveals the fluctuations in the $(J^{(1)}_{NM} - J^{(1)}_{WNM})/J^{(1)}_{NM}$ quantities which are similar to the ones discussed above. The origin of these fluctuations can again be traced back to the changes (as a function of proton number) in underlying single-particle structure.

Fig. 4.22 compares rigid body moments of inertia J_{rig} (Eq. (4.13)) with fully microscopic kinematic moments of inertia $J^{(1)}_{NM}$ (Eqs. (4.11) and (4.12)) obtained in the calculations with NM using the $(J_{rig} - J^{(1)}_{NM})/J_{rig}$ quantity. One can see that considerable deviations (in majority of the cases being in the window of $\pm 30\%$ but reaching $\pm 60\%$ in some nuclei) between these two moments of inertia are observed at normal deformation.

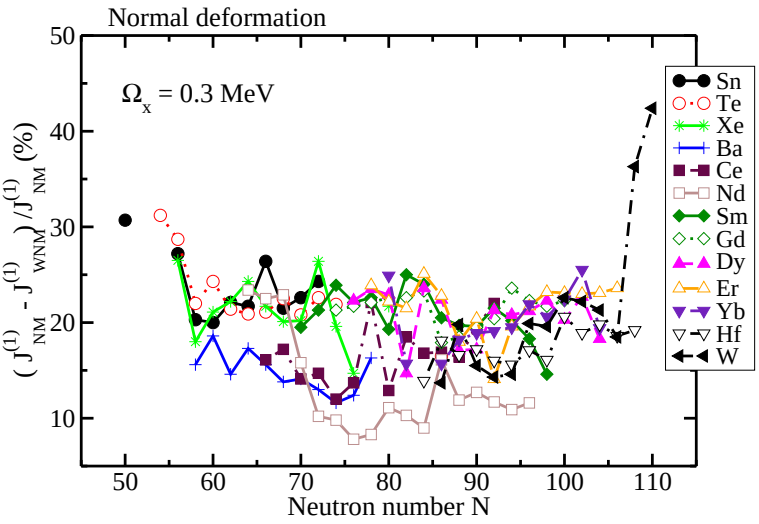

Figure 4.21

The contribution (in %) of NM to $J^{(1)}$ at normal deformation.

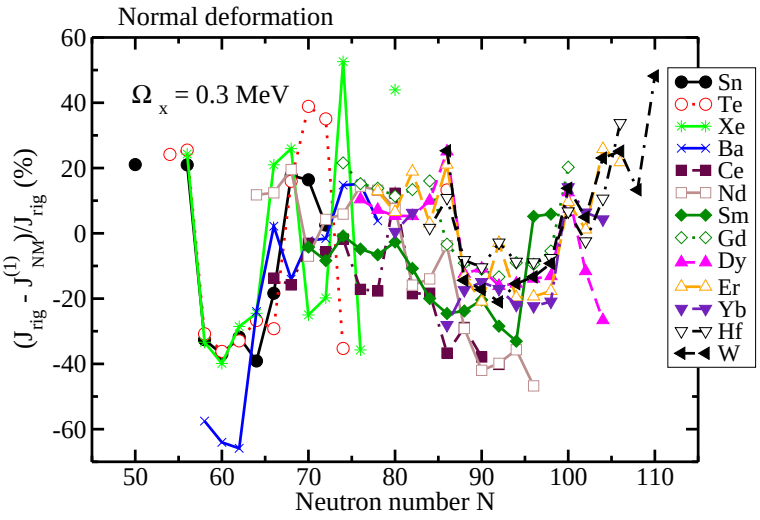

Figure 4.22

The difference (in %) between J_{rig} and $J^{(1)}$ calculated with NM.

The analysis within the framework of the periodic orbit theory [165] concluded that the deviations of the moments of inertia from the rigid-body value at high spin are determined by the shell structure of a system of independent fermions confined by a leptodermous potential. For the case of prolate deformation and the rotation perpendicular to the symmetry axis (the majority of the cases studied in the current manuscript fall under this category), the meridian orbits determine the shell moments of inertia because only they enclose rotational flux [165].

Large similarities are seen between the results of our calculations and the ones based on the cranked Woods-Saxon potential in Ref. [165]. For example, right bottom panel in Fig. 10 of Ref. [165] shows the difference $J_{pper} - J_{rig}$ between the moments of inertia J_{pper} calculated in the cranked Woods-Saxon potential and rigid-body moments of inertia J_{rig} for the case of prolate deformation and the rotation around the axis perpendicular to the symmetry axis. If one corrects for the difference in the representation of calculated quantities [($J_{pper} - J_{rig}$) in Ref. [165] and $(J_{rig} - J^{(1)}_{NM})/J_{rig}$ in the present manuscript], then one can see that our results show similar shell dependence of the $(J^{(1)}_{NM} - J^{1}_{rig})$ quantities as the one seen in Fig. 10 of Ref. [165]. Some differences between these two calculations are in part due to simplistic method of the calculation of the rigid-body moments of inertia in Ref. [165] (see Sec. IIB of Ref. [165] for details).

The CRMF calculations describe rather well the kinematic moments of inertia of normal-deformed [69, 57] and smooth-terminating [11, 57] bands at high spin where the pairing is negligible. Experimental data on kinematic moments of inertia of normal-deformed rotational bands at low spin [which are strongly affected by pairing] are also well

described in the cranked relativistic Hartree-Bogoliubov calculations [166, 39]. These results together with the ones presented in the current manuscript strongly support the conclusion that weakly- and normal-deformed nuclei show the moments of inertia which strongly deviate from the rigid-body value (see also Refs. [145, 165]).

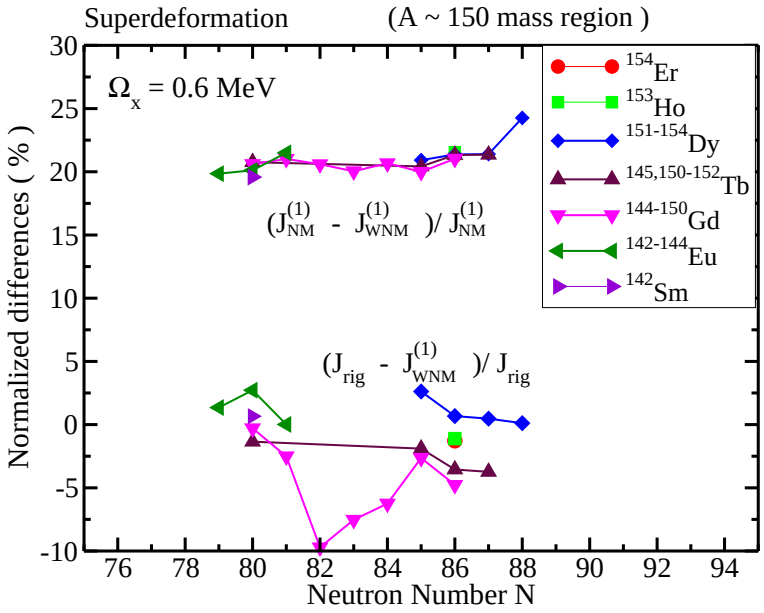

Figure 4.23

Similar to Figs. 4.21, 4.22

Figs. 4.23 and 4.24 show the results of calculations for yrast SD configurations in the $A \sim 150$ mass region of superdeformation and for yrast hyperdeformed (HD) configurations in the $Z = 40 - 58$ part of the nuclear chart, respectively. It is clearly seen that the $(J^{(1)}_{NM} - J^{(1)}_{WNM})/J^{(1)}_{NM}$ and $(J_{rig} - J^{(1)}_{NM})/J_{rig}$ quantities at these extreme deformations show much smaller fluctuations than the ones at normal deformation. Indeed, the contri-

bution of NM into kinematic moment of inertia at SD and HD is in narrow $20-27\%$ range (Figs. 4.23 and 4.24), while it covers much large $9-43\%$ range at normal deformation (Fig. 4.21). In addition, the values of kinematic moment of inertia calculated with NM are typically within 5% of the rigid body value for the moment of inertia at SD and HD (Figs. 4.23 and 4.24), while much larger fluctuations (typically within 40% of the rigid body value) are seen in the case of normal deformation (Fig. 4.22).

Microscopic origin of these features can be traced back to the underlying shell structure. The analysis within the periodic orbit theory [165] shows that the single-particle orbits that cause shell structure of prolate superdeformed nuclei do not carry rotational flux if the axis of rotation is perpendicular to the symmetry axis. Therefore, the moments of inertia of the SD bands in such nuclei should be equal to the rigid body value [165]. Such conclusion is in general supported by our microscopic calculations which show that the calculated moments of inertia are typically within 5% of rigid-body value. The experimental deviations (obtained under spin assignments of Refs. [104, 105]) from the rigid-body values are about 6% or less in the $A \sim 150$ region of superdeformation (see Fig. 5 in Ref. [165]).

We also expect that similar mechanism is also responsible for the observed features of the moments of inertia at HD. However, the periodic orbit theory analysis of such features is not available and it goes beyond the scope of the current manuscript.

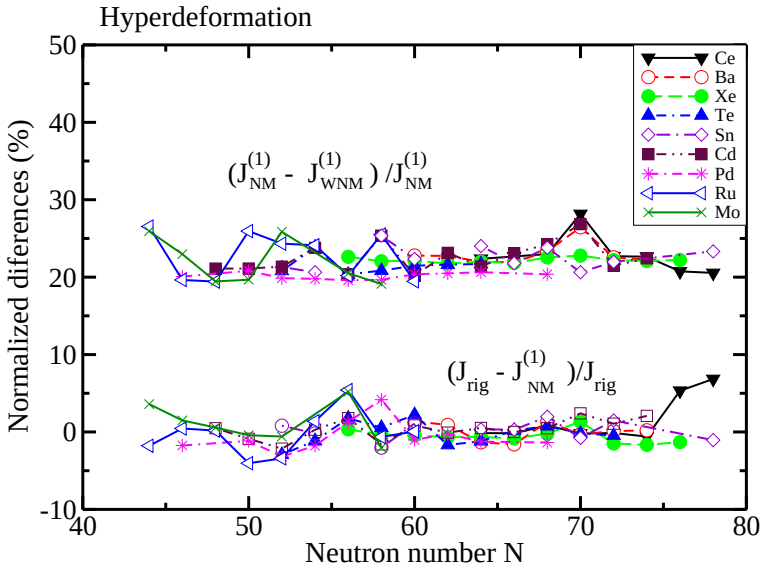

Figure 4.24

The same as in Fig. 4.23 but for the hyperdeformed configurations.

4.6 Currents in intrinsic (rotating) frame of collectively rotating nuclei

Current distributions in the intrinsic (rotating) frame have been studied earlier in several publications. It is well known that there are no currents in the intrinsic frame if the rigid non-spherical body rotates uniformly (rigid rotation) (see Sec. 6A-5 in Ref. [167]). The general aspects of the velocity (current) fields have been discussed in detail in the framework of single-particle Schrödinger fluid [168], which exhibits a remarkably rich variety of fluid dynamical features, including compressible flow and line vortices. Nuclear intrinsic vorticity and its coupling to global rotations have been studied within the so-called routhian approach both in semiclassical approach [169, 170] and in fully self-consistent cranked Hartree-Fock and Hartree-Fock-Bogoliubov approaches based on the Skyrme force [171]. The current distributions in rotating frame have been studied

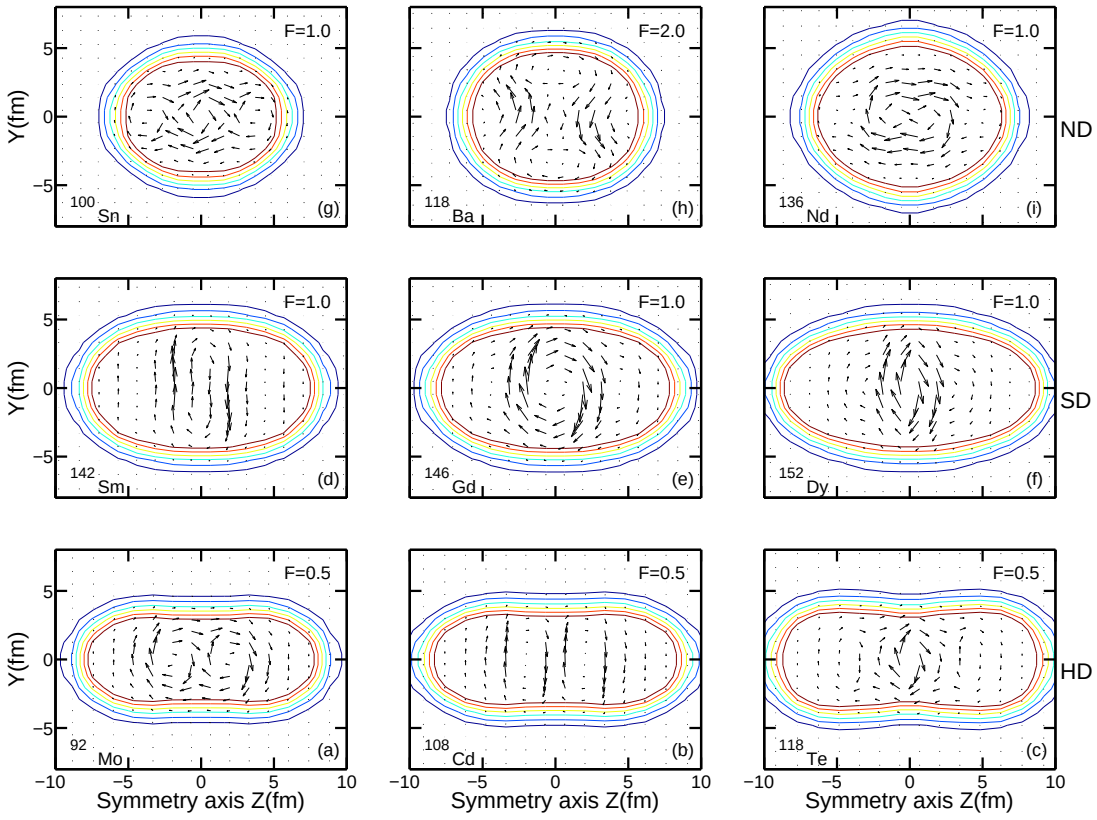

Figure 4.25

Total $\boldsymbol{j}^n(\boldsymbol{r})$ currents in the intrinsic frame in the $y-z$.

in phenomenological cranking approaches based on harmonic oscillator [172, 173, 174, 169] and Nilsson [175] potentials and in self-consistent cranking approaches based on the Skyrme force [176, 171]. Note that the intrinsic current field (as any vector field according to the Hemholtz's theorem) can be split into irrotational and intrinsic vortical fields [170].

Fig. 4.25 shows typical current distributions obtained in the CRMF calculations for selected normal-, super- and hyperdeformed nuclei. The results of calculations are shown at rotational frequencies $\Omega_x = 0.3$ MeV and $\Omega_x = 0.5$ MeV for the ND and SD configurations, respectively, and at the spin ($\Omega_x \sim 1.0$ MeV) at which the HD configurations become yrast (see Sec. 3.3.1 for details) in the case of HD configurations. Despite the fact that the moments of inertia of the SD and HD configurations are very close to the rigid-body values (Sec. 4.5), the presence of strong vortices[1] demonstrates the dramatic deviation of the currents from rigid rotation. For example, the HD configurations in ^{92}Mo (Fig. 4.25a) and ^{108}Cd (Fig. 4.25b) show two strong vortices centered at $z \approx \pm 2$ fm. Note that the vortices (i.e. the curl) of the current fields are aligned or antialigned along a principal x-axis of the ellipsoid because of the use of one-dimensional cranking approximation. On the other hand, the HD configuration in ^{118}Te (Fig. 4.25c) shows one very strong vortice centered at $z = 0$ fm, and 2 weaker vortices centered at $z \approx \pm 4.5$ fm. All three vortices rotate clockwise.

[1]The existence of vortices at these points implies non-vanishing current circulations which are defined as $\boldsymbol{C}(\boldsymbol{r}) = \boldsymbol{\nabla} \times \boldsymbol{j}(\boldsymbol{r})$ [174].

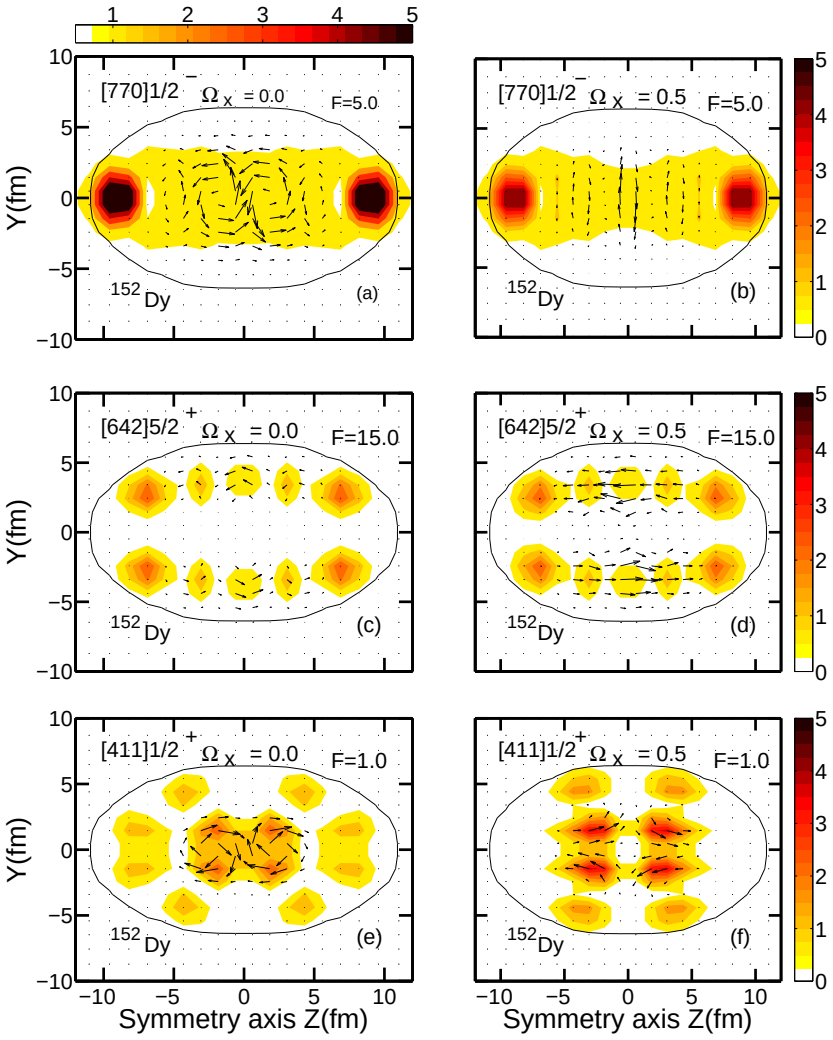

Figure 4.26

The $\boldsymbol{j}^n(\boldsymbol{r})$ produced by single neutron in the yrast SD configuration in ^{152}Dy.

The currents in the rotating frame of reference that is fixed to the body are caused by quantized motion of the fermions. Thus, the differences between the currents in ^{92}Mo and ^{108}Cd on one hand and the ones in ^{118}Te on the other hand are caused by the differences in the underlying single-particle configurations. Contrary to the HD configurations, the current distributions in the SD configurations of ^{142}Sm, ^{148}Gd and ^{152}Dy are characterized by a single very strong central vortice (Figs. 4.25d-f). Current patterns in normal deformed nuclei ^{100}Sn and ^{118}Ba look more disordered than in the SD and HD nuclei (Figs. 4.25g,h). This is because three (four) large vortices in ^{100}Sn (^{118}Ba) are spread out over the volume of the nucleus. On the other hand, the current pattern is dominated by a single large central vortice in the ND configuration of ^{136}Nd (Fig. 4.25i).

Note that all considered configurations are characterized by the weak current in the surface area. On the contrary, the average intrinsic current flows mainly in the nuclear surface in the semiclassical description of currents in normal and superfluid rotating nuclei [169]. This underlines the importance of quantum mechanical treatment of the currents.

The total current is the sum of Coriolis induced and magnetic potential induced currents. Total current is dominated by the Coriolis induced currents; magnetic potential induced currents represent approximately 5-20% [30%] of total current in the HD and SD [ND] nuclei shown in Fig. 4.25. The only exception is ^{92}Mo, in central region of which magnetic potential induced currents are larger than Coriolis induced currents by a factor close to 2. The spatial distribution of Coriolis induced and magnetic potential induced currents is similar in the majority of nuclei shown in Fig. 4.25. However, the spatial distribution of these two types of currents differ substantially in ^{92}Mo, ^{146}Gd and ^{118}Ba.

Comparing current patterns shown in Fig. 4.25, one can conclude that for a system of non-interacting fermions, the total current, being the sum of the single-particle currents (see Eq. (2.26)), is, in general, quite complicated. This is a consequence of the fact that the localization, the strength and the structure of the current vortices created by a particle in a specific single-particle state depend on its nodal structure (see Ref. [174] and Sec. 4.1.3. In this respect it is important to mention the results of Ref. [174] which showed that Coriolis induced current for a single-particle in a slowly rotating anisotropic harmonic oscillator potential has, in fact, a rather simple structure. It exhibits a number of localized circulations with precisely predictable centers and sense of rotation. The centers of the circulations are found at the nodes and peaks of the oscillator eigenfunctions, thus, forming a rectangular array somewhat similar to a crystal lattice.

The wavefunction of the CRMF approach is more complicated than that of a rotating anisotropic harmonic oscillator because of the presence of spin-orbit interaction and the split of the wavefunction into large and small components. Moreover, there are magnetic potential induced currents in addition to Coriolis induced ones. However, the analysis of single-particle vortices in rotating nuclei in general confirms the observations made in Ref. [174]. The typical features of the single-particle currents in the CRMF approach are considered below on the example of three neutron single-particle states occupied in the yrast SD configuration of ^{152}Dy. The current and density distributions of these states are shown in Fig. 4.26. Let us first consider the $\nu[642]5/2^+$ state. The comparison of Figs. 4.26c and 4.26d reveals that the rotation of a nucleus considerably increases the currents in this state. On the other hand, the density distribution is almost unaffected by

rotation. The rotation of a nucleus also leads to a change in the structure of the circulations. At $\Omega_x = 0.0$ MeV, there are three weak circulations centered around the nodes at $(y = 0 \text{ fm}, z = 0 \text{ fm})$ and $(y = 0 \text{ fm}, z \approx \pm 4 \text{ fm})$; they are due to magnetic potential. Only two much stronger circulations are visible at $\Omega_x = 0.5$ MeV: they are centered around the nodes located at $(y = 0 \text{ fm}, z \approx \pm 2.5 \text{ fm})$. This change of the structure of vortices can be attributed to additional currents produced by the Coriolis term as well as to the change of the structure of wave function with increasing rotational frequency. The wave function in terms of two largest components has the 86%[642]5/2+5%[633]5/2 and 63%[642]5/2+13%[651]3/2 structure[2] at $\Omega_x = 0.0$ MeV and $\Omega_x = 0.5$ MeV, respectively.

Even much large changes are induced by rotation into the structure of the $\nu[411]1/2^+$ state. The wave function in terms of two largest components has the 57%[411]1/2+ 23%[651]1/2 and 84%[411]1/2+13%[411]3/2 structure at $\Omega_x = 0.0$ MeV and $\Omega_x = 0.5$ MeV, respectively. One can see that the $\Delta N = 2$ interaction, leading to a considerable admixture of the [651]1/2 component into the structure of wave function, plays very important role at no rotation. The change in the wave function induced by rotation leads to a considerable changes both in the nodal structure of density distribution and in the current distribution (compare Fig. 4.26e with Fig. 4.26f).

The wave function of the $\nu[770]1/2^-$ state is changed considerably by the rotation: its structure in terms of two largest components is 62%[770]1/2+17%[761]1/2 at $\Omega_x = 0.0$ MeV and 39%[770]1/2+28%[761]3/2 and $\Omega_x = 0.5$ MeV. The increase of rotational fre-

[2]The percentages show the weights of respective components of the wave function in the total structure of the wave function. Note that only two largest components of the wave function are displayed.

quency does not lead to appreciable modifications in the density distribution but considerably decreases the strength of the currents and changes the shape of the circulations (see Figs. 4.26a,b). The latter is a consequence of additional Coriolis induced currents. It is interesting that for this state the currents show maximum strength at the densities far below the maximum densities. This most likely explains relative weakness of the currents in this state as compared with those in the $\nu[411]1/2^+$ state. On the contrary, for many single-particle states the strongest currents are seen at or close to local increases in the densities (see Figs. 4.26c,d,f,g and Fig. 4.6).

Our calculations show that the moments of inertia of the SD and HD configurations are very close to rigid-body values (Sec. 4.5). However, the intrinsic currents show the dramatic deviations from rigid rotation. Usually the deviations from the rigid-body moment of inertia imply that the flow pattern must substantially deviate from the current of a rigidly rotating mass distribution, i.e. there are strong net currents in the body-fixed frame [165]. However, the opposite is not true: the closeness of the moments of inertia to rigid body value does not necessary implies that the current distribution should correspond to rigid rotation. On a microscopic level, the building blocks of the total current, namely, the single-particle currents certainly do not have a rigid-flow character; on the contrary, they have the vortex-flow character (see Fig. 4.26).

Earlier non-relativistic studies also point to above discussed relations between currents and rigid body moments of inertia. For example, it was shown in Ref. [173] for Schrödinger equation that single-valuedness requirement for the wavefunction implies non-existence of rigid-flow in a quantum fluid. Furthermore, it was demonstrated for a

system of independent particles employing cranked harmonic oscillator potential that the current is not of the rigid-flow type even when the moment of inertia assumes the rigid-body value ([173], see also Ref. [172]).

Current distributions shown in Figs. 4.25 and 4.26 are typical for collective rotation around the $x-$axis perpendicular to the symmetry axis. Note that the alignment of the angular momentum vector of a particle is specified along the x-axis in one-dimensional cranking approximation (see also discussion in Sec. 4.1.3 of Ch. 4). The $\Omega = 1/2$ orbitals are aligned with the axis of rotation (x-axis) already at no rotation. As a result, the single-particle angular momentum vector of the $\Omega = 1/2$ orbitals performs the precession around the x-axis, thus orienting the currents predominantly in the $y - z$ plane. In addition, the $\Omega = 1/2$ orbitals show vortices which are concentrated in the central region of nucleus. For the configurations with $\Omega \neq 1/2$, this mechanism of alignment becomes active only when the rotation sets up. Moreover, with increasing Ω, the densities and currents are pushed away from the axis of symmetry of the nucleus toward the surface area (Figs. 4.26c,d and Fig. 4.6).

4.7 Frequency and configuration dependences of the impact of nuclear magnetism on the moments of inertia

In this section, the frequency dependence of the impact of NM on the moments of inertia is studied using considerable number of SD and highly-deformed configurations in ^{60}Zn obtained in unpaired CRMF calculations. The properties of yrast SD band in this nucleus were well described in this formalism above band crossing which takes place at $\Omega_x \sim 1$ MeV [177, 70], while the CRHB+LN formalism gave good description of this band in the band crossing region [148]. The neutron routhian diagram for this configuration obtained in the calculations with the NLSH parametrization is shown in Fig. 1 of Ref. [70]; the results with the NL1 parametrization are similar to the ones obtained with NLSH. All proton and neutron states below the $Z = 30$ and $N = 30$ SD shell gaps are occupied in this configuration (note that proton routhian diagram is similar to the neutron one). The configurations are labelled by the shorthand notation $[n, p]$, where n (p) is the number of occupied $g_{9/2}$ neutrons (protons). In this notation, the yrast SD band has the [2,2] configuration. Excited configurations under consideration are built by means of proton or/and neutron particle-hole excitations across the $Z = 30$ and $N = 30$ SD shell gaps.

The results of calculations for contributions of NM into dynamic ($\Delta J^{(2)}_{NM-contr}$) and kinematic ($\Delta J^{(1)}_{NM-contr}$) moments of inertia are shown in Fig. 4.27. At low frequencies, the average contribution of NM into kinematic moment of inertia is slightly larger than 20% (Fig. 4.27a) and the $\Delta J^{(1)}_{NM-contr}$ quantities show considerable dependence on configuration. The origin of the latter observation can be traced back to the specific features of some occupied single-particle orbitals.

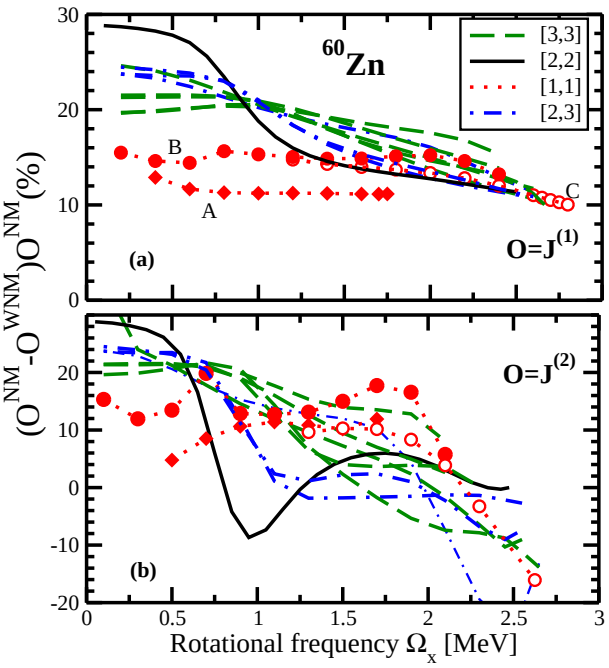

Figure 4.27

The contributions of NM to $J^{(1)}$ and $J^{(2)}$.

Let us consider as an example the [2,2] configuration. At low frequencies, the $\Delta J^{(1)}_{NM-contr}$ values for this configuration are considerable higher than the $\Delta J^{(1)}_{NM-contr}$ values averaged over all calculated configurations. This is due to the fact that upsloping branches of the proton and neutron $[440]1/2^+$ orbitals (in the $\Omega_x = 0.0 - 0.7$ MeV range, see Fig. 1 in Ref. [70]), characterized by the expectation values of the single-particle angular momentum $\langle \hat{j}_x \rangle_i$ strongly affected by NM, are occupied at $\Omega_x \leq 0.6$ MeV. At frequencies $\Omega_x \sim 0.8$ MeV, these orbitals strongly interact with proton and neutron $[431]3/2^+$ orbitals and exchange the character of the wavefunction. This leads to unpaired band crossing (see Ref. [70]) which is seen in considerable changes of $\Delta J^{(1)}_{NM-contr}$ and $\Delta J^{(2)}_{NM-contr}$ quantities. The band crossing process is completed above $\Omega_x = 1.1$ MeV, where the orbital

labeled as $[440]1/2^+$ is downsloping as a function of rotational frequency (see Fig. 1 in Ref. [70]). At these frequencies, the $\Delta J^{(1)}_{NM-contr}$ quantity for the [2,2] configuration is slightly below the value of $\Delta J^{(1)}_{NM-contr}$ averaged over all calculated configurations (Fig. 4.27a). Note that this unpaired band crossing is not active in the [1,1] configurations because neither proton nor neutron $[440]1/2^+$ orbitals are occupied. The calculations also suggest that it is considerably suppressed in the [3,3] configurations due to the changes in the deformations and currents induced by the occupation of third $g_{9/2}$ orbital both in proton and neutron subsystems. However, the presence of this crossing is still visible (especially, in the $\Delta J^{(2)}_{NM-contr}$ quantity) in some [2,3] configurations.

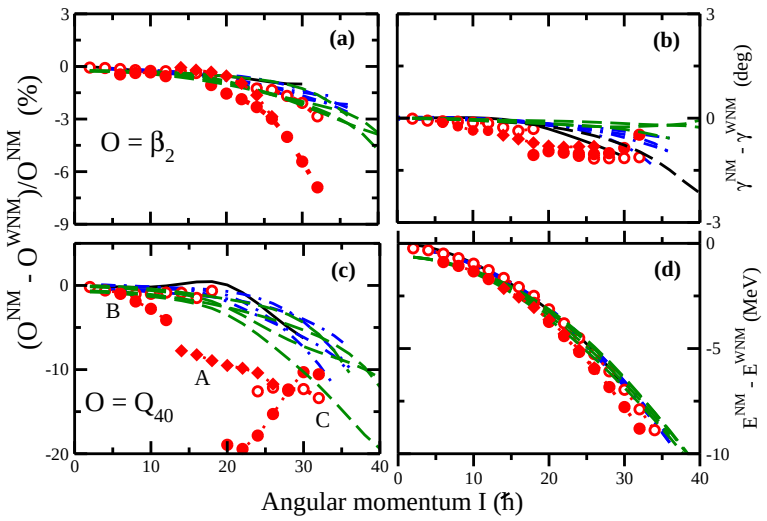

Figure 4.28

The contributions of NM to β_2, γ-deformation , Q_{40} and total energy E.

With increasing rotational frequency, the average contribution of NM into kinematic moments of inertia decreases and it falls below 15% at $\Omega_x \sim 2.5$ MeV (Fig. 4.27a). In addition, the configuration dependence of the $\Delta J^{(1)}_{NM-contr}$ quantities is weaker than the one at low frequencies. At these frequencies, the majority of occupied single-particle orbitals are either completely aligned or very close to complete alignment. However, NM do not modify the expectation values of the single-particle angular momenta $\langle j_x \rangle_i$ of completely aligned orbitals [136]. As a result, only remaining orbitals, which are still aligning, contribute into $\Delta J^{(1)}_{NM-contr}$. The combined contribution of these orbitals into $\Delta J^{(1)}_{NM-contr}$ is smaller than the one at lower frequencies because the alignment of these orbitals is not far away from complete.

The impact of NM on the dynamic moments of inertia is shown in Fig. 4.27b and it clearly displays much more complicated pattern as compared with the impact of NM on the kinematic moments of inertia. The irregularities in the $\Delta J^{(2)}_{NM-contr}$ quantities are related to the band crossings. For example, the dip in the $\Delta J^{(2)}_{NM-contr}$ values of the $[2,2]$ configuration at $\Omega_x \sim 0.9$ MeV is caused by the unpaired band crossings which take place at different frequencies in the calculations with and without NM. Similar deviations from smooth trend as a function of rotational frequency are visible in other configurations. However, one can see that for some configurations the contribution of NM into dynamic moment of inertia is a smooth function of rotational frequency over extended frequency range. In this frequency range, the configurations remain unchanged. It is interesting that for some of these configurations the contributions of NM into dynamic moments of inertia are either close to zero or even negative; such features have not been seen in the

previous analyzes of the impact on time-odd mean fields on the dynamic moments of inertia [68, 33, 20, 38].

The impact of NM on other physical observables of interest is shown in Fig. 4.28, in which the results of the NM and WNM calculations are compared as a function of total angular momentum. One can see that the quadrupole deformations β_2 (Fig. 4.28a) obtained in the calculations with and without NM differ by less than 3%. The only exception is configuration B for which this difference reaches 7%. The difference in mass hexadecapole moments Q_{40} obtained in the calculations with and without NM is larger but typically below 10% (Fig. 4.28c); the only exception is the configuration B for which this difference reaches 20% at $I \sim 20\hbar$. The γ-deformations obtained in the calculations with and without NM differ by less than 1.5° (Fig. 4.28b). The only significant difference is seen in the total binding energies (Fig. 4.28d), where the NM solution is more bound than the WNM solution. This effect, which is due to the modifications in the moments of inertia induced by NM, is very large: additional binding due to NM reaches 7-8 MeV at spin $I = 30\hbar$. These systematic results are consistent with the ones obtained in the previous studies of single SD configuration in ^{152}Dy [38] and single terminating configuration in ^{20}Ne [136]. They also give a hint why the cranked models based on the phenomenological potentials like Woods-Saxon or Nilsson, which do not include time-odd mean fields [33], are so successful in the description of experimental data. When considered as a function of spin the deformation properties of the rotating system are only weakly affected by time-odd mean fields, and the proper renormalization of the moments of inertia [145] takes care of the E versus angular momentum curve.

4.8 Parametrization dependence of the contributions of NM to the moments of inertia

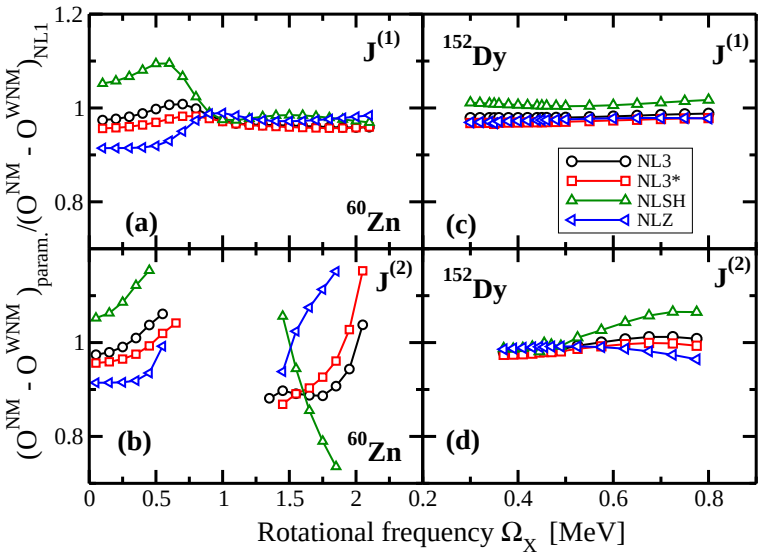

Figure 4.29

The contribution of NM to the physical observable O.

It was shown in Ch. 4 that additional binding due to NM in one-particle states only weakly depends on the RMF parametrization; this is also seen in the analysis of terminating states in Ref. [136]. In this context, it is important to understand how the contributions of NM to the kinematic and dynamic moment of inertia depend on the RMF parametrization.

The dependence of the dynamic moments of inertia on the RMF parametrization has earlier been analyzed on the example of the SD bands in ^{151}Tb and ^{143}Eu in Ref. [105] and

in ^{58}Cu and ^{60}Zn in Ref. [70] employing the NL1, NL3 [64] and NLSH [115] parametrizations of the RMF Lagrangian. The latter study includes also the results of calculations for kinematic moments of inertia. Additional calculations for these nuclei have also been performed with NL3* [57] and NLZ [116] parametrizations for the current manuscript. As follows from these results, the kinematic and dynamic moments of inertia depend only weakly on the parametrization of the RMF Lagrangian. Indeed, at given frequency all the results for kinematic [dynamic] moments of inertia fit into the window which have a width equal to approximately 5% ($\approx$ 8%) [approximately 6% ($\approx$ 10%)] of the value of kinematic [dynamic] moment of inertia in the $A \sim 150$ ($A \sim 60$) region of superdeformation. The larger spread of calculated values in the $A \sim 60$ mass region are most likely due to (i) larger softness of potential energy surfaces in these nuclei as compared with the ones in the $A \sim 150$ region of superdeformation and (ii) to larger relative importance of each particle and, thus, model uncertainties in the description of their single-particle energies.

Fig. 4.29 shows the dependence of the contributions of NM to the kinematic and dynamic moments of inertia on the parametrization of the RMF Lagrangian. For simplicity of comparison, these quantities are normalized to those obtained in the calculations with the NL1 parametrization. Very weak dependence (within 5% window with respect of the NL1 results) of the contribution of NM to the kinematic moment of inertia on the RMF parametrization is seen in whole frequency range in ^{152}Dy (Fig. 4.29c) and at frequencies $\Omega_x \geq 0.75$ MeV in ^{60}Zn (Fig. 4.29a). In the latter nucleus the deviation from the NL1 results reaches 10% at lower frequencies. The possible reasons for the larger dependence of calculated quantities on the parametrization in ^{60}Zn has been discussed above. On the

other hand, the deviations from the NL1 results are larger for the dynamic moments of inertia. These deviations can be as large as 8% at highest frequencies in the yrast SD configuration of ^{152}Dy (Fig. 4.29d) and as large as 20% in the yrast SD configuration in ^{60}Zn (Fig. 4.29b). Considering that the dynamic moment of inertia is related to the second derivative of the total energy with respect of spin, a larger dependence of the dynamic moment of inertia on the parametrization is expected.

These values can be used to estimate the uncertainty in the definition of the moments of inertia in the CRMF calculations due to the uncertainty in NM. The latter is related to the dependence of the $[O^{NM}-O^{WNM}]_{param}$ quantities (Fig. 4.29) on the RMF parametrization discussed above. Dependent on nuclear system and configuration, the NM contribution to the total kinematic and dynamic moments of inertia is approximately 10-25% (Secs. 4.5 and 4.7). Thus, the uncertainty of the definition of the absolute value of the total dynamic and kinematic moments of inertia due to the uncertainty in the definition of NM is modest, being in range 0.5-5.0%. The fact that the moments of inertia of rotational bands of different structure in unpaired regime are well (typically within 5% of experimental data [20, 105, 70, 11, 69, 178]) described in the CRMF calculations strongly suggests that NM and its impact on the moments of inertia is reasonably well defined in the CDFT theory.

4.9 Terminating states

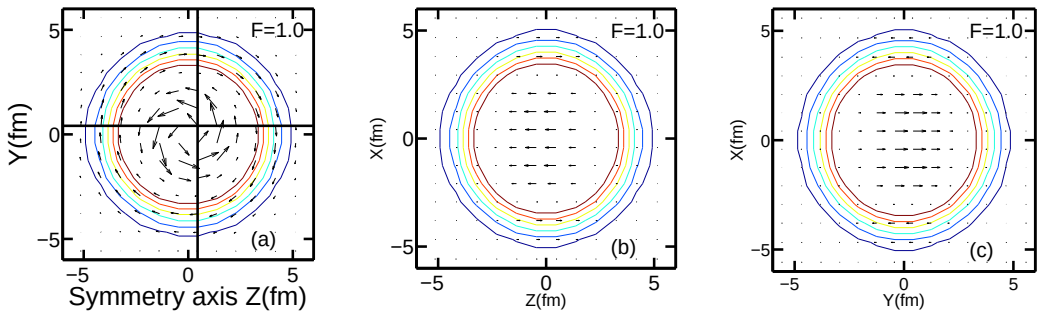

Figure 4.30

$\boldsymbol{j}^n(\boldsymbol{r})$ in the intrinsic frame for the state of ^{47}V terminating at $I = 17.5^+$.

The majority of rotational bands which do not have large deformation at spin zero will terminate in a non-collective terminating state at I_{max} [179, 180, 145] [3]. The regime of nuclear motion in terminating state is usually referred as 'non-collective rotation' [152, 145]. This is because of the fact that for an axially symmetric potential, the nucleon orbitals are not influenced by the rotation around the symmetry axis of this potential; thus, collective rotation about that axis is not possible. Non-collective rotation is also realized in the aligned states such as 'yrast traps' (or 'yrast isomers') [181, 14, 182]. The study of terminating states in the context of understanding of time-odd mean fields is of considerable interest because of several reasons. First, time-odd mean fields provide an additional binding to the energies of the specific configuration, and this additional binding increases

[3] Only recently the evidences for non-termination of some rotational bands at I_{max} have been found [146].

with spin and has its maximum exactly at the terminating state [136]. This suggests that the terminating states can be an interesting probe of time-odd mean fields [34, 147, 136] *provided that other effects can be reliably isolated [136]*. Second, at the band termination, the NM does not modify either total angular momentum or the expectation values of the single-particle angular momenta $\langle \hat{j}_x \rangle_i$ [136]. Third, terminating state is a (multi)-particle+(multi)-hole non-collective state in which the angular momenta of all particles and holes outside the core are aligned along the symmetry axis.

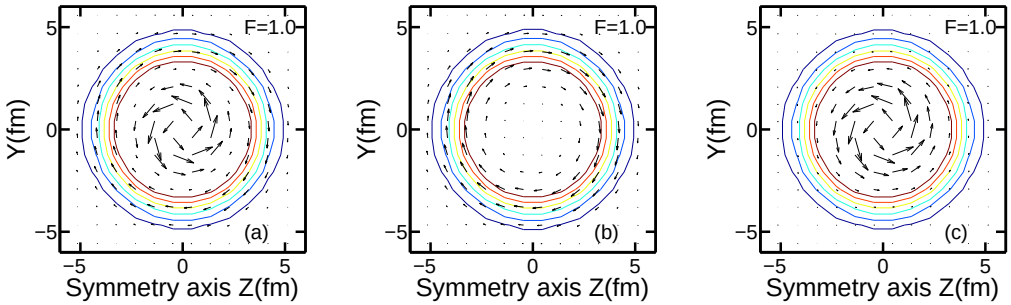

Figure 4.31

Same as Fig. 4.30.

We will consider in this section the $\pi(d_{3/2})^{-1}_{1.5}(f_{7/2})^4_8 \otimes \nu(f_{7/2})^4_8$ terminating state in ^{47}V, which has $I_{max} = 17.5^+$, as an example. The structure of this state is given with respect of the ^{40}Ca core. This state is characterized by the largest impact of NM on the binding energies amongst terminating states studied in Ref. [136]. It is nearly spherical with the quadrupole deformation $\beta_2 \sim 0.03$ (Fig. 6 in Ref. [136]). Our goal is to understand the

impact of NM on the current distribution and microscopic origin of additional binding due to NM.

In terminating states, the angular momenta of valence particles and holes are aligned along the symmetry axis (x-axis). As a consequence they perform precession around this axis, generating azimuthal currents with respect to the symmetry axis. This is illustrated in Fig. 4.30. One can see two azimuthal circulations in the $y-z$ plane: the circulation in the central region of nucleus is directed counterclockwise while the one in the surface region is directed clockwise. Fig. 4.31 shows total [left panel], Coriolis induced [middle panel] and magnetic potential induced [right panel] currents. One can see that surface circulation is generated by the Coriolis term, while the central circulation by the magnetic potential. The currents in the $x-z$ and $x-y$ planes are perpendicular to the x-axis (Fig. 4.30). This clearly shows that the currents are azimuthal.

In Ch. 4, the polarization effects induced by NM have been investigated in one- and two-particle configurations of odd and odd-odd non-rotating nuclei. Terminating states differ significantly from these configurations. First, they are multi-particle+multi-hole configurations. For example, the $\pi(d_{3/2})^{-1}_{1.5}(f_{7/2})^{4}_{8} \otimes \nu(f_{7/2})^{4}_{8}$ terminating state in ^{47}V has 8 particles and 1 hole outside the ^{40}Ca core. Second, the alignment of the angular momenta of these particles and holes generates considerable total angular momentum ($I = 17.5\hbar$ in the discussed terminating state of ^{47}V) aligned along the axis of symmetry; this momentum is much larger than the one in odd and odd-odd nuclei studied in Ch. 4. Third, terminating states are characterized by the azimuthal currents with respect to the symmetry axis, while the states in non-rotating nuclei are characterized by the currents shown in Figs. 4.4,4.5

and 4.6. Thus, it is interesting to see how these differences affect the polarization effects induced by NM and whether these polarization effects are similar in nature for these two classes of non-collective states, namely, low-spin one- and two-particle configurations of non-rotating nuclei and high-spin terminating states.

Table 4.5

The same as Table. 4.1 but for the state of ^{47}V terminating at $I = 17.5^{+}$.

Quantity	E_i^{WNM}	ΔE_i	ΔE_i^{pert}
1	2	3	4
E_{part}	-1217.668	-15.5	-7.296
E_{Cor}	42.0	0	
E_{σ}	-6381.875	-85.231	
$E_{\sigma NL}$	109.368	-2.815	
E_{ω}^{TL}	5371.721	79.291	
E_{ω}^{SL}	0.0	-3.51	-3.51
E_{ρ}^{TL}	0.549	-0.002	
E_{ρ}^{SL}	0.0	-0.038	-0.038
E_{Coul}	102.168	0.515	0.240
E_{cm}	-8.521	0.0	
E_{tot}	-386.121	-3.704	-3.983

Polarization effects induced by NM are investigated by considering NM impact on different terms of the total energy (Eq. (2.31)). The results of this study are shown in Table 4.5. Similar to the results in the non rotating nuclear system (See table. 4.1), the E_{ρ}^{TL} and E_{ρ}^{SL} terms are only weakly influenced by NM, and thus, they will not be discussed in detail. Somewhat stronger impact of NM is seen in the E_{Coul}, $E_{\sigma NL}$, and E_{ω}^{SL} terms. Note that only last term was appreciably affected in low-spin configurations of odd and odd-odd

nuclei in table. 4.1. Much larger polarization effects are seen in the E_{part}, E_σ and E_ω^{TL} terms. The E_σ and E_ω^{TL} terms depend only indirectly on time-odd mean fields through the polarizations of time-even mean fields induced by NM. One should keep in mind that only the $E_\sigma + E_\omega^{TL}$ quantity has a deep physical meaning, as it defines a nucleonic potential; this sum is modified by NM on -5.9 MeV.

Comparing these results with those presented in Ch. 4, one can conclude that polarization effects for different total energy terms in terminating state under study are stronger by at least one order of magnitude than in low-spin one- and two-particle configurations of non-rotating nuclei. This is a consequence of the fact that all particles (8) and holes (1) outside the ^{40}Ca core participate in building the total angular momentum and currents in terminating state, while only one (two) particle(s) participate in generating the currents in non-rotating odd (odd-odd) nuclei Sec. 4.1.3. Despite that the relative impact of NM on different terms of the total energy is, in general, similar in these two classes of non-collective states as can bee seen from tables 4.1, 4.2 and 4.5.

Total modifications of the energies due to NM in the mesonic sector are -11.79 MeV. Only one third of these modifications comes from the terms (E_ω^{SL}, E_ω^{SL}) which directly depend on nucleonic currents, whereas the rest from the modifications of time-even mean fields induced by NM.

It is interesting to compare the results of self-consistent and perturbative calculations[4]. The $\Delta E_i^{pert} = E_i^{NM} - E_i^{WNM}$ quantities will be used for simplicity in further discussion. These quantities are shown in columns 3 and 4 of Table 4.5. The ΔE_σ, $\Delta E_{\sigma NL}$, ΔE_ω^{TL} and ΔE_ρ^{TL} quantities are zero in perturbative calculations because time-even fields are fixed in these calculations. The ΔE_ω^{SL} and ΔE_ρ^{SL} are the same in self-consistent (column 3) and perturbative (column 4) calculations because the E_ω^{TL} and E_ρ^{TL} terms depend only on time-odd mean fields, which are the same in the parts of the calculations that include NM. Particle energies E_{part} are strongly modified by NM in self-consistent calculations; they change by -15.5 MeV. Perturbative calculations show that only one half of ΔE_{part} is coming directly from time-odd mean fields (see Sec. 4.2.2), the rest is due to polarization effects in time-even fields induced by NM. The same is true for the Coulomb energy term E_{Coul}.

It is evident from Table 4.5 that

$$\Delta E_{tot}^{self-const} \approx \Delta E_{tot}^{pert}. \tag{4.14}$$

Note that the superscript *'self-const'* and *'pert'* refers to fully self-consistent and perturbative results. The analysis of polarization effects in other terminating states of the $A \sim 40$ mass region shows the same relation. These results clearly indicate that the additional

[4]Fully self-consistent calculations with NM provide a starting point for perturbative calculations. Using their fields as input fields, only one iteration is performed in the calculations without NM: this provides perturbative results. Time-even mean fields are the same in both (fully self-consistent and perturbative) calculations. Then, the impact of time-odd mean fields on calculated quantities (for example, different terms in the total energy (Eq. (2.31)) is defined as the difference between the values of this quantity obtained in these two calculations. In this way, the pure effects of time-odd mean fields in fermionic and mesonic channels of the model are isolated because no polarization effects are introduced into time-even mean fields.

binding due NM is defined mainly by time-odd fields and that the polarization effects in fermionic and mesonic sectors of the model cancel each other to a large degree.

4.10 Signature-separated configurations

Signature separation phenomenon induced by time-odd mean fields has been found earlier in excited 4-particle SD configurations of ^{32}S [160, 148].It reveals itself in a considerable energy splitting of the $r_{tot} = +1$ and $r_{tot} = -1$ branches of the configurations which have the same structure in terms of occupation of single-particle states with given Nilsson labels. Such a signature separation could not have been obtained in phenomenological cranking models, such as the ones using the Woods-Saxon or Nilsson potentials, since time-odd mean fields are absent in these models.

However, the description of rotating $N \approx Z$ nuclei requires isospin projection [183] which can modify above mentioned results. Since this projection is beyond the current framework, we concentrate at the nuclei away from the $N = Z$ line. In Sec. 4.3 it was shown that signature separation is expected also in such nuclei, but it is weaker as compared with the one seen in the nuclei around the $N = Z$ line. Unfortunately, the survey of odd-odd $A = 20 - 52$ nuclei (some of which were studied in Ch. 4) does not reveal experimental bands in the nuclei away from the $N = Z$ line in which signature separation is expected.

Fig. 4.32 shows that signature separation phenomenon can also be present in heavier nuclei. This figure shows the results of calculations for odd-odd Eu isotopes in which odd proton occupies fixed $\pi[532]5/2^+$ state, and odd neutron occupies different neutron

states of the $r = \pm i$ signatures along the isotope chain. Additional binding due to NM is shown for total proton-neutron configurations with different total signatures $r_{tot} = \pm i$. Significant signature separation (on the level of 100-150 keV) is seen in the $\pi[532]5/2 \otimes \nu[523]5/2$ (^{156}Eu), $\pi[532]5/2 \otimes \nu[642]5/2$ (^{158,160}Eu), $\pi[532]5/2 \otimes \nu[633]5/2$ (^{196}Eu), and $\pi[523]5/2 \otimes \nu[752]5/2$ (^{204}Eu) configurations. Either $r = -1$ or $r = +1$ states can be more bound in signature separated configurations of Eu isotopes (Fig. 4.32). This depends on mutual orientation of proton and neutron currents induced by odd proton and odd neutron; the state with the same orientation of these currents is more bound.

Fig. 4.33 illustrates that four rotational sequences (two with total signature $r_{tot} = +1$ and two with $r_{tot} = -1$) can be built in the 2-particle configurations $\pi|a > (r = \pm i) \otimes \nu|b > (r = \pm i)$ (where $|a >$ and $|b >$ indicate the blocked proton and neutron Nilsson states, respectively) of odd-odd nuclei. For the case of ^{158}Eu we consider 2-particle configurations based on the $|a >= [532]5/2$ and $|b >= [642]5/2$ states. In the WNM calculations, the $r_{tot} = +1$ and $r_{tot} = -1$ configurations are almost degenerate in energy up to spin $I \sim 10\hbar$ (Fig. 4.33). On the contrary, there is a considerable signature separation (≈ 150 keV) due to time-odd mean fields between these configurations in the calculations with NM. *This feature is a strong spectroscopic fingerprint of the presence of time-odd mean fields.* Note that rotational sequences A and B undergo unpaired band crossings at $I \sim 20\hbar$.

Unfortunately, the experimental data on odd-odd Eu nuclei also do not reveal the configurations discussed above in which the signature separation is expected. This situation may be resolved by a systematic search of signature separated configurations both in the

experimental data on odd-odd rare-earth nuclei and in the model calculations. The best way to confirm the existence of this phenomenon would be to find in model calculations the configurations of odd-odd nuclei which show no signature splitting in the absence of time-odd mean fields and measurable signature separation in the presence of time-odd mean fields, and then to find their experimental counterparts which show signature separation. However, such an investigation is definitely beyond the scope of the current study. The difficulty of such a study is also underlined by the fact that existing interpretations of two-quasiparticle configurations in odd-odd nuclei are based on Woods-Saxon or Nilsson potentials. In these potentials, the signature degeneracy is considered to be a strong fingerprint of specific configurations. However, time-odd mean fields in EDF provide additional mechanism of breaking the signature degeneracy, so the experimental data on such configurations has to be reanalyzed in density functional calculations.

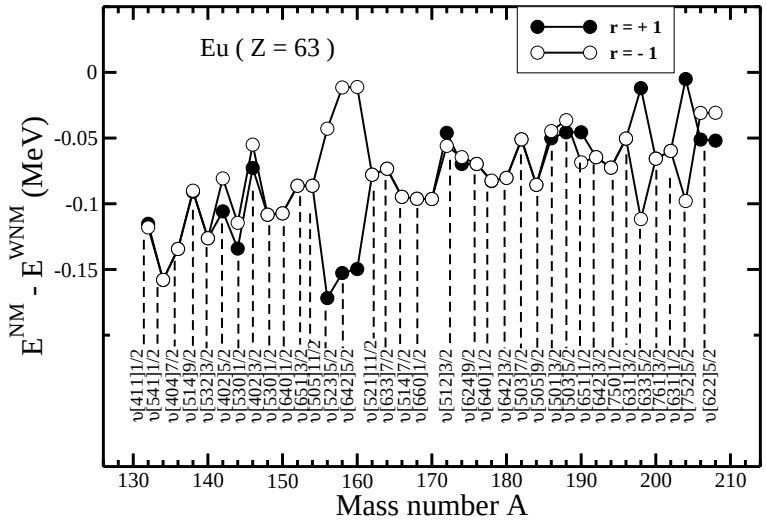

Figure 4.32

Similar to Fig. 4.3 but for odd-odd Eu ($Z = 63$) nuclei at $\Omega_x = 0.0$ MeV.

Although the model calculations clearly indicate the important role of time-odd mean fields in creating signature separation phenomenon in odd-odd nuclei, the direct comparison with experiment will be complicated by the number of model limitations which are related to

- the presence of residual proton-neutron interaction of unpaired proton and neutron,
- the coupling scheme of angular momenta vectors of unpaired proton and neutron at low spin.

In odd-odd nuclei the angular momenta of unpaired proton and unpaired neutron in 2-quasiparticle configurations can be coupled either in parallel or antiparallel fashion, namely into $K_> = \Omega_p + \Omega_n$, and $K_< = |\Omega_p - \Omega_n|$, where $\Omega_{p(n)}$ represents the projection of single quasiparticle angular momentum of proton (neutron) on the axis of symmetry. For example, in ^{158}Eu this will lead to rotational sequences with $K_< = 0$ and $K_> = 5$. The

degeneracy of the bandheads of the $K_{><}$ doublet pair (called Gallagher-Moszkowski doublet [161]) is lifted by inclusion of the residual proton-neutron interaction and also by the zero-point rotational energy. Relative energy ordering of the $K_{>}$ and $K_{<}$ bands is determined by the empirical Gallagher-Moszkowski (GM) rule which places the spin-parallel band lower in energy than its spin-antiparallel counterpart [161] in odd-odd nuclei (and vise versa in even-even nuclei [184]) and has only few exceptions [162, 185]. Another important consequence of the residual interaction of unpaired nucleons is the observed shift of the odd- and even-spin rotational levels relative to each other in the $K = 0$ bands; this feature is generally referred to as the Newby or odd-even shift [186].

Residual proton-neutron interaction of unpaired nucleons is neglected in the cranking models; we are not aware about any publication which includes it. So, neither Gallagher-Moszkowski splittings nor Newby shifts can be described in the current calculations. It is also necessary to recognize that 2-quasiparticle configurations in odd-odd and even-even nuclei show a daunting complexity due to the high density of states and the large number of couplings and interactions possible. The problem of the description of the Gallagher-Moszkowski splittings and Newby shifts is far from being settled even in the framework of conventional particle+rotor model [162, 185, 187, 188, 184]. For example, the residual interaction of unpaired proton and neutron in odd-odd nuclei shows pronounced dependence on the mass region under study [162, 185]. It is even more difficult to understand why in 2-quasiparticle configurations of the rare-earth region different residual interactions are required to describe the interaction between unpaired proton and neutron in odd-odd nuclei and between unpaired protons (neutrons) in even-even nuclei [184] despite the

expectations that they should be the same due to isospin symmetry. To our knowledge, self-consistent description of Gallagher-Moszkowski splittings and Newby shifts has been attempted only in the framework of the rotor+two-quasiparticle model based on Skyrme Hartree+Fock approach in Ref. [189].

At zero rotational frequency the angular momenta of odd proton and odd neutron are aligned (parallel or anti-parallel) with the symmetry axis which leads to band-head states with $K_> = \Omega_p + \Omega_n$ and $K_< = |\Omega_p - \Omega_n|$. However, in one-dimensional cranking approximation nuclear configuration on top of which rotational sequence is built does not depend on coupling of Ω_p and Ω_n. This is well known (although seldom stressed) deficiency of one-dimensional cranking approximation. However, with increasing rotational frequency the angular momenta of odd proton and odd neutron start to align with the axis of rotation which is perpendicular to the axis of symmetry. Although it is tempting to employ tilted axis cranking (TAC) approximation for the description of the combination of these two angular momenta coupling schemes at low spin, this does not resolve the problem of the description of signature separation since signature is no longer good quantum number in the TAC approximation [190]. On the contrary, one-dimensional cranking approximation used in the current manuscript has a clear advantage that it properly accounts for the alignments of valence particles and holes along the axis of rotation at medium and high spins where $I \geq K$ [182], and thus provides correct description of signature separation at these spins.

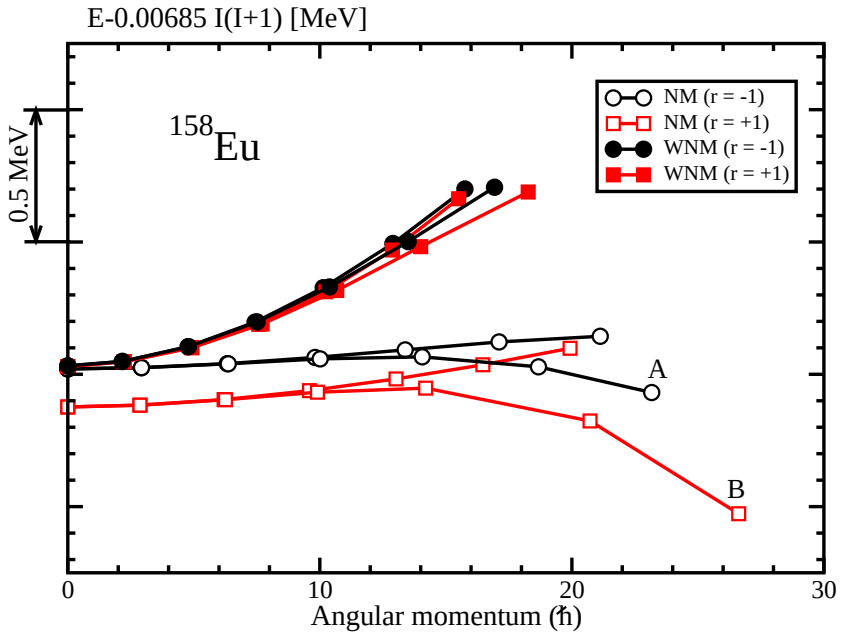

Figure 4.33

Energies of calculated bands in ^{158}Eu based on the $\pi[532]5/2^{\pm} \otimes \nu[642]5/2^{\pm}$.

CHAPTER 5

FISSION BARRIERS IN ACTINIDES AND SUPERHEAVY NUCLEI

The progress in the study of the fission barriers within CDFT has been slower than in its non-relativistic counterparts. Inner fission barriers in several nuclei have been calculated in the axially symmetric relativistic mean field (RMF) + BCS approach in Refs. [191, 90, 192, 193, 194]. However, these investigations employ the constant gap approximation in the BCS part. The recent study of pairing schemes used for the calculations of fission barriers clearly shows that this approximation leads to unphysical results for the fission barriers [195]. Thus, the results of these works have to be treated with a caution. Fission barriers have also been studied in axially symmetric RMF calculations within the BCS approximation using an effective density-dependent zero-range force in the pairing channel; this force represents a much more realistic approximation for pairing [195]. Recently also relativistic Hartree-Bogoliubov (RHB) calculations with the Gogny force D1S and with δ-forces in the pairing channel have been carried out [195] for a study of fission barriers with axial symmetry.

Unfortunately, axially symmetric calculations cannot be directly compared with experimental data since, as has been shown in non-relativistic calculations [43, 44], the lowering of fission barriers due to triaxiality is significant and can reach 3-4 MeV in some nuclei. At present, no systematic studies of the effects of triaxial degrees of freedom on the height of

inner fission barriers are available in the covariant density functional theory; this degree of freedom has only been studied in specific nuclei such as ^{264}Hs [52] and ^{240}Pu [10] within the RMF+BCS approach as well as ^{240}Pu [197] within the RHB approach. Thus, the main goal of the current manuscript is to perform a systematic investigation of the inner fission barriers within the triaxial RMF+BCS approach, and for the first time to confront these important experimental quantities with CDFT in a systematic way.

This chapter is organized as follows. The treatment of pairing strength is discussed in Sec. 5.1. Sec. 5.2 is devoted to the analysis of the effects of the truncation of the basis in the particle-hole channel of the model. Truncation effects in the pairing channel are considered in Sec. 5.3. The results of the calculation of the fission barriers, the role of triaxiality and the comparison with experiment are discussed in Sec. 5.4. Finally, in Sec. 5.6, we report on calculations with others relativistic parameter sets based on density dependent coupling constants.

5.1 Pairing strength

In Ref. [198] empirical pairing gap parameters

$$\Delta_n^{emp} = \frac{4.8}{N^{1/3}} \ \mathrm{MeV}, \qquad \Delta_p^{emp} = \frac{4.8}{Z^{1/3}} \ \mathrm{MeV} \tag{5.1}$$

have been determined by the systematic fit to experimental data on neutron and proton gaps in the normal deformed minimum.

These empirical gap parameters form the basis for the definition of the strength parameters G_τ in the current manuscript. Two procedures have been used: a) In the analysis of different truncation (Sec. 5.2) and pairing schemes (Sec. 5.3), the values $G_n(Z,N)$ and

$G_p(Z,N)$ are defined for each nucleus with neutron and proton number N and Z under study from the requirement that, in the normal deformed minimum, the calculated pairing gaps coincide with the empirical values. b) In the systematic calculations of potential energy surfaces and fission barriers in actinides the same procedure is used first for all even-even nuclei in the $Z = 90 - 100$ and $N - Z = 42 - 66$ ranges resulting in a set of the strengths $G_n(Z,N)$ and $G_p(Z,N)$. Then, the following expressions [199]

$$A \cdot G_n = G_1^n - G_2^n \frac{N-Z}{A} \quad \text{MeV} \tag{5.2}$$

$$A \cdot G_p = G_1^p + G_2^p \frac{N-Z}{A} \quad \text{MeV} \tag{5.3}$$

are used in the calculations. The parameters G_1^n, G_2^n, G_1^p and G_2^p are defined by the least square fit to the set of the $G_n(Z,N)$ and $G_p(Z,N)$. Their values depend on the parameter set of the Lagrangian and they are given in Table 5.1. In this way we have strength parameters for the effective pairing interaction depending in a smooth way on the neutron and proton numbers and, because of the changing level density, the gap parameters derived from those values show fluctuations as a function of the particle numbers.

Table 5.1

The pairing strength parameters [in MeV], $E_{\text{cutoff}} = 120$ MeV for actinides.

Force	G_1^n	G_2^n	G_1^p	G_2^p
NL3*	9.1	6.4	8.1	10.0
DD-PC1	9.2	5.4	8.0	11.4
DD-ME2	9.2	5.8	8.1	11.2

Table 5.2

The same as Table. 5.1 but for superheavy niclei

Force	G_1^n	G_2^n	G_1^p	G_2^p
NL3*	10.7	-10.4	7.40	18.9
DD-PC1	10.5	-7.38	7.5	19.2
DD-ME2	11.0	-10.3	7.9	17.0

Correlations beyond mean field can influence the calculated values of fission barrier height and the excitation energies of the superdeformed minima associated with the fission isomer [200]. The inclusion of rotational correlations can be performed by a symmetry restoration (angular momentum projection) and that of vibrations by a mixing of mean field states corresponding to different shapes by the method of generator coordinates (GCM). So far such an investigation has been performed only for ^{240}Pu within the generator coordinate method based on Skyrme DFT under the restriction to axially symmetric shapes [200]. It was found that compared to the ground state, angular momentum projection lowers the (axial) inner barrier by about 0.6 MeV and the fission isomer by about 1 MeV. In addition, it was found in Ref. [200] that the schematic rotational correction based on the Belyaev moment of inertia [201] frequently used in the literature gives a reduction of the fission barrier height which is appreciably larger than the one due to angular momentum projection. Based on these results, no rotational corrections are taken into account in our calculations. A similar approach has been used in the very successful calculations of Ref. [49].

5.2 Truncation effects in the particle-hole channel

The RMF+BCS equations are solved in the basis of an anisotropic three-dimensional harmonic oscillator in Cartesian coordinates characterized by the deformation parameters β_0 and γ_0 and the oscillator frequency $\hbar\omega_0 = 41A^{-1/3}$ MeV (see Refs. [66, 20] for details). The deformation parameters of the oscillator basis β_0 and γ_0 are selected to be close to expected values β_2 and γ of constrained solution; this improves the convergence and minimizes the computational time. The truncation of the basis is performed in such a way that all states belonging to the shells up to N_F fermionic shells and N_B bosonic shells are taken into account. The computational time increases considerably with the increase of N_F but it is much less dependent on N_B. Thus, special attention has been paid to the selection of N_F of the basis to be chosen for a systematic study of fission barriers for the nuclei of interest, which provides at the same time a reasonable numerical accuracy in the predictions of the physical observables.

The selection of the truncation scheme was guided by the detailed analysis of the convergence performed in axially symmetric RMF+BCS and RHB calculations of Ref. [195]. In this reference, extensive tests of numerical convergence have been performed in the spherical, normal-deformed and superdeformed ($\beta_2 \sim 0.7 - 1.0$) minima in the RMF calculations without pairing on the example of the nuclei ^{238}U and $^{304}120$ with $Z = 120$ and $N = 184$. Contrary to the previous studies of the convergence in the RMF framework which were based on the comparison of the N_F and $N_F + 2$ results, the "exact" solution (extending the calculations up to $N_F = 36, N_B = 36$) has been defined. Then it was shown that the binding energies and inner fission barriers for $N_F = 20$ and $N_B = 20$ were

described with an accuracy of approximately 200 keV and 100 keV, respectively, as compared with the exact solution. Therefore, the systematic calculations have been carried out with $N_F = 20$ and $N_B = 20$. This selection of the basis is in line with our previous convergence tests in different mass regions (see the discussion in Ch. 3) which clearly show that at large deformations full convergence of the binding energies is reached at larger values of N_F than at lower deformations. In addition, they show that larger sizes of the basis (larger N_F and N_B values) are needed for the nuclei with larger proton Z and neutron N numbers (see Refs. [70, 20]).

Of course, as long as the same number of fermionic shells N_F and the same deformation of the basis β_0 is used, calculations with the axial code should give identical results to those obtained with the triaxial code at $\gamma = 0^\circ$. In fact for nuclei under study we find agreement with an accuracy of approximately 50 keV throughout the deformation range of interest, which is caused by small differences in the mesh points of the Gaussian integrations for the matrix elements. As a result for axially symmetric shapes, the fission barrier heights which depend on the relative energies of the saddle point and normal deformed minimum differ by less than 50 keV in these two calculations.

Extensive convergence tests in axially symmetric Skyrme-Hartree-Fock calculations also show that a similar size of the basis is needed (see Sec. IIB in Ref. [110] for more details). The comparison of these convergence tests suggests that there is no big difference in the convergence of total energies as a function of the size of basis in the relativistic and non-relativistic approaches.

Because the fermionic basis contains large and small components of the Dirac spinor, the diagonalization of the Dirac equation is by a factor of approximately 8 more time consuming than the corresponding Schrödinger equation in the non-relativistic case. As a consequence, triaxial RMF+BCS calculations are more computationally demanding than the ones performed in the triaxial Skyrme EDF with BCS approximation of Ref. [43]. This is also a reason why we treat the pairing channel in the present triaxial RMF calculations in the BCS approximation despite the fact that triaxial cranked Relativistic Hartree+Bogoliubov approach has been developed in the end of nineties [196, 131, 166] and successfully applied to the description of rotational structures in the pairing regime in different mass regions [196, 131, 39, 69, 166]. The RMF+BCS calculations are less time-consuming than the RHB calculations. In addition, as follows from our experience of the calculations in axially deformed RMF+BCS and RHB codes [195], the RMF+BCS calculations are more stable (especially, in the saddle point region) than the RHB calculations.

5.3 Truncation effects in the pairing channel

It is rather customary to analyze the dependence of total binding energies (or other physical observables) on the truncation of basis (see Sec. 5.2). However, we were not able to find any detailed investigation where the impact of the size of the oscillator basis on the parameters of pairing in the BCS framework has been discussed in detail. Thus, we studied the dependence of the strength of the pairing interaction on the number N_F of fermionic shells under the condition that the proton and neutron pairing gaps in the normal deformed minimum are fixed for all values of N_F and cut-off energies $E_{\rm cutoff}$.

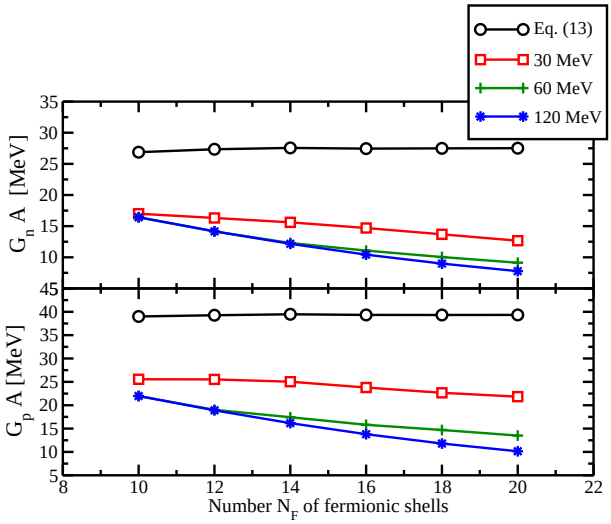

Figure 5.1

Neutron and proton pairing strengths.

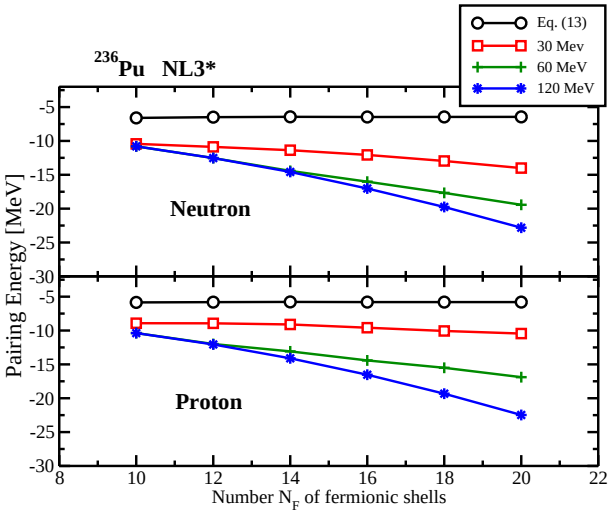

Figure 5.2

Neutron and proton pairing energies in the normal deformed minimum.

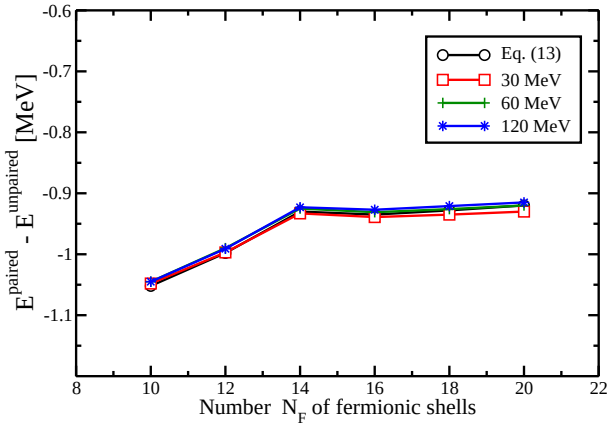

Figure 5.3

The dependence of additional binding due to pairing on N_F.

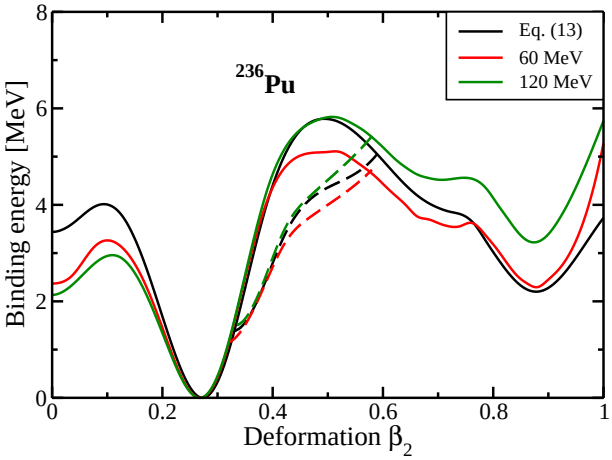

Figure 5.4

The fission barrier in ^{236}Pu. Solid (axial) line and dashed(triaxial) line.

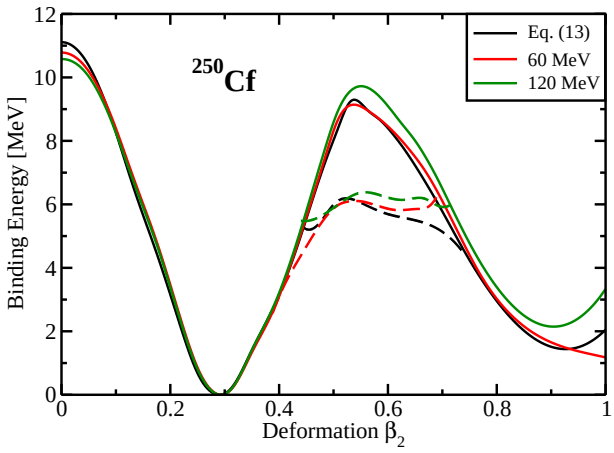

Figure 5.5

The same as in Fig. 5.4 but for ^{250}Cf.

RMF+BCS calculations in the normal-deformed minimum have been performed with several values of the cut-off energy $E_{\rm cutoff}$ in Eq. (2.47), namely $E_{\rm cutoff} = 30$, 60, and 120 MeV. In addition, the prescription of Ref. [202] (indicated as "Eq. (5.4)" in the figures) has been used. This prescription introduces smooth energy-dependent cut-off weights [203]

$$f_k = \frac{1}{1 + \exp[(\epsilon_k - \lambda_\tau - \Delta E_\tau)/\mu_\tau]} \tag{5.4}$$

for the evaluation of the local pair density. In this equation, ϵ_k are the eigenvalues of the Dirac equation and the chemical potentials λ_τ of the proton ($\tau = p$) or neutron ($\tau = n$) subsystems are determined by the particle numbers N_τ. The cut-off parameters ΔE_τ and $\mu_\tau = \Delta E_\tau/10$ are chosen self-adjusting to the actual level density in the vicinity of the Fermi energy. ΔE_τ is fixed from the condition that the sum of the cut-off weights includes approximately one additional shell of single-particle states above the Fermi surface

$$\sum_{k\in\Omega_\tau} f_k = N_\tau + 1.65\, N_\tau^{2/3} \quad . \tag{5.5}$$

In Eq. (5.5), Ω_τ denotes the single-particle space used in the calculations.

Figures 5.1, 5.2 and 5.3 summarize the results of this study for the normal-deformed ground state in ^{236}Pu. One can see in Fig. 5.1 that the strengths of the pairing interaction depends not only on the cut-off energy $E_{\rm cutoff}$ but also on the number N_F of fermionic shells employed in the calculations. This dependence is very weak for the prescription of Ref. [202] because here the effective pairing window is quite small being around 7 MeV. On the other hand, the dependence of the pairing strength on N_F increases with the increase of $E_{\rm cutoff}$. This can be understood in the following way: an increase of N_F brings more single-particle states into the pairing window thus effectively requiring the decrease of pairing strength in order to keep the pairing gap fixed. This effect becomes more pronounced for larger pairing windows, which explains the steeper decrease of the pairing strength as a function of N_F with increasing $E_{\rm cutoff}$.

The dependence of proton and neutron pairing energies $E^p_{\rm pair}$ and $E^n_{\rm pair}$ on the cut-off energy $E_{\rm cutoff}$ and on the number N_F of fermionic shells employed in the calculations is shown in Fig. 5.2. These energies depend only weakly on N_F in the case of prescription of Ref. [202] because of the small effective pairing window. However, similar to the pairing strengths the dependence of pairing energies on N_F increases significantly with increasing $E_{\rm cutoff}$. The origin of this feature is the same as in the case of the pairing strengths; it is discussed above.

Note, however, that the dramatic changes in the pairing energy cannot be seen directly in the change of the energy, because they are compensated to some extent by the fact that larger pairing seen in pairing energies causes a wider distribution of the occupation

probabilities v_k^2 around the Fermi surface. Therefore, we study in Fig. 5.3 the energy difference between the binding energies $E^{\rm pair} - E^{\rm unpair}$ obtained in two self-consistent calculations with and without pairing. It turns out that for $N_F \geq 14$ this difference, that reflects the real physical impact of pairing, is smaller than 1 MeV and it does neither depend on the cut-off energy $E_{\rm cutoff}$ nor on the value of N_F. Somewhat different values of $E^{\rm pair} - E^{\rm unpair}$ at lower N_F values are due to the fact that at these values of N_F the effects of the truncation of basis in the particle-hole channel have not been eliminated (see Sect. 5.2 for detail).

In Figs. 5.4 and 5.5 we compare the deformation energy curves for three different pairing schemes for the nuclei ^{236}Pu and ^{250}Cf. The deformation energy curve for the axially symmetric solution is obtained as the $\gamma = 0^\circ$ cross-section of the potential energy surface. The deformation energy curve for the triaxial solution is obtained by the minimization of potential energy surface along the β_2-direction. We show the deformation energy curve for the triaxial solution only in the range of β_2 values where it is lower in energy than the deformation energy curve of the axially symmetric solution. Note that the potential energy surfaces are normalized to zero at the normal-deformed minimum. As discussed in Ref. [195] we can see that these different schemes predict somewhat different fission barriers. In the systematic calculations presented in the following sections, we use the cut-off energy $E_{\rm cutoff} = 120$ MeV. The selection of this value is based on the results of Ref. [195], where it was shown that the difference in the height of fission barriers obtained in the RHB calculations with finite range D1S Gogny force and zero-range δ-force is minimal when the cut-off energy $E_{\rm cutoff} = 120$ MeV is used (see Fig. 6 in Ref. [195]).

5.4 Fission barriers in actinides

In this section we carry out a systematic investigation of fission barriers of even-even nuclei in the actinide region based on the parameter set NL3* and the pairing strength parameters given in Table 5.1. In Fig. 5.6 we show as an example the potential energy surface of the nucleus ^{240}Pu in the β-γ plane. For axial symmetry we find the normal deformed minimum of the ground state at a deformation $\beta \sim 0.28$, a maximum at $\beta \sim 0.52$ and a superdeformed minimum at $\beta \sim 0.96$. We observe that the fission path (the part of blue dashed line between normal and superdeformed minima) bypasses the axial barrier between the normal and superdeformed minima. The barrier height is determined by the maximum of the energy along this fission path. The deformation energy curves

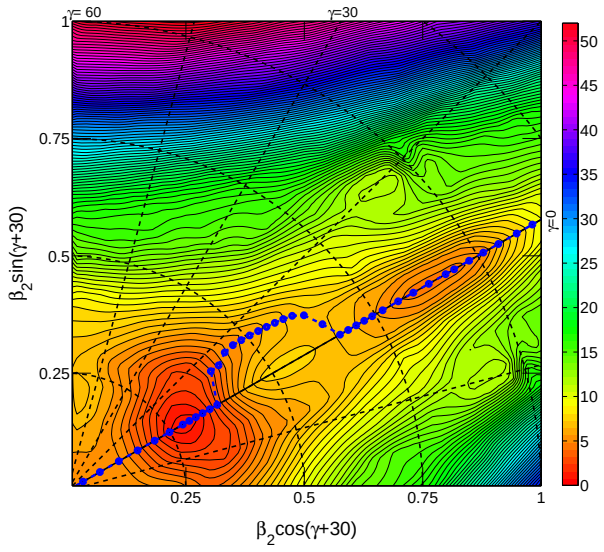

Figure 5.6

Potential energy surface in ^{240}Pu. Equipotential lines are seprated by 0.5 MeV.

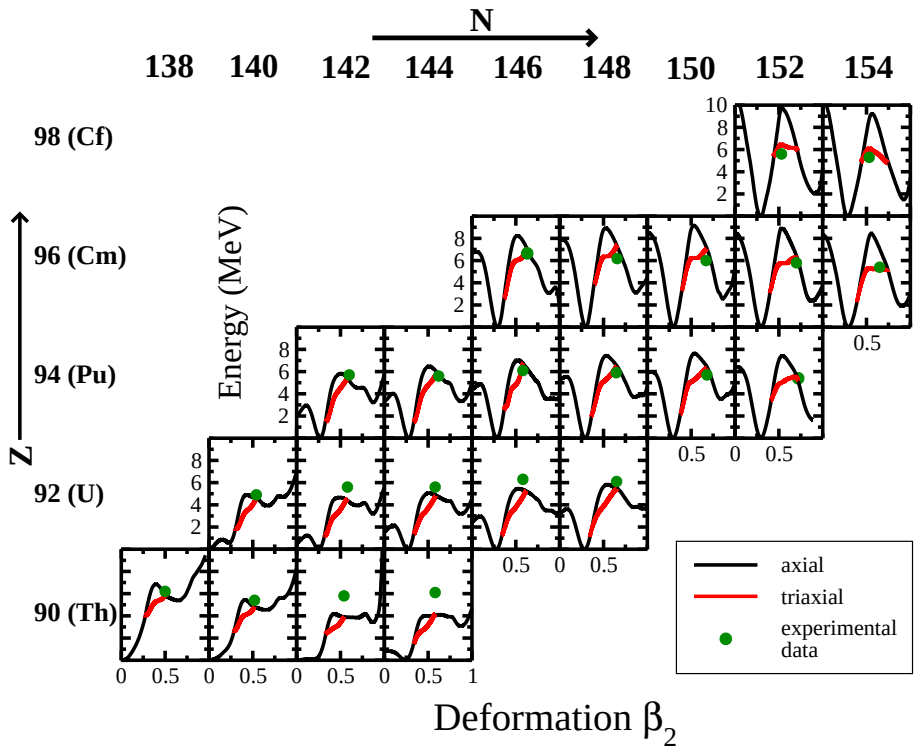

Figure 5.7

Deformation energy curves of actinide nuclei with NL3* parameterization.

for other even-even nuclei in this region obtained in these calculations are shown in Fig. 5.13. Full black lines show axially symmetric solutions, while we show the values of the deformation energy curves along the triaxial fission path by red full curves. One can see that by allowing for triaxial deformation the fission barrier heights are reduced by $1-4$ MeV as compared with axially symmetric solutions. This lowering depends on the proton and neutron numbers. It also brings in average the results of the calculations in closer agreement with experimental data shown by green solid circles in Fig. 5.13. These circles display the height of the experimental fission barrier at the calculated β-deformation of

the saddle point. The calculated γ-deformations of the triaxial parts of the fission path are shown in Fig. 5.8. On average they are close to 10°. The microscopic origin of the lowering of the barrier due to triaxiality can be traced back to the changes of the level density in the vicinity of the Fermi level induced by triaxiality. Fig. 5.9 shows the Nilsson diagrams for protons and neutrons for the axially symmetric solution in ^{242}Pu. The blue boxes in these diagrams define the deformation and energy ranges in which the axially symmetric and triaxial solutions are compared in Fig. 5.10. The lower (upper) deformation in these boxes corresponds to the deformation range over which the triaxial solution (red curve in Fig. 5.13) is lower in energy than the corresponding axially symmetric solution (black curve in Fig. 5.13). The lower and upper energy values in these boxes are defined approximately as $\varepsilon_{\mathrm{F}} \pm 3$ MeV.

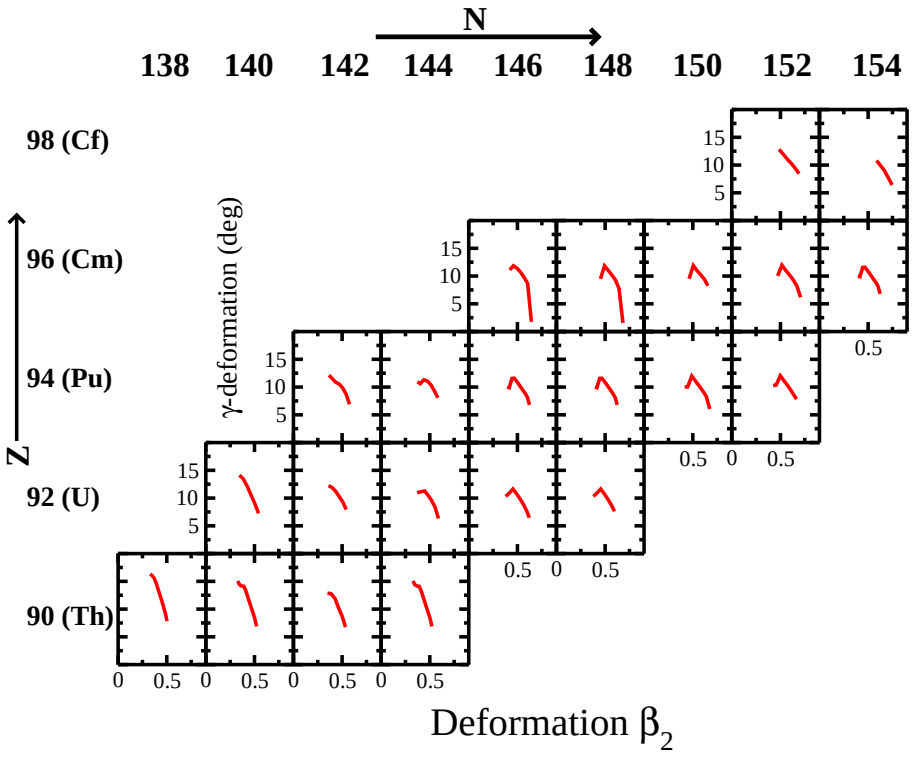

Figure 5.8

The γ-deformations of the calculations shown by red lines in Fig. 5.7.

Proton and neutron single-particle energies within these deformation and energy ranges are shown for axially symmetric and triaxial solutions in Fig. 5.10. One can see that the single-particle level density at the Fermi level is lower for triaxial solutions than for axially symmetric solutions. This is especially clear at the deformation corresponding to the saddle point of the axially symmetric solution (indicated by vertical dotted blue lines in Fig. 5.10) which correspond to a maximal level density and maximal pairing correlations. A lowering of the level density at the Fermi surface leads to a more negative shell correction energy (as compared with axially symmetric solution), and, as a consequence, to a lower fission barrier. This is in agreement with the analysis of Ref. [47] which also attributes the lowering of the inner fission barrier due to triaxiality to microscopic (shell correction) part of the macroscopic+microscopic model. A similar mechanism is responsible for the lowering of the asymmetric saddle with respect to symmetric saddle at outer fission barrier (see Sect. VI in Ref. [49]).

Figures 5.11 and 5.12 show the differences between calculated and experimental heights of inner fission barriers. The average deviation between theory and experiment is 0.76 MeV. This is comparable with the results obtained in the macroscopic+microscopic method (see Sec. IVC and Fig. 11 in Ref. [48] and Sec. VII A in Ref. [49]) which describe experimental fission barriers with an average error of around 1 MeV.

It is necessary, however, to say that neither proton nor neutron particle number dependences of fission barrier height are completely reproduced in these calculations. This is clearly seen in Figs. 5.11 and 5.12. However, the same problem exists also in macroscopic+microscopic calculations (see Fig. 11 in Ref. [48] and Figs. 23-32 in Ref. [49]).

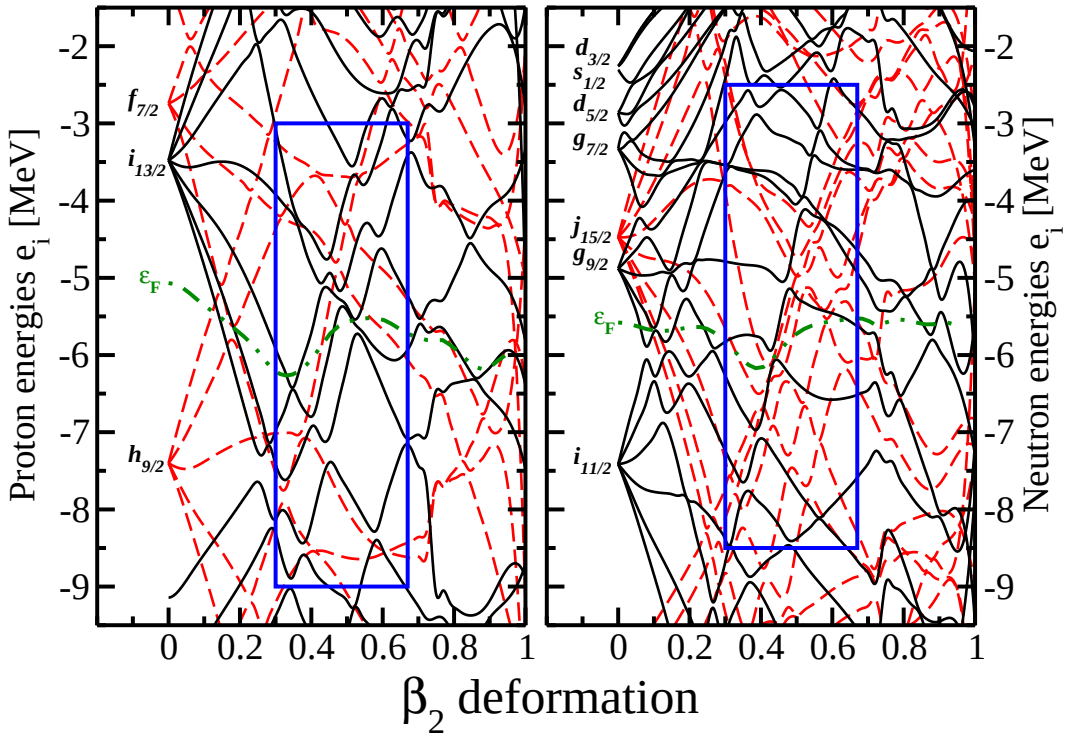

Figure 5.9

The same as Fig. 3.22 but for ^{242}Pu.

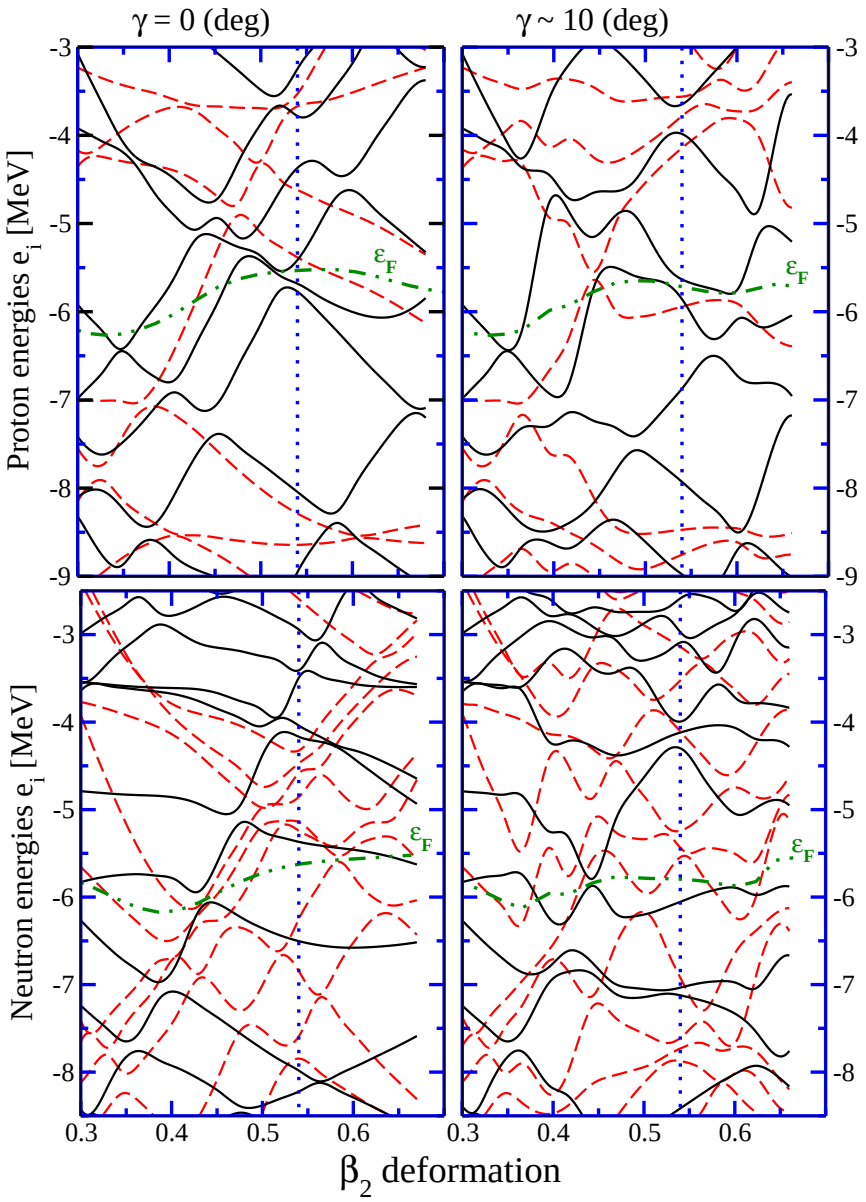

Figure 5.10

A comparison of single-particle energies at axially and triaxial solutions.

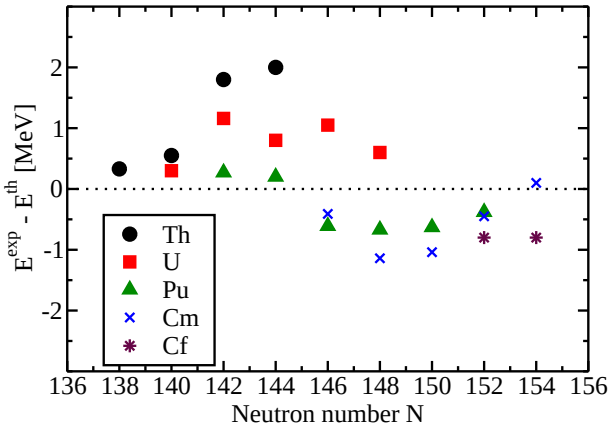

Figure 5.11

E^{exp} - E^{th} of inner fission barriers.

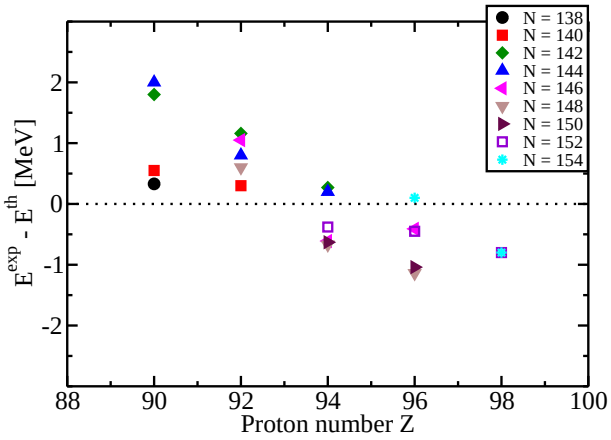

Figure 5.12

The same as in Fig. 5.11 but as a function of proton number Z.

There are very few energy density functional calculations of the fission barriers with triaxiality included, and neither of them confronts in a systematic way experimental data in actinides. However, limited results in the Skyrme EDF presented in Ref. [53] show similar unresolved particle number dependences for the inner fission barrier heights.

5.5 Fission barrires in superheavies

The nucleus ^{292}120 is predicted to be a spherical doubly magic nucleus in CDFT [52, 39]. Its potential energy surface in the $\beta - \gamma$ plane is shown in Fig. 5.6. It is interesting to compare it with the PES of the nucleus ^{240}Pu shown in Fig. 5.6. These two PES's are representative examples of typical PES's in actinides and superheavy nuclei. The gross structure of these two PES's is defined by the fact that the total energy is generally increasing when moving away from the $\gamma = 0^\circ$ axis; so it looks like a canyon. However, there are local structures inside the canyon which define the differences between the two mass regions with respect to the impact of triaxiality on the inner and outer fission barriers.

In ^{240}Pu, a large hill is located at the axial shape $\beta_2 \sim 0.5$ inside a canyon. As a consequence, the fission path from the normal deformed minimum initially proceeds along axially symmetry, then bypasses the axial β_2=0.5 hill via a path with $\gamma \sim 10^\circ$, and then proceeds along the bottom of the canyon on an axially symmetric path. As a result of this bypass, the inner fission barrier heights of the actinides are lowered by $1 - 4$ MeV due to triaxiality. However, the calculated outer fission barriers of the actinides are not affected by triaxiality.

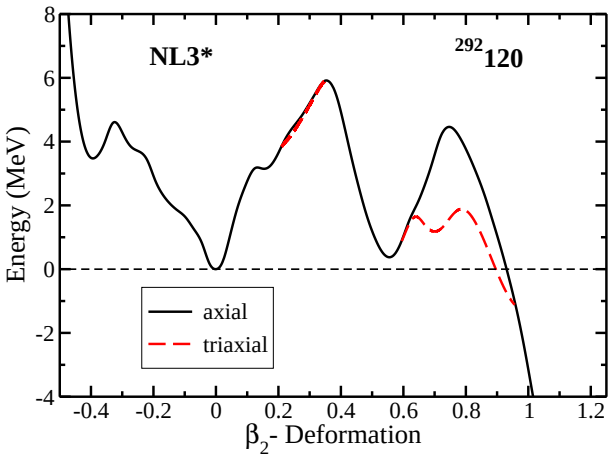

Figure 5.13

The Same as Fig. 5.7 but for the $Z = 120,\ N = 172$ nucleus

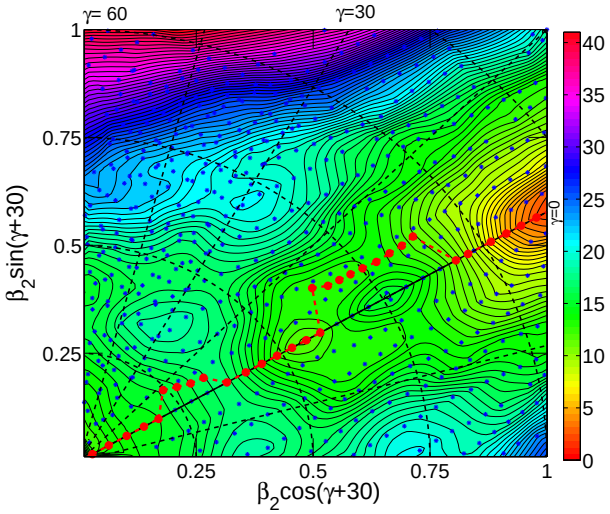

Figure 5.14

The same as in Fig. 5.6 but for $Z = 120, N = 172$ nucleus

The properties of the PES of the nucleus ^{292}120 along the fission path are completely opposite to the case of ^{240}Pu since there are two triaxial and one axial hills inside the PES canyon of ^{292}120. Two triaxial hills are located at moderate deformations ($\beta_2 \sim 0.35,\ \gamma \sim \pm 30°$), while the axial hill is superdeformed ($\beta_2 \sim 0.75$). The fission path (shown by red dashed line with solid circles in Fig. 5.6) starts at a spherical shape, then proceeds between two triaxial hills ($\beta_2 \sim 0.35,\ \gamma \sim$30°) and bypasses the axial hill at $\beta_2 \sim$0.75 via a $\gamma \sim 7°$ path. The γ-softness of the PES, which exists between the two triaxial hills, has only a minor effect on the shoulder of the inner fission barrier; the triaxial solution is lower than the axial one by 100-200 keV at $\beta_2 = 0.2 - 0.3$ deformations (see Fig. 5.7). However, this figure shows that the height of inner fission barrier is not affected by triaxiality. On the contrary, the triaxiality has a considerable impact on the shape and the height of outer fission barrier which is lowered by $\sim$ 3 MeV. Thus, one can conclude that due to the structure of the PES in the fission path valley, we observe in the superheavy region situation opposite to the one in actinide nuclei where the triaxiality has a considerable (no) impact on inner (outer) fission barriers.

Fig. 5.17 shows deformation energy curves for the $Z = 112,\ 114$ and 116 nuclei for the three classes of CDFT models. Experimental estimates of inner fission barrier heights were obtained for these nuclei in Ref. [40]. The potential energy structure of these nuclei is similar to the one seen in ^{292}120 (Fig. 5.6); the only difference is that the ground states are somewhat deformed in these nuclei (see Figs. 5.17 and 5.15b). Thus, similar to the ^{292}120 nucleus the triaxiality does not affect the inner fission barriers. However, it has considerable impact on the shape and height of the outer fission barriers; the decrease of

the heights of the outer fission barriers due to triaxiality is typically in the range of 1.5-2.0 MeV and it depends on particle number and on the RMF parametrization. Note that this decrease reaches 3 MeV in some calculated nuclei not shown in Fig. 5.17.

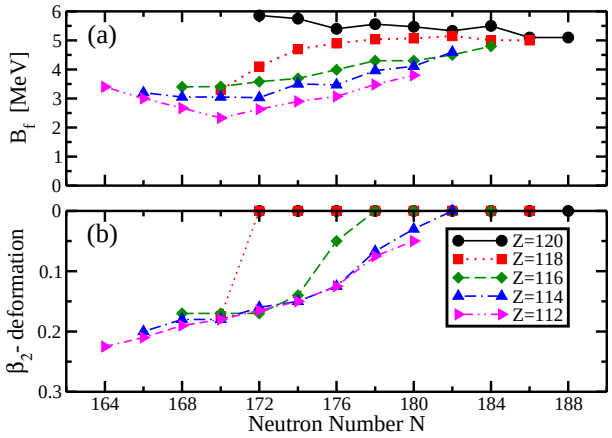

Figure 5.15

The height of inner fission barrier and the deformation of the ground state.

There is only one experimental work [40] in which some estimates on the heights of inner fission barriers in superheavy $Z = 112, 114$ and 116 nuclei have been obtained. Unfortunately, experimentally the fission barriers are accessible only indirectly and a model-dependent analysis is used to obtain these quantities, which causes an ambiguity in the comparison with theoretical results. Even in the actinide region where the fission barrier heights were extracted from a number of independent experiments with high statistics (see, for example, Ref. [49]), a typical uncertainty in the experimental values, as suggested by the differences among various compilations, is of the order of ± 0.5 MeV [110]. These

uncertainties are expected to be higher in superheavy nuclei since the estimates of Ref. [40] are based on experimental data represented by low statistics and on a method which differs from the methods used in the analysis of fission barrier heights in actinides. In addition, there is no independent confirmation of the inner fission barrier height estimates of Ref. [40]. The interpretation of experimental data on cross sections in terms of fission barrier height becomes even more complicated when the fission path has a double hump structure, which according to many calculations may be the case in superheavy nuclei. The widening of the barrier due to the second hump (or its remnant) would require the lowering of the inner fission barrier height; this possibility has not been taken into account in the analysis of Ref. [40]. Based on this discussion it is clear that the level of the confidence of fission barrier height estimates in superheavy nuclei is significantly lower than the one in the actinides.

According to Ref. [40], the estimated lower limits for fission barrier heights in even-even $Z = 112, 114$ and 116 nuclei shown in Fig. 5.17 are 5.5, 6.7 and 6.4 MeV, respectively. Our results for the heights of inner fission barrier in these nuclei are always smaller than the experimental data by $1 - 3$ MeV. Considering the discussion above, it is not clear at this moment how serious this discrepancy is. However, the results of the calculations suggest one possible way to increase the heights of inner fission barriers. Potential energy surfaces in the ground state region of these nuclei are extremely soft (see Fig. 5.17). For such nuclei, the correlations beyond mean field taken, for example, by generator coordinate method can lower the energy of the ground state by a few MeV, thus effectively increasing the height of inner fission barrier.

Systematic calculations of inner fission barriers have been performed for even-even $Z = 112 - 120$ nuclei with $N - Z = 52 - 68$ using the NL3* parametrization. Similar to the earlier discussed nuclei, the triaxiality has no impact on the heights of the inner fission barriers. The evolution of the heights of the inner fission barriers as a function of the neutron number N is shown in Fig. 5.15a.

The $Z = 112, 114$ and 116 isotope chains show the general trend of increasing the barrier height with the increase of the neutron number. Fig. 5.15b suggests that the origin of this trend can be traced back to the deformation of the ground state. At low values of the neutron number, these nuclei are deformed in the ground state. However, they gradually become spherical when approaching $N = 184$ because there is a spherical shell gap at this neutron number (see, for example, Fig. 28 in Ref. [39]). The negative shell correction energy at the ground state is larger in absolute value in the vicinity of the $N = 184$ spherical shell gap than at lower neutron numbers, where the ground state is deformed and characterized by a larger level density in the vicinity of the Fermi level. The level density (and, as a consequence, the shell correction energy) at the saddle point of the inner fission barrier does not change so drastically as the one at the ground state. As a result, the heights of inner fission barriers, which are defined as the energy differences between the binding energies of the ground state and saddle point, show the observed features.

The $Z = 118, 120$ nuclei (with the exception of the $^{288}118$ nucleus) are spherical in the ground state due to the presence of the $Z = 120$ spherical shell gap. Apart of two lightest $Z = 118$ isotopes, the fission barrier heights of the $Z = 118$ isotopes are nearly constant as a function of neutron number and they are close to 5 MeV. The $^{292}120$ nucleus

has the highest value of the fission barrier among studied nuclei, which is connected with its doubly magic nature in CDFT. In the $Z = 120$ isotope chain, moving away from the $N = 172$ shell closure, shell effects at spherical shape become less pronounced which leads to the decrease of the inner fission barrier, the height of which in these nuclei is defined with respect of spherical ground state.

It is interesting to compare current results with the ones obtained in other models. The results of Skyrme DFT calculations of Ref. [54] for the $N = 184$ isotones show that the impact of triaxiality on the inner fission barrier is small in the $Z = 112$ nucleus, but it increases with increasing Z (see Fig. 4 in Ref. [54]). The lowering of the height of the inner fission barrier due to triaxiality is around 2 MeV in the $Z = 120$ nucleus and exceeds 3 MeV in the $Z = 126$ nucleus. In the extended Thomas-Fermi plus Strutinsky integral (ETFSI) model calculations [51] the inner fission barriers are lowered due to triaxiality in the $(Z = 112, N = 182)$ and $(Z = 114, N = 184)$ nuclei by 0.5 and 1.1 MeV, respectively. In the macroscopic+microscopic calculations of Ref. [204] the largest reduction of the inner barrier height due to triaxiality is about 2 MeV and it appear in the region around $Z \approx 122$, $N \approx 180$ (see Fig. 2 in Ref. [204]).

These results are in clear contradiction with the ones obtained for superheavy which do not show the impact of triaxiality on inner fission barriers. However, this feature is not surprising. As mentioned in the previous Sec. 5.4, the reduction of inner fission barrier height due to triaxiality is caused by the level densities in the vicinity of the Fermi level which are lower at triaxial shape as compared with axial one. As a consequence, shell correction energies are more negative at triaxial shapes which leads to the fission

path along $\gamma \sim 10^{\circ}$ bypassing the axial saddle. However, the different location of the "magic" shell gaps in superheavy nuclei in non-relativistic (at $Z = 114, N = 184$ in macroscopic+microscopic method and predominantly at $Z = 126, N = 184$ in Skyrme DFT) and CDFT (at $Z = 120, N = 172$) results in deformed single-particle structures at the deformations typical for the saddle of the inner fission barrier and particle numbers under study which favor (disfavor) triaxiality near the saddle in non-relativistic (relativistic) theories.

Our calculations indicate that triaxiality plays an important role at the outer fission barriers. Usually, the triaxiality of these barriers is not mentioned in the publications. To our knowledge, it is only Ref. [48] which states that in actinides the non-axial degree of freedom plays an important role in the description of outer fission barriers.

As discussed above, the reduction of inner fission barrier due to triaxiality depends on the underlying single-particle structure in the vicinity of the Fermi level at the deformations of the first saddle. This structure depends only weakly (through deformation changes) on the pairing model. This suggests that the change of the pairing model (BCS to RHB) or the type of pairing (constant G or zero-range δ-force to finite range Gogny force) would not significantly affect our conclusions with respect of the impact of triaxiality on the heights of inner fission barriers. Thus, already published studies within the axially symmetric RMF+BCS model with δ-pairing [205] and axially symmetric relativistic Hartree-Bogoliubov calculations with the finite-range Gogny D1S force in pairing channel of Ref. [195] should remain valid. The inner fission barrier heights of the nuclei, for which experimental estimates exist [40], obtained with the NL3 parametrization

in the RMF+BCS [205] and RHB [195] calculations are by approximately 0.5 and 1.0 MeV higher than our results. Note that the inner fission barrier heights are always higher in the models employing a pairing interaction of finite range than in those based on zero-range δ-pairing (see Ref. [195] for details). Only RHB calculations with the DD-ME2 parametrization give inner fission barriers the heights of which are close to the estimates of Ref. [40]. However, a comparative analysis of the results of Sec. 5.4 and [195] suggests that this parametrization will systematically overestimate the fission barriers in actinides by $1-2$ MeV.

One should note, however, that our results for outer fission barriers should be taken with care since it is known that reflection-asymmetric (octupole deformed) shapes become important at the deformations corresponding to second fission barrier and beyond it (see Refs. [43, 49] and reference therein). However, dependent on particle number triaxial reflection symmetric shapes may compete in this region with axially symmetric reflection asymmetric shapes. Our results suggest that in some superheavy nuclei the combination of two deformations (triaxiality and odd-multipole deformations) may be important in the definition of the fission path at $\beta_2 \geq 0.5$. The CDFT calculations with both deformations included are at present not yet possible, but require further investigations.

5.6 Results for the parameter sets DD-ME2 and DD-PC1

In order to investigate to what extent our results depend on the density functional under investigation we performed also an analysis of the fission barriers of the two nuclei ^{240}Pu and ^{236}U using the parameter sets DD-ME2 [59] and DD-PC1 [65]. The first is a

representative of the class of the RMF models [58, 59] where the nucleus is described as a system of Dirac nucleons interacting via the exchange of mesons with finite masses leading to interactions of finite range. An explicit density dependence for the meson-nucleon vertices is used. The DD-PC1 parameterization belongs to the class of the RMF models in which the finite-range meson exchange is replaced by zero-range interactions with density dependent coupling constants and derivative terms [206, 207, 65].

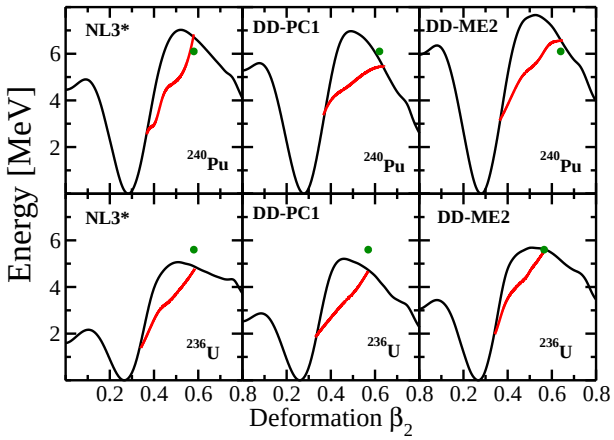

Figure 5.16

The same as in Fig. 5.7 but for fission barriers in ^{240}Pu and ^{236}U.

In Fig. 5.16 we compare the deformation energy curves of ^{240}Pu and ^{236}U obtained in the calculations with the three parameter sets NL3*, DD-PC1 and DD-ME2 of the RMF Lagrangian. Although there are some differences between the deformation energy curves obtained in the calculations with different parameterizations, in general, they show

the same features. In addition, calculated fission barrier heights reasonably agree with experimental data.

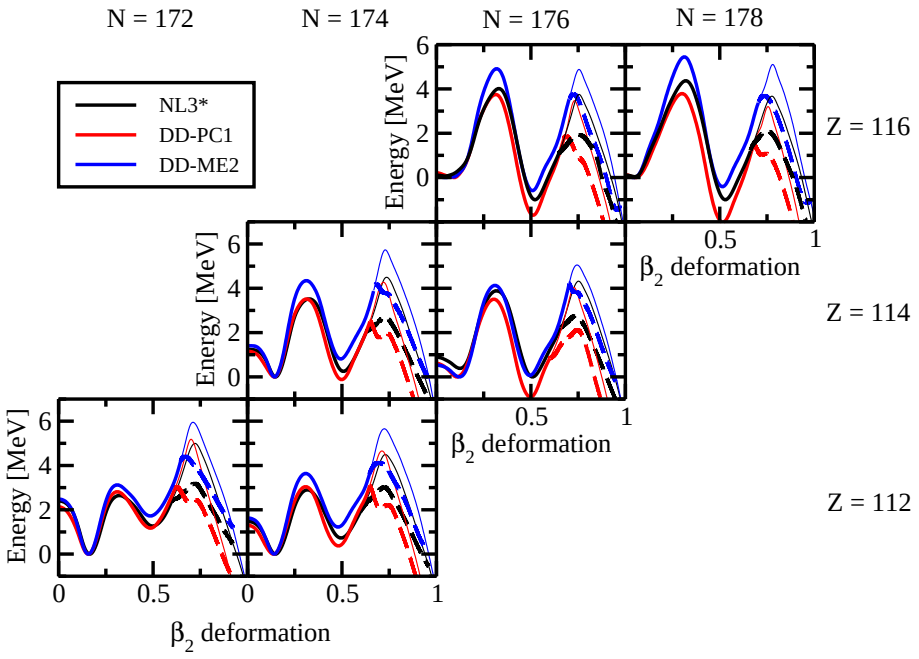

Figure 5.17

Deformation energy curves for the $Z = 112, 114$ and 116 nuclei.

Fig. 5.17 shows deformation energy curves for the $Z = 112, 114$ and 116 nuclei for three classes of the CDFT models. In Fig. 5.17 solid lines display the deformation energy curves for the axially symmetric solutions, while dashed lines the deformation energy curves along the triaxial part of the fission path. Thick lines are used for the lowest in energy solutions, while thin solid lines show the axially symmetric solutions in the deformation range in which the triaxial solutions are lower in energy. Experimental estimates of inner fission barrier heights were obtained for these nuclei in Ref. [40]. The potential energy structure of these nuclei are similar to the one seen in $^{292}120$ (Fig. 5.14); the only difference is that the ground states are somewhat deformed in these nuclei (see Figs. 5.17 and 5.15b). Thus, similar to the $^{292}120$ nucleus the triaxiality does not affect inner fission barrier. However, it has considerable impact on the shape and height of outer fission barrier; the decrease of outer fission barrier due to triaxiality is typically in range 1.5-2.0 MeV and it depends on particle number and on the RMF parametrization.

Among different classes of the CDFT models, the DD-ME2 parametrization always gives the highest values of inner and outer fission barrier heights which are (in average) by 1 and 1.5 MeV higher than the ones obtained in the NL3* and DD-PC1 parametrizations. With the exception of the $(Z = 116, N = 178)$ and $(Z = 114, N = 176)$ nuclei, the heights and the shapes of inner fission barriers are similar in the NL3* and DD-PC1 parametrizations. The outer fission barriers also come close to each other in these two parametrizations; they differ substantially from the ones obtained in the DD-ME2 parametrization.

CHAPTER 6

CONCLUSION

In this dissertation, covariant density functional theory (CDFT) has been successfully applied to describe and explain several physical phenomena that are of interest to the nuclear physics community. These phenomena are studied for the first time in a systematic manner in the frame work of CDFT.

6.1 Super- and hyperdeformation at high spin

Super- and hyperdeformation at high spin was studied in a systematic way within the framework of a fully self-consistent: the cranking relativistic mean field theory in Ch. 3. Recently observed excited super-deformed (SD) bands in ^{154}Dy were interpreted within this theor. The high-*N* intruder configuration $\pi 6^4 \nu 7^2$ was suggested for SD1 band, while $\pi 6^4 \nu 7^3$ was suggested for SD3, SD5, and SD6 bands at frequencies above $\hbar\omega \sim 0.5$ MeV. The rise of dynamic moment of inertia with increasing rotational frequency, seen in bands SD2 and SD4, may indicate the presence of pairing and of band crossings. Those features cannot be addressed in the current calculations within the unpaired formalism. The study of hyperdeformation (HD) covers even-even nuclei in the $Z = 40 - 58$ part of nuclear chart. In this study, the crossing spins I_{cr}^{HD}, at which the HD configurations become yrast, were calculated and found to be lower for proton-rich nuclei. This is a feature seen in the

most of studied isotope chains; by going from the β-stability valley towards the proton-drip line one can lower I_{cr}^{HD} by approximately $10\hbar$. Near these spins (the crossings spins) the density of the HD bands is high in the majority of the cases. For such densities, the feeding intensity of an individual HD band will most likely drop below the observational limit of modern experimental facilities. The physics of hyperdeformation at high spin is also defined by the fission barriers; the competition with fission certainly makes the population of the HD states difficult. The stability of the HD minimum is defined by its depth, the fission barrier height and the height of the barrier between the HD and normal-deformed/superdeformed minima [21, 97]. The results obtained in Ch.3 clearly indicate that the HD minimum is localized in the potential energy surface.

Our calculations indicate Cd isotopes (see Sect. 3.3.5 for details) as the best candidates for the search of discrete HD bands. Our analysis for these isotopes indicates ^{96}Cd as a doubly magic HD nucleus in this part of nuclear chart; its magicity is due to large $Z = 48$ and $N = 48$ HD shell gaps. However, experimental study of HD in this nucleus is problematic with existing facilities due to its $N = Z$ status. The low density of the neutron single-particle states in the vicinity of the $N = 59$ and 61 HD shell gaps and sizable $Z = 48$ HD shell gap lead to appreciable gaps between the yrast and excited HD bands in $^{107-109}$Cd nuclei, thus offering better opportunities to observe discrete HD bands. Among these three nuclei, the best candidate for observing the discrete HD bands with existing facilities is ^{107}Cd nucleus. The microscopic+macroscopic (MM) calculations of Refs. [86, 97] indicate that the fission barriers are sufficiently large in the nuclei around ^{108}Cd so that the HD minimum could survive fission for a significant range of angular

momentum. An alternative candidate is the doubly magic extremely superdeformed band in ^{111}I, the deformation of which is only slightly lower than that of the HD bands, and which may be observed with existing experimental facilities.

This high density of the HD bands will most likely favor the observation of the rotational patterns in the form of ridge-structures in three-dimensional rotational mapped spectra. The study of these patterns as a function of proton and neutron numbers, which seems to be possible with existing facilities, will provide a valuable information about hyperdeformation at high spin. The HD shapes undergo a centrifugal stretching, with a very few exceptions, that results in an increase of the values of the transition quadrupole Q_t and mass hexadecapole Q_{40} moments as well as the dynamic moments of inertia $J^{(2)}$ with increasing rotational frequency. The kinematic moments of inertia $J^{(1)}$ show very small variations in the frequency range of interest. These are general features of the HD bands which distinguish them from the normal- and superdeformed bands. Such features have not been seen before in the calculations without pairing. In unpaired regime, the Q_t, $J^{(2)}$ and $J^{(1)}$ values decrease with rotational frequency in the SD configurations; the only exceptions are the regions of unpaired bands crossings. The individual properties of the single-particle orbitals are not lost at HD. In the future, they will allow the assignment of the configurations to the HD bands using the relative properties of different bands. Such methods of configuration assignment were originally developed for superdeformation. In contrast to the case of SD, our analysis in the $A \sim 125$ mass region shows that only simultaneous application of the methods based on effective alignments and relative transition quadrupole moments by comparing experimental and theoretical $(i_{eff}, \Delta Q_t)$ values will

lead to a reliable configuration assignment for the HD bands. Moreover, additional information on the structure of the HD bands will be obtained from the band crossing features; the cases of strong interaction of the bands in unpaired regime at HD will be more common as compared with the situation at SD.

6.2 The physics of time-odd mean fields

Time-odd mean fields (nuclear magnetism) have been studied in nonrotating and rotating nuclear systems in a systematic way within the framework of covariant density functional theory in Ch. 4.

In odd-mass nuclei, it was found that nuclear magnetism always leads to an additional binding indicating its attractive nature in the CDFT. This additional binding only weakly depends on the parametrization of the RMF Lagrangian. On the contrary, time-odd mean fields in Skyrme EDF can be attractive and repulsive and show considerable dependence on the parametrization of density functional. This additional binding is larger in odd-neutron states than in odd-proton ones in the CDFT framework. The underlying microscopic mechanism of additional binding due to NM has been studied in detail. The perturbative results clearly indicate that additional binding due NM is defined mainly by time-odd fields and that the polarization effects in fermionic and mesonic sectors of the model cancel each other to a large degree. This additional binding due to NM can have a profound effect on the properties of odd-proton nuclei in the ground and excited states in the vicinity of the proton-drip line. In some cases it can transform the nucleus which is proton unbound (in the calculations without NM) into the nucleus which is proton bound.

This additional binding can significantly affect the decay properties of proton unbound nuclei by (i) increasing the half-lives of proton emitters (by many orders of magnitude in light nuclei) or (ii) moving the Q_p value inside or outside the Q_p window favorable for experimental observation of proton emission.

In the medium and heavy mass nuclei, the relative energies of different (quasi)particles are shown to be weakly affected by time-odd mean fields. Which is a result of that the additional bindings due to NM show little dependence on blocked single-particle state. This suggests that time-odd mean fields can be neglected in the fits of covariant density functionals aimed at accurate description of the energies of the single-particle states. Within specific configuration the impact of NM on the binding energies reaches its maximum at the terminating state [136]. Underlying microscopic mechanism for additional binding due to NM at such states has the same features as those seen in low-spin one- and two-particle configurations of odd and odd-odd nuclei. However, the magnitude of the effects is significantly larger. The perturbative results clearly indicate that additional binding due NM at terminating states is defined mainly by time-odd fields and that the polarization effects in fermionic and mesonic sectors of the model cancel each other to a large degree.

The phenomenon of signature separation [160] and its microscopic mechanism was addressed in both non-rotating and rotating systems. In non-rotating systems, it was found to be active in the configurations of odd-odd nuclei, configurations that have the same blocked proton and neutron states show an enhancment of this phenomena; this takes place either at ground state or at low excitation energy in the nuclei at or close to the $N = Z$ line. Some configurations away from the $N = Z$ line also show this effect but

signature separation is appreciably smaller. In rotating systems it is shown that the effects neglected in the current approach such as the residual interaction of unpaired proton and neutron and the coupling scheme of angular momenta vectors of these particles at low spin considerably complicate quantitative description of the spectra of odd-odd nuclei. The best way to confirm the existence of this phenomenon would be to find (both in experiment and in calculations) the configurations of odd-odd nuclei which show no signature splitting in the absence of time-odd mean fields and measurable signature separation in the presence of time-odd mean fields.

NM affects the band crossing and it can considerably modify its features (crossing frequencies, the properties of kinematic and dynamic moments of inertia in the band crossing region). In the calculations without pairing, these modifications depend on the underlying changes in the single-particle properties such as alignments and energies induced by NM. These effects are also active in the calculations with pairing. In addition, in the calculations with pairing the gradual breaking of high-j pairs proceeds faster in the presence of NM, which is reflected in a faster decrease of pairing with increasing Ω_x. Thus we can specify this effect as *an anti-pairing effect induced by NM*. Outside the band crossing regions, the contribution of NM to the kinematic and dynamic moments of inertia only weakly depends on the RMF parametrization.

The moments of inertia of super- and hyperdeformed configurations in unpaired regime come very close to the rigid-body values. Despite that the presence of strong vortices demonstrates the dramatic deviation of the currents from rigid rotation. On the contrary,

the moments of inertia of normal-deformed nuclei deviate considerably from the rigid-body value in the calculations without pairing.

Complicated structure of the currents in the rotating systems of independent fermions is the consequence of the fact that total current is the sum of the single-particle currents. The single-particle currents show vortices (circulations), the strength and localization of which depend on the single-particle state.

Although time-odd mean fields affect different physical observables, this investigation clearly shows that rotating nuclei still offer one of the best probes of this channel of density functional theories. This is because the impact of time-odd mean fields is significant representing on average 20% of kinematic and dynamic moments of inertia. In addition, it shows appreciable variations with configuration, particle number and rotational frequency; these variations provide a useful tool for a better test or definition of time-odd mean fields. Significant amount of the data on different types (normal- [69], superdeformed [20, 105, 70, 208, 104, 11], and smooth terminating [145, 11]) of rotational bands in unpaired regime available in different mass regions offers a testing ground for time-odd mean fields. This data is also extremely useful for fitting the parameters of time-odd mean fields as needed, for example, in Skyrme energy density functionals, in which these fields are not well defined (Refs. [33, 164]). Our investigation, however, suggests that such fit has to be performed to a significant set of rotational structures representing different mass regions and different configurations and spanned over significant frequency range in order to minimize the dependence of the fit parameters on the choice of experimental data.

6.3 Fission barriers in actinides and superheavy nuclei

The study of fission barriers in Ch. 5 was the first systematic investigation of the effect of triaxiality on the height of the fission barriers in the actinide and superheavy regions within covariant density functional theory. The calculations have been carried out with the parameter set NL3* and they have been compared in specific cases with the results of parameter sets DD-ME2 and DD-PC1. Pairing correlations are taken into account in the BCS approximation using seniority zero forces adjusted to empirical values of the gap parameters. In the actinide region it is found that with only one exception (^{234}Th) in all the nuclei under investigation the height of the inner fission barrier is reduced by allowing for triaxial deformations by $1-4$ MeV. The fission path avoids a maximum of the axially symmetric potential energy surface between the first and the second minimum by going through a valley in the (β,γ) plane with a triaxial deformation $\gamma \approx 10^{\circ}$. A systematic comparison of our results with experimentally determined fission barriers in this region shows reasonable agreement with data comparable with the best macroscopic+microscopic calculations.

Contrary to the results in actinides, triaxiality does not play a role for inner fission barrier in superheavy. However, it lowers the outer fission barriers by 2-3 MeV in reflection symmetric calculations. Inner and outer fission barriers obtained in the NL3* and DD-PC1 parametrizations are similar. On the contrary, the DD-ME2 parametrization produces barriers which are by 1-1.5 MeV higher than the ones obtained with NL3* and DD-PC1. The comparison of our results of calculations with those in non-relativistic models clearly shows that CDFT predictions for the heights of inner fission barriers still remain on the

lower end among nuclear structure models used so far. They are also lower than the estimates of inner fission barrier heights of Ref. [40].

REFERENCES

[1] R. J. Furnstahl and B. D. Serot, Nucl. Phys. A 673, 298 (2000).

[2] Extended Density Functionals in Nuclear Structure Physics, Springer Lecture Notes in Physics, Springer Berlin/Heidelberg, Eds. G. Lalazissis, P. Ring, and D. Vretenar, vol. 641, 2004.

[3] R. J. Furnstahl, Proc. of the ECT* school on "Renoralization Group and Effective Field Theory Approaches to Many-Body Systems", to be published in Springer Lecture Notes in Physics; arXiv:0708.1602 at xxx.lanl.gov.

[4] R. J. Furnstahl, G. Rupak and T. Schäfer, Ann. Rev. Nucl. Part. Sc. 58, 1 (2008).

[5] P. Hohenberg and W. Kohn, Phys. Rev. 136, B864 (1964).

[6] W. Kohn and L. J. Sham, Phys. Rev. 140, A1133 (1965).

[7] W. Kohn, Rev. Mod. Phys. 71, 1253 (1999).

[8] R. M. Dreizler and E. K. U. Gross, *Density Functional Theory* (Springer-Verlag, Berlin, 1990).

[9] B. D. Serot and J. D. Walecka, Int. J. Mod. Phys. E6, 515 (1997).

[10] M. Bender, P.-H. Heenen, and P.-G. Reinhard, Rev. Mod. Phys. 75, 121 (2003).

[11] D. Vretenar, A. V. Afanasjev, G. A. Lalazissis, and P. Ring, Phys. Rep. 409, 101 (2005).

[12] B. G. Carlsson, J. Dobaczewski, and M. Kortelainen, Phys. Rev. C 78, 044326 (2008).

[13] A. Sobiczewski and K. Pomorski, Prog. Part. Nucl. Phys. 58, 292 (2007).

[14] P. Ring and P. Schuck, The Nuclear Many-body Problem, (Springer Verlag, Heidelberg, 1980).

[15] B. D. Serot and J. D. Walecka, Adv. Nucl. Phys. 16, 1 (1986).

[16] R. J. Furnstahl and B. D. Serot, Nucl. Phys. A671, 447 (2000).

[17] P. J. Twin, B. M. Nyakó, A. H. Nelson, J. Simpson, M. A. Bentley, H. W. Cranmer-Gordon, P. D. Forsyth, D. Howe, A. R. Mokhtar, J. D. Morrisson, J. F. Sharpey-Schafer, and G. Sletten, Phys. Rev. Lett. 57, 811 (1986).

[18] B. Singh, R. Zywina, R. B. Firestone, Nucl. Data Sheets 97, 241 (2002).

[19] C. Baktash, B. Haas, and W. Nazarewicz, Ann. Rev. Nucl. Part. Sc. 45, 485 (1995).

[20] A. V. Afanasjev, J. König and P. Ring, Nucl. Phys. A608, 107 (1996).

[21] J. Dudek, K. Pomorski, N. Schunck and N. Dubray, Eur. Phys. J A20, 15 (2004).

[22] N. Chamel, Nucl. Phys. A747, 109 (2005).

[23] A. Krasznahorkay *et al*, Phys. Rev. Lett. 80, 2073 (1998).

[24] C. M. Brink, H. Friedrich, A. Weiguny and C. W. Wong, Phys. Lett. B33, 143 (1970).

[25] A. Galindo-Uribarri *et al*, Phys. Rev. Lett. 71, 231 (1993).

[26] G. Viesti *et al*, Phys. Rev. C51, 2385 (1995).

[27] B. Herskind *et al*, Phys. Scr. T125, 108 (2006).

[28] W. von Oertzen, V. Zherebchevsky, B. Gebauer, Ch. Schulz, S. Thummerer, D. Kamanin,G. Royer,and Th. Wilpert, Phys. Rev. C78, 044615 (2008).

[29] I-Y. Lee, AIP Conf. Proc 656, 343 (2003).

[30] D. Bazzacco, AIP Conf. Proc. 701, 265 (2004).

[31] I-Y. Lee, Nucl. Phys. A520, 641c (1990).

[32] U. Post, E. Wüst and U. Mosel, Nucl. Phys. A437, 274 (1985).

[33] J. Dobaczewski and J. Dudek, Phys. Rev. C 52, 1827 (1995).

[34] H. Zduńczuk, W. Satula, and R. A. Wyss, Phys. Rev. C 71, 024305 (2005).

[35] M. Bender, J. Dobaczewski, J. Engel, and W. Nazarewicz, Phys. Rev. C 65, 054322 (2002).

[36] U. Hofmann and P. Ring, Phys. Lett. B 214, 307 (1988).

[37] K. Rutz, M. Bender, P.-G. Reinhard, and J. A. Maruhn, Phys. Lett. B468, 1 (1999).

[38] A. V. Afanasjev and P. Ring, Phys. Rev. C 62, 031302(R) (2000).

[39] A. V. Afanasjev, T. L. Khoo, S. Frauendorf, G. A. Lalazissis, and I. Ahmad, Phys. Rev. C 67, 024309 (2003).

[40] M. G. Itkis, Y. T. Oganessian, and V. I. Zagrebaev, Phys. Rev. C65, 044602 (2002).

[41] M. Arnould and K. Takahashi, Rep. Prog. Phys. 62, 395 (1999).

[42] A. Mamdouh, J. M. Pearson, M. Rayet, and F. Tondeur, Nucl. Phys. A679, 337 (2001).

[43] A. Staszczak, A. Baran, J. Dobaczewski, and W. Nazarewicz, Phys. Rev. C80, 014309 (2009).

[44] M. Warda, J. L. Egido, L. M. Robledo, and K. Pomorski, Phys. Rev. C66, 014310 (2002).

[45] J. Dobaczewski, J. Dudek, and R. Wyss, Phys. Rev. C 67, 034308 (2003).

[46] P. Möller, A. J. Sierk, and A. Iwamoto, Phys. Rev. Lett. 92, 072501 (2004).

[47] A. Sobiczewski and M. Kowal, Phys. Scripta T125, 68 (2006).

[48] J. Dobrowolski, K. Pomorski, and J. Bartel, Phys. Rev. C75, 024613 (2007).

[49] P. Möller, A. J. Sierk, T. Ichikawa, A. Iwamoto, R. Bengtsson, H. Uhrenholt, and S. Åberg, Phys. Rev. C79, 064304 (2009).

[50] A. Dobrowolski, B. Nerlo-Pomorska, K. Pomorski, and J. Bartel, Acta Phys. Polonica B40, 705 (2009).

[51] A. K. Dutta, J. M. Pearson, and F. Tondeur, Phys. Rev. C61, 054303 (2000).

[52] M. Bender, K. Rutz, P.-G. Reinhard, J. A. Maruhn, and W. Greiner, Phys. Rev. C58, 2126 (1998).

[53] L. Bonneau, P. Quentin, and D. Samsoen, Eur. Phys. J. A21, 391 (2004).

[54] A. Staszczak, J. Dobaczewski, and W. Nazarewicz, Acta Phys. Polonica B B38, 1589 (2007).

[55] M. Warda, Eur. Phys. J. A42, 605 (2009).

[56] R. Rodríguez-Guzmán, P. Sarriguren, L. M. Robledo, and J. E. Garcia-Ramos, Phys. Rev. C81, 024310 (2010).

[57] G. A. Lalazissis, S. Karatzikos, R. Fossion, D. Pena Arteaga, A. V. Afanasjev, P. Ring, Phys. Lett. B671, 36 (2009).

[58] S. Typel and H. H. Wolter, Nucl. Phys. A656, 331 (1999).

[59] G. A. Lalazissis, T. Nikšić, D. Vretenar, and P. Ring, Phys. Rev. C71, 024312 (2005).

[60] Y. K. Gambhir, P. Ring, and A. Thimet, Ann. Phys. (N.Y.) 198, 132 (1990).

[61] W. Kohn and L. J. Sham, Phys. Rev. 137, A1697 (1965).

[62] J. D. Walecka, Ann. Phys. (N.Y.) 83, 491 (1974).

[63] J. Boguta and A. R. Bodmer, Nucl. Phys. A292, 413 (1977).

[64] G. A. Lalazissis, J. König and P. Ring, Phys. Rev. C 55, 540 (1997).

[65] T. Nikšić, D. Vretenar, and P. Ring, Phys. Rev. C78, 034318 (2008).

[66] W. Koepf and P. Ring, Nucl. Phys. A493, 61 (1989).

[67] W. Koepf and P. Ring, Nucl. Phys. A511, 279 (1990).

[68] J. König and P. Ring, Phys. Rev. Lett. 71, 3079 (1993).

[69] A. V. Afanasjev and S. Frauendorf, *Phys. Rev.* C71, 064318 (2005).

[70] A. V. Afanasjev, I. Ragnarsson and P. Ring, Phys. Rev. C 59, 3166 (1999).

[71] D. R. Inglis, Phys. Rev. 96, 1059 (1954).

[72] P.-G. Reinhard, M. Rufa, J. Maruhn, W. Greiner and J. Friedrich, Z. Phys. A323, 13 (1986).

[73] W. Greiner, *Relativistic Quantum Mechanics* (Springer-Verlag, Berlin, 1990).

[74] M. Yamagami and K. Matsuyanagi, Nucl. Phys. A672, 123 (2000).

[75] P. Ring, Y. K. Gambhir, and G. A. Lalazissis, Comp. Phys. Comm. 105, 77 (1997).

[76] P. Ring, private communication (2009).

[77] A. Bohr and B. Mottelson, Nuclear Structure, vol. II, Benjamin, New York (1975).

[78] R. Bengtsson, I. Ragnarsson, S. Åberg, A. Gyurkovich, A. Sobiczewski, and K. Pomorski, Nucl. Phys. A473, 77 (1987).

[79] R. R. Chasman, Phys. Lett. B302, 134 (1993).

[80] J. Dudek, in: The Variety of Nuclear shapes, eds. J. D. Garrett. (World Scientific, Singapore, 1988) p.195.

[81] S. Åberg, Nucl. Phys. A557, 17c (1993).

[82] S. Ćwiok, W. Nazarewicz, J. X. Saladin, W. Płóciennik, and A. Johnson, Phys. Lett. B322, 304 (1994).

[83] T. Werner, and J. Dudek, At. Data Nucl. Data Tables 59, 1 (1995).

[84] R. R. Chasman and L. M. Robledo, Phys. Lett. B351, 18 (1995).

[85] L. Jönsson, and S. Åberg, Nucl. Phys. A627, 53 (1997).

[86] R. R. Chasman, Phys. Rev. C64, 024311 (2001).

[87] J. L. Egido, L. M. Robledo, and R. R. Chasman, Phys. Lett. B393, 13 (1997).

[88] A. Staszczak, J. Dobaczewski, and W. Nazarewicz, Int. J. Mod. Phys. E16, 310 (2007).

[89] S. Hilaire and M. Girod, Eur. Phys. J. A33, 237 (2007).

[90] K. Rutz, J. A. Maruhn, P.-G. Reinhard, and W. Greiner, Nucl. Phys. A590, 680 (1995).

[91] A. V. Afanasjev and S. Frauendorf, Phys. Rev. C 72, 031301(R) (2005).

[92] T. Inakura, S. Mizutori, M. Yamagami, and K. Matsuyanagi, Nucl. Phys. A710, 261 (2002).

[93] V. V. Pashkevich, Nucl. Phys. A169, 275 (1971).

[94] P. Möller and J. R. Nix, Physics and Chemistry of Fission 1973 (IAEA, Vienna, 1974) Vol. 1, p. 103.

[95] R. M. Clark *et al*, Phys. Rev. Lett. 87, 202502 (2001).

[96] A. Görgen *et al*, Phys. Rev. C65, 027302 (2002).

[97] N. Schunck, J. Dudek, and B. Herskind, Phys. Rev. C75, 054304 (2007).

[98] B. M. Nyakó *et al*, Acta Phys. Pol. B36, 1033 (2005).

[99] H. Hübel, Acta Phys. Pol. B36, 1015 (2005).

[100] D. R. LaFosse *et al*, Phys. Rev. Lett. 74, 5186 (1995).

[101] D. R. LaFosse *et al*, Phys. Rev. C54, 1585 (1996).

[102] J. N. Wilson *et al*, Phys. Rev. C56, 2502 (1997).

[103] T. Bengtsson, I. Ragnarsson and S. Åberg, Phys. Lett. B208, 39 (1988).

[104] I. Ragnarsson, Nucl. Phys. A557, 167c (1993).

[105] A. V. Afanasjev, G. Lalazissis, and P. Ring, Nucl. Phys. A 634, 395 (1998).

[106] W. Satuła, J. Dobaczewski, J. Dudek and W. Nazarewicz, Phys. Rev. Lett. 77 5182 (1996).

[107] M. Matev, A. V. Afanasjev, J. Dobaczewski, G. A. Lalazissis, W. Nazarewicz, Phys. Rev. C76, 034304 (2007).

[108] S. T. Clark, G. Hackman, R. V. F. Janssens, R. M. Clark, P. Fallon, S. N. Floor, G. J. Lane, A. O. Macchiavelli, J. Norris, S. J. Sanders, and C. E. Svensson, Phys. Rev. Lett. 87, 172503 (2001).

[109] R. W. Laird *et al*, Phys. Rev. Lett. 88, 152501 (2002).

[110] M. Samyn, S. Goriely and J. M. Pearson, Phys. Rev. C72, 044316 (2005).

[111] W. Nazarewicz and I. Ragnarsson, in *Handbook on Nuclear Properties*, edited by D. N. Poenaru and W. Greiner (Claredon Press, Oxford, 1996), p. 80.

[112] A. V. Afanasjev, D. B. Fossan, G. J. Lane and I. Ragnarsson, Phys. Rep. 322, 1 (1999).

[113] G. A. Lalazissis and P. Ring, Phys. Lett. B427, 225 (1998) 225.

[114] M. Devlin, A. V. Afanasjev, R. M. Clark, D. R. LaFosse, I. Y. Lee, F. Lerma, A. O. Macchiavelli, R. W. MacLeod, I. Ragnarsson, P. Ring, D. Rudolph, D. G. Sarantites and P. G. Thirolf, Phys. Rev. Let. 82, 5217 (1999).

[115] M. M. Sharma, M. A. Nagarajan and P. Ring, Phys. Lett. B312, 377 (1993).

[116] M. Rufa, P.-G. Reinhard, J. A. Maruhn, W. Greiner, and M. R. Strayer, Phys. Rev. C38, 390 (1988).

[117] G. de France *et al.*, Phys. Lett. B331, 290 (1994).

[118] B. Cederwall *et al*., Phys. Lett. B346, 244 (1995).

[119] J. K. Johansson et al., Phys. Rev. Lett. 63, 2200 (1989).

[120] I. Ragnarsson, Phys. Lett. B264, 5 (1991).

[121] Y. R. Shimizu *et al.*, Rev. Mod. Phys. 61, 131 (1989).

[122] W. Nazarewicz, R. Wyss, and A. Johnson, Nucl. Phys. A503, 285 (1989).

[123] T. Lauritsen *et al*, Phys. Rev. Lett. 88, 042501 (2002).

[124] P. J. Dagnall *et al*., Phys. Lett. B335, 313 (1994).

[125] G. E. Rathke *et al.*, Phy. Lett. B209, 177 (1988).

[126] I. Ragnarsson, private communication (2009)

[127] F. G. Kondev *et al*, Phys. Lett. B437, 35 (1998).

[128] E. S. Paul *et al*, Phys. Rev. C 71, 054309 (2005).

[129] H. Hübel, private communication 2008.

[130] R. Wyss and W. Satuła, Phys. Lett. B351, 393 (1995).

[131] A. V. Afanasjev, P. Ring, and J. König, Nucl. Phys. A676, 196 (2000).

[132] G. Hackman *et al*, Phys. Rev. C 52, R2293 (1995).

[133] A. V. Afanasjev and P. Ring, Nucl. Phys. A654, 647c (1999).

[134] P. Fallon, Nucl. Phys. A752, 231c (2005).

[135] K. Rutz, M. Bender, P.-G. Reinhard, J. A. Maruhn, and W. Greiner, Nucl. Phys. A634, 67 (1998).

[136] A. V. Afanasjev, Phys. Rev. C 78, 054303 (2008).

[137] Y. M. Engel, D. M. Brink, K. Geoke, S. J. Krieger, and D. Vauterin, Nucl. Phys. A249, 215 (1975).

[138] V. O. Nesterenko, W. Kleinig, J. Kvasil, P. Vesely, and P.-G. Reinhard, Int. J. Mod. Phys. E 17, 89 (2008).

[139] N. Hinohara, T. Nakatsukasa, M. Matsuo, and K. Matsuyanagi, Prog. Theor. Phys. 115, 567 (2006).

[140] A. S. Umar and V. E. Oberacker, Phys. Rev. C 73, 054607 (2006).

[141] W. Satula, in *Nuclear Structure 98*, edited by C. Baktash, AIP Conf. Proc. No. 481 (AIP, New York, 1999), p. 114.

[142] T. Duguet, P. Bonche, P.-H. Heenen, and J. Meyer, Phys. Rev. C 65, 014310 (2001).

[143] J. Dobaczewski, B. G. Carlsson and M. Kortelainen, J. Phys. G37 075106 (2010) .

[144] J. W. Negele, in *Effective interactions and Operators in Nuclei*, Lecture Notes in Physics 40 (Springer, Berlin, 1975), p.250

[145] A. V. Afanasjev, D. B. Fossan, G. J. Lane and I. Ragnarsson, Phys. Rep. 322, 1 (1999).

[146] J. J. Valiente-Dobón *et al*, Phys. Rev. Lett. 95 232501 (2005).

[147] W. Satula and R. Wyss, Rep. Prog. Phys. 68, 131 (2005).

[148] A. V. Afanasjev, P. Ring and I. Ragnarsson, Proc. Int. Workshop PINGST2000 "Selected topics on $N = Z$ nuclei", 2000, Lund, Sweden, Eds. D. Rudolph and M. Hellström, (2000) p. 183.

[149] K. Langanke and M. Wiescher, Rep. Prog. Phys. 64, 1 (2001).

[150] J. Rikovska Stone, J. Phys. G31, R211 (2005).

[151] M. Zalewski, J. Dobaczewski, W. Satula, and T. R. Werner, Phys. Rev. C 77, 024316 (2008).

[152] Z. Szymanski, “Fast Nuclear Rotations”, Oxford studies in physics, Claredon press, Oxford, 1983

[153] J. Dobaczewski, P. Magierski, W. Nazarewicz, W. Satula, and Z. Szymański, Phys. Rev. C 63, 024308 (2001).

[154] G. F. Bertsch, C. A. Bertulani, W. Nazarewicz, N. Schunck, and M. V. Stoitsov, Phys. Rev. C 79, 034306 (2009).

[155] T. Duguet, P. Bonche, P.-H. Heenen, J. Meyer, Phys. Rev. C 65, 014311 (2001).

[156] S. Åberg, P. B. Semmes, and W. Nazarewicz, Phys. Rev. C 56, 1762 (1997).

[157] G. A. Lalazissis, D. Vretenar, and P. Ring, Nucl. Phys. A679, 481 (2001).

[158] P. J. Woods and C. N. Davids, Annu. Rev. Nucl. Part. Sci. 47, 541 (1997).

[159] V. I. Goldansky, Nucl. Phys. 19, 482 (1960).

[160] H. Molique, J. Dobaczewski and J. Dudek, Phys. Rev. C 61, 044304 (2000).

[161] C. J. Gallagher Jr., and S. A. Moszkowski, Phys. Rev. 111, 1282 (1958).

[162] J. P. Boisson, R. Piepenbring and W. Ogle, Phys. Rep. 26, 99 (1976).

[163] J. F. Berger, M. Girod, and D. Gogny, Comp. Phys. Comm. 63, 365 (1991).

[164] N. Schunck, J. Dobaczewski, J. McDonnell, J. Móre, W. Nazarewicz, J. Sarich, and M. V. Stoitsov, Phys. Rev. C 81, 024316 (2010).

[165] M. A. Delaplanque, S. Frauendorf, V. V. Pashkevich, S. Y. Chu, and A. Unzhakova, Phys. Rev. C 69, 044309 (2004).

[166] A. V. Afanasjev, J. König, P. Ring, L. M. Robledo, J. L. Egido, Phys. Rev. C 62, 054306 (2000).

[167] A. Bohr and B. Mottelson, Nuclear Structure, vol. II, Benjamin, New York (1975).

[168] K.-K. Kan and J. J. Griffin, Phys. Rev. C 15, 1126 (1977).

[169] M. Durand, P. Schuck, and J. Kunz, Nucl. Phys. A439, 263 (1985).

[170] I. N. Mikhailov, P. Quentin, and D. Samsoen, Nucl. Phys. A627, 259 (1997).

[171] H. Laftchiev, D. Samsoen, P. Quentin, and I. N. Mikhailov, Phys. Rev. C 67, 014307 (2003).

[172] M. Radomski, Phys. Rev. 14, 1704 (1976).

[173] P. Gulshani and D. J. Rowe, Can. J. Phys. 56, 468 (1978).

[174] P. Gulshani and D. J. Rowe, Can. J. Phys. 56, 480 (1978).

[175] J. Kunz and U. Mosel, Nucl. Phys. A323, 271 (1979).

[176] J. Fleckner, J. Kunz, U. Mosel, and E. Wuest, Nucl. Phys. A339, 227 (1980).

[177] C. E. Svensson *et al*, Phys. Rev. Lett. 82, 3400 (1999).

[178] Q. A. Ijaz *et al*, Phys. Rev. C 80, 034322 (2009).

[179] T. Troudet and R. Arvieu, Annals of Physics 134, 1 (1981).

[180] S. G. Nilsson and I. Ragnarsson, *Shapes and Shells in Nuclear Structure*, Cambridge University Press, 1995.

[181] C. G. Andersson, G. Hellström, G. Leander, I. Ragnarsson, S. Åberg, J. Krumlinde, S. G. Nilsson and Z. Szymański, Nucl. Phys. A309, 141 (1978).

[182] M. J. A. de Voigt, J. Dudek and Z. Szymański, Rev. Mod. Phys. 55, 949 (1983).

[183] W. Satula, J. Dobaczewski, W. Nazarewicz, and M. Rafalski, Phys. Rev. C 81, 054310 (2010).

[184] A. Goel and A. K. Jain, Phys. Rev. C 45, 221 (1992).

[185] D. Nosek, J. Kvasil, R. K. Sheline, P. C. Sood, and J. Nosková, Int. J. Mod. Phys. E3, 967, 1994.

[186] N. D. Newby Jr., Phys. Rev. 125, 2036 (1962).

[187] A. K. Jain, R. K. Sheline, D. M. Headly, P. C. Sood, D. G. Burke, I. Hrǐvnácová, J. Kvasil, and D. Nosek, R. W. Hoff, Rev. Mod. Phys. 70, 843 (1998).

[188] A. K. Jain, J. Kvasil, R. K. Sheline, and R. W. Hoff, Phys. Rev. C 40, 432 (1989).

[189] L. Bennour, J. Libert, M. Meyer, and P. Quentin, Nucl. Phys. A465, 35 (1987).

[190] S. Frauendorf, Rev. Mod. Phys. 73, 463 (2001).

[191] V. Blum, J. Maruhn, P.-G. Reinhard, and W. Greiner, Phys. Lett. B323, 262 (1994).

[192] Z. Ren, F. Tai, and D.-H. Chen, Phys. Rev. C66, 064306 (2002).

[193] W. Zhang, S.-S. Zhang, S.-Q. Zhang, and J. Meng, Chin. Phys. Lett. 20, 1694 (2003).

[194] W. H. Long, N. Van Giai, and J. Meng, Phys. Lett. B640, 150 (2006).

[195] S. Karatzikos, A. V. Afanasjev, G. A. Lalazissis, and P. Ring, Phys. Lett. B689, 72 (2010).

[196] A. V. Afanasjev, J. König, and P. Ring, Phys. Rev. C60, 051303(R) (1999).

[197] Z. P. Li, T. Nikšić, D. Vretenar, P. Ring, and J. Meng, to be published.

[198] P. Möller and J. Nix, Nucl. Phys. A536, 20 (1992).

[199] J. Dudek, A. Majhofer and J. Skalski, J. Phys. G6, 447 (1980).

[200] M. Bender, P.-H. Heenen, and P. Bonche, Phys. Rev. C70, 054304 (2004).

[201] S. T. Belyaev, Mat. Fys. Medd. Dan. Vid. Selsk. 31, No. 11 (1959).

[202] M. Bender, K. Rutz, P.-G. Reinhard, and J. A. Maruhn, Eur. Phys. J. A8, 59 (2000).

[203] S. J. Krieger, P. Bonche, H. Flocard, P. Quentin, and M. S. Weiss, Nucl. Phys. A517, 275 (1990).

[204] M. Kowal, P. Jacimowicz, and A. Sobiczwski Phys. Rev. C82, 014303 (2010)

[205] T. Bürvenich, M. Bender, J. A. Maruhn and P. -G. Reinhard, Phys. Rev. C69, 014307 (2004)

[206] A. A. Nikolaus, T. Hoch, and D. Madland, Phys. Rev. C46, 1757 (1992).

[207] T. Bürvenich, D. G. Madland, J. A. Maruhn, and P.-G. Reinhard, Phys. Rev. C65, 044308 (2002).

[208] B. Singh, R. Zywina and R. B. Firestone, Nucl. Data Sheets 97, 241 (2002).

[209] I. Muntian, Z. Patyk, and A. Sobiczewski, Acta Phys. Polonica B B32, 691 (2001).

[210] P. Moller, J. R. Nix, K.-L. Kratz, At. Data Nucl. Data Tables 66, 131 (1997)

[211] J.-P. Delaroche, M. Girod, H. Goutte, and J. Libert, Nucl. Phys. A771, 103 (2006).

APPENDIX A

DETAILS OF THE CONSTRAINED CALCULATIONS AND CURRENTS PLOTTING

A.1 Details of constrained calculations

The aim of the constrained calculations is to calculate the properties of the atomic nuclei under study at any deformation and shape. In the calculations of the fission barrier one needs to calculate the binding energy as a function of quadrupole deformation.

The number of points needed to plot a two-dimensional potential energy surface (PES) in the (β, γ) plane, exceeds 200 points per nucleus. Fig. A.1 shows the points in the (q_{20},q_{22}) plane. Running these extensive calculations on a single processor would requires months of computer power. Fig.A.2 shows the time required to get a convergent solution for deformation near the normal- and superdeformed minima, as well as the dependence of the binding energy, on number of fermonic shells N_F. It clearly shows that for the actinide and superheavy regions $N_F = 20$ is required to achieve an accuracy around 100 KeV for the binding energy. One point in the deformation space near the normal-deformed minimum requires around 12 hours, while near the superdeformed minimum it takes almost a day to get a convergent solution.

The interface is built to run the code using Message Passing Interface (MPI) libraries. The program reads from the input file the points of the deformation space, at which the calculations are required. The user has the option to specify how many constrains to run and what are the constrained operators are. The user can run the constrains on either Q_{20} and, Q_{22} moments or both of them. To obtain axially symmetric solution both Q_{20}, Q_{22} should be constrained. However, the later should be constrained to zero.

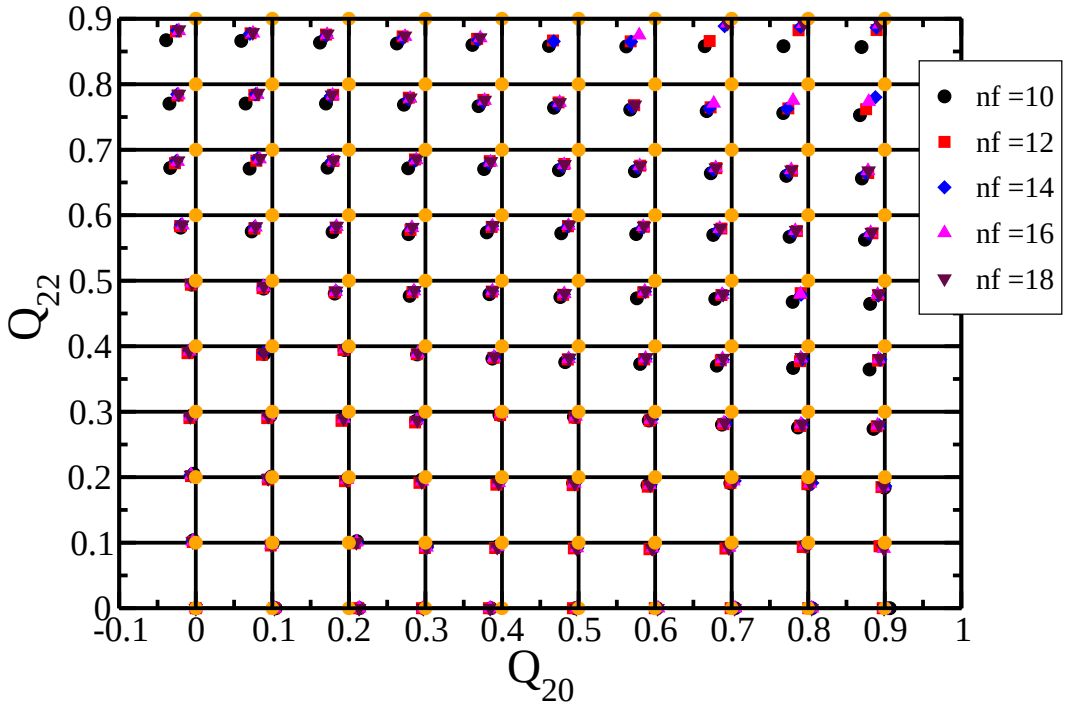

Figure A.1

The difference between the desired and calculated deformation.

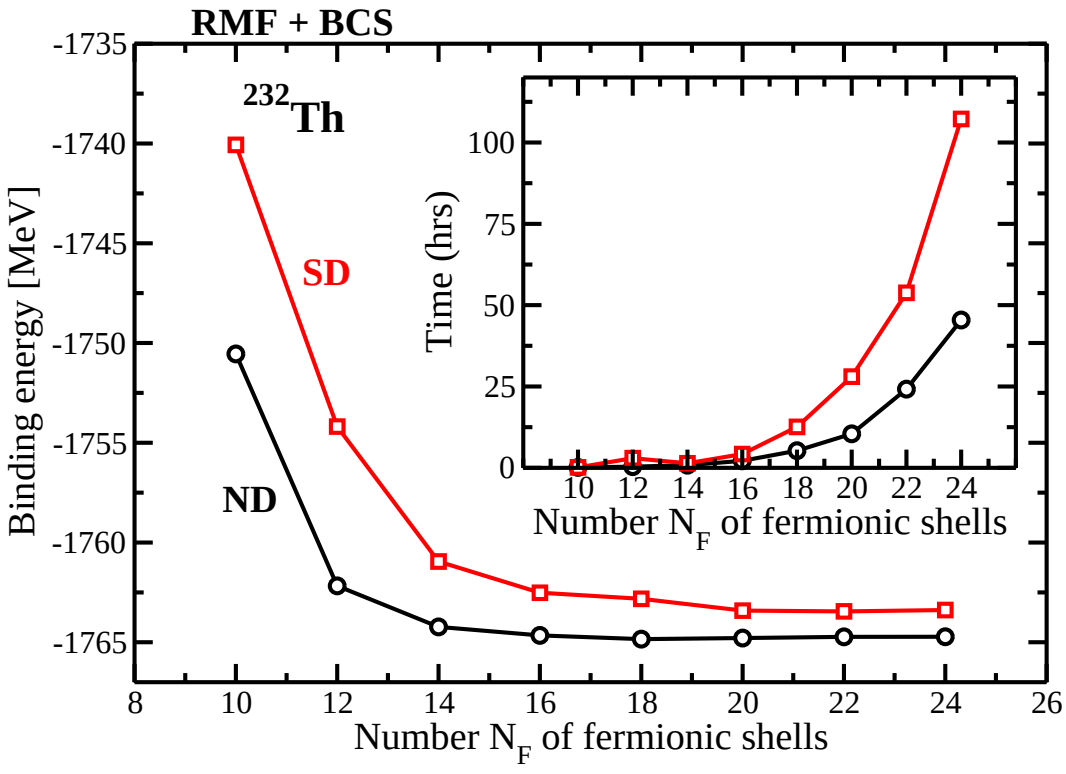

Figure A.2

The binding energy and the time required for convergence for ^{232}Th.

It is worth to note that in the calculations one never gets exactly the desired point in the deformation space. Fig. A.1 shows the difference between the desired points and calculated points in the (Q_{20},Q_{22}) plane. The dependence of this difference on the number of fermonic shells N_F is also shown. The difference between the desired and calculated points increases with the increasing values of the constrained operators. There is almost no difference in the values of these points near the axially symmetric shapes. However, when deviate from axial shapes and the value of the γ deformation increase the difference start to increase.

A.2 Currents plotting

In the case of reflection symmetry, the solution of the CDFT equations is obtained only in one octant of a sphere. One has to perform reflection of the currents into the other octant, in order to create the current plot in the xy-plane or in the two planes. However, the currents are vector quantities and one has to follow a specific reflection rules for the vectors.

The reflections rules for the components of the current vectors are

- Reflection around the x-axis:

$$\begin{aligned} j_x(-x,y,z) &= -j_x(x,y,z) \\ j_y(-x,y,z) &= j_y(x,y,z) \\ j_z(-x,y,z) &= j_z(x,y,z) \end{aligned} \tag{A.1}$$

- Reflection around the y-axis:

$$\begin{aligned} j_x(x,-y,z) &= -j_x(x,y,z) \\ j_y(x,-y,z) &= j_y(x,y,z) \\ j_z(x,-y,z) &= -j_z(x,y,z) \end{aligned} \tag{A.2}$$

- Reflection around the z-axis:

$$\begin{aligned} j_x(x,y,-z) &= -j_x(x,y,z) \\ j_y(x,y,-z) &= -j_y(x,y,z) \\ j_z(x,y,-z) &= j_z(x,y,z) \end{aligned} \tag{A.3}$$

A matlab code has been developed to plot the currents, which was used to plot Figs. (4.4,4.5,4.6, 4.25,4.26,4.30 and 4.31) in Ch. 4. The currents in those figures were plotted at an arbitrary scale F for better visualization.